Ultra-Wideband Radar Tomography Using an Agilent E5071B Vector Network Analyzer and Rotating Platform

Lanche Linden Grootboom

A dissertation submitted to the Department of Electrical Engineering,
University of Cape Town, in fulfilment of the requirements
for the degree of Master of Science in Engineering.

Cape Town, January 2013

Declaration

I declare that this dissertation is my own, unaided work. It is being submitted for the degree of Master of Science in Engineering to the University of Cape Town. It has not been submitted before for any degree or examination in any other university.

Signature of Author ..... Signed by candidate .....

Cape Town

January 2013

Abstract

Ultra-Wideband (UWB) technology has become very famous amongst the radar imaging community. This system is well suited for tomographic imaging as it offers high spacial resolution and a low probability of detection. Some of the UWB applications include ground penetrating radar, medical imaging and some military applications.

In this thesis an UWB radar imaging system has been designed and implemented using an Agilent E5071B Vector Network Analyzer and a rotating pedestal. The two ports of the device are used as a transmitter and receiver, measuring the frequency domain data of the scene in front of the antennas at each angular position as the rotating pedestal rotates in front of the antennas. This data is then put through a time domain back-projection algorithm which reconstructs an image of the scene. This is done in 2D space and then later extended to 3D space.

This project is dedicated to God, my parents Madeline and Selvin Grootboom, my family and loved ones, without whom none of this would have been possible. This project has been carried out to the best of my ability.

Acknowledgements

I would like to thank Assoc. Prof. A.J.Wilkinson for his help and supervision throughout the project, the CSIR Ledger Program for the funding of my project and studies and the University of Cape Town for the opportunity for me to complete my Masters of Science in Electrical Engineering at their facilities.

Contents

Declaration i

Abstract ii

Acknowledgements iv

List of Symbols xiv

Nomenclature xvi

1 Introduction 1

1.1 Introduction to Radar Tomography and Ultra-Wideband Radar 1

1.2 Background 2

1.3 Objectives 3

1.4 Limitations and Scope of Thesis 3

1.5 Thesis Outline 4

2 Literature Review 5

2.1 Ultra-Wideband Signals and Systems 5

2.1.1 Definition 5

2.1.2 Ultra-Wideband Waveforms 6

2.2 Tomography 9

2.2.1 Transmission Tomography 9

2.2.2 Reflection Tomography 13

3 System Design and Control 17

3.1 Overall System Design 17

3.2 System Overview 20

3.3 Rotating Platform Design 21

3.4 VNA Design Considerations 23

3.4.1 Frequency Selection 24

3.4.2 Frequency Spacing . . . 25
3.4.3 Output Power . . . 26
3.4.4 S-Parameter Measurements . . . 27
3.5 Antennas . . . 30
3.6 Signal Processing . . . 35
3.6.1 Antenna Calibration . . . 36
3.6.2 Background Subtraction . . . 36
3.6.3 Windowing . . . 39
3.6.4 Zero Padding . . . 40
3.6.5 Reconstruction Algorithm . . . 41

4 Simulation **47**
4.1 2-Dimensional Simulations . . . 47
4.1.1 Transmitted Signal . . . 49
4.1.2 Simulation of Single Target . . . 51
4.1.3 Simulation of Multiple Targets . . . 63
4.1.4 Effect of Targets at Different Heights . . . 72
4.2 3-Dimensional Simulations . . . 75
4.2.1 Simulation of Single Target . . . 76
4.2.2 Simulation of Multiple Target . . . 79

5 Results **83**
5.1 2-Dimensional Experiments . . . 83
5.1.1 Single Thin Long Target . . . 84
5.1.2 Single Brick Shaped Target . . . 93
5.1.3 Single Rectangular Shaped Target . . . 98
5.1.4 Multiple Cylindrically Shaped Targets . . . 101
5.1.5 Multiple Targets with Various Shapes . . . 104
5.1.6 Complex Target . . . 110
5.2 3-Dimensional Experiment . . . 116
5.2.1 Single Point Target . . . 117
5.2.2 Multiple Point Targets . . . 123
5.2.3 Single cylindrically Target . . . 128

6 Conclusions and Recommendations **134**

A Cobham H-1498 Series Broadband Horn Antenna **137**

B Bourns 6539/6639 Precision 10 $k\Omega$ Potentiometer **139**

C LabVIEW GUI **141**

C.1 Control Pedestal Function 141

C.2 Move to Set Position Function 142

C.3 Experiment Function 143

C.4 Radar Mode Function 144

C.5 Signal Processing Function 145

C.6 Capture Data Function 146

D Software Source Code **147**

Bibliography **148**

List of Figures

2.1 Plots showing the 3 dB bandwidth of an impulse signal and a bandlimited impulse signal [9] . . . 7
2.2 Plot of a 100-400 MHz chirp signal in the time and frequency domain [13] 8
2.3 Plot of a step-frequency waveform [17] . . . 8
2.4 An object function and $f(x,y)$ and it's projections $P_\theta(t)$[18] . . . 10
2.5 Fourier slice theorem [18] . . . 11
2.6 Transducer illuminating an object with a wide fan-beam and measuring line integrals over circular arcs of the objects reflectivity function[18] . . 14

3.1 Pictures of the hardware that was used . . . 19
3.2 UWB radar tomography system . . . 20
3.3 1-axis rotating pedestal that was used. . . . 22
3.4 Azimuth over elevation (2-axis) rotating pedestal that was used. . . . 22
3.5 Parallel port [26] . . . 23
3.6 S-parameters of a 2-port network . . . 27
3.7 Picture of the horn antennas . . . 30
3.8 S_{11} measurement of the horn antenna . . . 31
3.9 Frequency domain data (transfer function) of horn antennas at different distances . . . 32
3.10 Horn antenna beam pattern . . . 34
3.11 Block diagram of the UWB system. . . . 35
3.12 Picture of the antenna location when measuring antennas transfer function 36
3.13 Figure showing the effects of background subtraction when no clutter present . . . 37
3.14 Figure showing the effects of background subtraction when clutter is present 39
3.15 Image of the experiment scene . . . 41
3.16 Reconstruction algorithm . . . 42
3.17 Block Diagram of reconstruction algorithm . . . 44

4.1 Simulation setup 48
4.2 Image showing the location of the simulated point target 51
4.3 Simulated received data in the frequency domain 52
4.4 Simulated frequency and time domain data at 270 degree azimuth rotation 53
4.5 Simulated locus of target and reconstructed image of scene 55
4.6 Cut through brightest point in reconstructed scene 55
4.7 Simulated data for system bandwidth of 4.5 GHz 56
4.8 Cut through brightest point in reconstructed scene for bandwidth of 4.5 GHz 57
4.9 Simulated data for system bandwidth of 1 GHz 57
4.10 Cut through brightest point in reconstructed scene for bandwidth of 1 GHz 58
4.11 Rotating scene with targets on the pedestal 59
4.12 Effect of aperture sampling 61
4.13 Change in down range distance of centre of rotation 63
4.14 Change in cross range distance of centre of rotation 63
4.15 Illustration of viewing angle 64
4.16 Illustration of viewing angle with smaller synthesized aperture 65
4.17 Image showing the location of the simulated point target 66
4.18 Simulated data with 10 degree viewing angle 67
4.19 Vertical and horizontal slices for 10 degree viewing angle 67
4.20 Simulated data with 30 degree viewing angle 68
4.21 Vertical and horizontal slices for 30 degree viewing angle 68
4.22 Simulated data with 90 degree viewing angle 69
4.23 Vertical and horizontal slices for 90 degree viewing angle 69
4.24 Simulated data with 180 degree viewing angle 70
4.25 Vertical and horizontal slices for 180 degree viewing angle 70
4.26 Simulated data with 360 degree viewing angle 71
4.27 Vertical and horizontal slices for 360 degree viewing angle 71
4.28 Figure of the simulated point target 73
4.29 Simulated frequency and time domain data 74
4.30 Simulated processed data 74
4.31 Figure of the simulated point target 76
4.32 Simulated data with 10 degree viewing angle 77
4.33 Vertical and horizontal slices 77
4.34 3D image of the reconstructed point target 78
4.35 Figure of the simulated point target 79
4.36 Simulated data with 10 degree viewing angle 80

4.37 Vertical and horizontal slices 80
4.38 3D image of the reconstructed point targets 81
4.39 Vertical and horizontal slices through single target 82

5.1 Diagram showing the experiment setup 84
5.2 Diagram and photograph of the experiment for a single thin long target . . 87
5.3 Photograph of scene for single thin long target 87
5.4 Frequency and time domain data for single thin long target 88
5.5 Standard deviation of 5 measurements per angular position 89
5.6 Locus of target and reconstructed image of scene for single thin long target 90
5.7 Cut through brightest point in reconstructed scene 90
5.8 2D reconstructed image of scene and Top view photograph of scene . . . 91
5.9 Focusing algorithm output by adjusting down range and cross distance of centre of rotation 92
5.10 Diagram and photograph of the experiment for a single brick shaped target 94
5.11 Photograph of scene for single brick shaped target 94
5.12 Frequency and time domain data for single brick shaped target 95
5.13 Locus of Target and Reconstructed Image of Scene for Single Brick Shaped Target 95
5.14 Magnitude and phase extracted along brightest point on locus 96
5.15 Cut through brightest point in reconstructed scene 96
5.16 2D reconstructed image of scene and top view photograph of scene . . . 97
5.17 Diagram and photograph of the experiment for a single rectangular shaped target 98
5.18 Photograph of scene for single rectangle shaped target 98
5.19 Frequency and time domain data for single rectangular shaped target . . . 99
5.20 Locus of target and reconstructed image of scene for single rectangular shaped target 99
5.21 2D reconstructed image of scene and top view photograph of scene 100
5.22 Diagram and photograph of the experiment for multiple cylindrically shaped targets 101
5.23 Photograph of experiment for multiple cylindrically shaped targets 101
5.24 Frequency and time domain data for multiple cylindrically shaped targets 102
5.25 Locus of target and reconstructed image of scene for multiple cylindrically shaped targets 102
5.26 2D reconstructed image of scene and top view photograph of scene 103

5.27 Diagram and photograph of the experiment for multiple various shaped targets . . . 104
5.28 Photograph of experiment for multiple various shaped targets . . . 104
5.29 Frequency and time domain data for multiple various shaped targets . . . 105
5.30 Locus of target and reconstructed image of scene for multiple various shaped targets . . . 105
5.31 2D reconstructed image of scene and top view photograph of scene . . . 106
5.32 Diagram and photograph of the experiment for multiple various shaped targets . . . 107
5.33 Diagam showing the setup of the experiment and position of multiple various shaped targets . . . 107
5.34 Frequency and time domain data for for multiple various shaped targets . 108
5.35 Locus of target and reconstructed image of scene for for multiple various shaped targets . . . 108
5.36 2D reconstructed image of scene and top view photograph of scene . . . 109
5.37 Diagram and photograph of the experiment for multiple complex targets . 110
5.38 Photograph of experiment for multiple complex targets . . . 110
5.39 Frequency and time domain data for multiple complex targets . . . 111
5.40 Locus of target and reconstructed image of scene for multiple complex targets . . . 111
5.41 2D reconstructed image of scene and top view photograph of scene . . . 112
5.42 Diagram and photograph of the experiment for multiple complex targets . 113
5.43 Photograph of the scene from the front of the antennas . . . 113
5.44 Frequency and time domain data for multiple complex targets . . . 114
5.45 Locus of target and reconstructed image of scene for multiple complex targets . . . 114
5.46 2D reconstructed image of scene and top view photograph of scene . . . 115
5.47 Diagram and photograph of the experiment for a single point target . . . 117
5.48 Photograph of scene for single point target . . . 117
5.49 Frequency and time domain data for single point target at height of platform 118
5.50 Locus of target at different elevation angles . . . 119
5.51 2D reconstructed image of scene at height of platform and top view photograph of scene . . . 120
5.52 3D image of reconstructed scene . . . 121
5.53 Cut through brightest point in reconstructed scene . . . 122
5.54 Diagram and photograph of the experiment for a multiple point targets . . 123
5.55 Photograph of scene for multiple point targets . . . 123

5.56 Frequency and time domain data for multiple point targets at different heights above platform 124
5.57 Locus of target at different elevation angles 125
5.58 2D reconstructed image of scene at height of platform and top view photograph of scene 126
5.59 3D image of reconstructed scene 127
5.60 Cut along location of targets in reconstructed scene 127
5.61 Diagram and photograph of the experiment for a single cylindrically shaped target 128
5.62 Photograph of scene for single cylindrically shaped target 128
5.63 Frequency and time domain data for single cylindrically target at height of platform 129
5.64 Locus of Target at Different Elevation Angles 130
5.65 2D reconstructed image of scene at height of platform and top view photograph of scene 131
5.66 3D image of reconstructed scene 132
5.67 Cut along location of targets in reconstructed scene 132

List of Tables

3.1 Common windowing functions which can be used for suppression of side-lobes [5]. 40

4.1 Table showing the change in target distance from the antennas with different rotation angles 60

4.2 Table showing the cross range resolution 73

List of Symbols

B	—	Transmitted RF bandwidth
B_{eff}	—	Effective bandwidth of step-frequency waveform
c	—	Speed of light
f_c	—	Carrier frequency
f_H	—	Highest frequency of interest
f_L	—	Lowest frequency of interest
η	—	Relative bandwidth
$\triangle R$	—	Range resolution
$\triangle R_{cr}$	—	Cross range resolution
τ	—	Pulse duration
N	—	Number of pulses in waveform
$\triangle f$	—	Frequency spacing
T_{max}	—-	Maximum unambiguous time to target
R_{max}	—	Maximum unambiguous range to target
f_{span}	—	Frequency span of vector network analyzer
$f_{spacing}$	—	Frequency spacing on vector network analyzer
δt	—	3 dB width of the time domain signal
$\triangle t$	—	Sample spacing in the time domain
λ	—	Wavelength
d_{far}	—	Far field distance
D	—	Aperture length
σ	—	Radar cross section or standard deviation
σ_{avg}	—	Average standard deviation
a	—	Amplitude of received signal
r	—	Radius of platform
$\Delta\theta$	—	Angular increment
θ_{3dB}	—	3dB beamwidth of the antennas
θ_{view}	—	Angular range over which antennas view targets
$P_\theta(t)$	—	Projection along angle θ
S_θ	—	Fourier transform of projection P_θ
μ	—	Mean value of a group of n samples

κ	—	Variable used to adjust the sample spacing of the reconstructed 2D and 3D image
$\triangle\theta_{azimuth}$	—	Azimuth incremental angle
$\triangle\theta_{elevation}$	—	Elevation incremental angle
$R_x(\theta)$	—	Rotation matrix around the x-axis
$R_y(\theta)$	—	Rotation matrix around the y-axis
$R_z(\theta)$	—	Rotation matrix around the z-axis
R_{tx}	—	Distance between transmitter and the target
R_{rx}	—	Distance between the receiver and the target
R_{tot}	—	Total 2-way distance between antennas and target

Nomenclature

2D—2-Dimension

3D—3-Dimension

ADC—Analogue to Digital Converter

Azimuth—Angle in a horizontal plane, relative to a fixed reference, usually north or the longitudinal reference axis of the aircraft or satellite

Beamwidth—The angular width of a slice through the main-lobe of the radiation pattern of an antenna in the horizontal, vertical or other plane

CAT—Computerized Axial Tomography

Cross Range—The direction orthogonal to the radar's line of sight

CSIR—Council for Scientific and Industrial Research

DAQ—Data Acquisition

DC—Direct Current

Doppler frequency—A shift in the radio frequency of the return from a target or other object as a result of the object's radial motion relative to the radar

Down Range—The direction of the radar's line of sight

GUI—Graphical user interface

GPIB—(General Purpose Interface Bus) This is an IEEE 488 standard for parallel interfaces which is used for attaching sensors and programmable instruments to a computer

ISAR—Inverse Synthetic Aperture Radar

LabVIEW—(Laboratory Virtual Instrumentation Engineering Workbench) System design platform and development environment for a visual programming language from National Instruments

PWM—Pulse Width Modulation

Range—The radial distance from a radar to a target

SAR—Synthetic Aperture Radar. A signal-processing technique for improving the azimuth resolution beyond the beamwidth of the physical antenna actually used in the radar system.

UWB—Ultra-Wideband

VISA—Standard I/O language that is used for instrumentation programming

VNA—Vector Network Analyzer

Chapter 1

Introduction

1.1 Introduction to Radar Tomography and Ultra-Wideband Radar

Tomography refers to an imaging technique for cross-sectional imaging of an object. This imaging consists of a set of one-dimensional projections of the scene of interest. The data can be collected in two different ways. It can be collected by transmission data or reflected data which has illuminated an object from different azimuth angles [18]. This gives rise to two categories of tomography, that being transmission tomography and reflection tomography.

Transmission tomography refers to an imaging technique whereby the transmitter and receiver are placed in such a way that they face each other and the target of interest is placed between the them [7, 18]. The transmitter illuminates the target and the receiver measures the forward scattered field. This forward scattered field is measured at each angle as the transmitter and receiver pair are rotated around the object of interest.

Reflection tomography refers to an imaging technique where the transmitter and receiver are placed next to one another (or separated by some distance and angle) [7, 18]. In this case the transmitter illuminates the target and the receiver measures the reflected scattered field. This reflected scattered field is measured at each angle as the transmitter and receiver pair are rotated around the object of interest.

All the data that is collected at each angular position is processed by a reconstruction algorithm and this produces an image of the object of interest. There are many reconstruction algorithms that can be applied to a data set in order to create an image of the scene. These algorithms are dependent on the type of tomography that is used and the method in which the tomography experiments are carried out. Two common reconstruction algorithms are the Filtered Back Projection algorithm and the Fourier Domain Inversion algorithm [7, 18]. The Filtered Back Projection method involves taking the received projections at various angular positions, and filtering them using a low pass filter. The results from this filtering is then smeared back onto the image plane along certain trajectories.

The Fourier Domain Inversion algorithm makes use of projections and the Fourier-Slice theorem. These fill up the 2D Fourier Domain of the image of the object which is to be constructed. A simple 2D Fourier transform produces the image in the spatial domain [7, 18].

Ultra-Wideband (UWB) is defined in the Federal Communication Commission (FCC) on February 2002 as a signal or system that has a bandwidth greater than 500 MHz or instantaneous fractional bandwidth greater than 0.2 [1]. UWB radars offer many advantages over the conventional narrow band radars. These advantages include high spatial resolution which allow for detecting targets which are closely spaced as well as a lower probability of detection which could be exploited by stealthy military applications [9, 32].

1.2 Background

Currently at UCT there exists an UWB radar system which was built by a former Masters student, Ms P. Chao, in the Department of Electrical Engineering. This radar was used as a short range imaging system. It consists of two transmitting channels and four receiving channels [7, 9]. This system operates between the 1 GHz - 2 GHz frequency band and can be used as a through wall imaging system for detecting targets behind a brick wall. The bandwidth of this system is however limited to 1 GHz.

The imaging system designed in this project makes use of a Vector Network Analyzer (VNA). This device is commonly used to characterize the gain of RF components by measuring the S-parameter of the device. This function of the VNA is exploited by connecting two antennas, one to each port, and measuring the S-parameter (S_{21}) of the scene which is placed in front of the antennas. By doing this, the transfer function of the scene can be directly measured in the frequency domain. The VNA that is available in the Department of Electrical Engineering (Agilent E5071B Vector Network Analyzer) is operational over the frequency range between 300 kHz and 8.5 GHz, which allows for a bandwidth of approximately 8.5 GHz. The effect of using a radar with a high bandwidth is it's effect on range resolution. A high bandwidth system offers very fine range resolution, which improves the resolution of the image that is formed and allows for distinguishing closely spaced targets.

All of the signal processing is done in software. This makes the design of the system less hardware orientated and will reduce the cost implications on the project. Although the VNA is capable of operating over a frequency range of 8.5 GHz, the bandwidth of the system is also limited by the operating frequencies of the antennas that are used, and this will be discussed during the course of this document. This project was carried out to demonstrate the abilities of this system.

Real world applications of UWB signal include systems which are capable of detecting of breast cancer [24]. This system uses the ability of microwave signals to penetrate tissue

in order to detect cancer. Research work has also been done by the CSIR using ISAR techniques to extract helicopter blade parameters, such as number of blades, blade length, blade tip velocity and the helicopter blade's angular velocity [4]. UWB radar and ISAR techniques are also used in applications for detecting concealed weapons [28]. This thesis shows the best possible images that can be created over the specified frequency band.

1.3 Objectives

The objectives of this dissertation is to:

1. Design and create an UWB Radar Tomography system, using an Agilent E5071B Vector Network Analyzer, capable of creating 2D and 3D images of targets placed in front of a transmitter/receiver pair.
2. Control all equipment, including the VNA and rotating pedestal, from a Windows XP computer using LabVIEW.
3. Design and implement a graphical user interface (GUI) in LabVIEW for controlling the operation of the UWB Tomographic system.
4. Simulate an UWB Tomographic imaging system in Matlab and comparing simulations to experimental results.

1.4 Limitations and Scope of Thesis

The scope of this project is to create an UWB Radar Tomography system using an Agilent E5071B Vector Network Analyzer. The system is required to create 2D images of targets placed in front of the transmitter/receiver pair. This 2D model will then be extended to the 3D model. The recorded data is measured in a laboratory using the available Agilent E5071B Vector Network Analyzer.

The UWB tomographic system will strictly be used in reflection mode. For this case, the simulations are also based on this tomographical mode. The measured data and results will be compared to the simulations and conclusions drawn from this. The system is designed as a short-range imaging device and thus all experiments are carried out over a small scene (10 m in range).

The project was carried out in two stages. The first involved using a 1-axis rotating pedestal which was used to create 2D images of the scene. Part two of the project extended this 2D model into 3D space by using a 2-axis rotating pedestal. The 1-axis rotating platform that was used contained a DC stepper motor which is capable of rotating a minimum of 1.8 degrees per step. The 2-axis rotating pedestal also contains two DC motors who's speed was controlled by a PWM signal to each motor. The angular position of the motor was measured using a rotary potentiometer.

The Agilent E5071B Vector Network Analyzer was used as the transmitting and receiving channels of the UWB tomographic imaging system. This instrument has several limitations. The instrument can measure over a frequency range of 300 kHz to 8.5 GHz. The number of samples that can be recorded on the VNA ranges from 2 to 1601 points. These number of samples limits the frequency spacing on the VNA. The frequency spacing also limits the maximum unambiguous distance to which measurements can be taken. The sweep time of the device (i.e. the time it takes to sweep across all frequencies) is limited to a minimum of 53 ms. The VNA device also adds its own noise to all trace measurements. The device also has a limited output power. This ranges between -50 dBm to 10 dBm. The other limits of the device can be found in the user manual of the device.

The antennas that were used in the experiments are two Cobham H-1498 series broadband horn antennas which are specified to operate between 2 GHz - 18 GHz. This limits the frequency over which measurements can be taken. The beam pattern and 3 dB beamwidth of the antenna is determined by the dimensions of the antenna as well as the operating frequency. From the data sheet of the antennas it can be seen that the beamwidth of the antennas are 80 degrees in the E-plane and 50 degrees in the H-plane. This allows for a wide viewing angle for imaging, however this is still a limiting factor to the viewing angle. The characteristics of the antennas can be seen in the attached appendix.

1.5 Thesis Outline

This thesis is arranged into the following sections:

- Chapter 2 is a literature review on UWB systems and the tomographic imaging techniques. It describes the various types of UWB systems and how they are created. It also focuses on the two different methods of tomographic imaging, these being the transmission and reflection tomography.
- Chapter 3 will give an overview of the UWB radar system that will be implemented. It will include the design specifications of the entire system.
- Chapter 4 will discuss the simulations that were created and the imaging algorithm that was implemented in the system.
- Chapter 5 presents results from the experiments that were carried out and will have comparisons between these and the simulated results from Chapter 4.
- Chapter 6 concludes the thesis and makes recommendations for future work on the UWB radar imaging system.

Chapter 2

Literature Review

2.1 Ultra-Wideband Signals and Systems

2.1.1 Definition

An Ultra-Wideband system refers to a system that has a bandwidth greater than 500 MHz or an instantaneous fractional bandwidth greater than 0.2 [9]. This (relative bandwidth) is defined by [15]

$$\eta = \frac{B}{f_c}, \qquad 0 \leq \eta \leq 1 \tag{2.1}$$

where B is the absolute bandwidth of the system and f_c is the carrier (or centre) frequency. For signals which have no carriers and are non-sinusoidal, the relative bandwidth is defined as

$$\eta = \frac{f_H - f_L}{f_H + f_L}, \qquad 0 \leq \eta \leq 1. \tag{2.2}$$

In Equation 2.2, f_H and f_L are the highest and the lowest frequencies of interest respectively. The conventional technology of radar is developed by using a small relative bandwidth, usually in the range of $0.01 \leq \eta \leq 0.25$. The relative bandwidth of an UWB system is characterized by $0.25 \leq \eta \leq 1$ [15].

UWB systems offer many advantages over conventional narrowband radars that operate at the same centre frequency. These include high spatial resolution which allows for detecting targets which are closely spaced and it has a lower probability of detection which is advantages for stealth like military applications [9]. They are also very useful for weather radars, ground penetrating radar and for enhanced clutter suppression for detecting low flying targets [15]. The high spatial resolution can be attributed to the bandwidth of the system. The down range resolution of the system is dependent on its bandwidth by [6, 20, 30]:

$$\triangle R = \frac{c}{2B}, \tag{2.3}$$

where $\triangle R$ represents the range resolution, c represents the speed of light and B represents the bandwidth of the system.

The UWB radar return signal carries large signal bandwidth information. This allows for sensing capabilities which are beyond that of simple target detection [32]. The waveform content of the reflected UWB impulse signals changes depending on the shape and material of the target. There has been experimental work done in the Singularity Expansion Method (SEM) radar which uses a single "impulse" signal. These experiments showed that the radar return waveforms that were received were changed by the structure and characteristics of the target. This is equivalent to determining the characteristics of a system from its impulse response. From these experiments it was seen that the signal characteristics of the reflected impulse appeared to be unique enough to allow for target identification [32]. All radar signals which are sent out to a target will have some target-related change. The difficulty that comes about is detecting the change and to uniquely relate it to a reflector.

2.1.2 Ultra-Wideband Waveforms

There are three main categories of UWB waveforms. These include impulse, linear frequency modulation and step-frequency waveforms [9]. The effective bandwidth for each type of waveform is achieved differently, however the range resolution $\triangle R$, for all three categories is obtained by Equation 2.3.

Impulse (Short Pulse)

An impulse signal in the UWB context is one which has a pulse width which is typically less than 1ns [9]. The 3 dB bandwidth B of the Fourier transform of this signal can be determined by

$$B \approx \frac{1}{2\tau}, \tag{2.4}$$

where τ is the duration of the pulse.

In practice, the antennas that are used will bandlimit the signals that are transmitted. Thus the width of the 3 dB bandwidth of the bandlimited signal changes and is related to the pulse width by

$$B \approx \frac{1}{\tau}. \tag{2.5}$$

An illustration of this 3 dB bandwidth can be seen in Figure 2.1, along with the effect of the bandlimited signal.

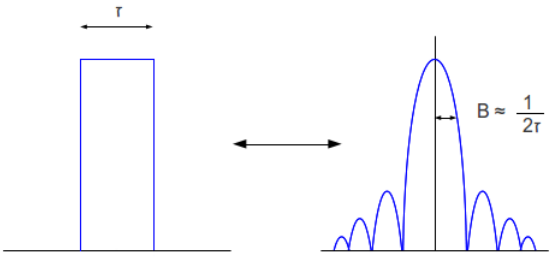

(a) Plot of an impulse signal

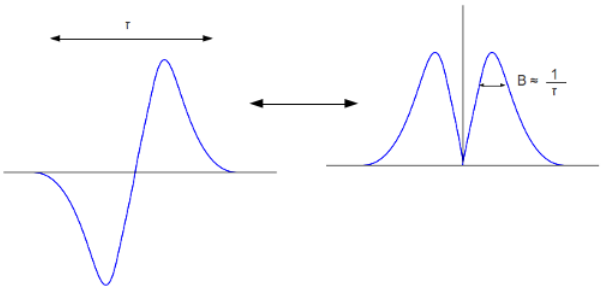

(b) Plot of a bandlimited impulse signal

Figure 2.1: Plots showing the 3 dB bandwidth of an impulse signal and a bandlimited impulse signal [9]

A sub-nanosecond impulse signal has spectral components which extends from close-to-DC up to several GHz [9]. This high bandwidth gives rise to the high range resolution which is thus achieved with each impulse.

Chirp Pulse

A chirp signal, or linear frequency modulated chirp, is extensively used in high-resolution radar applications. This is a waveform that sweeps linearly over a range of frequencies during the pulse transmission time [20]. The time and frequency domain of a 100-400 MHz chirp signal with a chirp length of 1 μs is illustrated in Figure 2.2.

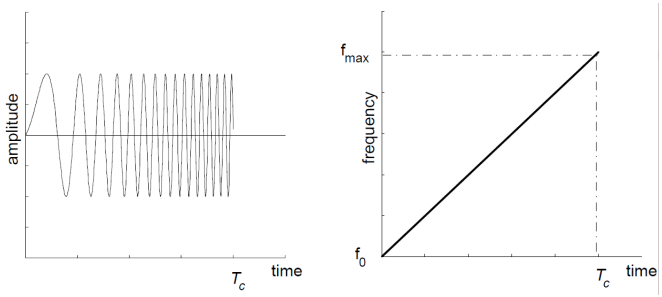

(a) Time (left) and time-frequency (right) domain

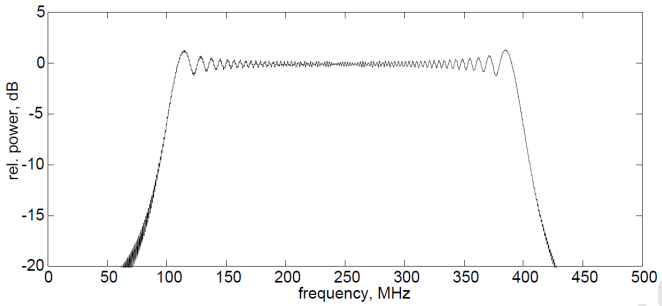

(b) Frequency domain

Figure 2.2: Plot of a 100-400 MHz chirp signal in the time and frequency domain [13]

By increasing it's frequency with time, the chirp signal can attain large bandwidths [9]. This is advantageous of increasing the signal energy while maintaining the radar's high-resolution.

Step-Frequency Waveform

A step-frequency waveform is a sequence of pulses in which the frequency from pulse to pulse is increased by a fixed frequency increment. This is illustrated in Figure 2.3.

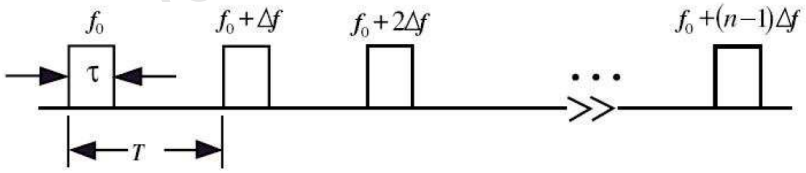

Figure 2.3: Plot of a step-frequency waveform [17]

The pulse width of all the pulses in the step-frequency waveform are the same. These pulses are usually narraw in bandwidth, thus narrowband equipment can be used when implementing a step-frequency radar [9]. The step-frequency waveform has an effective bandwidth which can be determined by

$$B_{eff} = N\triangle f, \tag{2.6}$$

where N represents the number of pulses in the waveform and $\triangle f$ is the frequency spacing. Each pulse that is received is located in a different band in the frequency spectrum. The receiving echoes of the radar are recorded separately for different bands [9]. The

recorded data are then combined and reconstructed to create a large portion of the scene's spectrum.

2.2 Tomography

Tomography is a technique for cross-sectional imaging of an object. This imaging is done by collecting either transmission or reflected data from an object at different azimuth angles [18]. This measured data set consists of one-dimensional projections of the scene of interest. The way in which this data is collected creates two forms of tomography, being transmission tomography and reflection tomography.

2.2.1 Transmission Tomography

Transmission tomography refers to an imaging technique whereby a transmitter is used to illuminate a target and the receiver is placed directly opposite the transmitter [7]. The target is placed between the transmitter and receiver and the forward scattered field is measured by the receiver. There are two categories of targets that can be placed between the transmitter and receiver. These are diffracting sources and non-diffracting sources. With non-diffracting sources the straight ray assumptions hold whereas for the diffracting sources the effects of refraction and diffraction distort the straight ray assumptions. This dissertation focuses on the second tomographic category, that being reflection tomography.

A popular method used for demonstrating the transmission tomography technique is the X-ray CAT. This can also be used to derive the filtered back-projection algorithm [18]. In this technique a parallel beam which propagates through the target. The receiver then takes measurements on the far side of the target. This is illustrated in Figure 2.4.

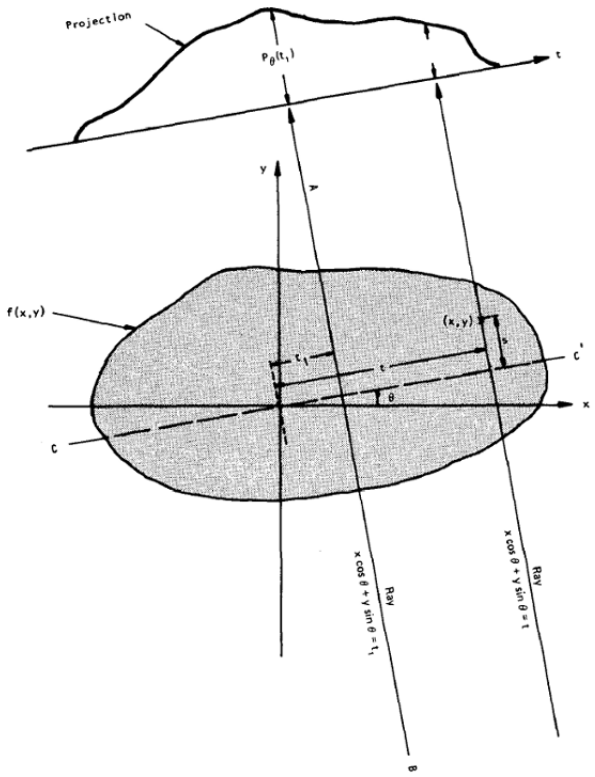

Figure 2.4: An object function and $f(x,y)$ and it's projections $P_\theta(t)$[18]

Algorithm Derivation [18]

Consider a 2D slice of an object which is represented by a two dimensional absorption function $f(x,y)$. This can be seen in Figure 2.4. Each line integral is represented by the (θ,t) parameter. The Equation of this line is denoted by

$$t = x\cos\theta + y\sin\theta. \tag{2.7}$$

Equation 2.8 gives the line integral which is computed along a line which is a distance of 't' units from the origin (perpendicular to a line through the origin) and sub-tending an angle θ with the horizontal.

$$P_\theta(t) = \int_{(\theta,t)line} f(x,y)ds \tag{2.8}$$

A "projection" is formed from a set of these line integrals [18]. Using the delta function in Equation 2.8, the line integral can be written as

$$P_\theta(t) = \int_{-\infty}^{\infty}\int_{-\infty}^{\infty} f(x,y)\delta(x\cos\theta + y\sin\theta - t)dxdy. \tag{2.9}$$

The function $P_\theta(t)$ in Equation 2.9 is know as the Radon transform of the function $f(x,y)$ [18].

Define a 2D inverse Fourier transform of the object function as [7, 18]

$$f(x,y) = \int_{-\infty}^{\infty}\int_{-\infty}^{\infty} F(u,v)e^{j2\pi(ux+vy)}dudv. \tag{2.10}$$

Substitute:

$$u = w\cos\theta$$

$$v = w\sin\theta$$

$$dudv = wdwd\theta$$

into Equation 2.10 and the inverse Fourier transform gets reduced to

$$f(x,y) = \int_{0}^{2\pi}\int_{0}^{\infty} F(w,\theta)e^{j2\pi w(x\cos\theta+y\sin\theta)}wdwd\theta. \tag{2.11}$$

Simplify Equation 2.11 and substitute Equation 2.7 to get [7, 18]

$$f(x,y) = \int_{0}^{\pi}\int_{-\infty}^{\infty} F(w,\theta)|w|e^{j2\pi wt}dwd\theta. \tag{2.12}$$

The Fourier slice theorem states that the Fourier transform of a projection of an image $f(x,y)$ which is taken at an angle θ is equal to a slice of the 2D Fourier transform, $F(u,v)$, of the object function $f(x,y)$ sub-tending an angle θ with the u-axis [7, 18]. This theorem is illustrated in Figure 2.5.

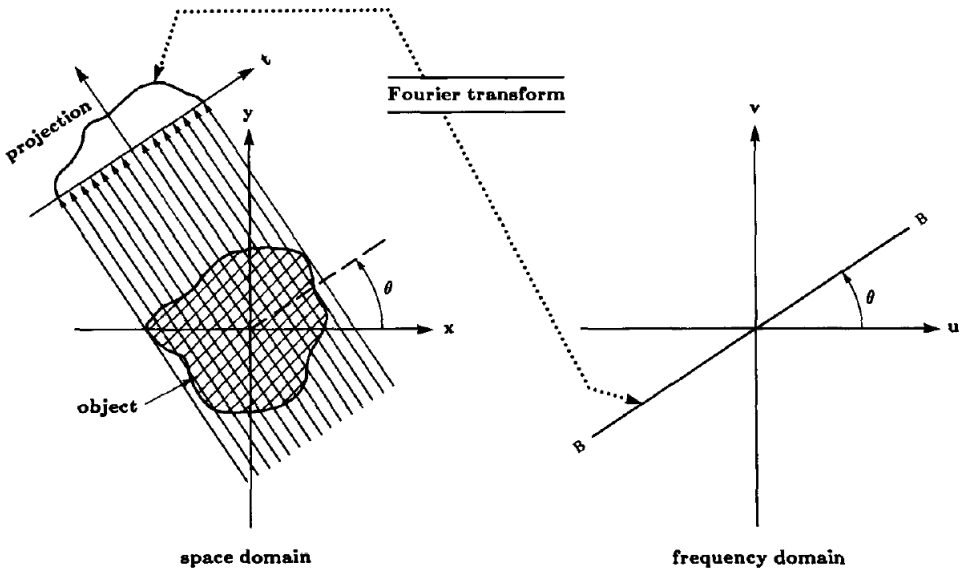

Figure 2.5: Fourier slice theorem [18]

This theorem is derived as follows [18]:

Define the two-dimensional Fourier transform of the object function as

$$F(u,v) = \int_{-\infty}^{\infty}\int_{-\infty}^{\infty} f(x,y)e^{-j2\pi(ux+vy)}dxdy,$$

and a projection at an angle θ, $P_\theta(t)$, along with its Fourier transform by

$$S_\theta(w) = \int_{-\infty}^{\infty} P_\theta(t) e^{-j2\pi wt} dt.$$

A projection at $\theta = 0$ is the simplest example to show the Fourier Slice Theorem. The Fourier transform of the object along the projection $v = 0$ in the frequency domain simplifies to [18]

$$F(u,v) = \int_{-\infty}^{\infty} \int_{-\infty}^{\infty} f(x,y) e^{-j2\pi ux} dx dy.$$

This integral can be split into two parts because the phase factor has no dependence on y. It is written as

$$F(u,v) = \int_{-\infty}^{\infty} \left[\int_{-\infty}^{\infty} f(x,y) dy \right] e^{-j2\pi ux} dx. \tag{2.13}$$

The term in brackets is the equation for a projection along lines of constant x, which is

$$P_{\theta=0}(x) = \int_{-\infty}^{\infty} f(x,y) dy.$$

Substituting this into Equation 2.13 we have:

$$F(u,v) = \int_{-\infty}^{\infty} P_{\theta=0}(x) e^{-j2\pi ux} dx. \tag{2.14}$$

The integral in this equation represents the one-dimensional Fourier transform of the projection $P_{\theta=0}$. The relationship between the vertical projection and the 2D transform of the object function is given by [18]

$$F(u,v) = S_{\theta=0}(u)$$

which is the simplest form of the Fourier Slice Theorem. Using this theorem, Equation 2.12 can be simplified even more by making the following substitution [7, 18]:

$$S_\theta(w) = F(w,\theta)$$

where S_θ is a Fourier transform of a projection P_θ. This is defined as:

$$S_\theta(w) = \int_{-\infty}^{\infty} P_\theta(t) e^{-j2\pi wt} dt$$

Using this substitution, Equation 2.12 can be written as:

$$f(x,y) = \int_0^{\pi} Q_\theta(x\cos\theta + y\sin\theta) d\theta \tag{2.15}$$

where

$$Q_\theta(t) = \int_{-\infty}^{\infty} S_\theta(w)|w|e^{j2\pi wt}dw \tag{2.16}$$

Equation 2.16 represents a filtering operation. The frequency response of this filter is denoted by$|w|$ [7, 18]. For this reason, $Q_\theta(w)$ is called a filtered projection.

Equation 2.15 makes the suggestion that by summing up all the filtered projections between *0* and π radians, the object function can be reconstructed. Thus Equation 2.15 back-projects each filtered projection [18]. This filtering operation as well as the back-projection process forms the filtered back-projection algorithm. It creates a reference from which radar imaging techniques can be expressed and explained as tomographic processes [7, 18].

2.2.2 Reflection Tomography

Reflection tomography is concerned with gathering reflected data from different azimuth positions around a scene. In this tomographic process the transmitter and receiver are placed side by side [7]. The transducer pair can either be collocated or they can be separated by a finite distance. It is possible to use both narrowband and broadband signals in transmission tomography, but when using reflection tomography, only broadband signals are acceptable for this tomographic technique [18]. Reflection tomography is used as an alternative to transmission tomography where the forward scattering field is highly attenuated as it propagates through the target and it is not possible to get a good reading. This method is also used if the transmission power is limited [7]. The understanding of radar imaging as a tomographic process is facilitated by this process. The cross-sectional reflectivity function of the target is being imaged for the reflectivity data in this tomographic technique.

Algorithm Derivation

Reflection tomography is a technique which is based on the measurement of line integrals of an object's reflectivity function of an object [18]. If one is to consider a single point transducer which illuminates an object with a very wide fan-shaped beam, and the incident field of the beam is an impulse in the time domain, then the signal that is received at time t is a representation of all the reflectors that are a distance tc away from the transducer [18]. This can be seen in Figure 2.6. Thus the locus of all points that are at the same distance from the transducer is a circle. This mode of reflection tomography thus measures line integrals over circular arcs.

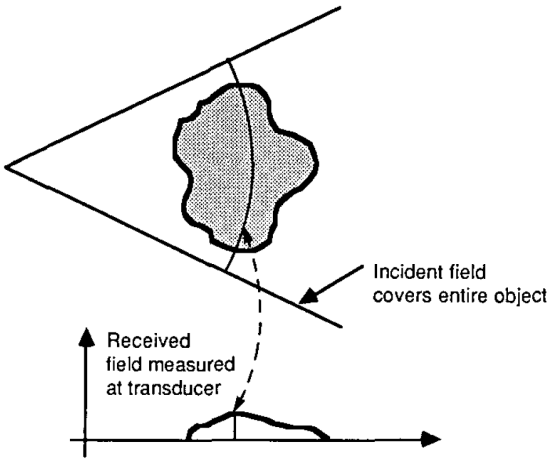

Figure 2.6: Transducer illuminating an object with a wide fan-beam and measuring line integrals over circular arcs of the objects reflectivity function[18]

By moving the transducer on a sphere which surrounds the object, it is possible to reconstruct the entire object by obtaining enough line integrals. Reflection tomography makes use of plane waves which propagate to and from the target of interest. The Equation of the field of an ideal plane wave transducer can be seen in Equation 2.17. This occurs when the transducer is excited by the waveform $p_t(t)$.

$$\psi_i(x,y,t) = p_t(t - \frac{x}{c}),\ x > 0 \tag{2.17}$$

In the receive mode, the situation is slightly different. Let the scattered field be represented by $\psi_r(x,y,t)$. The signal which is generated at the electrical terminals of the transducer is proportional to the integral of this field [18]. Thus the electrical received signal, $p_r(t)$, can be represented as:

$$p_r(t) = \int \psi_r(0,y,t)dy \tag{2.18}$$

It is important to consider how the waves propagate back to the transducer if one wants to derive an expression for the received waveform given the field at points distant from the transducer. If one considers a line of reflectors located at $x = x_0$ that reflect a portion, $f(x = x_0, y)$ of the field, then we can write the scattered field at the line $x = x_0$ as the product of the incident field and the reflectivity parameter [18]. This can be seen in Equation 2.19.

$$\psi_i(x = x_0,y,t) = \psi_i(x = x_0,y,t)f(x = x_0,y) = p_t(t - \frac{x}{c})f(x = x_0,y) \tag{2.19}$$

It is necessary to find the Fourier transform of the field and then propagate each plane wave to the transducer face if we want to find the field at the transducer face. This can be done by finding the spatial and temporal Fourier transform of the field first, at the line of

reflectors [18].

$$\tilde{\psi}_s(k_y,\omega) = \int_{-\infty}^{\infty}\int_{-\infty}^{\infty} \psi_i(x=x_0,y,t)e^{-jk_y y}e^{j\omega t}dydt \tag{2.20}$$

The function $\tilde{\psi}_s(k_y,\omega)$ represents the amplitude of the plane wave. This plane wave is propagating with direction vectors $(-\sqrt{(\frac{\omega}{c})^2-k_y^2},k_y)$ [18]. Using this plane wave expansion it is easy to propagate the plane waves back to the face of the transducer. If one considers an arbitrary plane wave:

$$\psi(x,y) = e^{j(k_x x+k_y y)}$$

where k_x is negative and represents a wave traveling back towards the transducer. Using Equation 2.18 it can be shown that the electrical received signal for all plane waves is zero when $k_y \neq 0$ [18]. This comes about because:

$$\int_{-\infty}^{\infty} e^{jk_y}dy = \delta(k_y)$$

As a result of the propagation distance x_0, all plane waves which travel perpendicular to the face of the transceiver ($k_y = 0$) will experience a delay. This is represented by a $e^{j\omega(\frac{x_0}{c})}$ factor in the frequency domain. If a unit amplitude plane wave is to be transmitted, then its electrical response will be:

$$P_r(\omega,k_y) = \delta(k_y)e^{j\omega(\frac{x_0}{c})}$$

If one takes the sum of each plane wave at frequency ω from Equation 2.20, then the total electrical response from the plane $x = x_0$ due to the scatterers located at this position is given by [18]:

$$\tilde{P}_r(\omega) = \tilde{\psi}_s(k_y=0,\omega)e^{j\omega(\frac{x_0}{c})}$$

In the time domain, this can be represented as:

$$p_r(t) = \frac{1}{2\pi}\int_{-\infty}^{\infty} \tilde{\psi}_s(k_y=0,\omega)e^{j\omega(\frac{x_0}{c})}e^{-j\omega t}d\omega$$

By substituting Equation 2.17, 2.19 and 2.20 into this expression, then the received signal can be written as [18]:

$$p_r(t) = \frac{1}{2\pi}\int_{-\infty}^{\infty} e^{-j\omega t}d\omega \int_{-\infty}^{\infty}\int_{-\infty}^{\infty} \psi_s(x=x_0,y,t')\cdot e^{j\omega(\frac{x_0}{c})}e^{-jk_y y}e^{j\omega t'}dydt'|_{k_y=0}$$

which can be written as:

$$p_r(t) = \frac{1}{2\pi}\int_{-\infty}^{\infty} e^{-j\omega t}d\omega \int_{-\infty}^{\infty}\int_{-\infty}^{\infty} \psi_i(x=x_0,y,t')\cdot f(x=x_0,y)e^{j\omega(\frac{x_0}{c})}e^{j\omega t'}dydt'$$

This Equation can be reduced to [18]:

$$p_r(t) = \frac{1}{2\pi}\int_{-\infty}^{\infty} e^{-j\omega t} d\omega \int_{-\infty}^{\infty}\int_{-\infty}^{\infty} p_t(t' - \frac{x_0}{c}) \cdot f(x = x_0, y) e^{j\omega(\frac{x_0}{c})} e^{j\omega t'} dy dt'$$

By interchanging the order of the integrals, the Equation can be simplified to:

$$p_r(t) = p_t(t - 2\frac{x_0}{c}) \int_{-\infty}^{\infty} f(x = x_0, y) dy$$

This Equation is a representation of the measured signal as a result of a line of scatterers placed at $x = x_0$. If the total reflectivity of the object along the line $x = x_0$ is denoted by $f_1(x_0)$ [18]. The assumption is made that the Born approximation is satisfied, and thus the signal that is received from all parts of the object can be written as the sum of each individual line. The total measured field can thus be written as:

$$p_r(t) = \int_{-\infty}^{\infty} p_t(t - 2\frac{x}{c}) f_1(x) dx$$

From this Equation it is evident that the transmitted pulse is convolved with the reflectivity of the object. In this case the reflectivity is summed over the part of the object which is illuminated by the incident field [18]. While using reflection tomography, a wide beam is used, and thus each measurement that is received corresponds to a line integral through the object. If one wants to find the reflectivity of the object, then one can deconvolve the effects of the incident field. By approximating the incident field as an impulse, the reflectivity of the object over the line integrals is:

$$f_1(x) = p_r(2\frac{x}{c})$$

If the object is not an impulse, then the line integrals can be recovered using the following deconvolving process [18]:

$$F_1(\omega) = \frac{P_r(\omega)}{P_t(2\frac{\omega}{c})}$$

where $F_1(\omega)$, $P_r(\omega)$ and $P_t(\omega)$ represents the Fourier transform of the corresponding time or spatial domain. The line integral which was obtained can thus be used in the Fourier Slice Theorem to construct a reconstruction of the object [18]. Equation 2.21 shows the relationship that can be used to find the object's reflectivity:

$$\hat{f}(x,y) = \int_0^{2\pi}\int_{-\infty}^{\infty} S_\theta(\omega)|\omega| e^{j\omega t} d\omega d\theta \tag{2.21}$$

$S_\theta(\omega)$ represents the Fourier transform of the projection data. This is measured with the transducer face at θ degrees from the horizontal [18] and

$$t = x\cos\theta + y\sin\theta$$

Chapter 3

System Design and Control

This chapter will describe the design and control of the UWB system that was implemented. The design specifications of the UWB system will be described as well as the control of the equipment that was involved in the project. It outlines the design decisions that were made for the parameters that were used in the simulations as well as during the execution of experiments. It also includes the signal processing techniques that were used.

3.1 Overall System Design

The UWB radar system that was created in this project consisted of the following parts:

Hardware

1. Controlling computer with Windows XP operating system, utilizing:
   (a) LAN port for connection to the VNA
   (b) General Purpose Interface Bus (GPIB) connection from Data Acquisition Card
2. Agilent Technologies E5071B ENA Series 300 kHz - 8.5 GHz Network Analyzer
   (a) LAN port for connection to the controlling computer
3. National Instruments PCI-MIO-16E-1 Data Acquisition Card (500 kS/s (1-Channel), 250 kS/s (Multchannel), 12-Bit, 16-Analogue -Input Multifunction DAQ)
4. Single axis stepper motor driven platform for 2D experiments
5. Azimuth over Elevation (2-axis) rotating pedestal for 3D experiments
6. Voltcraft 0-30V/1.2A DC Power Supply
7. Cobham H-1498 Series Horn Antenna (X2)

8. Bourns 6539/6639 $10\,k\Omega$ precision potentiometer
9. LAN cable (X2)
10. Coaxial cable (X2)

Software

1. National Instruments LabVIEW 2010 Professional Development System
2. Matlab 7.9.0 (R2009b)
3. Agilent IO Control Version 15.0.10528.0

The UWB Radar Imaging system is made up of all the components listed above. A GUI was created in LabVIEW which can be operated by the user on the controlling computer. This GUI allows the user to set up all equipment parameters including the VNA and rotating pedestal. Photographs of the components are shown in Figure 3.1 .

(a) Agilent Technologies E5071B ENA Series 300 kHz - 8.5 GHz vector network analyzer

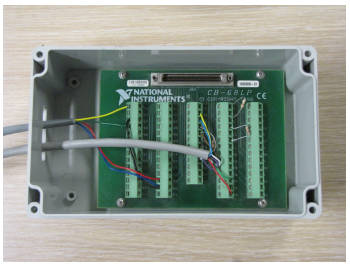

(b) National Instruments PCI-MIO-16E-1 Data Acquisition Card output pins

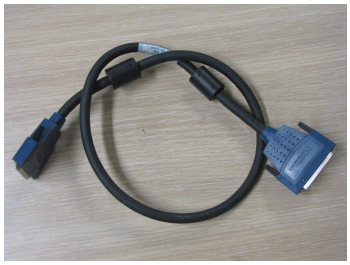

(c) Data Acquisition Card cable

(d) 1-axis rotating pedestal

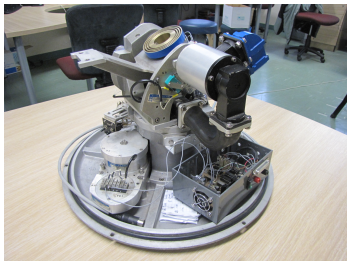

(e) Azimuth over elevation (2-axis) rotating pedestal

(f) Power supply

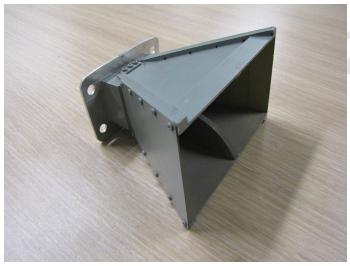

(g) H-1498 series horn antenna

(h) Bourns 6539/6639 precision potentiometer

(i) LAN cable

(j) Coaxial cable

Figure 3.1: Pictures of the hardware that was used

3.2 System Overview

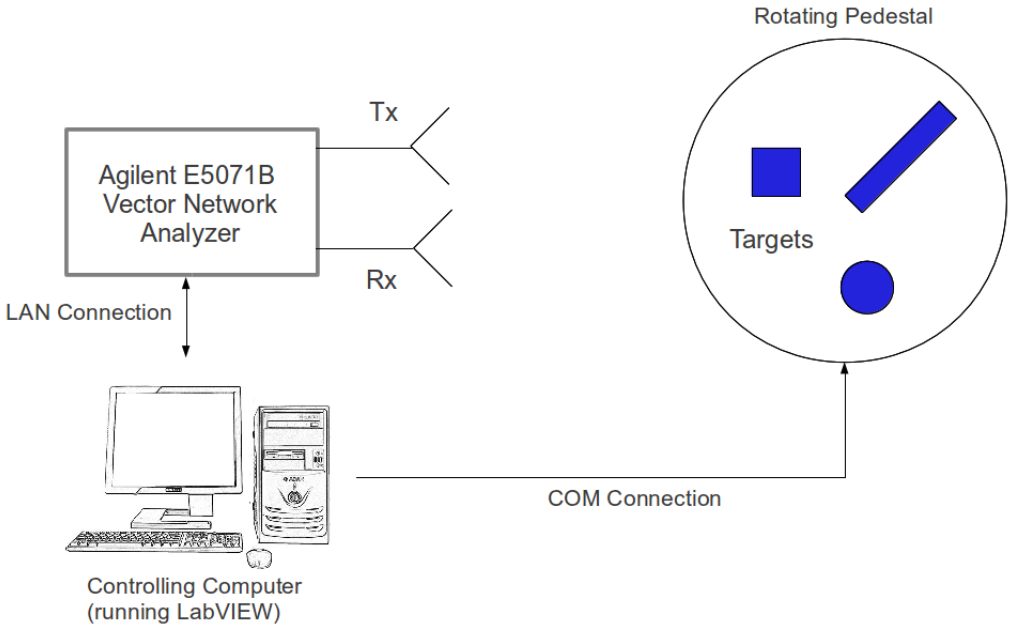

Figure 3.2: UWB radar tomography system

Figure 3.2 shows a block diagram of the UWB system that was used. The system is made up of the controlling computer, VNA, rotating pedestal and the horn antennas. All equipment in the system is controlled via the controlling computer. A LabVIEW GUI was created which allows the user to manually set any parameters on the VNA as well as the rotating pedestal. The different functions of this GUI can be seen in Appendix C.

During the operation of an experiment, the user will set the required parameters for the experiment on the controlling computer. This will include the frequency range, sweep time, output power, number of points, etc. on the VNA. All these parameters are sent through a LAN connection to the VNA. For the 2D experiments a 1-axis rotating pedestal is used which rotates at a fixed angular step (1.8 degrees) in the azimuth direction. For the 3D experiments, the 2-axis rotating pedestal was used and the start and stop rotation azimuth and elevation angle of the pedestal is set in the GUI. The incremental angular steps in both the azimuth and elevation directions are also set by the user. For the 2D experiments the process starts by LabVIEW setting all the parameters on the VNA. The 1-axis rotating pedestal is then rotated by 1.8 degrees and a measurement is recorded from the VNA. The pedestal is then rotated through another 1.8 degrees and another measurement taken. This process is repeated until the pedestal has rotated through 360 degrees. For the 3D experiments the process starts by LabVIEW setting all the parameters on the VNA. Power is then applied to the motors of the elevation and azimuth axis to make it rotate. It monitors the position of the pedestal via potentiometers which have been mounted to each axis. A Bourns 6539/6639 precision potentiometer was used to measure the angular position of the pedestal. The pedestal moves to the start elevation and azimuth angle. Each motor on the 2-axis pedestal (azimuth and elevation motor) is connected to the shaft of a rotating

potentiometer via gears. The gearing ratio is one-to-one, so one full revolution of the elevation or azimuth axis will result in one full revolution of the potentiometer. In this way, each angular position has a specific voltage output associated with it, which is set by the potentiometer. The power supplied to the potentiometer is taken from the analogue output port of the PCI DAQ card. The DAQ card that was used in this project was a National Instruments PCI-MIO-16E-1 Data Acquisition Card. It has a 12-bit resolution ADC, 16 channel multiplexer and 1.2 MS/s (Mega Samples per second). By using this DAQ card a very fine voltage can be read in from the potentiometers. The supply voltage for the potentiometers were set to 5 V, but as a result of voltage drops across small components, the voltage swing range of the potentiometers is 0 - 3.55 V. Each angular position is thus converted to a voltage within this range. This voltage is read into the analogue input port of the PCI DAQ card. The card has a 12-bit resolution and each voltage level is represented by a 1.22 mV change. This voltage is read into LabVIEW and fed into a control algorithm. The algorithm checks what the next angular position is, and what the associated voltage is for that angular position. It rotates the pedestal in a particular direction until the angular position, to which the pedestal is set to move to, is reached, within an error of 0.1 degrees in both directions. When the pedestal reaches this angular position the motor is switched off. The VNA then sweeps over the frequency range that was set by the user and the data is then saved to a CSV file in a directory specified by the user. The number of sweeps and sweep time are all set by the user. After the frequency sweeps are complete, the pedestal moves to the next azimuth angle and repeats the frequency sweeps. This is done until all azimuth angles for the particular elevation angle have been covered. The pedestal then moves to the next elevation angle and repeats the process for each azimuth angle. This is done until all elevation and azimuth angles have been complete as set by the user.

3.3 Rotating Platform Design

The project would be carried out in two stages, namely 2D experiments and 3D experiments. For the 2D experiments, only a 1-axis rotating pedestal was required. This pedestal would rotate in the azimuth direction with targets placed on it and will give range information of the target as it rotates on the pedestal. The result of these experiments would give a 2D plot of the targets that are placed on the pedestal. For the 3D experiments a 2-axis rotating pedestal was required. This pedestal would be capable of rotating in both the azimuth and elevation direction. By using a 2-axis rotating pedestal it increases the viewing angles over which the antennas can view the targets and allows for the extraction of both range and height information from the targets. It should be noted that alternative methods can be used to acquire data for the 3D experiments. The antennas could be attached to a straight pole and measurements taken at different heights as the pedestal rotates in front of the antennas. Alternatively the antennas could be mounted onto a circular arm which rotates around the object, viewing it from different angles.

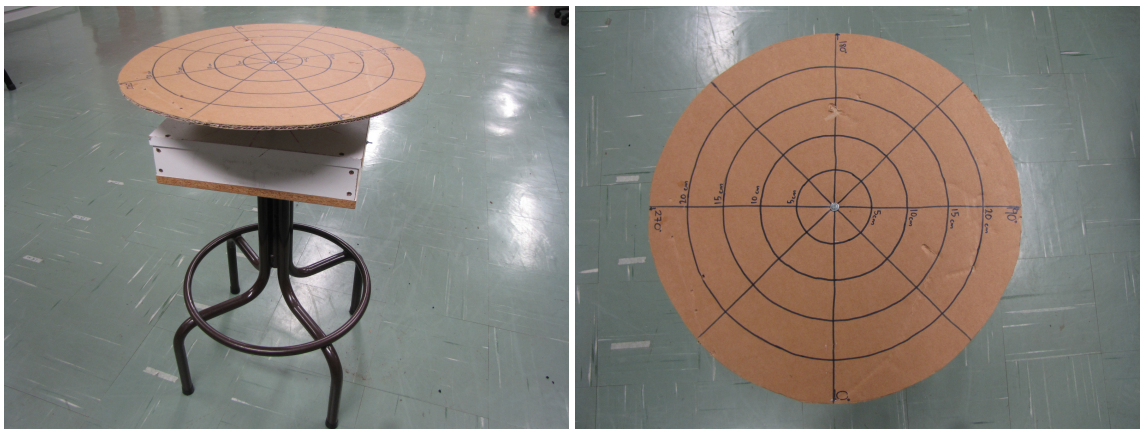

Figure 3.3: 1-axis rotating pedestal that was used.

The 1-axis rotating pedestal that was used for the 2D experiments can be seen in Figure 3.3. This pedestal contained a stepper motor (Stepper Motor, DC 24V, 1.8° steps, Type KP56LM2.019 No. 7602, Japan Servo Co. Ltd) which would rotate by a set angle (1.8 degrees) when a single positive going pulse was sent to it. The connection between the computer and the 1-axis rotating pedestal made use of a COM port connection, where three control lines were sent from the computer to the pedestal. One line for ground, one for direction and one for step. These lines were all controlled through LabVIEW. The aim of this was to test and see if images of targets could be created in a 2D plane before extending the model to a 3D space.

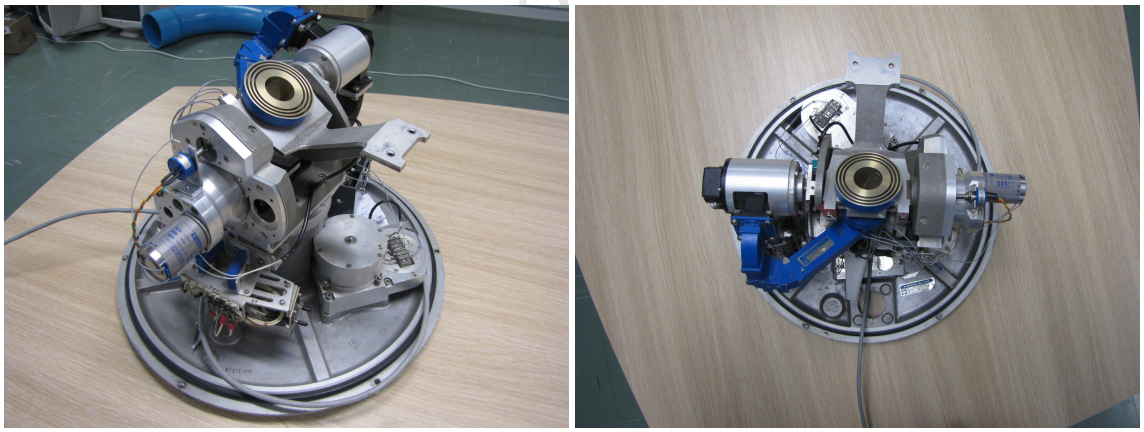

Figure 3.4: Azimuth over elevation (2-axis) rotating pedestal that was used.

For the 3D experiments, a 2-axis rotating pedestal was used. This pedestal was donated to UCT from the South African Navy and was previously used on one of it's vessels. It can be seen in Figure 3.4. The same angular constraints that were set for the 1-axis pedestal was set for both the azimuth and elevation axes of the 2-axis rotating pedestal. The control of the 2-axis rotating pedestal was however not the same as for the 1-axis rotating pedestal. As there were two motors on the pedestal (one for each axis), each motor had to be controlled separately. All information pertaining to the 2-axis pedestal can be found in [26].

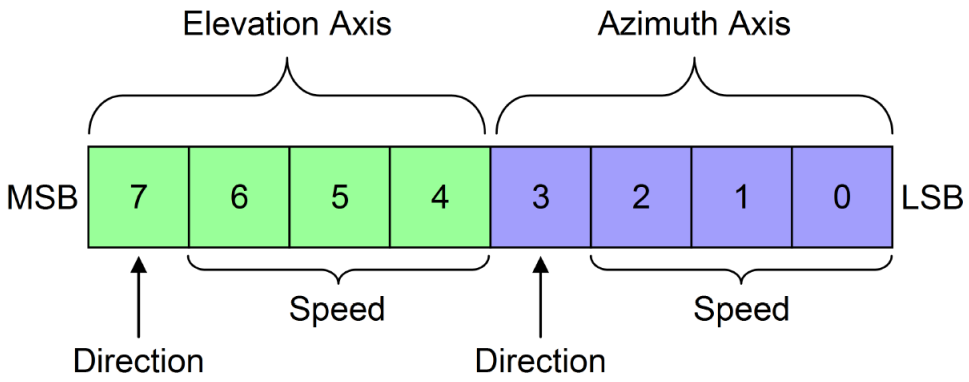

Figure 3.5: Parallel port [26]

The motor is controlled by a parallel port which contains 8 bits [26]. This can be seen in Figure 3.5. The 8 bit port is divided into two. The left most 4 bits control the elevation axis and the right most 4 bits control the azimuth axis. Bit 7 and 3 control the direction of the motors via an H-bridge. The remaining 3 bits control the speed of the motor. The motor thus has 7 speed settings. For this project it was only necessary to rotate the pedestal at one speed, and thus the lowest speed setting was chosen. The 8 bits of the parallel port were set by the DAQ card through LabVIEW. This would be set at each instant when the VNA was done recording the data and storing it.

The control of the 2-axis rotating pedestal was different from that of the 1-axis rotating pedestal. The motors on the 2-axis pedestal were not stepper motors, but DC motors. The control of this pedestal was implemented by a previous undergraduate student and was done in the Linux environment. Each motor on the pedestal was directly coupled to a 3-phase synchronous motor which would output three voltages (phase shifted by 120 degrees). This voltage was then fed into a synchronous-to-digital card which would convert these 3-phase voltages into an angular position. In this way, the exact angular position of each motor can be monitored and controlled. Upon embarking on using this pedestal it was found that the synchronous-to-digital card was faulty and an alternative method was to be used to measure and control the angular position of each motor. It was decided that precision potentiometers would be used. Each potentiometer was mounted onto a gear on each of the axes of the rotating pedestals.

3.4 VNA Design Considerations

In this project the Agilent E5071B vector network analyzer was used as the radar measurement system. This device is owned by the UCT Department of Electrical Engineering and has an operational bandwidth of 8.5 GHz. This is a measuring device which is used for measuring the network parameters such as the gain and stop-band rejection of electrical devices such as amplifiers, filters and other RF components [33]. It is commonly used to measure the S-parameter of a device which involves the reflection and transmission of power through a network. This can then be used to characterize the network or device

under test. As its name suggests, it is a vector network analyzer and thus it is capable of measuring both magnitude and phase of a received signal at specific frequencies. It is a 2-port device and was set up in such a way that port one was connected to the transmitting antenna and port two was connected to the receiving antenna. This device operates between the frequency range of 300 kHz to 8.5 GHz. This high bandwidth is what makes the system an UWB system and allows for very fine spatial resolution as the range resolution of the system is dependent on the system bandwidth [5, 9]. This fine spatial resolution allows for distinguishing very closely spaced targets. This project utilizes the S-parameter measurement from the VNA, and by connecting an antenna to both available ports on the VNA, a reflection measurement is taken of the scene in front of the antennas. This data is then run through signal processing algorithms and reconstruction algorithms to create an image of the scene. There are many parameters which are set on the device during the experiments, and these are discussed here.

The physical connection between the computer and the VNA is a LAN connection. By knowing the IP address of the VNA, it is possible to control the device by using specific VISA commands. The VNA and computer can be connected in two ways. Either by direct connection between the two devices or they can be connected via a network. For the experiments that were carried out in this project the devices were connected to each other through the UCT network and for experiments that were not within a laboratory environment with access to the UCT network, the connection was made directly between the computer and the VNA.

In order to get access to the VNA, the Agilent IO Suite had to be installed and the device was to be found through this program. All documentation concerning the location of the install file and installation process, as well as the method on how to go about this can be found on the information CD. Once this program has been installed and the device has been found and connected over the network, the driver for the device was downloaded from the National Instruments website and installed into LabVIEW. This driver would allow full access and control of all the functions and buttons on the VNA and this is what was used to control the settings on the device.

3.4.1 Frequency Selection

An UWB system is defined as a system which has a bandwidth greater than 500 MHz or an instantaneous fractional bandwidth greater than 0.2 [9]. Because the VNA under consideration is operational over the frequency range from 300 kHz to 8.5 GHz, this makes it ideal for use in an UWB system. This high frequency span also allows for very fine spatial resolution with regards to imaging targets that are very closely spaced. It was decided that the full frequency spectrum of the device would be used. In this way the highest range resolution could be extracted from the device for imaging targets. Any unwanted frequencies could then be removed in software.

3.4.2 Frequency Spacing

The frequency spacing of the system is determined by the maximum round trip time to the furthest target in the time domain. This relationship is shown in Equation 3.1, where T_{max} represents the maximum round trip time [30].

$$\triangle f = \frac{1}{T_{max}} \tag{3.1}$$

This value (T_{max}) also has a direct relationship with the maximum distance (R_{max}) to which targets can be detected. This is given by

$$R_{max} = \frac{cT_{max}}{2} \tag{3.2}$$

where c represents the speed of light ($3\text{x}10^8$ m.s^{-1}). From these Equations it is evident that there is a direct relationship between the frequency spacing and the maximum distance to which a target can be detected. Rearranging Equation 3.1 and substituting this into Equation 3.2 the Equation simplifies to

$$\triangle f = \frac{c}{2R_{max}}. \tag{3.3}$$

For this project it was decided that 10 m would be the maximum range to which imaging (or target detection) would be done. This maximum range was chosen because of the limitations of the laboratory environment as well as simplifying calculations. Using Equation 3.3, it was calculated that a frequency spacing of 15 MHz would be required. The frequency span that was to be used by the VNA was between 300 kHz - 8.5 GHz. With a frequency spacing of 15 MHz this meant that the number of points that would be set on the VNA was 566. This was calculated using Equation 3.4 where n_{VNA} is the number of points to be set on the VNA, f_{span} is the frequency span of the system and $f_{spacing}$ is the frequency spacing.

$$n_{VNA} = \frac{f_{span}}{f_{spacing}} \tag{3.4}$$

The data that is received from the VNA will all be in the frequency domain and can be translated back to the time domain by an inverse Fourier transform. By doing this it will create a time profile of the scene. This time profile can then be converted to a range profile using Equation 3.2. The distance of the target relative to the antennas can be read off from this range profile. A peak will be displayed on this range profile at the distance where the target is located. The width of this peak can be approximated by Equation 3.5 where δt represents the width of the peaks and B is the bandwidth of the system [5, 30].

$$\delta t \approx \frac{1}{B} \tag{3.5}$$

Using the full bandwidth of the VNA, Equation 3.5 shows that the width of the peaks of the range profiles would be approximately 66.6 ns wide when plotted on a time scale. In order for the range profile to be plotted smoothly and the peaks to be clearly defined, there should be a sufficient amount of samples taken within the peaks of the range profiles. To prevent excessive computational calculations while still obtaining a smooth shaped time domain plot, it was decided that 10 samples within the peak should be sufficient, i.e.

$$\Delta t = \frac{\delta t}{10}. \tag{3.6}$$

When using Equation 3.6, the calculated time spacing is 0.666 ps. The number of sample points in the time domain is equivalent to the number of sample points in the frequency domain [30]. This can be calculated using Equation 3.7 where N represented the number of time and frequency samples that will be required by the UWB system.

$$N = \frac{T_{max}}{\Delta t} \tag{3.7}$$

After computing Equation 3.7, the next highest power of 2 was taken as the number of points that was to be used in the time and frequency domain [5]. The reason for this is that fast Fourier transforms (FFT's) are more efficient in powers of two. It was calculated that 8192 points were needed. The number of points that can be set on the VNA is limited to 1601 and the maximum frequency can be set to 8.5 GHz. The number of points on the VNA was set to 566 with a frequency spacing of 15 MHz and the remaining frequency points above 8.5 GHz were zero padded in software.

3.4.3 Output Power

The VNA that was used is capable of outputting power between the ranges of -55 dBm and 10 dBm (3.16×10^{-6} to 10 mW) of power through each port. The output power can be changed according to the user specifications. By increasing the output power, this will allow for imaging of targets which are further away from the antennas. This is because the received power is inversely proportional to the fourth power of the distance between the transducers and the targets [5, 30]. For the purposes of this project the output power of the VNA was set to the default value of 0 dBm (1 mW), which was sufficient for imaging the targets within 1 m of the antennas. An attempt was made to insert a Mini-circuits ZHL-42 Coaxial Amplifier transmitter chain of the system. This power amplifier is operational over the frequency range between 700 MHz to 4200 MHz. This reduced the overall bandwidth of the system to 2.7 GHz which equated to a range resolution of 5.55 cm, but increased the signal-to-noise ratio of the system. When using this device, stronger echoes were received from targets. Unfortunately after a day of testing, the device failed and a replacement was not received in time to do experimentation. For this reason, no extra amplifier was used in the transmitter chain of this UWB imaging system.

3.4.4 S-Parameter Measurements

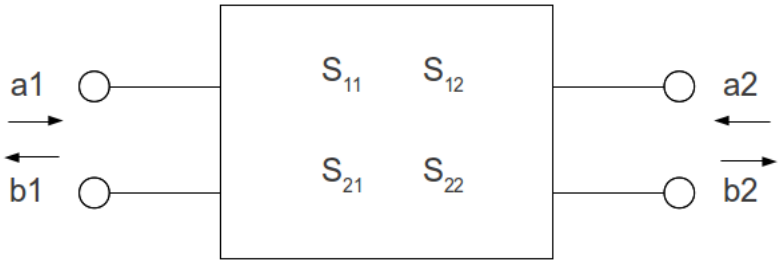

Figure 3.6: S-parameters of a 2-port network

In the experiments that were carried out, the VNA was set to record the S-parameter information. The S-parameter set is a measurement which shows the response of a N-port network to sinusoidal voltage signals present at each port as a result of an injected sinusoidal voltage on a particular port [23]. The first digit in the subscripts is a reference to the output port (or measured port) and the second digit refers to the port at which the voltage is inserted. Thus a S_{21} measurement would refer to a response voltage on port 2 as a result of an applied voltage on port 1 [23]. Figure 3.6 shows the different S-parameters for a 2-port device. The S-parameters of such a 2-port network (terminated in an impedance of Z_o) can be written as [23]:

$$S_{11}=\frac{b1}{a1}$$

$$S_{12}=\frac{b1}{a2}$$

$$S_{21}=\frac{b2}{a1}$$

$$S_{22}=\frac{b2}{a2}$$

where a_i and b_i are the amplitudes of the incident and reflected sinusoidal voltage waves. The VNA S-parameter that was measured from the VNA was the S_{21} parameter. All the data that is recorded is in the frequency domain, and thus the S_{21} measurement which is taken from the VNA is in fact the Fourier transform (or transfer function) of the scene and the antennas.

In any data acquisition system there are 2 statistical quantities that are very important when considering the noise that is present in the signal [16]. These two quantities are the mean (or average value) and standard deviation of the noise. The mean value is denoted by $E[X]$ where X is a sample of the noise. The standard deviation is calculated by calculating the difference between the square of the mean and $E[X^2]$. The square root of this value is taken to be the standard deviation [16]. In defining the mean and standard deviation

terms, it is assumed that all the variables (or data samples) are independent and identically distributed. This means that each sample value has no impact on the value of the next, or any subsequent, sample values and they are independent of each other. The assumption also includes identically distributed samples. This means that the means and standard deviations of each of the samples are the same.

Averaging

In a data acquisition system, the accuracy/precision of the data that is collected is very important. The standard deviation on the measurement is a very important measurement as it shows the spread of the samples that are taken. It can be shown mathematically that by taking many measurements and averaging them, the standard deviation of the average of these samples can be reduced to a value which is smaller than the standard deviation of each individual measurement [16]. The proof of this can be seen below:
Consider a group of n samples (X_i) who's mean is represented by μ where:

$$\mu = E[X_i]$$

All the samples have the same mean and standard deviation. This is because they are identically distributed. The standard deviation of the samples can be represented by σ, where

$$\sigma^2 = E[(X_i - \mu)^2]$$

$$= E[X_i^2 - 2\mu X_i + \mu^2]$$

$$= E[X_i^2] - 2\mu^2 + \mu^2$$

$$\sigma^2 = E[X_i^2] - \mu^2$$

and i refers to any of the samples. The calculated average value over n samples (X_i) can be written as:

$$X_{avg} = \frac{1}{n}\sum_{i=1}^{n} X_i$$

If μ_{avg} represents the mean of the average and σ_{avg} the standard deviation of the average then:

$$\mu_{avg} = E[X_{avg}] = E\left[\frac{1}{n}\sum_{i=1}^{n} X_i\right] = \frac{1}{n}\sum_{i=1}^{n} E[X_i] = \frac{1}{n}\sum_{i=1}^{n} \mu = \mu \ .$$

This shows that μ_{avg} is an unbiased estimator for μ. The variance of X_{avg} is:

$$\sigma_{avg}^2 = E[X_{avg}^2] - \mu_{avg}^2 = E\left[\left(\frac{1}{n}\sum_{i=1}^{n} X_i\right)^2\right] - \mu^2$$

$$= E\left[\left(\frac{1}{n}\sum_{i=1}^{n} X_i\right)\left(\frac{1}{n}\sum_{j=1}^{n} X_j\right)\right] - \mu^2$$

$$= E\left[\frac{1}{n^2}\sum_{i=1}^{n}\sum_{j=1}^{n} X_i X_j\right] - \mu^2$$

$$= \frac{1}{n^2}\sum_{i=1}^{n}\sum_{j=1}^{n} E\left[X_i X_j\right] - \mu^2$$

It is assumed that the samples that are taken are independent. This property can be used as it shows that:

$$E[X_i X_j] = E[X_i]E[X_j] = \mu\mu = \mu^2 \text{ when i<>j}$$

Using this assumption, the first term can be split into two terms:

$$\sigma_{avg}^2 = \frac{1}{n^2}\sum_{i=1}^{n} E[X_i^2] + \frac{1}{n^2}\sum_{i=1}^{n}\sum_{j\neq i} E[X_i X_j] - \mu^2$$

$$= \frac{1}{n^2}\sum_{i=1}^{n} (\sigma^2 + \mu^2) + \frac{1}{n^2}\sum_{i=1}^{n}\sum_{j\neq i} \mu^2 - \mu^2$$

$$= \frac{1}{n}(\sigma^2 + \mu^2) + \frac{n-1}{n}\mu^2 - \mu^2$$

$$= \frac{1}{n}\sigma^2$$

thus

$$\sigma_{avg} = \sigma\sqrt{\frac{1}{n}}$$

From this it can be seen that by taking more measurements, the standard deviation of the average of the measurements is $\sqrt{\frac{1}{n}}$ times smaller than the standard deviation of each sample. By taking more samples, the standard deviation of the average would be much smaller than the standard deviation on each sample. During the experiment however, more samples would require more time and so it was decided that 10 samples would be sufficient to reduce the standard deviation by a factor of 0.32. In a data acquisition system, there can be many sources of noise in the system. This noise affects the data that is received and can influence signal processing operations. It can also affect an image that is created. Thus it is important to make use of methods which reduce the effects of noise on the system. There are many techniques that can be used to reduce the noise in a data acquisition system. A simple technique could be to use a filter to filter out any out-of-band noise which has effects on the system. This however does not get rid of the noise that falls within the band limited region that is being used for signal processing methods [16]. The in-band noise can be reduced by taking multiple measurements of the same scene and then averaging the results of those results. This averaging technique reduces the effect of noise.

3.5 Antennas

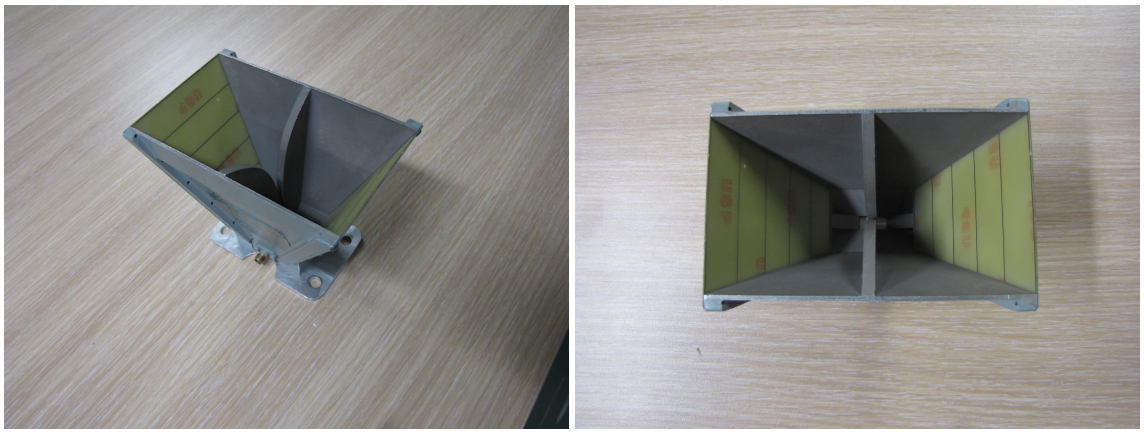

Figure 3.7: Picture of the horn antennas

This project made use of UWB signals, which meant that a large operating frequency range would be required. For this reason, UWB antennas were chosen so that the highest bandwidth could be extracted using these antennas. Two Cobham H-1498 series broadband horn antennas were used as they were available in the department. The antennas can be seen in Figure 3.7. Their specifications can be seen in Appendix A. The specified operating frequency of these antennas is from 2 to 18 GHz. A S_{11} measurement was taken of the antennas, which can be seen in Figure 3.8 and it was found that it could be used from 1.5 GHz. The operating frequency of these antennas affect the range of frequencies which can be used for signal processing. Even though the VNA is capable of taking measurements over the frequency range 300 kHz to 8.5 GHz, this frequency range is limited by the antennas. Any frequencies below the specified frequency range of the antennas would be severely attenuated and would negatively affect the SNR of the measured frequency domain data. By using these antennas, the total system bandwidth is reduced to between 1.5 GHz and 8.5 GHz. This changed the system bandwidth from 8.5 GHz to 7 GHz. From Equation 2.3, a decreased bandwidth will worsen the range resolution, i.e. make it more difficult to distinguish targets that are closely spaced. With 7 GHz of bandwidth, the range resolution changes to 2.49 cm as compared to 1.76 cm with 8.5 GHz of bandwidth. This means that targets that are located closer than 2.5 cm apart cannot be distinguished as two separate targets, but will show up as a single or overlapping target.

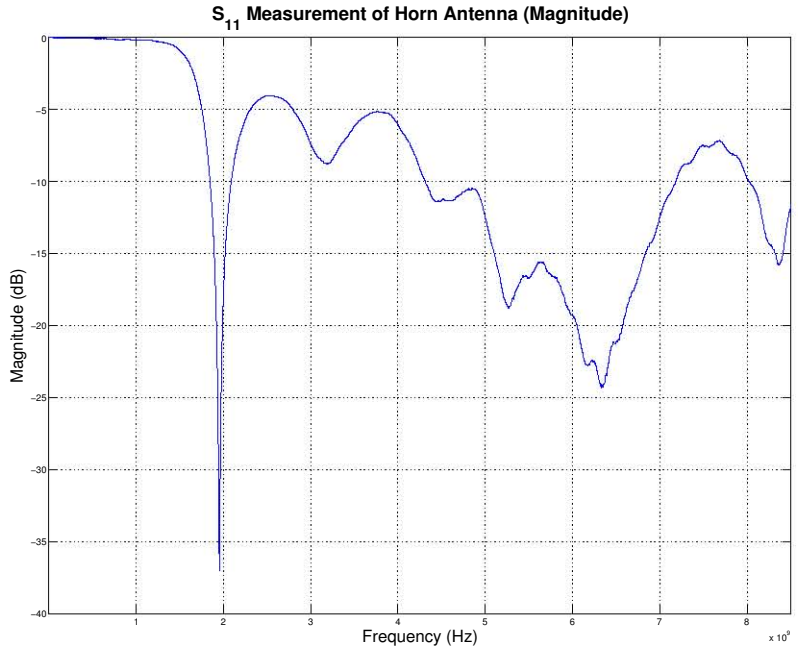

(a) S_{11} magnitude measurement

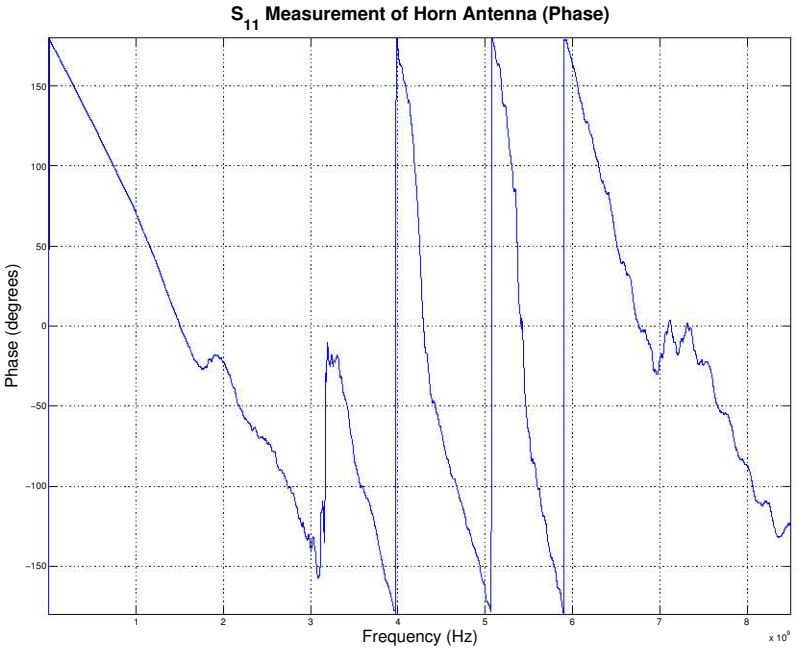

(b) S_{11} phase measurement

Figure 3.8: S_{11} measurement of the horn antenna

The S_{11} measurement of the antennas can be seen in Figure 3.8. From this figure it can be seen that the antennas are operational for frequencies above 1.5 GHz as the reflection coefficient is not too high. The transfer function of the antennas can be seen in Figure 3.9. This transfer function is the S_{21} measurement from the VNA on a dB scale when the two antennas are facing each other at different distances. These transfer functions were used in the calibration process. As can be seen from the figure, the shape of the transfer function at each position is the same, but at a lower dB level. This is because what is displayed is

the received power relative to the transmitted power, and this received power is inversely proportional to the square of the distance between the antennas [5, 30]. Thus, the further the antennas are placed apart, the less power is received. There are some differences between the shape of the transfer functions at 0 cm, 10 cm and 20 cm as compared to the others. This could be as a result of multiple reflections at this distance, causing resonance at 2.1 GHz and the antennas are not in the far field of each other.

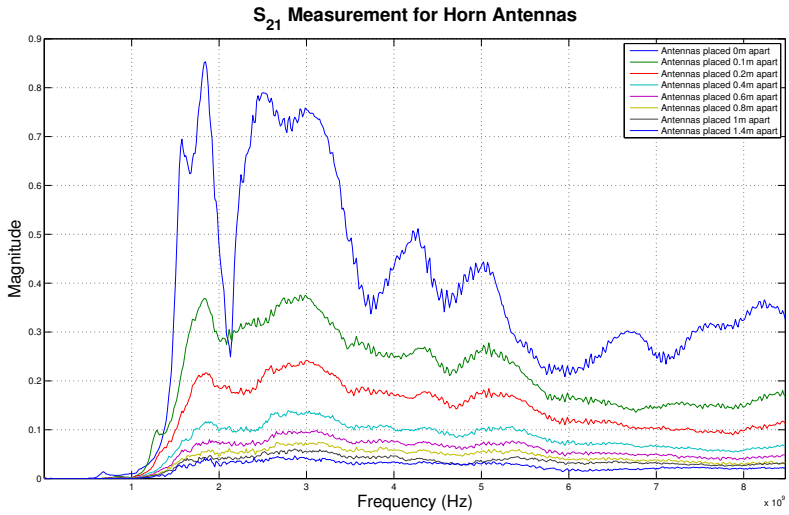

(a) Linear plot of S_{21} measurement

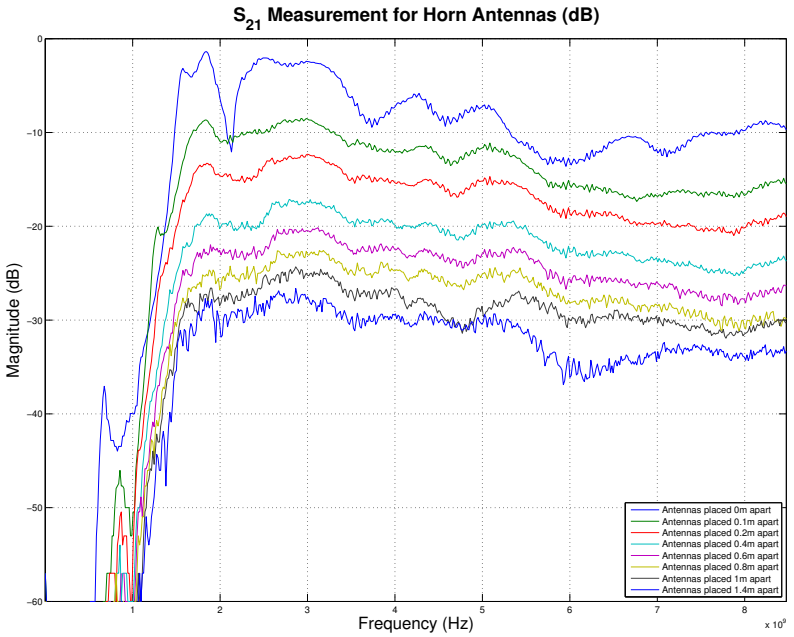

(b) Decibel plot of S_{21} measurement

Figure 3.9: Frequency domain data (transfer function) of horn antennas at different distances

The far-field is defined as the region around an antenna where the angular field distribution is not dependent on the distance from the antenna [6]. The far field region can be calculated by

$$d_{far} = \frac{2D^2}{\lambda} \tag{3.8}$$

where D is the aperture length and λ is the wavelength at the centre frequency (5 GHz). Using Equation 3.8 the far field distance was calculated as $d_{far} = 51.634\,cm$. Because the antennwindowas are not in the far field for the 0 and 10 cm plots the far-field equation is not obeyed and these plots do not have the same shape as the others. This falls within the near-field region of the antenna. During all the experiments the targets were placed in the far field region of the antennas.

The data sheet of the antennas states that the 3 dB beamwidths of the antennas are 80 degrees in the E-plane and 50 degrees in the H-plane. This difference in beamwidth is as a result of the dimension of the horn antenna in the horizontal and vertical plane and of the aperture distribution function. It can be shown that the 3 dB beamwidth of an antenna is inversely proportional to the length of the antenna aperture [5, 30]. The beamwidth is related to the aperture length by $\theta_{3\,dB} \approx \frac{\lambda}{D}\ rad$, where λ is the wavelength and D is the aperture length. The beamwidth of the antenna was measured, in the E-plane and H-plane, at each frequency over the range 1.5 GHz to 8.5 GHz. The beamwidth of the centre frequency (5 GHz) is displayed in Figure 3.10 as its beamwidth best matched the data sheet of the antenna. This is because the beam pattern and 3 dB beamwidth of an antenna is dependent on the operating frequency as specified by $\theta_{3\,dB} \approx \frac{\lambda}{D}\ rad$ [5, 30]. The beamwidth is larger at lower frequencies and narrower at higher frequencies. The 3 dB beamwidth can be read off and measured from the half power points on Figure 3.10. From the figure it can be seen that the beam pattern at 5 GHz is approximately 80 degrees in the E-plane (as specified by the data sheet) and 60 degrees in the H-plane. The errors in the measurements could be as a result of the beam pattern experiment setup. It is however very close to the specified data sheet indicators.

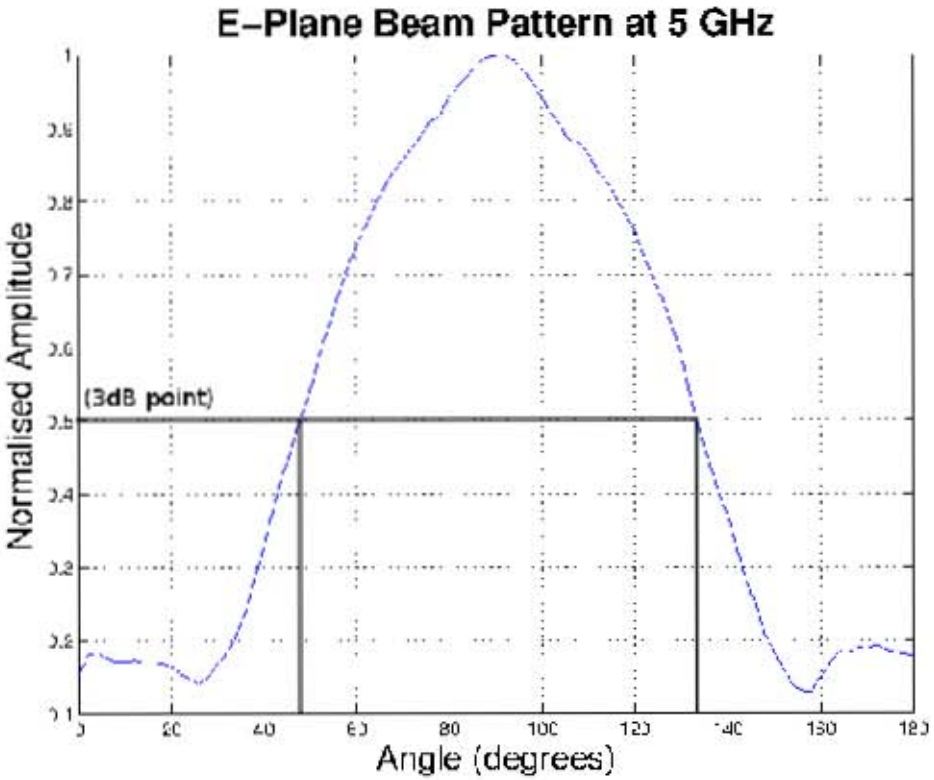

(a) Beam pattern in the E-plane

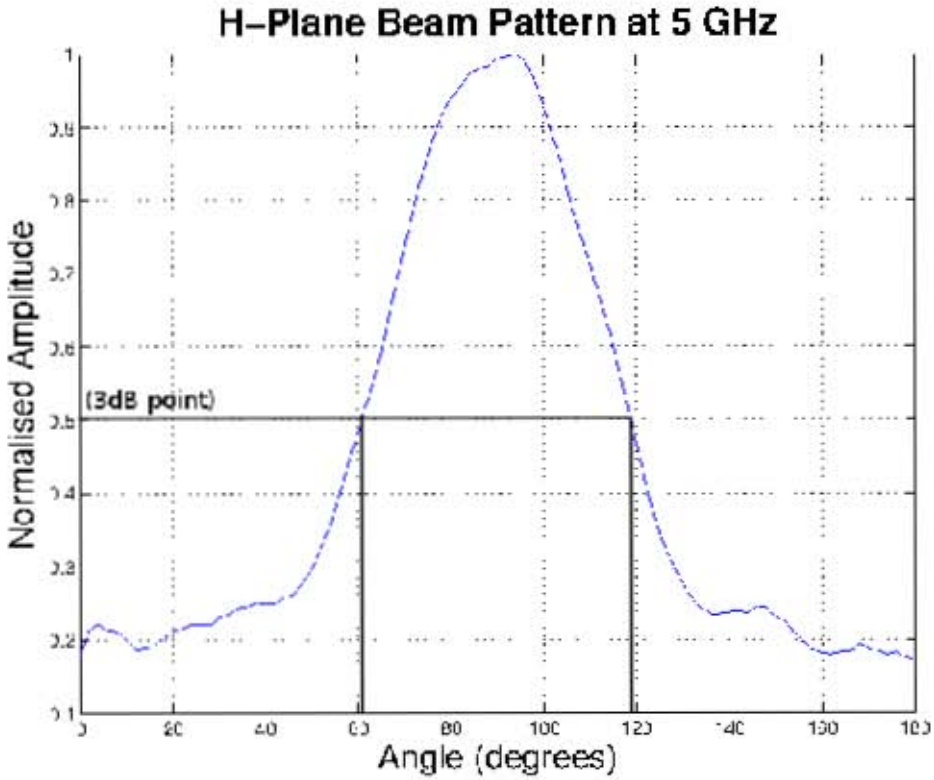

(b) Beam pattern in the H-plane

Figure 3.10: Horn antenna beam pattern

3.6 Signal Processing

After the data is collected from the VNA and saved to a file, the data has to be processed and an image created. All signal processing is done in Matlab. By implementing these operations in software, it reduces the physical hardware needed to perform these operations. The techniques and procedures that are carried out are described here. A simplified block diagram of the radar system can be seen in Figure 3.11. This block diagram shows the transfer function of the UWB radar system. $V_{tx}(f)$ represents the transmitted signal, $V_{rx}(f)$ the received signal and $H(f)$ the transfer function of the scene and the antennas. The transfer function of the antennas is $H_1(f)$ and the transfer function of the scene is $H_2(f)$.

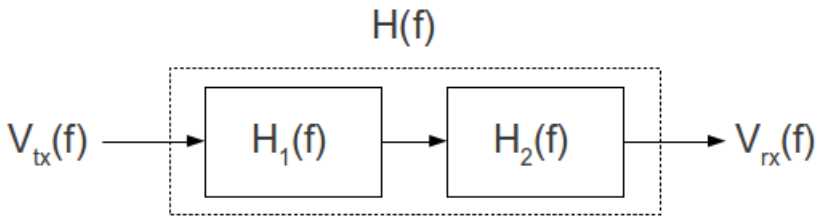

Figure 3.11: Block diagram of the UWB system.

All the data that is recorded from the VNA is in the RF range. All the data is basebanded before any signal processing is done. Basebanding is the process whereby the high frequency data is converted down to a lower frequency [5]. This method of down conversion is done by multiplying the frequency domain data with a cosine signal whose frequency is the centre frequency of the frequency domain data that is being down converted. By doing this, the frequency domain data is converted to a lower frequency band centered around 0 Hz. The effect of basebanding is that for the return from an ideal point scatterer the phase of the baseband signal is constant over the peak of the time domain signal [5].

The data that is collected from the VNA is in the frequency domain. In order to get this data to the time domain it can be converted by an inverse Fourier transform. This time domain data can then be converted to range data by using equation 3.2. This converts the data from a time domain axis to a range axis. This range axis will show the distance to the reflectors which are located at a certain distance from the antennas, up to a maximum distance of R_{max}. These reflector will show up as a peak on the range axis.

3.6.1 Antenna Calibration

(a) Antennas placed 40 cm apart (b) Antennas placed 60 cm apart

Figure 3.12: Picture of the antenna location when measuring antennas transfer function

The main aim of the signal processing is to extract the transfer function of the scene in front of the antennas so that an image can be formed from it in the reconstruction algorithm. In order to obtain the transfer function of the scene only, the full transfer function has to be measured. This includes the transfer function of the antennas as well as the scene. This is represented by H(f) in Figure 3.11. The transfer function of the scene, $H_2(f)$, needs to be extracted from H(f). Since H(f) is the product of the two individual transfer functions, $H_1(f)$ of the antennas and $H_2(f)$ of the scene, the transfer function of the scene can be extracted by multiplying the full transfer function, H(f), with the inverse transfer function of the antennas, $H_1(f)$, provided that $H_1(f)$ is non-zero over the frequency range under consideration. This is known as the inverse filter method. This can be written as [9]:

$$H_{IF}(f) = \begin{cases} \frac{1}{H_1(f)} & -\frac{B}{2} \leq f \leq \frac{B}{2} \\ 0 & elsewhere \end{cases}$$

By doing this, the transfer function of the antennas are catered for and there effects on the received signal is removed. The transfer functions of the antennas are collected by placing the antennas in such a way that they are facing each other. This can be seen in Figure 3.12. The distance between the antennas is chosen so that the antennas are placed in the far-field. The distance between the antennas is measured and recorded. By incorporating the effects of the antennas, the phase shift associated with the distance between the antennas also has to be incorporated. If not, then the peak of the time domain signal will not display the correct distance of reflectors.

3.6.2 Background Subtraction

Background subtraction is a technique which is used to remove any unwanted background clutter or noise from the signal of interest [9]. The experiments and measurements were

taken in an indoor environment which contained many unwanted objects such as chairs and tables. When measuring the transfer function H(f), these unwanted objects influence the measured transfer function of the scene. The direct coupling between the antennas can also be regarded as background noise as there are some signals which travel directly from the transmitter to the receiver without interacting with the scene. Thus the profiles that are measured will contain these objects and unwanted noise. It should be noted that these objects will not move during the experiment, so they can be removed in software. This can be done by taking a measurement of the background scene without the targets present. By placing the target in the scene and taking readings, we can subtract the transfer function of the background scene from that of the scene when the targets were present. In this way we are able to get rid of any background noise or clutter which is present and unwanted in the scene [9].

(a) Picture of the scene with no target present

(b) Picture of the scene with target present

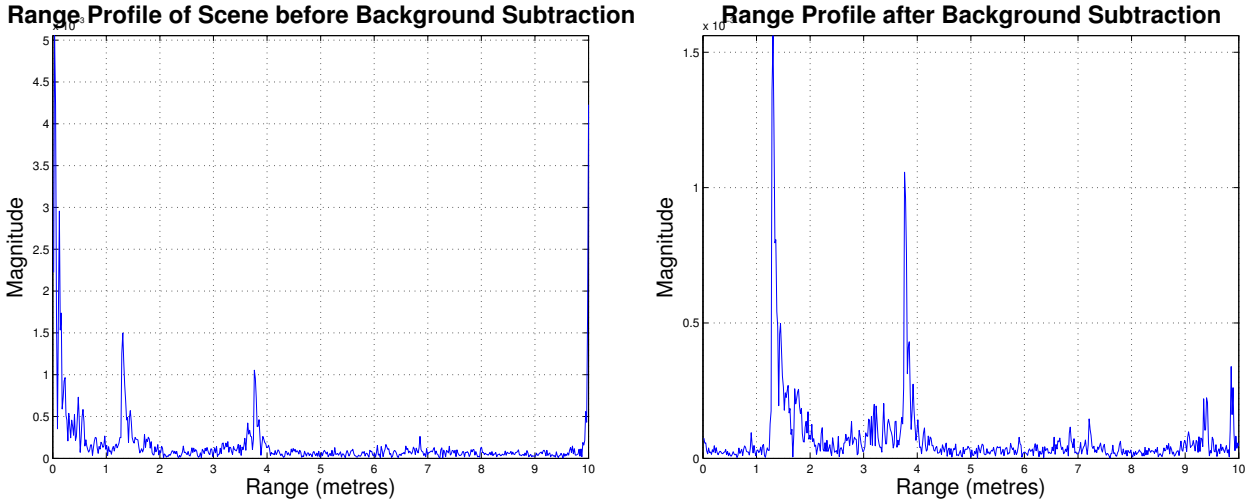

(c) Range profile of the scene without background subtraction

(d) Range profile of the scene with background subtraction applied

Figure 3.13: Figure showing the effects of background subtraction when no clutter present

The effect of background subtraction can be seen in Figure 3.13 and 3.14. It demonstrates the effect of background subtraction of the chair. In Figure 3.13, a background scene was

taken where chairs, desks and antenna coupling form part of the background. Two grid reflectors were then placed in front of the antennas. The range profile of the scene before and after background subtraction can be seen. In the range profile without background subtraction the effect of antenna coupling can be clearly seen. This is represented by the peak close to 0 m from the antennas. The level of this signal is much higher than that of the reflected signals from the reflectors. After background subtraction, it can be seen that this antenna coupling is removed from the range profile. The two targets can clearly be seen in the range profile. In Figure 3.14, one of the reflective grids was included as part of the background. A second reflector was placed at a distance further away from the antennas. Without background subtraction it can be seen that the direct coupling between the antennas is strongest. The reflection from the first metal grid is also higher than that of the second grid as it is placed closer to the antennas. In this way it is difficult to see the reflection from the second grid which is further away without background subtraction. After applying background subtraction , the first grid reflector as well as the antenna coupling is removed from the scene and only one grid reflector is present in the range profile. This is because the grid reflector which is closer to the antennas formed part of the background scene.

(a) Picture of the scene with no target present

(b) Picture of the scene with target present

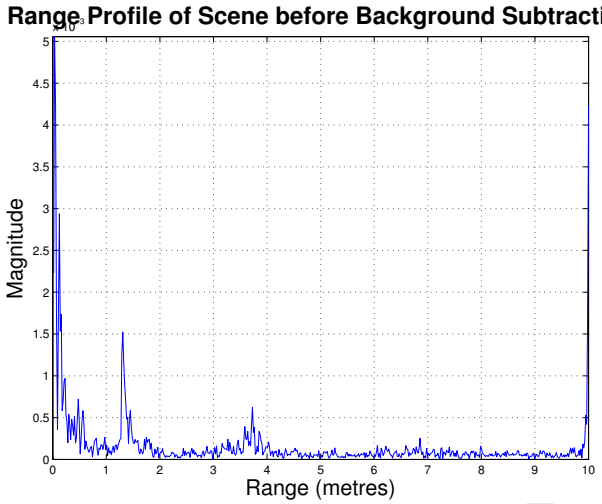

(c) Range profile of the scene without background subtraction

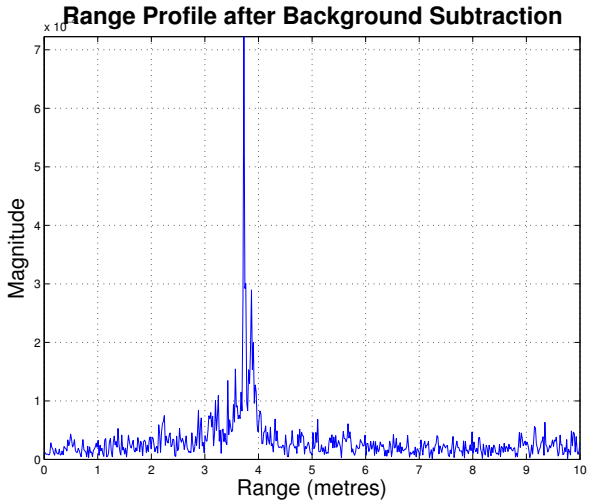

(d) Range profile of the scene with background subtraction applied

Figure 3.14: Figure showing the effects of background subtraction when clutter is present

3.6.3 Windowing

All the measurements that are taken are measured in the frequency domain and then transfered to the time domain by an inverse Fourier transform. There are certain frequencies which are included in the measurement which may not be wanted. This could be as a result of various reasons. Horn antennas were used in these experiments and the specified operating frequency of these antennas stretch from 2 GHz to 18 GHz. They were tested and it was evident that they could be used from frequencies as low as 1.5 GHz. Any frequencies below 1.5 GHz can be removed in software by applying a windowing function to the data so that the unwanted frequencies are suppressed. There are many windowing functions which could be applied to the recorded data.

A possible filter to use would be a rectangular window. This will remove all unwanted frequencies. The impulse response of this filter is a $\frac{sin(x)}{x}$ (Sinc) function, which has very high sidelobes [5]. These sidelobes are unwanted and would need to be suppressed. This

can be done by smoothly tapering the edges of the windowing function. The results of this smoothing effect would be a Hann or Hamming window. By tapering the ends of the rectangular function reduces the sidelobes of the impulse response. This reduction of the sidelobes comes at the expense of a broadening in the main lobe. Table 3.1 shows common weighting functions and their effects on sidelobe reduction and mainlobe broadening [5]. The Hamming window function was used during signal processing.

Weighting function (over range $\mid f \mid \leq$B)	Peak Sidelobe (dB)	3dB Mainlobe width (relative)	Sidelobe decay f'n
Uniform	-13.2	1.0	$\frac{1}{t}$
$0.33+0.66\cos^2(\frac{\pi f}{B})$	-25.7	1.23	$\frac{1}{t}$
$\cos^2(\frac{\pi f}{B})$	-31.7	1.65	$\frac{1}{t^3}$
Hann: $0.5+0.5\cos(\frac{2\pi f}{B})$	-31	1.6	$\frac{1}{t}$
Taylor: ($\overline{n}$=8)	-40	1.41	$\frac{1}{t}$
Dolph-Chebyshev	-40	1.35	1
Hamming: $0.54+0.46\cos(\frac{2\pi f}{B})$	-41	1.50	$\frac{1}{t}$
Blackman: $0.42+0.5\cos(\frac{2\pi f}{B})+0.08\cos(\frac{4\pi f}{B})$	-57	1.9	

Table 3.1: Common windowing functions which can be used for suppression of sidelobes [5].

3.6.4 Zero Padding

The data that is recorded from the VNA is limited by the frequency limits of the device. As mentioned before, the device operates between 300 kHz and 8.5 GHz. The maximum target detection range is 10 m and this relates to a frequency spacing of 15 MHz on the VNA. With this frequency range and frequency spacing, it allows for 566 samples to be measured from the VNA. The number of samples in the frequency domain is related to the number of samples in the time domain. All the data that is recorded in the frequency domain from the VNA is translated to the time domain by an inverse Fourier transform. Equations from Section 3.4.2 were used to calculate the appropriate variable values. From these calculations, the number of samples in the array that was to be inverse Fourier transformed was 8192. The VNA recorded 566 samples, and the remaining 7626 samples were filled with zeros. By zero padding the tail end of the data that is received from the VNA, it reduces the sample spacing of the time domain data. Any frequencies above 8.5 GHz are not wanted, or cannot be measured, and thus it is appropriate to fill the frequencies above this with zeros.

3.6.5 Reconstruction Algorithm

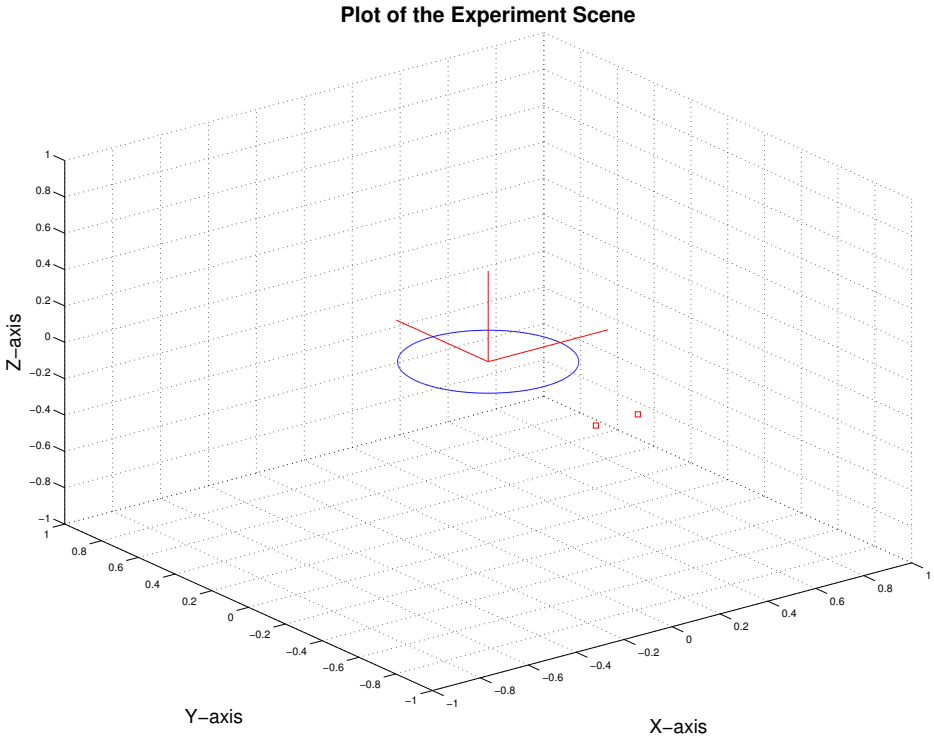

Figure 3.15: Image of the experiment scene

The reconstruction algorithm that was used in this project is known as the time domain back-projection algorithm. It is similar to the coherent aperture synthesis used for SAR. In this algorithm, the scene is divided into a regular cube where [27]:

$$\triangle x = \triangle y = \triangle z = \frac{\lambda}{4\kappa}$$

where λ is the wavelength of the highest measured frequency and κ being a variable that was used to adjust the sample spacing of the image. From this calculation it was decided that $\triangle x = \triangle y = \triangle z = 0.005\,m$ was sufficient for creating an image. The experiment scene can be seen in Figure 3.15. From the figure the location of the antennas and the platform can be seen. It is noted that the centre of the scene is located at the centre of rotation of the platform. The antennas are located side by side at a fixed distance along the y-axis at the same height as the platform.

During the 2D experiments, the platform is rotated to each azimuth angular position by rotating the platform around the azimuth axis. During the 3D experiment the platform is rotated to the first elevation angle, by rotating it around the elevation axis. It is then rotated to the first azimuth angle by rotating the platform around the azimuth axis. The platform is then rotated to each angular position by $\triangle\theta_{azimuth}$ degree increments. When the final azimuth angle has been reached, the platform then rotates in elevation by $\triangle\theta_{elevation}$ degree increments around the elevation axis.

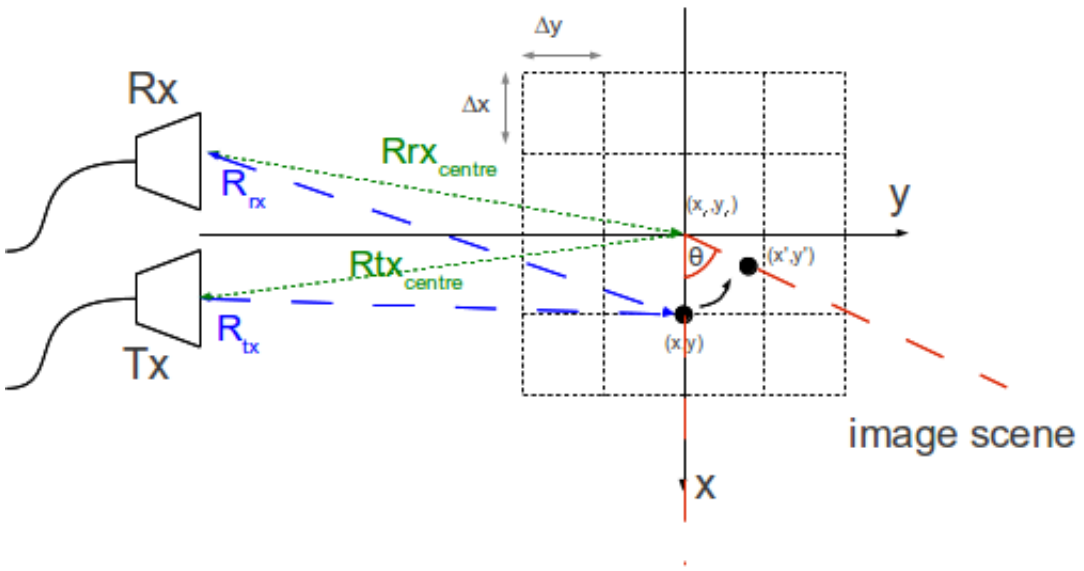

Figure 3.16: Reconstruction algorithm

The reconstruction algorithm is implemented as follows:

Figure 3.16 shows the top view of the scene. This 2D scene is divided into a 2D grid of pixels, each with a x and y coordinate and the spacing between the pixels is given by $\triangle x$ and $\triangle y$. The location of the transmitter is given by (x_{tx}, y_{tx}) and the location of the receiver is given by (x_{rx}, y_{rx}). It is noted that the centre of the scene is located at the centre of rotation of the platform (x_c, y_c). (x, y) is the start position of a given pixel. The rotation matrix is given by:

$$R_\theta = \begin{bmatrix} cos\theta & -sin\theta \\ sin\theta & cos\theta \end{bmatrix}$$

where θ is the angle by which the platform is rotated. The next position of the pixel (after the rotation by θ degrees) is given by (x', y') and is calculated as follows:

$$\begin{bmatrix} x' \\ y' \end{bmatrix} = \begin{bmatrix} x & y \end{bmatrix} \begin{bmatrix} cos\theta & -sin\theta \\ sin\theta & cos\theta \end{bmatrix}$$

which expands to

$$x' = xcos\theta + ysin\theta$$

and

$$y' = -xsin\theta + ycos\theta$$

The distance between the antennas and the centre of rotation is calculated as:

$$Rtx_{centre} = \sqrt{(x_{tx} - x_c)^2 + (y_{tx} - y_c)^2}$$

$$Rrx_{centre} = \sqrt{(x_{rx} - x_c)^2 + (y_{rx} - y_c)^2}$$

where Rtx_{centre} is the distance between the transmitter and the centre of rotation and Rrx_{centre} is the distance between the receiver and the centre of rotation. The 2-way distance between the antennas and the centre of rotation is given by

$$R_c = Rtx_{centre} + Rrx_{centre}.$$

The total distance between the pixel and the antennas is calculated as

$$R_{tot} = R_c + \sqrt{(x')^2 + (y')^2}$$

$$= R_c + \sqrt{(xcos\theta + ysin\theta)^2 + (-xsin\theta + ycos\theta)^2}.$$

Let $P_\theta(t)$ represents the range profile of the scene, at a particular angle θ, in the time domain (i.e. $P_\theta(t)$ is the inverse Fourier transform of the frequency domain data $S_\theta(f)$, at a particular angle, which is received from the VNA), where

$$P_\theta(t) = F^{-1}(S_\theta(f)).$$

The received signal is a time delayed version of the transmitted signal and is dependent on the distance between the targets and the antennas. This time can be calculated as

$$\tau = \frac{2R_{tot}}{c}$$

where R_{tot} is the distance between the antennas and the pixel. In the reconstruction algorithm, the distance to the pixel is calculated at each angular position. The magnitude value of the pixel at this distance is obtained from the range profile, $P_\theta(t)$. This magnitude value of the pixel is obtained for each angular position, and the final value of this pixel in the reconstructed scene is the sum of all the collected magnitude values at each angular position. This can be written as

$$|Pixel_{xy}| = \sum_{n=1}^{N_\theta} P_n(\tau)$$

where n represents the angle index, N_θ represents the number of angles and $|Pixel_{xy}|$ represents the magnitude of the pixel at position (x,y) in the final reconstructed image. This process is repeated for each pixel in the scene and a 2D image is created of the scene.

This reconstructed algorithm is similar to the one discussed in Chapter 2, which is given by

$$\hat{f}(x,y) = \int_0^{2\pi} \int_{-\infty}^{\infty} S_\theta(\omega)|\omega| e^{j\omega t} d\omega d\theta$$

where $S_\theta(\omega)$ represents the Fourier transform of the projection data at an angle θ. The reconstruction algorithm described in Chapter 2 does not take into consideration the beam

pattern of the antennas. The beam pattern of the antennas is a 3D shape and is frequency dependent. It becomes narrower with increased frequency [6]. In this project the beam pattern has been compensated for as an antenna calibration measurement was taken prior to each experiment. The effects of the antennas are removed during the signal processing stage by dividing the received signal from a target by the received signal when the antennas were facing each other. The model described in Chapter 2 assumes that the antennas are co-located, whereas in the experiments the antennas were placed side by side. The signal processing that was implemented also included range correction for the targets as they move further away from and closer to the antennas while rotating on the pedestal. A block diagram showing the procedure of the reconstruction algorithm can be seen in Figure 3.17.

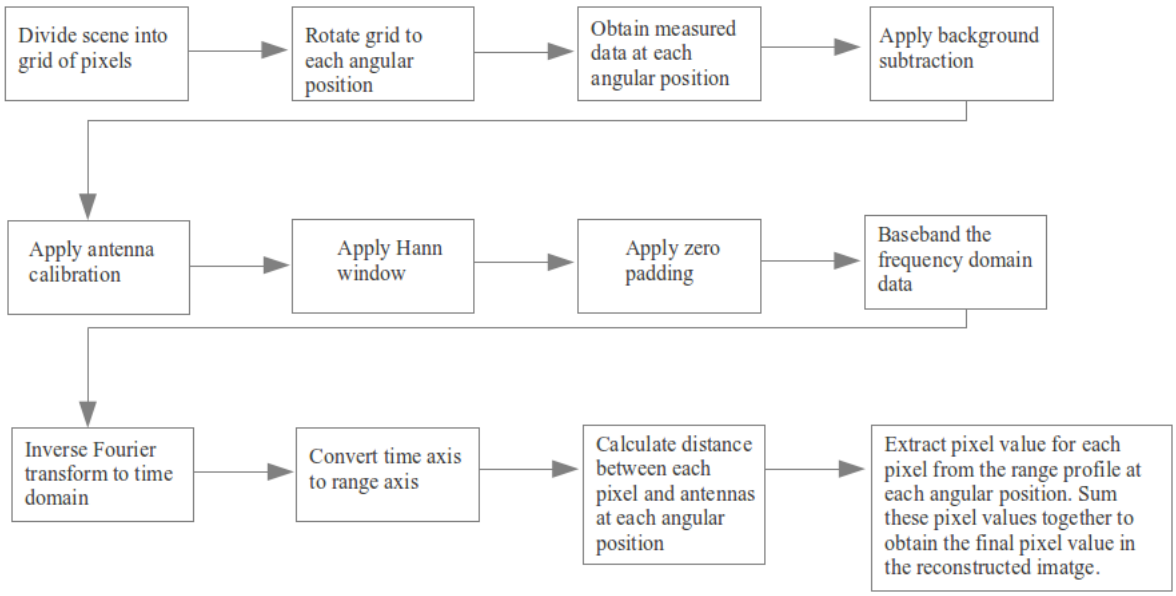

Figure 3.17: Block Diagram of reconstruction algorithm

A 3D reconstruction algorithm was implemented for the 3D experiments. The same process, as for the 2D case, was followed for the 3D case. A third dimension, height of target (z), was included in this reconstruction algorithm. The location of the transmitter is given by (x_{tx}, y_{tx}, z_{tx}) and the location of the receiver is given by (x_{rx}, y_{rx}, z_{rx}). The centre of the scene is located at the centre of rotation of the platform (x_c, y_c, z_c). (x, y, z) is the start position of a given pixel. The rotation matrices are given as:

$$R_x(\theta) = \begin{bmatrix} 1 & 0 & 0 \\ 0 & cos\theta & -sin\theta \\ 0 & sin\theta & cos\theta \end{bmatrix}$$

$$R_y(\theta) = \begin{bmatrix} cos\theta & 0 & sin\theta \\ 0 & 1 & 0 \\ -sin\theta & 0 & cos\theta \end{bmatrix}$$

$$R_z(\theta) = \begin{bmatrix} cos\theta & -sin\theta & 0 \\ sin\theta & cos\theta & 0 \\ 0 & 0 & 1 \end{bmatrix}$$

where θ is the angle by which the platform is rotated. During the experiments, the pedestal is first rotated around the azimuth axis, for all azimuth angles. This is given by:

$$\begin{bmatrix} x' \\ y' \\ z' \end{bmatrix} = \begin{bmatrix} x & y & z \end{bmatrix} \begin{bmatrix} cos\theta_{az} & -sin\theta_{az} & 0 \\ sin\theta_{az} & cos\theta_{az} & 0 \\ 0 & 0 & 1 \end{bmatrix}$$

where θ_{az} is the angular rotation in the azimuth direction. This expands to

$$x' = xcos\theta + ysin\theta,$$

$$y' = -xsin\theta + ycos\theta$$

and

$$z' = z.$$

The distance between the antennas and the centre of rotation is calculated as:

$$Rtx_{centre} = \sqrt{(x_{tx} - x_c)^2 + (y_{tx} - y_c)^2 + (z_{tx} - z_c)^2}$$

$$Rrx_{centre} = \sqrt{(x_{rx} - x_c)^2 + (y_{rx} - y_c)^2 + (z_{tx} - z_c)^2}.$$

The 2-way distance between the antennas and the centre of rotation is given by

$$R_c = Rtx_{centre} + Rrx_{centre}.$$

The total distance between the pixel and the antennas is calculated as

$$R_{tot} = R_c + \sqrt{(x')^2 + (y')^2 + (z')^2}$$

$$= R_c + \sqrt{(xcos\theta + ysin\theta)^2 + (-xsin\theta + ycos\theta)^2 + z^2}.$$

After the platform has been rotated to each azimuth angle it is then rotated around the elevation axis. This is given by:

$$\begin{bmatrix} x'' \\ y'' \\ z'' \end{bmatrix} = \begin{bmatrix} x' & y' & z' \end{bmatrix} \begin{bmatrix} cos\theta_{el} & 0 & sin\theta_{el} \\ 0 & 1 & 0 \\ -sin\theta_{el} & 0 & cos\theta_{el} \end{bmatrix}$$

where θ_{el} is the angular rotation in the azimuth direction. The distance calculation is then done for each azimuth angle at the new elevation angle. This process is repeated for all azimuth and elevation angles.

The same process is followed, as was done in the 2D case, where the magnitude value of a pixel is extracted from the range profile at each azimuth and elevation angular position. The final value of the pixel in the 3D reconstructed image is the sum of all the collected magnitude values at each azimuth and elevation angular position.

This can be written as

$$|Pixel_{xyz}| = \sum_{m=1}^{M_\theta} \sum_{n=1}^{N_\theta} P_n(\tau)$$

where n represents the azimuth angle index, N_θ represents the number of azimuth angles, m represents the elevation angle index, M_θ represents the number of elevation angles and $|Pixel_{xyz}|$ represents the magnitude of the pixel at position (x, y, z) in the final reconstructed image.

Chapter 4

Simulation

Before any experiments were carried out, the entire UWB system was simulated in Matlab. These simulations would give insight into the operation of the system and what to expect from the experiments. The outputs from these simulations would serve as a reference to the outputs that will be received from the experiments. This chapter will show the simulation of the signal processing techniques and algorithms that will be carried out in the experiments. Since the project was divided into two parts, namely 2D and 3D experiments, the simulations were also carried out in the same way. A Matlab script was written for the 2D case, followed by the experiments in 2D. This 2D model was then extended to 3D simulations followed by 3D experiments.

Since a VNA, a device which measures data in the frequency domain, would be used during the experiments, all simulations were done in the frequency domain. The simulations and algorithms were created in the same way as the data would be collected from the devices during the experiment. The reason for this was that when the data was collected during experiments, the data could then be passed through the same algorithms. A comparison could then be made between the simulated data and the experimental data.

4.1 2-Dimensional Simulations

Chapter 3 outlines all the parameters that are to be set in the simulation. The simulations would be used as a tool to change these parameters and see the effect on the output of the system. These parameters are explored in further detail below. It was decided that the full frequency range on the VNA would be used. Any unwanted frequencies could then be removed in software. As mentioned before, the frequency spacing that was to be used would depend on the maximum target detection range. It was decided that the maximum target detection range would be 10 m. Any targets located further than 10 m away would alias (or wrap around) into the 0 - 10 m range profile. The simulations were carried out in such a way that the reference axis was located at the centre of rotation, with the cross range along the x-axis, down range being along the y-axis and height along the z-axis. This can be seen in Figure 4.1.

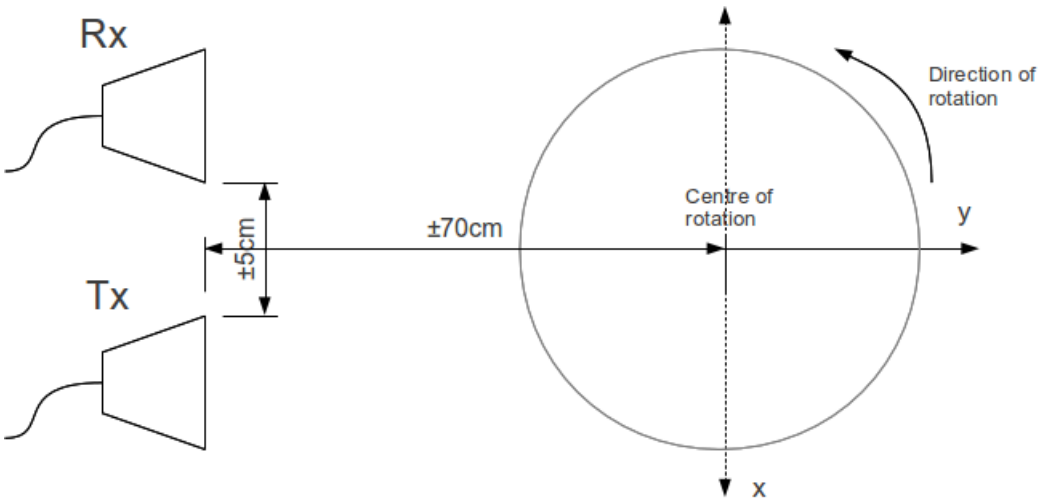

Figure 4.1: Simulation setup

The parameters for the simulations were set up as follows:

- Start Frequency: 300 kHz
- Stop Frequency: 8.5 GHz
- System Bandwidth: 8.5 GHz
- Maximum Imaging Range: 10 m
- Maximum Simulation Time on Range Profile: 66.7 ns
- Time Spacing on Range Profile: 0.06 ns
- Frequency Spacing: 15 MHz
- Number of Frequency Samples on VNA: 566
- Number of Time Samples: 8192
- Direction of Azimuth Rotation: Anti-Clockwise
- Angular Azimuth Range: 0 - 360 degrees
- Angular Increments: 1.8 degrees
- Transmitter coordinates in metres (x,y) : (-0.0875 ,-0.7)
- Receiver coordinates in metres (x,y): (0.0875 ,-0.7)
- Scene Radius: 0.25 m
- Scene x-axis limits (metres): $-0.35 \leq x \leq 0.35$
- Scene y-axis limits (metres): $-0.35 \leq y \leq 0.35$

4.1.1 Transmitted Signal

The VNA is a device which sweeps over a selected range of frequencies and takes magnitude and phase measurements at each specified frequency. Thus the simulations that follow were done in the frequency domain. The VNA transmits a sine wave from the selected port. The range of frequency values of this sine wave can be set by adjusting the start and stop frequency of the device, as well as the number of points (which relates to the frequency steps) between each frequency value. The instrument measures the magnitude and phase of the voltage waves that is received on port two relative to the sine wave that was transmitted out of port one. The S_{21}measurement is computed and displayed on the device's screen as a magnitude and phase measurement at each frequency. As the signal is transmitted it travels to the target, interacts with the surface of the target and a portion of the signal is reflected back to the receiving antenna. The signal that is received is an amplitude scaled and phase shifted version of the transmitted sinusoidal signal [30]. This magnitude and phase change is what is displayed by the VNA. The signal which is simulated has an amplitude of 2 V and a phase of 0 degrees at the antennas. The point targets that are simulated have a radar cross section of a small cylinder with height 10 cm and radius of 2 cm. These dimensions were chosen because these were the dimensions of the toilet roll targets that were going to be used. The radar cross section, σ , for a small cylindrically shaped target can be calculated by [30]

$$\sigma = \frac{2\pi r h^2}{\lambda}$$

where r is the radius of the cylinder in metres, h is the height of the cylinder in metres and λ is the wavelength at a particular frequency. The radar cross section of the targets may change depending on the shape of the target as well as the frequency, but for simulation purposes these parameters were chosen because the targets that were used in the experiments had these dimensions. The amplitude a of the received signal is related to many parameters as seen in Equation 4.1 [30]:

$$a \propto \sqrt{\frac{G^2 \sigma \lambda^2}{(4\pi)^3 R^4}} \tag{4.1}$$

G represents the gain of the antennas, λ the wavelength of the signal, R the distance to the target and σ is the radar cross section of the reflecting rod. The phase change of the received signal is related to the flight time of the signal before it returns to the receiver. This is in turn related to the distance that the target is from the antennas. This phase change can be written as [5, 30]:

$$\theta_n = -\omega_0 t_n$$

where t_n represents the flight time to target n. This can be expanded to:

$$\theta_n = -2\pi f \frac{2R_n}{c} \tag{4.2}$$

$$= -2\pi \frac{c}{\lambda} \frac{2R_n}{c}$$

$$= -\frac{4\pi R_n}{\lambda}$$

Thus as the signal travels to and from the target, this vector representation of the signal rotates around the complex axis. The simulation of the UWB calculates the magnitude and phase of the returned signal, at each frequency, from targets placed in the scene. For multiple targets placed in the scene, the received signal is the sum of amplitude scaled, phase shifted versions of the transmitted signal at each frequency sample [5, 27]. The signal processing methods, as specified in Chapter 3, are then carried out on the received signal and the output is displayed.

4.1.2 Simulation of Single Target

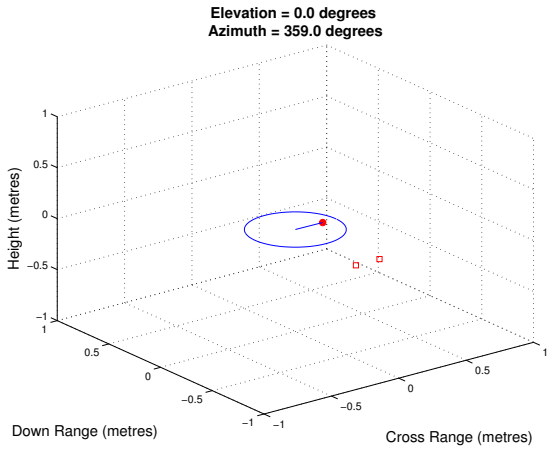

(a) 3D view of the simulated point target

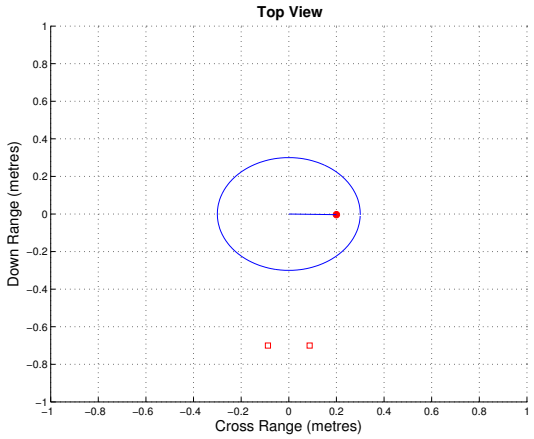

(b) Top view of the simulated point target

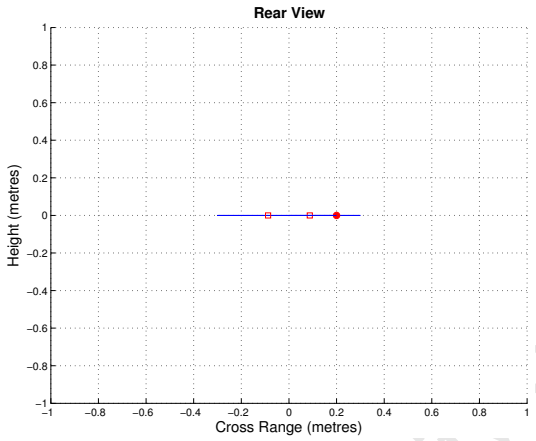

(c) Rear view of the simulated point target

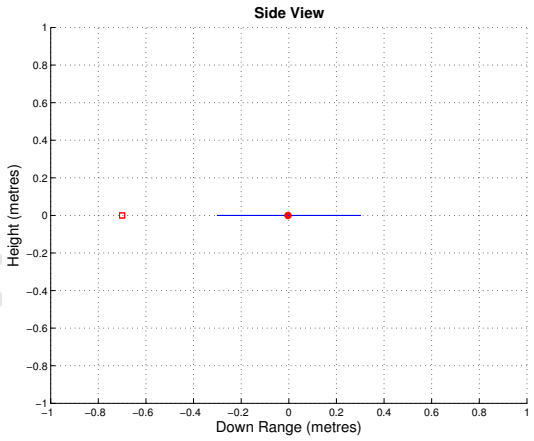

(d) Side view of the simulated point target

Figure 4.2: Image showing the location of the simulated point target

In this simulation, a single point target was placed on the rotating pedestal and run through the simulation. All parameters were set to the desired values. The outputs of the simulations were measured and plotted. Figure 4.2 shows the 3D view of the location of the point targets in the simulation. The location of the antennas relative to the position of the pedestal is indicated by the square blocks in Figure 4.2. The edge of the rotating platform is drawn and the point target is indicated by a red dot located on the rotating pedestal.

Figure 4.3 shows the simulated received data in the frequency domain for a single point target. The data is then passed through a windowing function and zero padded. Figure 4.3 also shows the windowing function which has been applied as well as the zero padded data. By zero padding the data above 8.5 GHz it increases the resolution of the time domain plots. The data is then basebanded so that the phase of the time domain data can be constant along the peak of the magnitude of the time domain data. This basebanded data is then transfered to the time domain by an inverse Fourier transform. The time axis is converted into a range axis so that the distance to the target can be read off from the graph.

Figure 4.4 shows the baseband frequency and the time domain data. In the simulations, imaging was done up to a maximum target detection range of 10 m, however the centre of rotation of the rotating pedestal would be placed a distance of 0.7 m from the antennas. Thus any targets which are placed on the platform will not exceed a down range distance of 1 m from the antennas and will always be in the far field of the antennas. Thus a 0-1 m zoomed plot of the range profile has been shown. From this range profile a peak appears at the down range distance where the target is located. For a single target only a single peak will appear, whereas for multiple targets there will be multiple peaks.

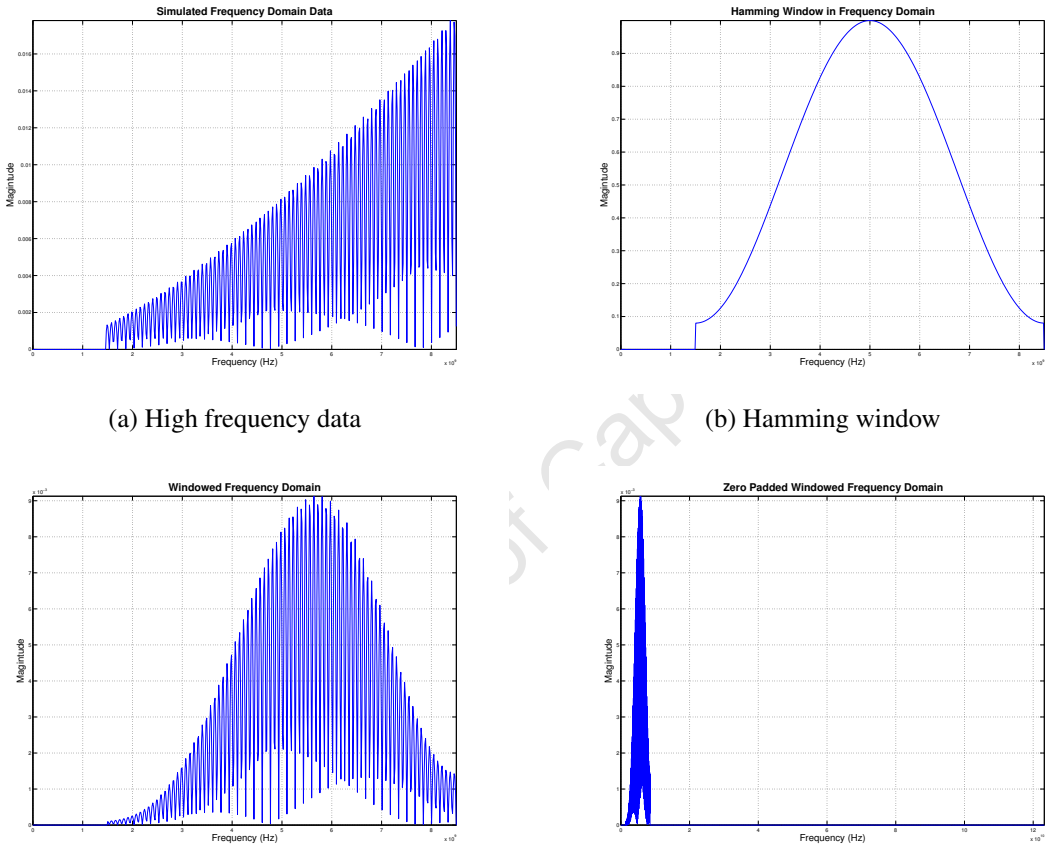

(a) High frequency data

(b) Hamming window

(c) Windowed frequency domain data

(d) Zero padded data

Figure 4.3: Simulated received data in the frequency domain

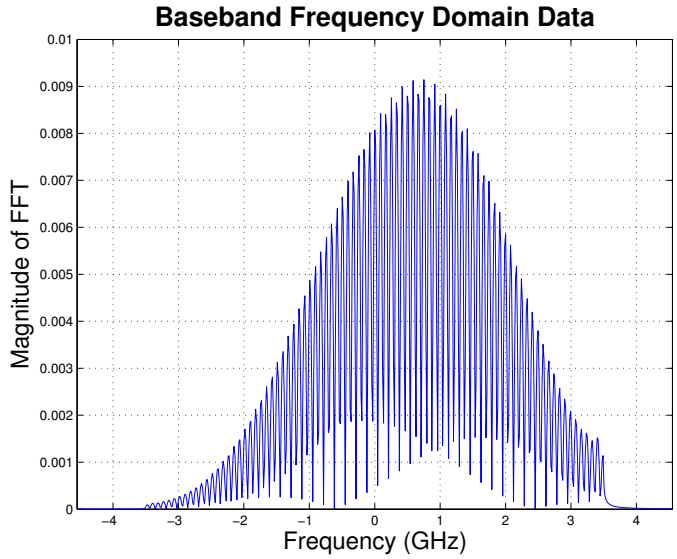

(a) Baseband frequency domain data

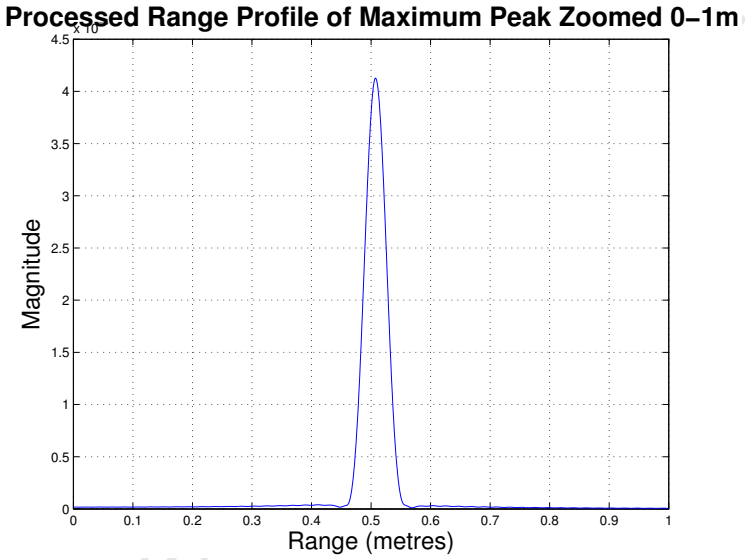

(b) Range profile zoomed to 0-1 m

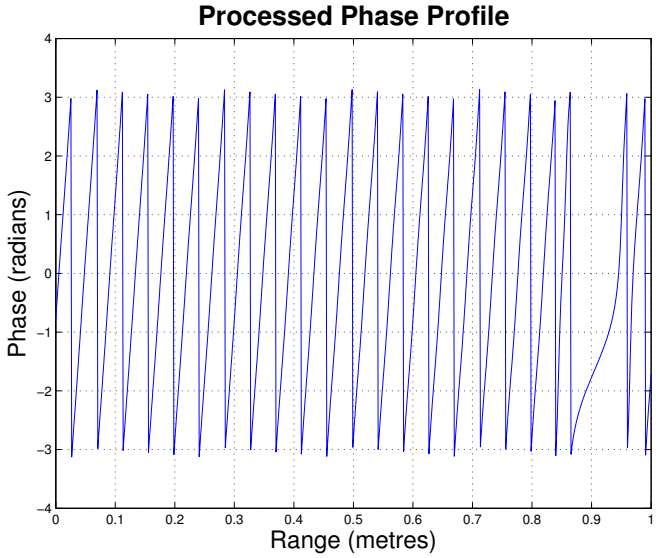

(c) Phase profile zoomed to 0-1 m

Figure 4.4: Simulated frequency and time domain data at 270 degree azimuth rotation

Figure 4.5a shows the range compressed data of the target. This is also known as the locus of the target as it displays the path that is traveled by the target as it rotates on the pedestal in 1.8 degree increments. This locus displays a sinusoidal shape as the target is rotating in a circular position around a centre of rotation and the antennas are located in a fixed position. It is obtained by placing the range profiles, of the target at each angular position, next to one another. Due to the location of the target, it can be seen from the plot that as the pedestal rotates, the target first moves further away from the antennas and then closer to the antennas and ends at the same position where it started. The colour intensity on the plot is indicated by the legend. It shows that darker colours represent lower measurement values and lighter colours represent higher measurement values. Taking this into consideration it can be seen that as the target moves further from the antennas, the received power is reduced. This is indicated by a darker red colour. As the target moves closer to the antenna, the received power increases, indicated by the lighter yellow colour. This corresponds to the radar equation which states that power is inversely proportional to the fourth power of the distance to the target, and hence the magnitude is proportional to the square of the distance [5, 6]. Less power is received for a target that is located further from the antennas.

Figure 4.5b also shows the reconstructed 2D image that is built up using the range compressed data. This image is created by using the time domain back-projection algorithm as mentioned in Chapter 3. From the figure the location of the target on the platform can be seen. This reconstruction algorithm is however heavily dependent on the centre of rotation of the pedestal and the effect of this on the reconstructed image will be explored later. Figure 4.6 shows a vertical and horizontal slice through the brightest point where the point target is located. This figure displays the down range resolution and cross range resolution, which will be explored later. It also shows the location of the target along the x-axis and y-axis.

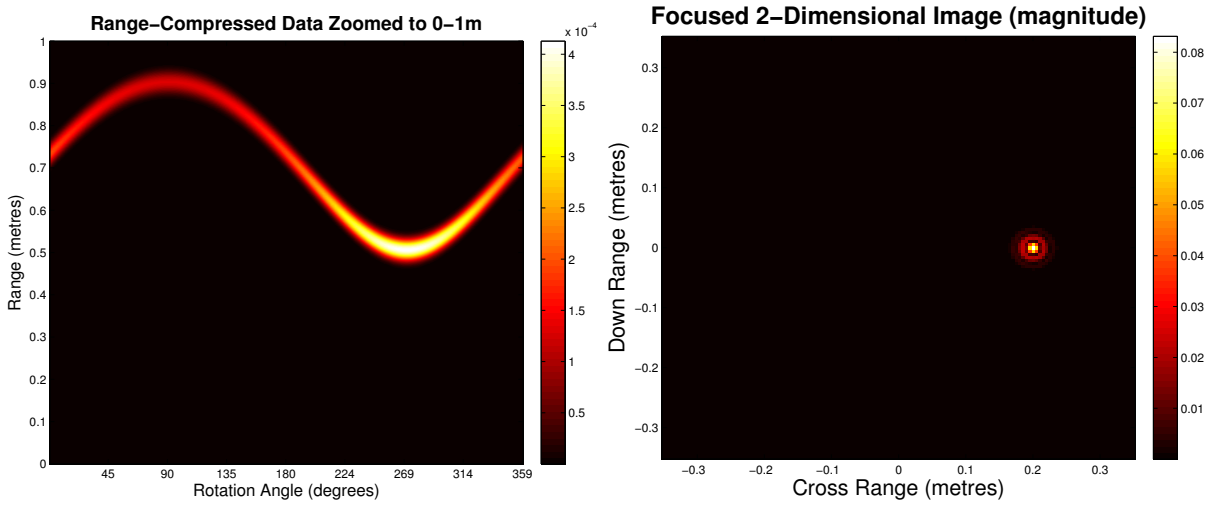

(a) Range compressed data/locus of target

(b) 2D reconstructed image of scene

Figure 4.5: Simulated locus of target and reconstructed image of scene

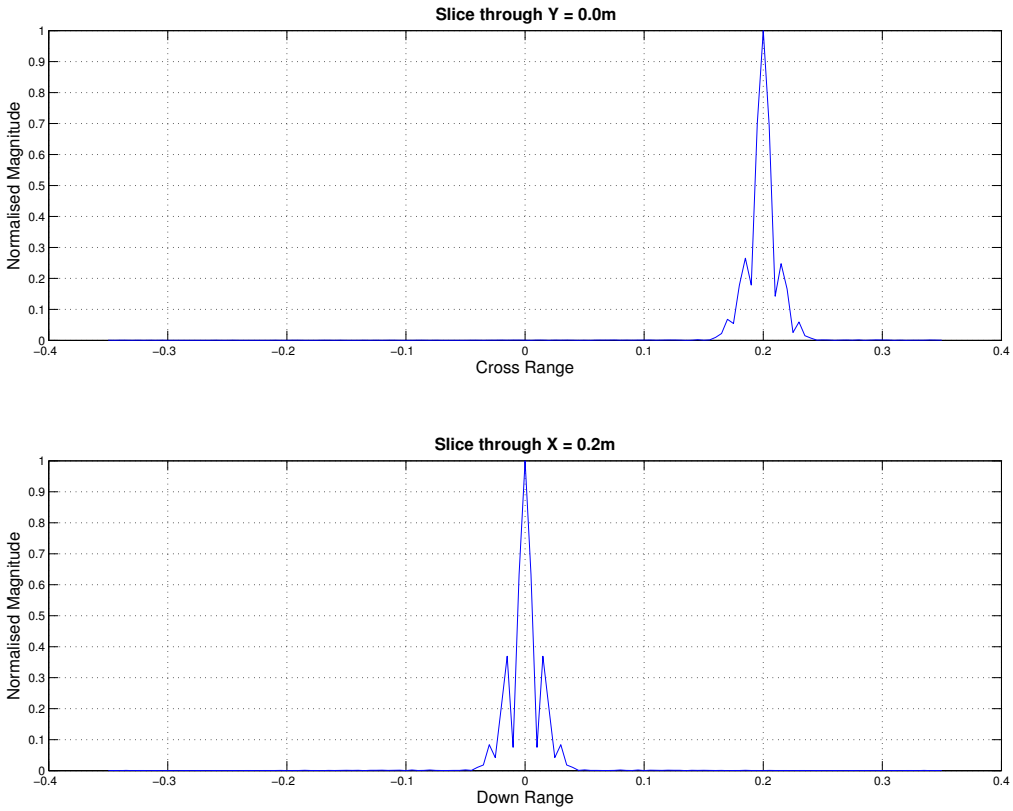

Figure 4.6: Cut through brightest point in reconstructed scene

Effect of Bandwidth

The bandwidth of the UWB system directly affects the range resolution of the system. Equation 2.3 shows the relationship between bandwidth and range resolution. It can be seen that there is an inverse proportionality between the two parameters thus a higher bandwidth would allow for a finer range resolution. By having a finer range resolution it will allow for distinguishing targets that are closely spaced. Figure 4.5 shows the frequency domain data and range profile when using a bandwidth of 7 GHz. Figure 4.7 shows the effect of using a bandwidth of 4.5 GHz while Figure 4.9 shows the effect of using a bandwidth of 1 GHz. From the figures it is evident that a decrease in the system bandwidth increases the main lobe of the time domain data, i.e. the range resolution becomes more course. In turn an increase in the width of the time domain data plots widens the swath of the locus that is created as the pedestal rotates. This can be seen in the range compressed data plots. The reconstructed image that is created is also unfocused. This can be seen in the plots of the reconstructed images when using reduced bandwidth. This highlights the importance of system bandwidth on distinguishing targets that are very closely spaced.

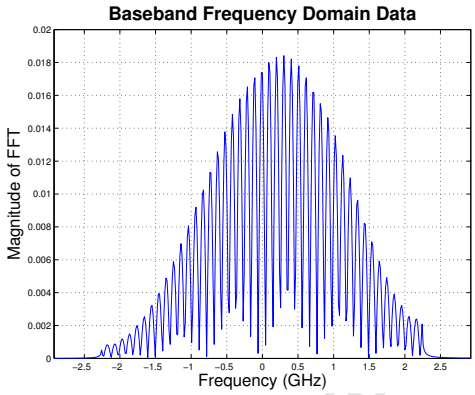

(a) Baseband frequency domain data

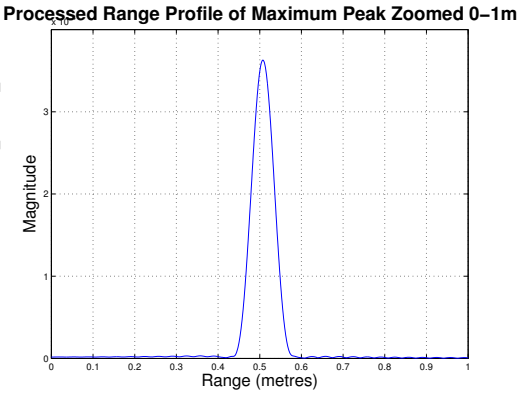

(b) Processed range profile

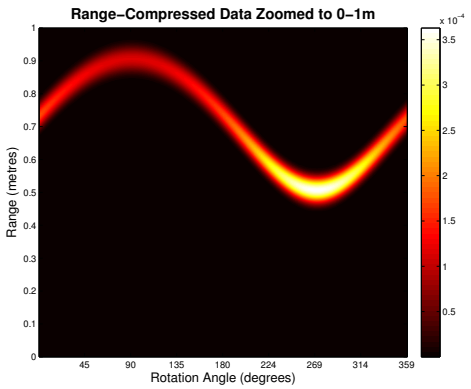

(c) Range compressed data

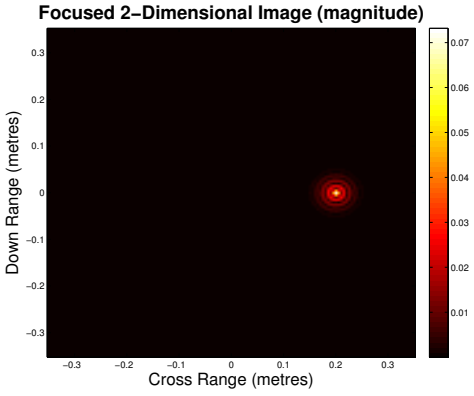

(d) Reconstructed 2D image

Figure 4.7: Simulated data for system bandwidth of 4.5 GHz

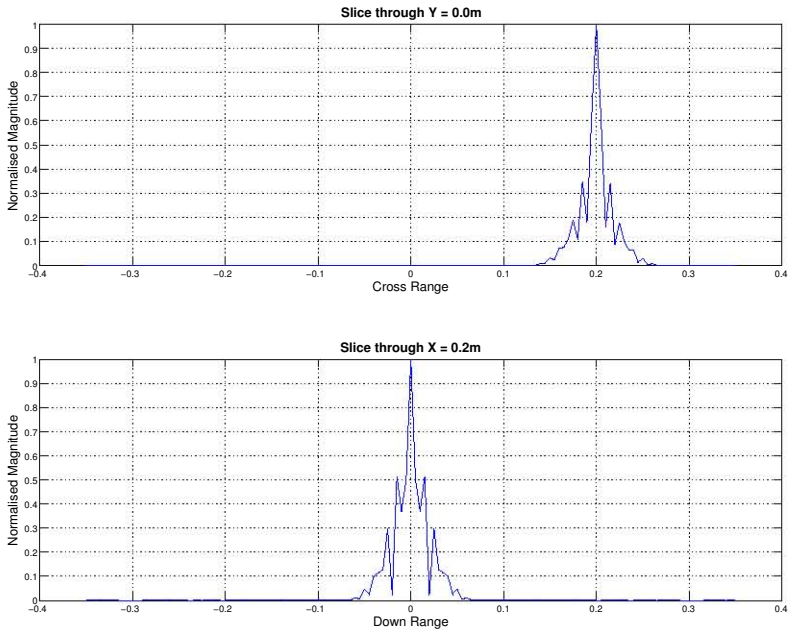

Figure 4.8: Cut through brightest point in reconstructed scene for bandwidth of 4.5 GHz

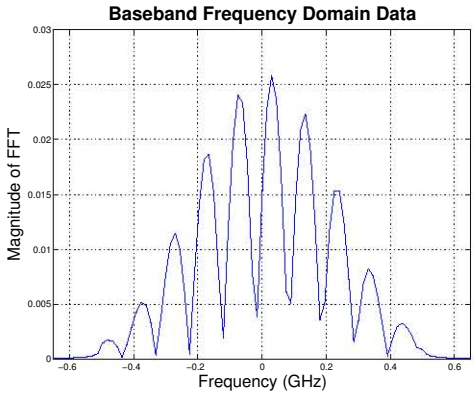

(a) Baseband frequency domain data

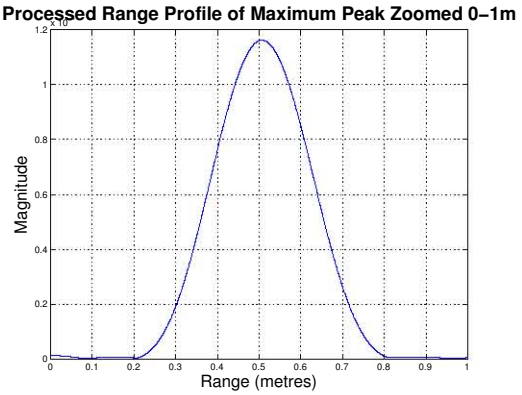

(b) Processed range profile

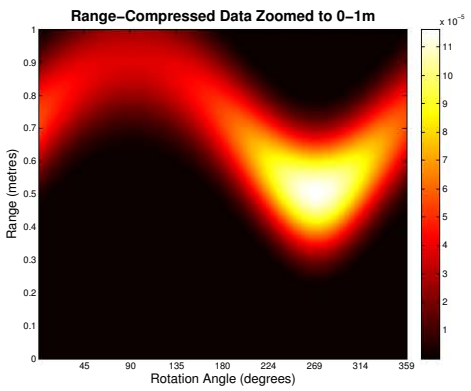

(c) Range compressed data

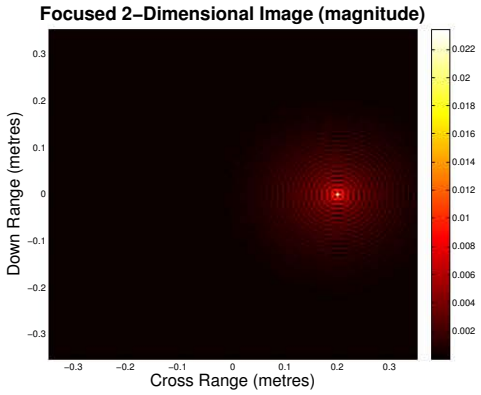

(d) Reconstructed 2D image

Figure 4.9: Simulated data for system bandwidth of 1 GHz

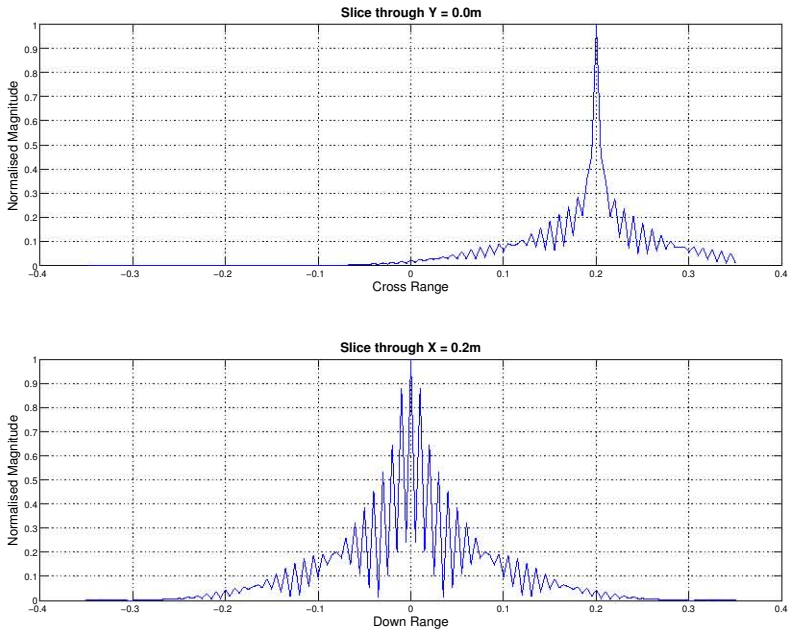

Figure 4.10: Cut through brightest point in reconstructed scene for bandwidth of 1 GHz

Effect of Under-sampled Angular Rotation

Rotating a pedestal in front of a pair of stationary antennas is equivalent to moving the antennas around a circular arc and taking samples to make up a synthesized aperture (like in SAR [30]). In order for the best image to be reconstructed, a certain angular increment should be chosen in such a way as to satisfy the equivalent Nyquist sampling rate of the system. The sinusoidal return echo from a target is an amplitude scaled and phase shifted version of the transmitted signal. The phase shift of this sinusoidal signal is related to the distance that the target is from the antennas [30]. This can be seen in Equation 4.2. This return signal can be viewed as a complex vector which has some magnitude and phase. As the target rotates in the azimuth direction on the pedestal, this vector changes in magnitude and rotates around the complex axis. An angular change in the azimuth direction should not bring about a measured phase change greater than half a cycle (equivalent to π radians), i.e. the vector should not rotate by more than 180 degrees. If this does happen it will bring about ambiguity with regards to the location of the target. The minimum angular change in the azimuth direction can be calculated as follows:

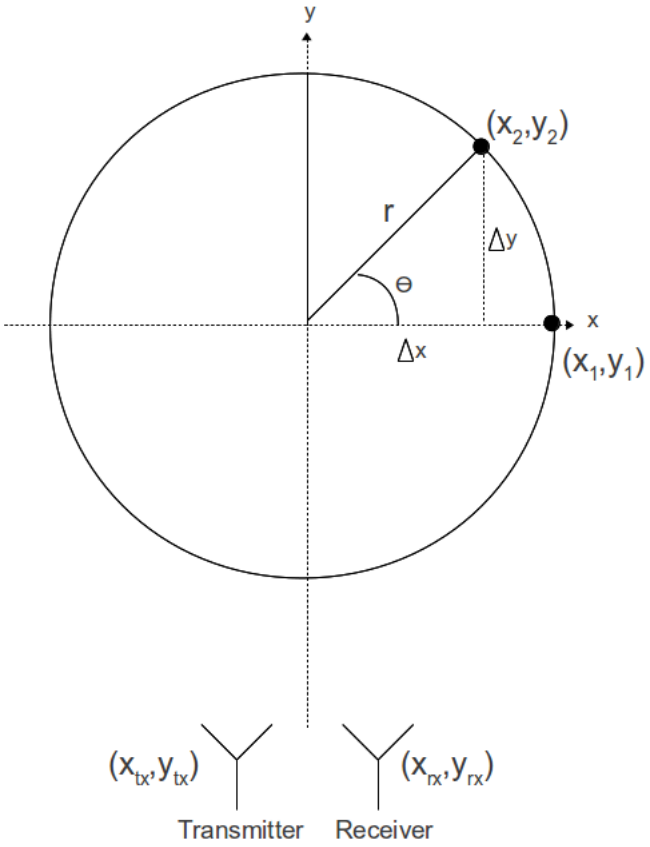

Figure 4.11: Rotating scene with targets on the pedestal

For far enough: $2\pi(\frac{2\triangle y}{\lambda}) < \pi$

$$\therefore \triangle y < \frac{\lambda}{4}$$

If one thinks of the phase of a rotating phasor, the Nyquist criterion is equivalent to measuring at least two samples per cycle. All the calculations have been carried out using the parameters set above. The angular change in the pedestal brings about a change in distance between the antennas and the target. (x_1,y_1) is the location of the point target before the rotation and (x_2,y_2) is the location of the target after the rotation. The radius of the platform is defined by $r = 0.25\,m$. By rotating the target by an angle $\triangle\theta$, the new position of the target can be calculated.

$$x_2 = rcos(\triangle\theta)$$

$$y_2 = rsin(\triangle\theta)$$

The distance between the antennas and the target at location x,y can be calculated by:

$$R_{tx} = \sqrt{(x - x_{tx})^2 + (y - y_{tx})^2}$$

$$= \sqrt{(0.7cos(\triangle\theta) + 0.0875)^2 + (0.7sin(\triangle\theta) + 0.7)^2}$$

$$R_{rx} = \sqrt{(x - x_{rx})^2 + (y - y_{rx})^2}$$

$$= \sqrt{(0.7cos(\triangle\theta) - 0.0875)^2 + (0.7sin(\triangle\theta) + 0.7)^2}$$

$$R_{tot} = R_{tx} + R_{rx}$$

where R_{tx} is the distance between the transmitter and the target and R_{rx} is the distance between the receiver and the target. Using this Equation, the change in distance is calculated for different rotation angles and the results are recorded in Table 4.1.

Angular Rotation (degrees)	R_{tx} (metres)	R_{rx} (metres)	R_{tot} (metres)	Change in Distance (metres)
0	0.77711	0.71861	1.4957	
1	0.78103	0.72286	1.5039	0.008
2	0.78492	0.72708	1.512	0.016
3	0.78877	0.73129	1.5201	0.024
5	0.79639	0.73965	1.536	0.040
10	0.81487	0.76016	1.575	0.079
20	0.8491	0.79922	1.6483	0.152

Table 4.1: Table showing the change in target distance from the antennas with different rotation angles

The VNA can measure up to 8.5 GHz, corresponding to $\lambda = 0.03527\,m$ and $\frac{\lambda}{4} = 0.00882$ m. In baseband processing [5], the phase of the processed point scatterer response depends on the centre frequency in the band, and not the highest frequency. e.g. if processing from 1.5 GHz to 8.5 GHz, then $f_0 = \frac{1.5+8.5}{2} = 5\,GHz$, $B = 7\,GHz$, $\lambda = 0.06\,m$ and $\frac{\lambda}{4} = 0.015\,m$ and this satisfies the requirements to prevent ambiguity.

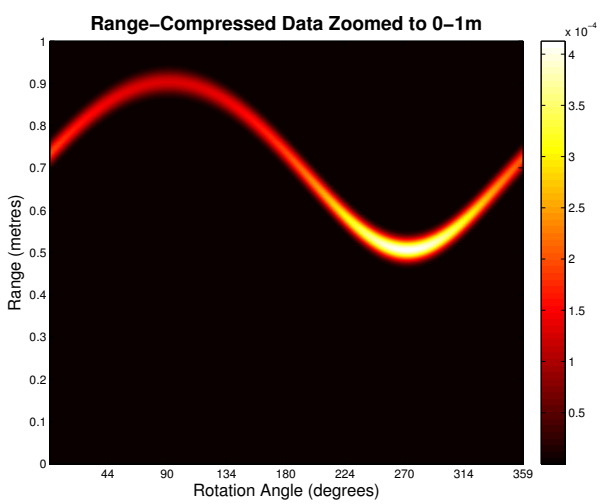

(a) Range compressed data with 2 degree incremements

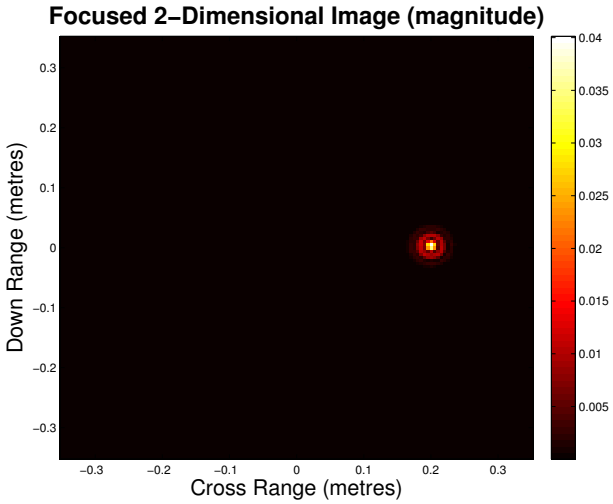

(b) Reconstructed 2D image 2 degree incremements

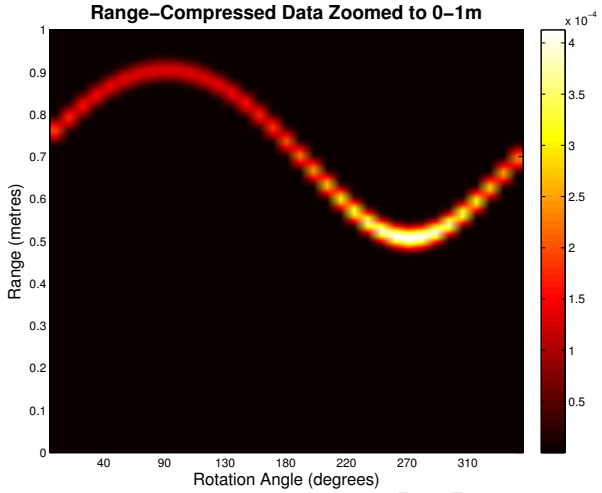

(c) Range compressed data with 10 degrees incremements

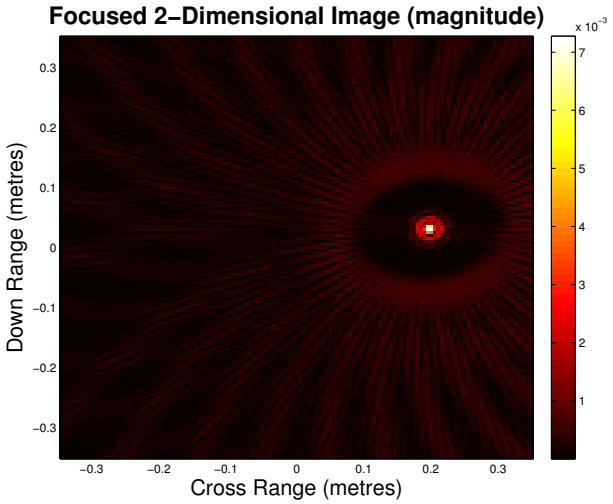

(d) Reconstructed 2D image 10 degrees incremements

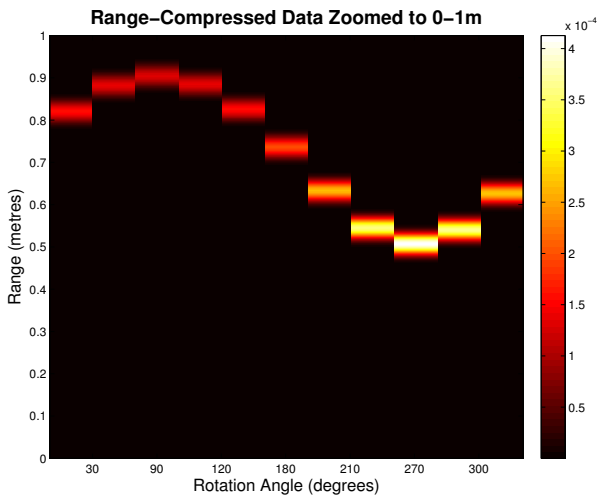

(e) Range compressed data with 30 degrees incremements

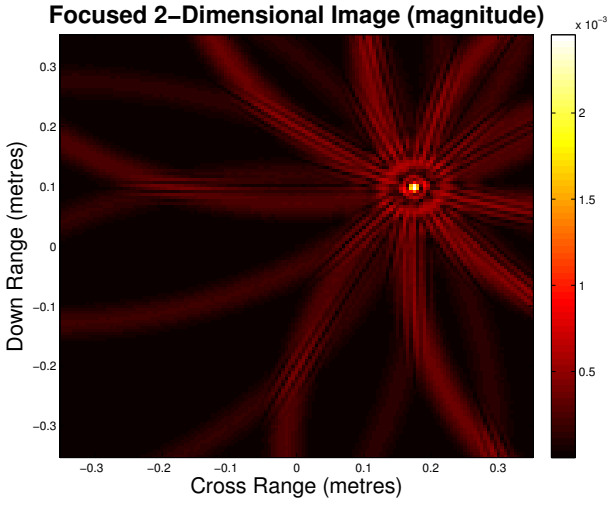

(f) Reconstructed 2D image 30 degrees incremements

Figure 4.12: Effect of aperture sampling

In order to show the effect of different angular step sizes, three angular step sizes were

simulated, namely $\triangle\theta$ =2, 10 and 30 degrees. As can be seen from Figure 4.12, increasing $\triangle\theta$ reduces the number of range profiles captured over the 360 degree rotation. When the step size is smaller, the range compressed data has a smoother appearance as compared to its rugged appearance when the sampling angle is bigger. The effect of under-sampling brings about artifacts in the reconstructed image which are not present if the Nyquist sampling rate is met. The image also appears to be defocused. From the table and simulations it can be concluded that rotating the pedestal by 1.8 degrees (as is done by the 1-axis rotating pedestal that is to be used for the 2D experiments) will not introduce any aliasing-related ambiguities or distortions.

Effect of Different Centre of Rotation

The time domain back-projection algorithm described in Section 3.6.5 was used in this UWB system in order to reconstruct the image of the scene in front of the antennas. The precision of the focusing algorithm is heavily dependent on the location of the centre of rotation of the rotating pedestal relative to the location of the antennas. By changing the assumed centre of rotation in the reconstruction algorithm, the reconstructed image can be focused. The centre of rotation can be changed until the clearest image is formed of the targets. Both the down range and cross range distance, relative to the antennas, can be changed. Each of these parameters have a different effect on the reconstructed image. It can be seen that by changing the down range distance, the target is not clearly focused to a single point but to a circular radius. This can be seen in Figure 4.13a and Figure 4.13b. Figure 4.13a shows the effect of an over estimate of the down range distance to the centre of rotation by 10 cm. Figure 4.13b shows the effect of an under estimate of the down range distance to the centre of rotation by 10 cm. By changing the cross range distance, the target also defocuses and is shifted down or up, from the original simulated starting point, depending on whether the cross range distance was an over estimate or an under estimate respectively. Figure 4.14a shows the effect of an over estimate of the cross range distance of the centre of rotation by 20 cm and Figure 4.14b shows an under estimate of the cross range distance of the centre of rotation by 20 cm.

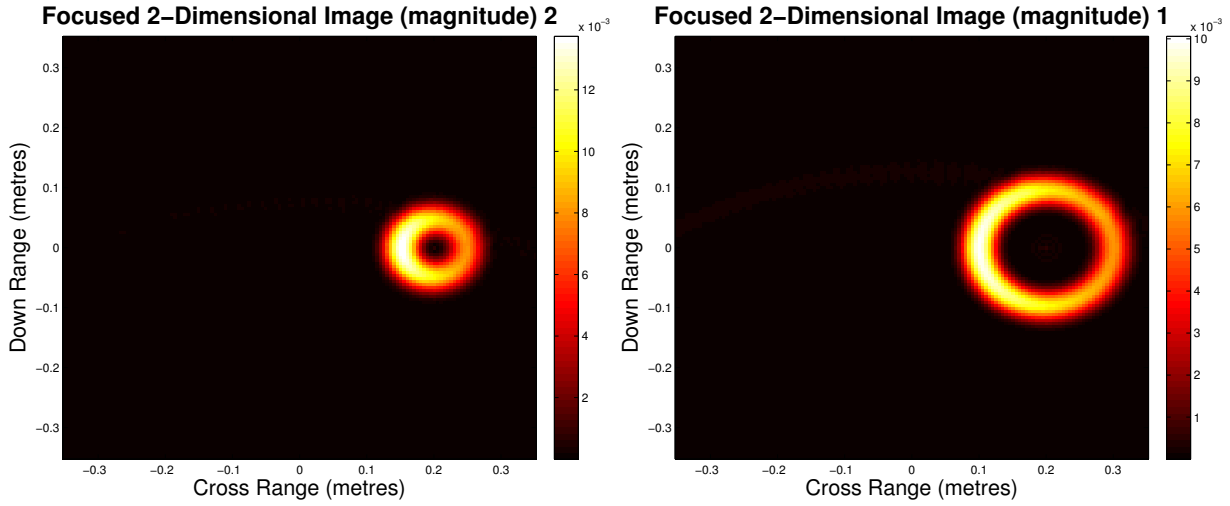

(a) 10 cm over-estimate of the down range centre of rotation location

(b) 10 cm under-estimate of the down range centre of rotation location

Figure 4.13: Change in down range distance of centre of rotation

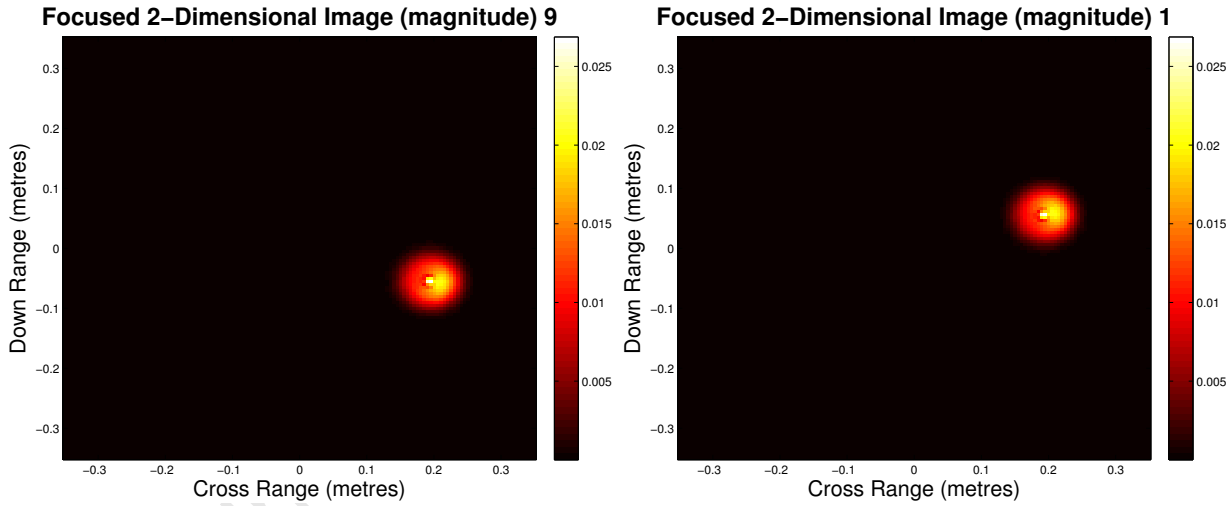

(a) 20 cm over-estimate of the cross range centre of rotation location

(b) 20 cm under-estimate of the cross range centre of rotation location

Figure 4.14: Change in cross range distance of centre of rotation

4.1.3 Simulation of Multiple Targets

A simulation was run with multiple targets to see if the reconstruction algorithm is capable of recreating images of multiple targets. This would also be used to demonstrate the effect of cross range resolution. All these targets were located at the same height above the pedestal.

Effect of Reduced Viewing Angle

The viewing angle (or angular range), θ_{view} , relates to the overall angular range over which the antennas are viewing the objects of interest. This is illustrated in Figure 4.15.

By rotating the platform and keeping the antennas stationary is equivalent to moving the antennas along an arc and keeping the platform stationary. Data is recorded at selected angular positions as the pedestal rotates and this arc makes up a synthesized aperture, which is sampled at each angular position. Figure 4.15 shows the start and stop position of the antennas as well as the synthesized arc that is formed. The length of this arc is dependent on the distance of the antennas relative to the centre of rotation of the pedestal as well as the total angular rotation of the pedestal. By reducing the total rotation of the pedestal (while keeping the antennas at the same distance from the centre of rotation), reduces the arc that is formed and in turn reduces the synthesized aperture that is formed. This reduced aperture can be seen in Figure 4.16.

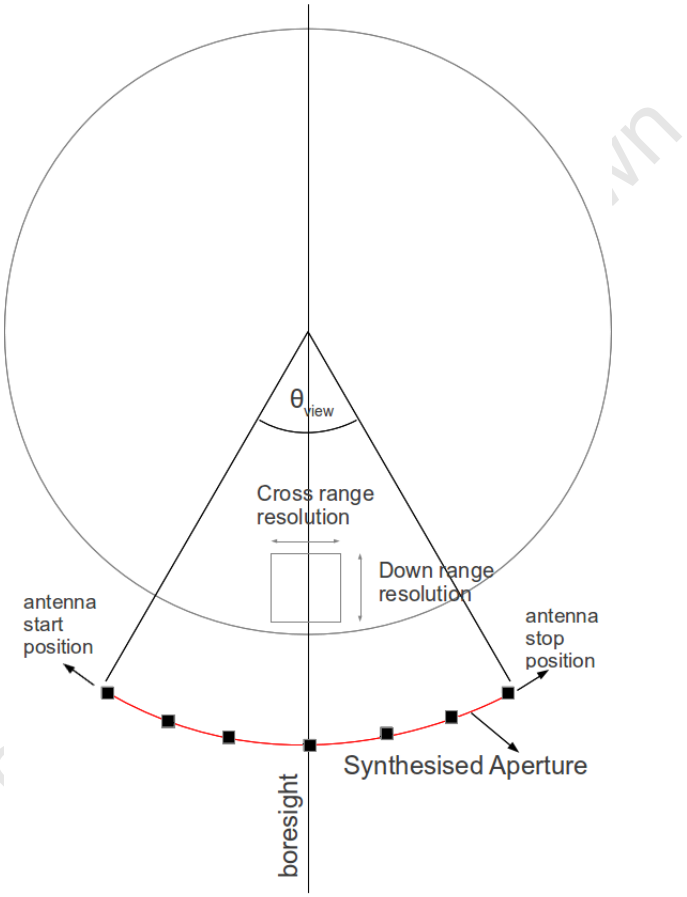

Figure 4.15: Illustration of viewing angle

The viewing angle affects the cross range resolution of the image [27, 30]. The cross range resolution is defined as

$$\triangle R_{CR} = R\theta_B \tag{4.3}$$

where R refers to the down range distance of the target and θ_B refers to the 3 dB beamwidth of the aperture antenna. This can be simplified further as $\theta_B \approx \frac{\lambda}{D}$, where λ is the wavelength and D is the aperture length. Using this, Equation 4.3 can be simplified to:

$$\triangle R_{CR} = R\frac{\lambda}{D} \tag{4.4}$$

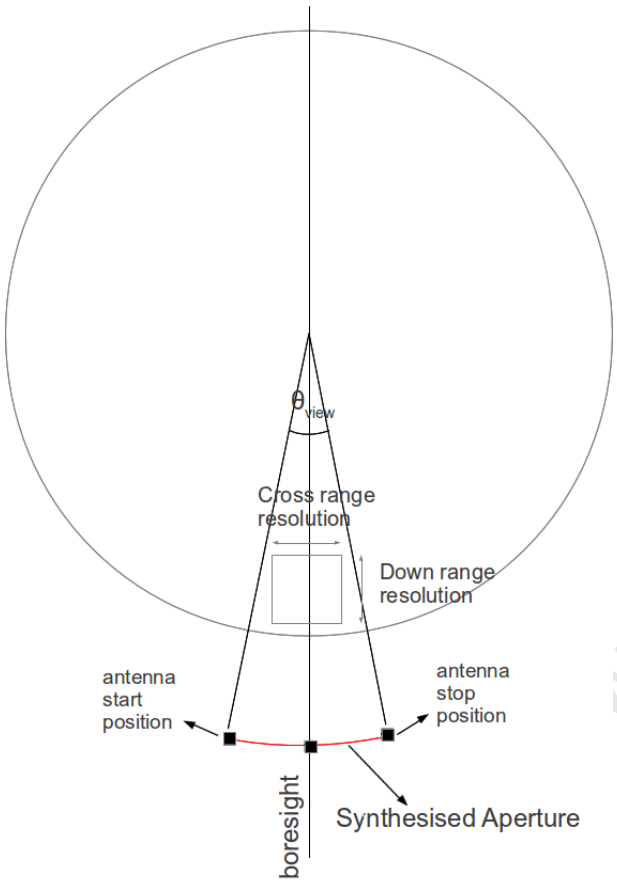

Figure 4.16: Illustration of viewing angle with smaller synthesized aperture

If, in a SAR situation for example, $\lambda = 3\,cm$, $D = 2\,m$ and $\theta_B = 0.015\,radians$, this would equate to a cross range resolution of 1.5 km at a range of 100 km. In order to obtain finer resolution one can increase the length of the aperture and implement coherent processing [30]. In order to increase the effective aperture size of an antenna, while using the same antenna, a synthetic aperture can be created by moving the antenna along a predefined path in space. The path length of this synthetic aperture will determine the cross range resolution [30].

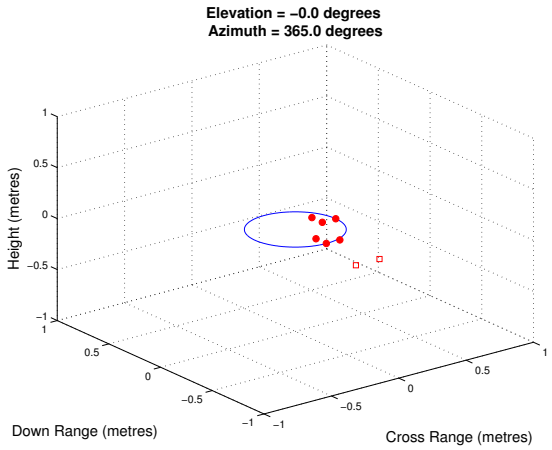

(a) 3D View of the simulated point target

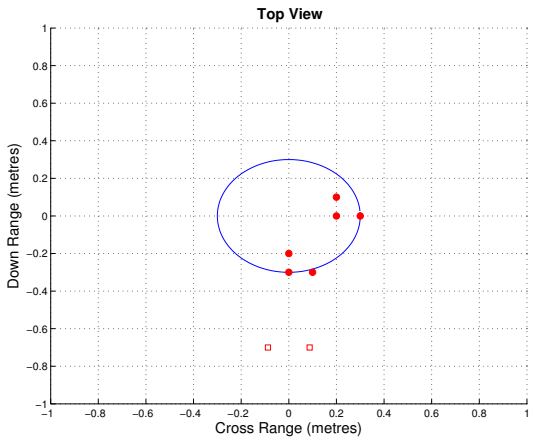

(b) Top view of the simulated point target

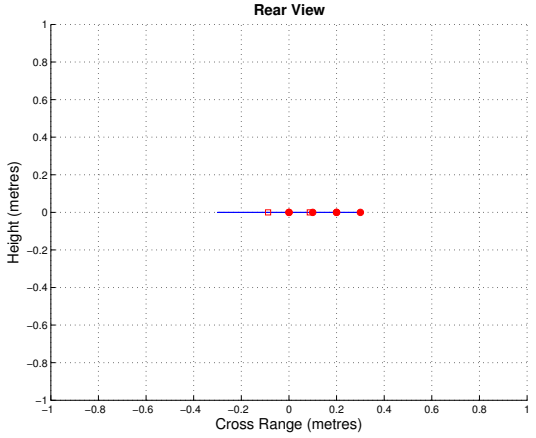

(c) Rear view of the simulated point target

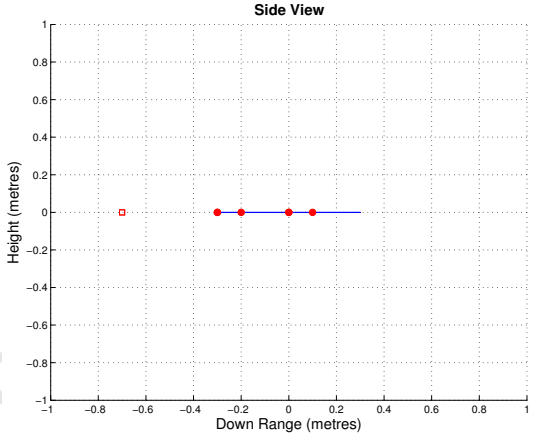

(d) Side view of the simulated point target

Figure 4.17: Image showing the location of the simulated point target

Simulations have been run to see the effect of changing the synthesized aperture size and seeing the effects on the cross range resolution. Six point targets were simulated in different positions as can be seen in Figure 4.17. Three targets were placed directly along boresight three were placed off boresight. They were placed in such a way that the effect of range and cross range resolution could be observed. The simulated azimuth rotation was such that the targets that were located along boresight would start at a x,y position before the boresight line and will end at an x,y position after the boresight line. The angular range (span) was also tested by changing the span of the viewing angle. This was done because the rotation angle of the 2-axis pedestal (in the elevation direction) is limited to 60 degrees. The pedestal is also constructed out of many metallic and reflective materials which would influence readings. The viewing angle was chosen to minimize the effects of the reflective materials. The time taken to run the experiments is also affected by the number of viewing angles and incremental angular steps.

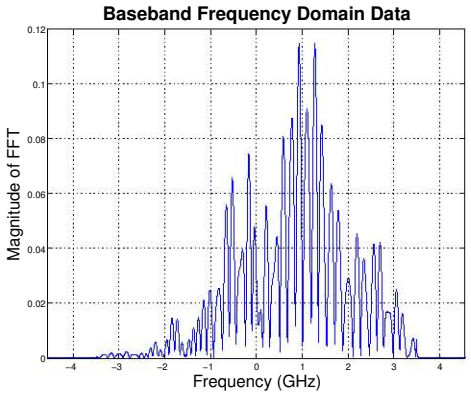

(a) Baseband frequency domain data

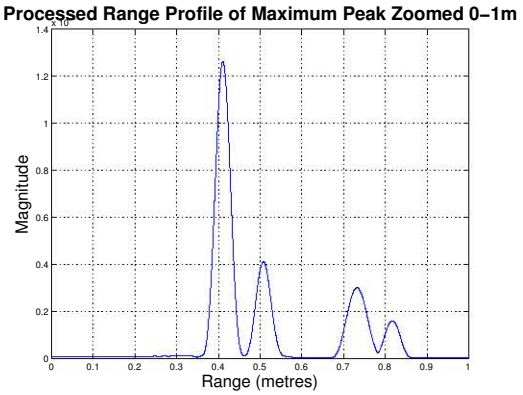

(b) Processed range profile

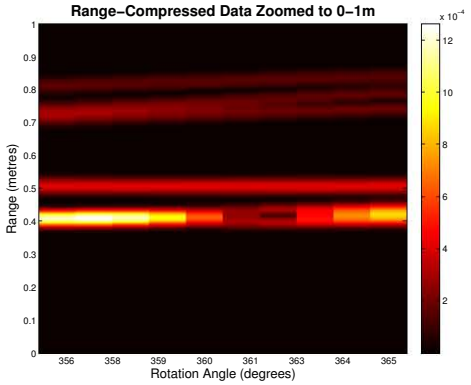

(c) Range compressed data

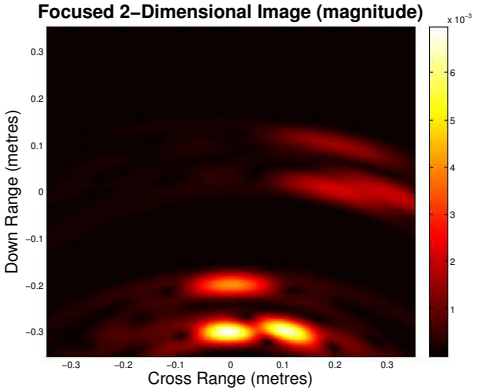

(d) Reconstructed 2D image

Figure 4.18: Simulated data with 10 degree viewing angle

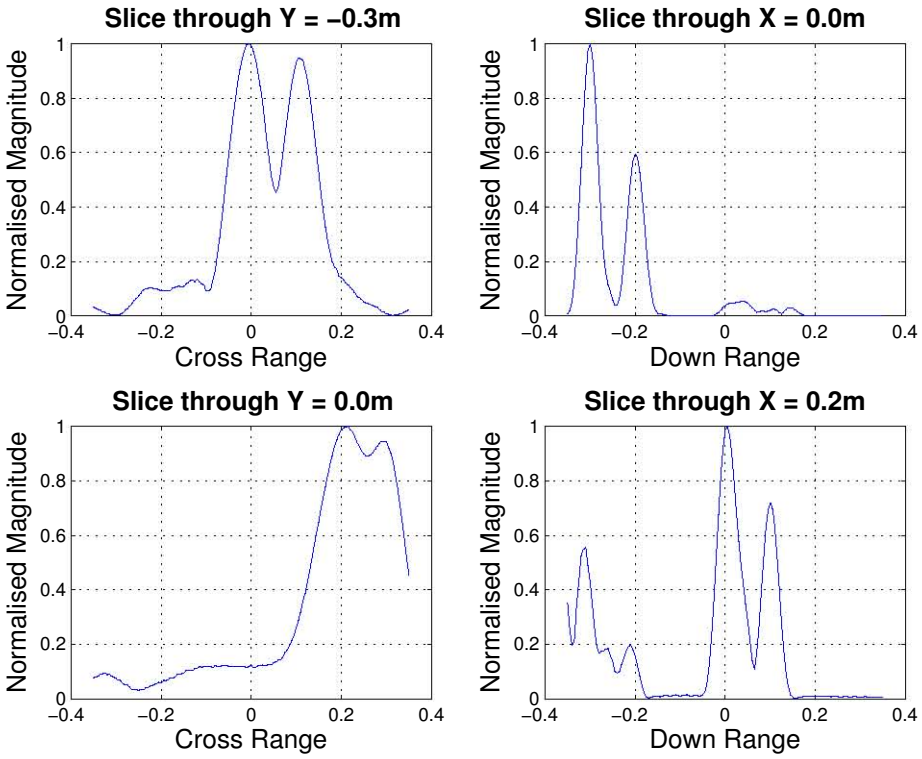

Figure 4.19: Vertical and horizontal slices for 10 degree viewing angle

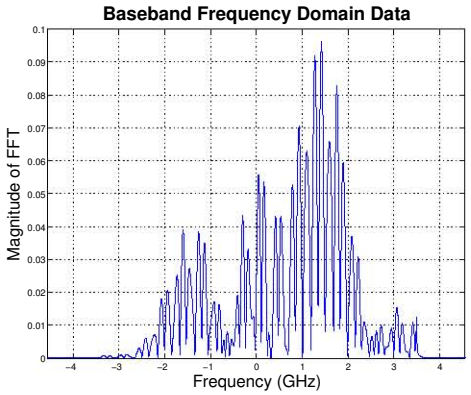

(a) Baseband frequency domain data

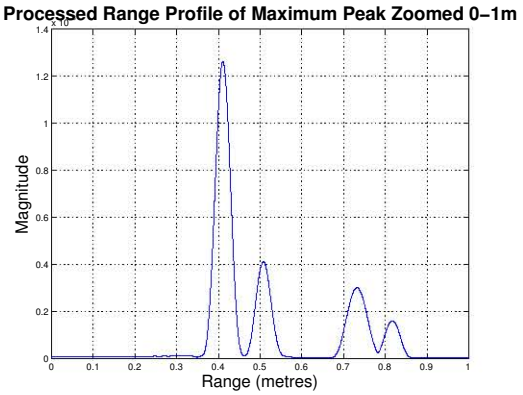

(b) Processed range profile

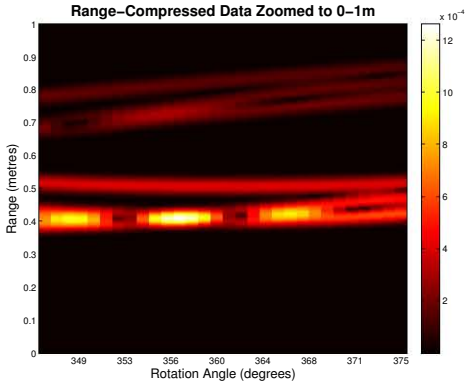

(c) Range compressed data

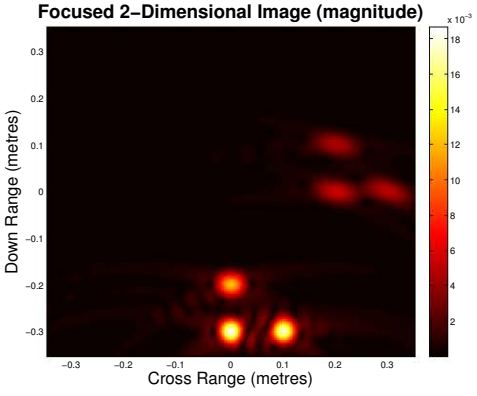

(d) Reconstructed 2D image

Figure 4.20: Simulated data with 30 degree viewing angle

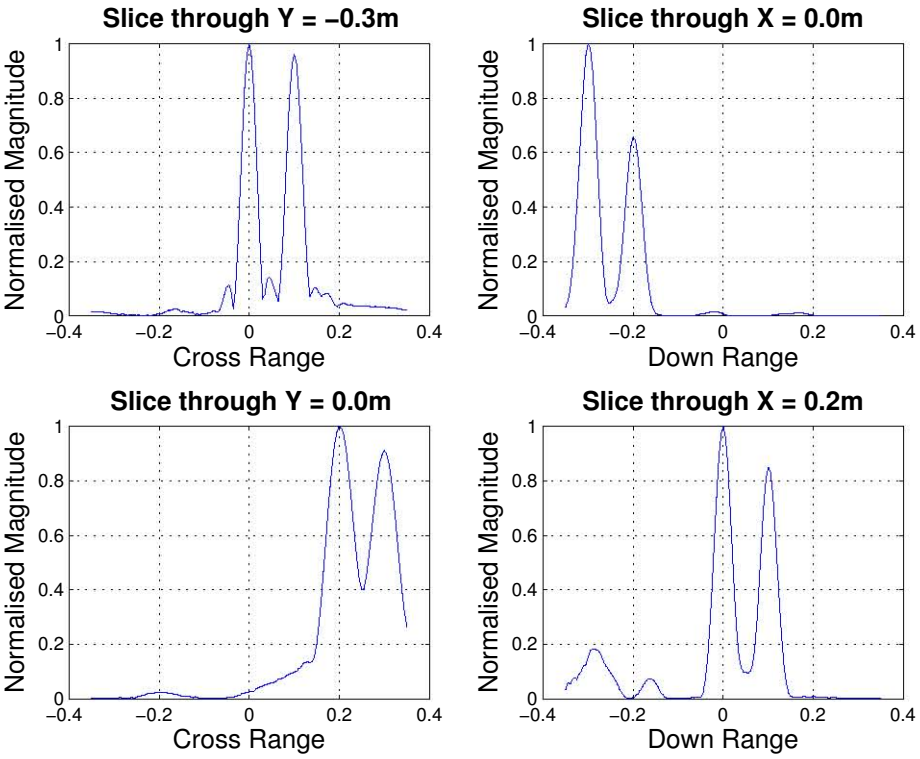

Figure 4.21: Vertical and horizontal slices for 30 degree viewing angle

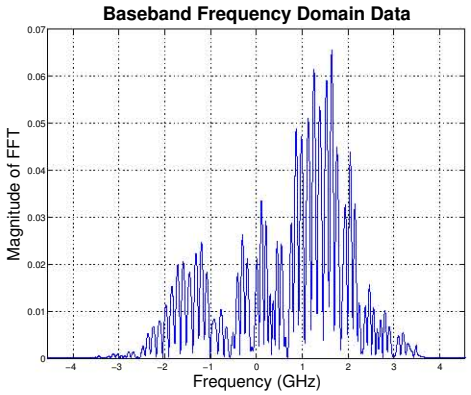

(a) Baseband frequency domain data

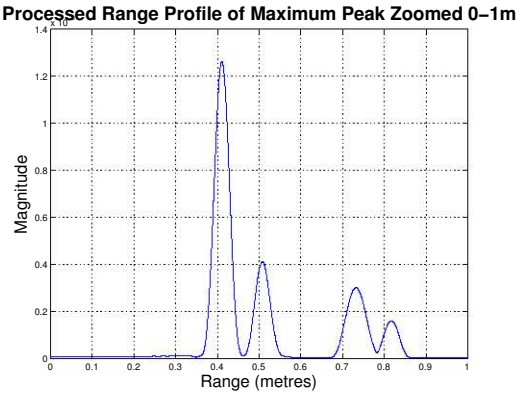

(b) Processed range profile

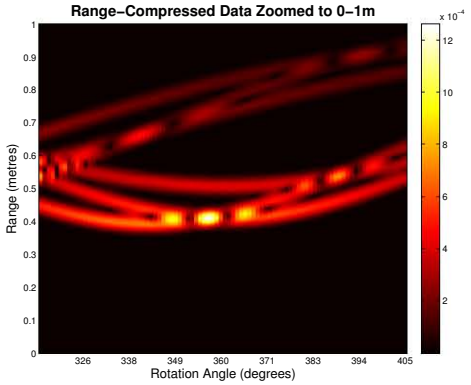

(c) Range compressed data

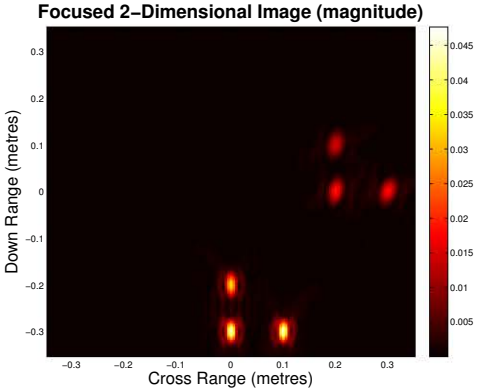

(d) Reconstructed 2D image

Figure 4.22: Simulated data with 90 degree viewing angle

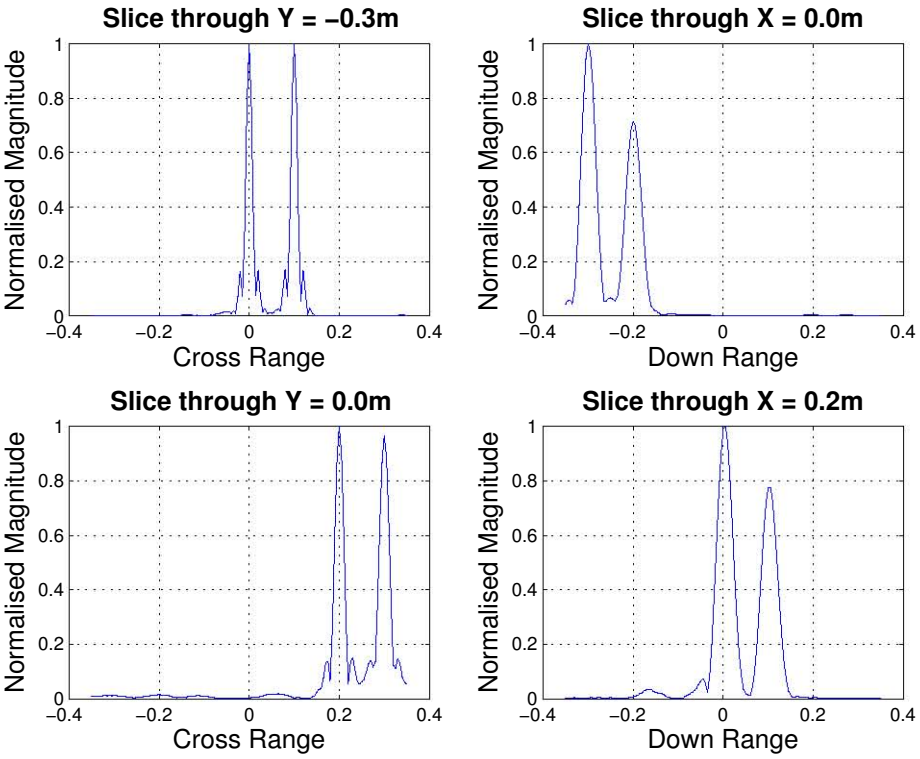

Figure 4.23: Vertical and horizontal slices for 90 degree viewing angle

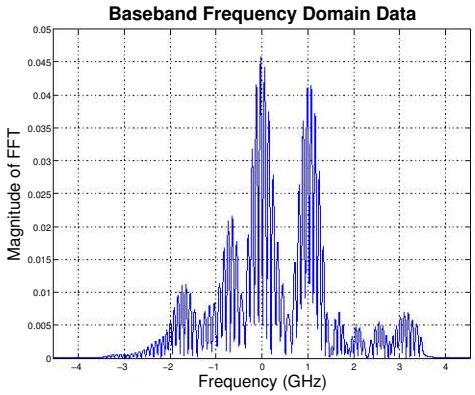

(a) Baseband frequency domain data

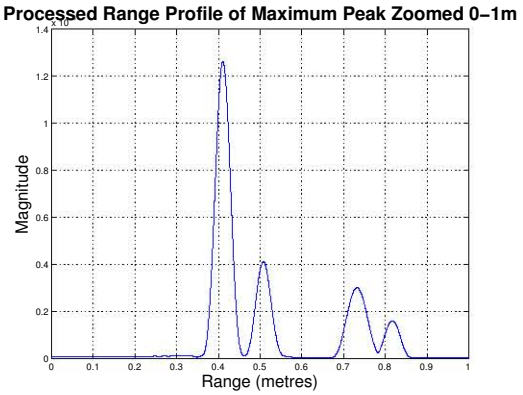

(b) Processed range profile

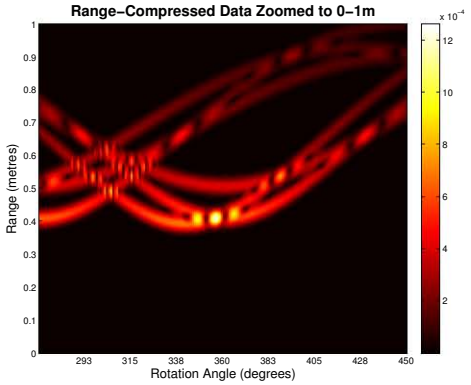

(c) Range compressed data

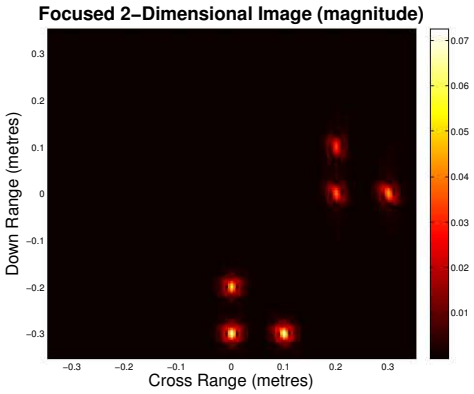

(d) Reconstructed 2D image

Figure 4.24: Simulated data with 180 degree viewing angle

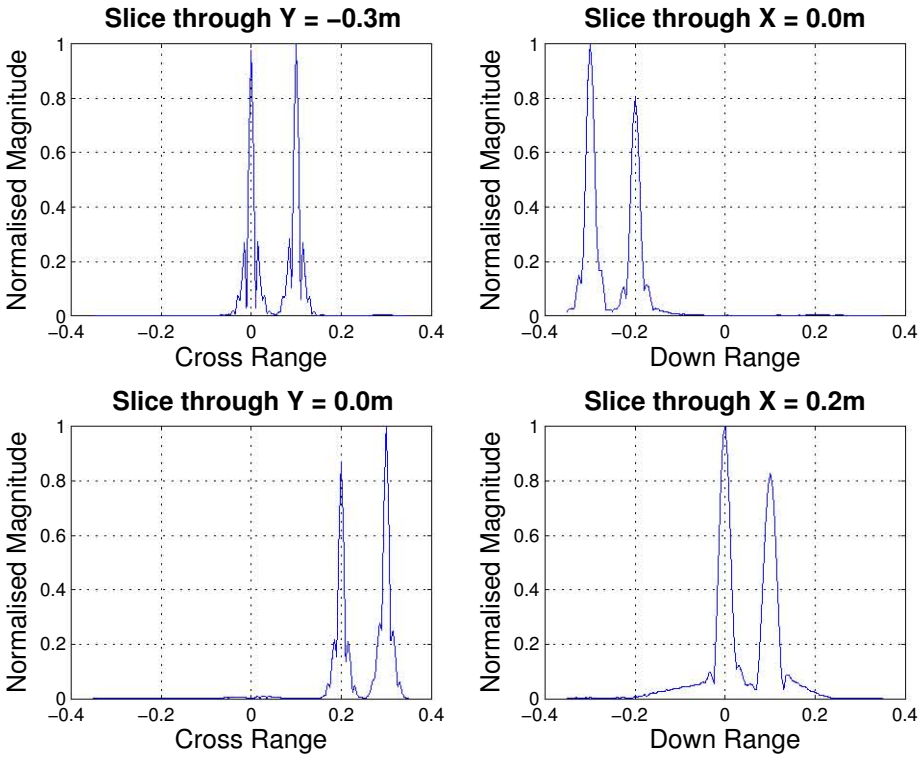

Figure 4.25: Vertical and horizontal slices for 180 degree viewing angle

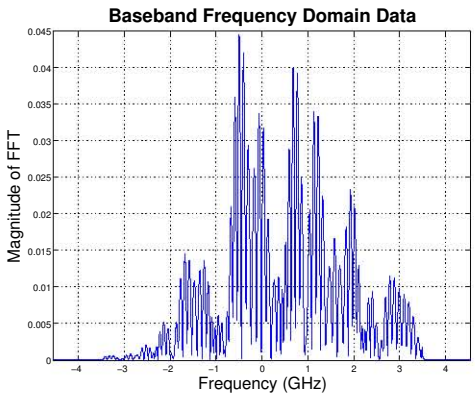

(a) Baseband frequency domain data

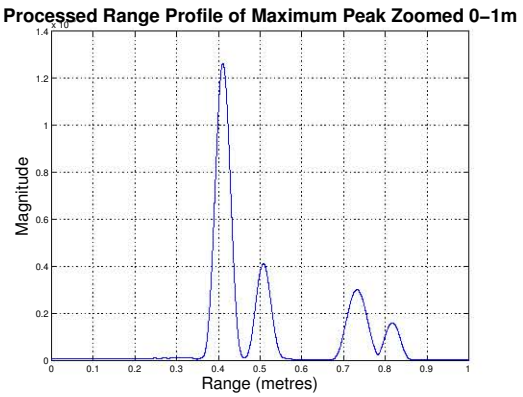

(b) Processed range profile

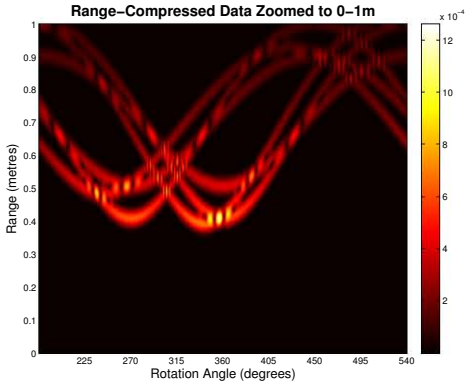

(c) Range compressed data

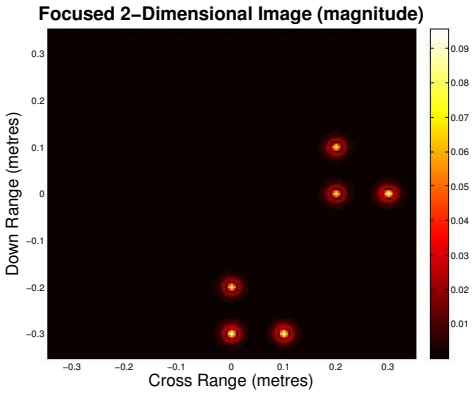

(d) Reconstructed 2D image

Figure 4.26: Simulated data with 360 degree viewing angle

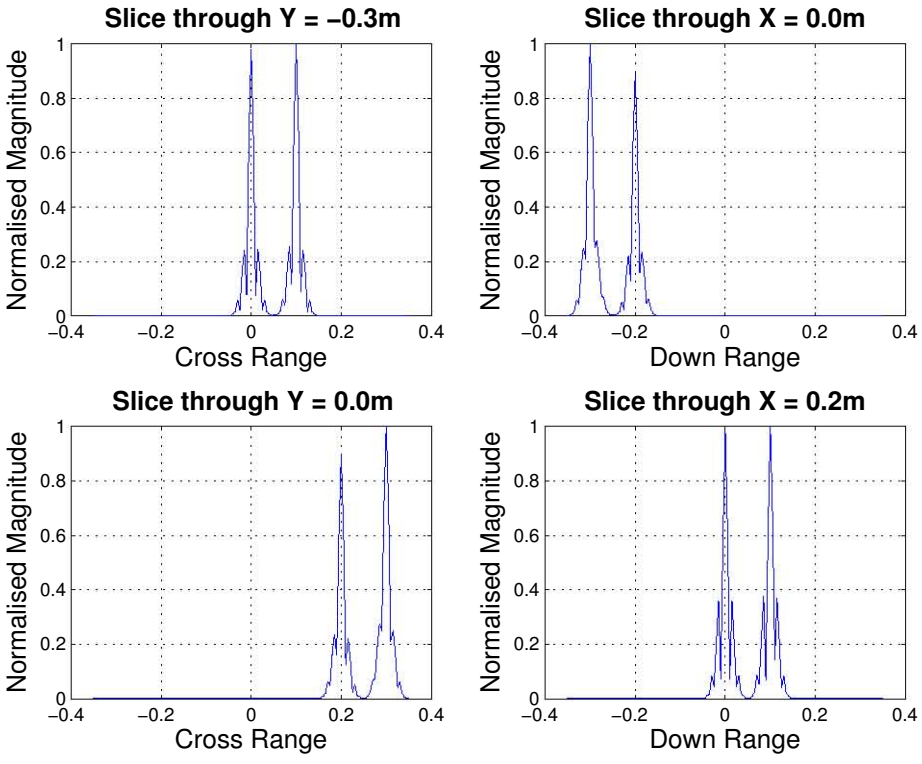

Figure 4.27: Vertical and horizontal slices for 360 degree viewing angle

Five angular ranges were tested, that being θ_{view} =10, 30, 90, 180 and 360 degrees. The recorded simulated data as well as the reconstructed 2D image can be seen in Figure 4.18, 4.20, 4.22, 4.24 and 4.26 respectively. From Figure 4.18d, 4.20d, 4.22d, 4.24d and 4.26d it can be observed that as the angular range of the viewing angle increases, the reconstructed images become more focused. This is because as the angular range θ_{view} increases, so the cross range resolution$\triangle R_{cr}$ becomes finer. This allows for targets which are closely spaced to be clearly distinguished. In Figure 4.18d, the two targets located along 0 m downrange appear to be joined in the reconstructed image. The dimensions of the targets cannot be determined as the image appears smeared. In contrast, Figure 4.26d shows that the targets are clearly distinguishable and the number of targets and their location can be seen. Figure 4.26c shows the locus of the targets as they rotate on the pedestal. The locus is sinusoidal as a result of the circular movement of the targets in front of the stationary antennas. It shows the change in down range distance to the targets as the pedestal rotates. There are areas along the locus which are brighter or darker than others. This occurs where two targets are located at the same distance from the antenna and the received signals from these targets cause constructive and destructive interference. Vertical and horizontal slices have been taken through the location of the targets in the reconstructed images and these can be seen in Figure 4.19, 4.21, 4.23, 4.25 and 4.27 respectively. These show the down range and cross range resolution of the system. Slices along x=0 m and x=0.2 m shows the down range resolution and slices along y=-0.3 m and y=0 m shows the cross range resolution. The images show that increasing the angular range, θ_{view}, makes the cross range resolution finer. It is clear from the simulations of different view angles that the viewing angle has a significant effect on the reconstructed image and the cross range resolution of the targets. The reconstructed image becomes clearer, while the cross range resolution becomes finer. Cross range is the direction along the x-axis while down range is the distance along the y-axis.

By taking the centre frequency of the system (5 GHz), corresponds to $\lambda = 0.06$ m . At a target distance of 0.5 m away from the antenna, the cross range resolution has been calculated using Equation 4.4 and tabulated in Table 4.2. These calculations agree with the observations from Figure 4.19, 4.21, 4.23, 4.25 and 4.27. By computing the cross range resolution for each viewing angle it is evident that by increasing the size of the synthesized aperture results in a finer cross range resolution. It can also be concluded that a 30 degree angular range is sufficient to reconstruct an image of the targets. This was tested and proved in the simulations as clear distinguishable targets could be seen using this an angular range of 30 degrees.

4.1.4 Effect of Targets at Different Heights

One of the objectives of this project was to develop a system which is capable of imaging targets in 3D space. The 2D algorithm that was used to recreate the images of the targets was designed for a 2D image where all targets were located in the same plane as the an-

Antenna Aperture (metres)	Viewing Angle (θ_{view} indegrees)	Synthetic Aperture Length (arc length in metres)	Cross Range Resolution (metres)
0.125	10	0.021817	1.3750
0.125	30	0.06545	0.4584
0.125	90	0.19635	0.1528

Table 4.2: Table showing the cross range resolution

tennas and platform. The limits of this 2D algorithm was also investigated. A simulation was run placing targets at different heights above the platform and then performing the 2D time domain back-projection algorithm on them.

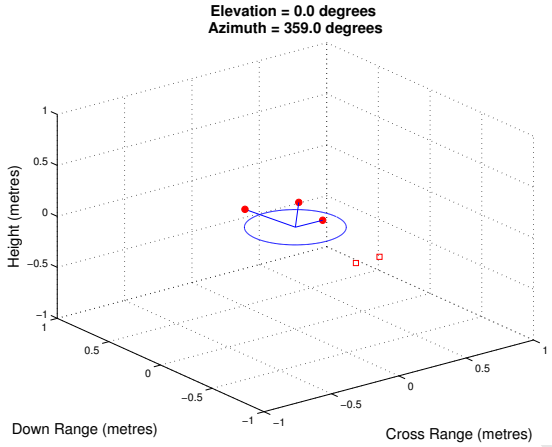

(a) 3D view of the simulated point target

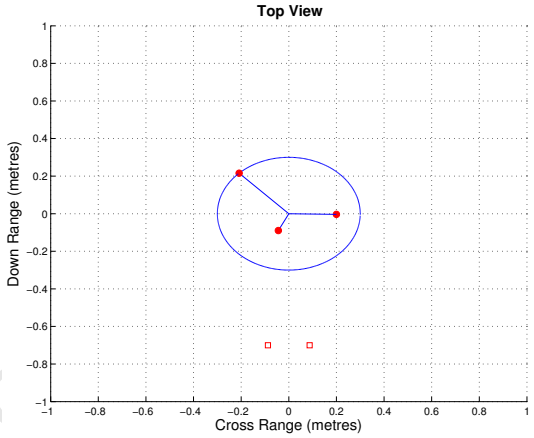

(b) Top view of the simulated point target

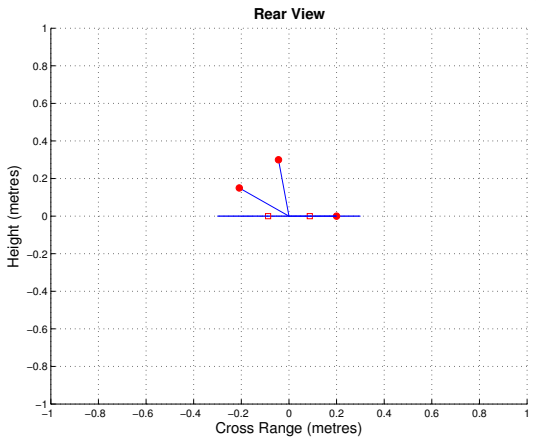

(c) Rear view of the simulated point target

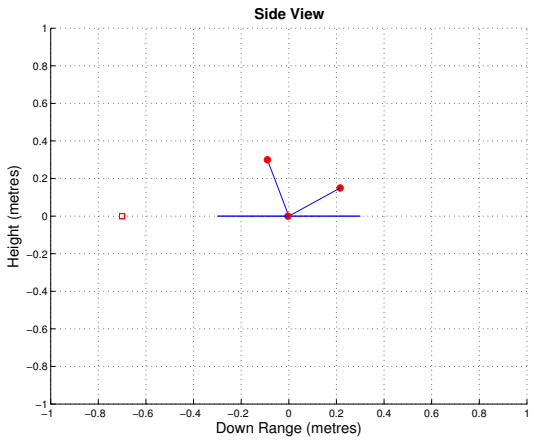

(d) Side view of the simulated point target

Figure 4.28: Figure of the simulated point target

The location of the three point targets can be seen in Figure 4.28. The frequency domain data and range profiles can be seen in Figure 4.29. Three peaks can be seen in the range compressed data as there are three point targets present on the pedestal. Figure 4.30 shows the range compressed data which shows the locus of the targets. It is evident that there are three targets. The reconstructed image can also be seen in Figure 4.30. From the reconstructed image, it is not clear that there are three point targets as only one target has been focused correctly and the remaining two are severely defocused. This is because the

reconstruction algorithm is matched to targets located on the platform and not at different heights. In this way the image is only reconstructed correctly for the target placed at 0 m above the pedestal. The locus of the target placed at a height above the platform will not match the assumed locus of a target on the platform, hence the defocussing. Based on these results a 3D simulation must be implemented, along with a 3D algorithm which is capable of reconstructing a 3D image of the scene, independent of the target's height above the platform.

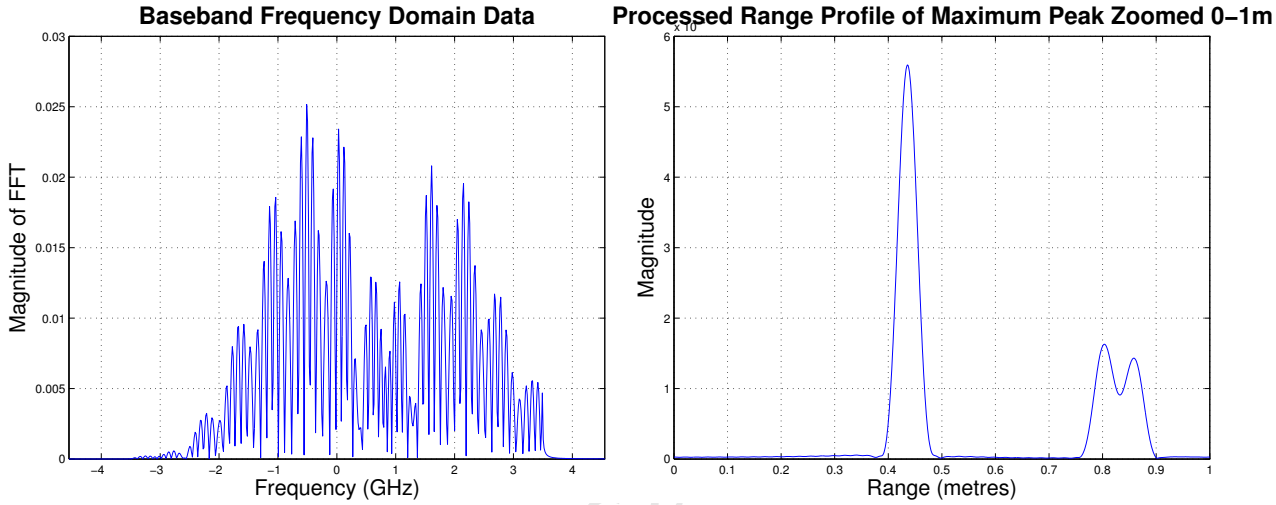

(a) Baseband frequency domain data

(b) Range profile zoomed to 0-1 m

Figure 4.29: Simulated frequency and time domain data

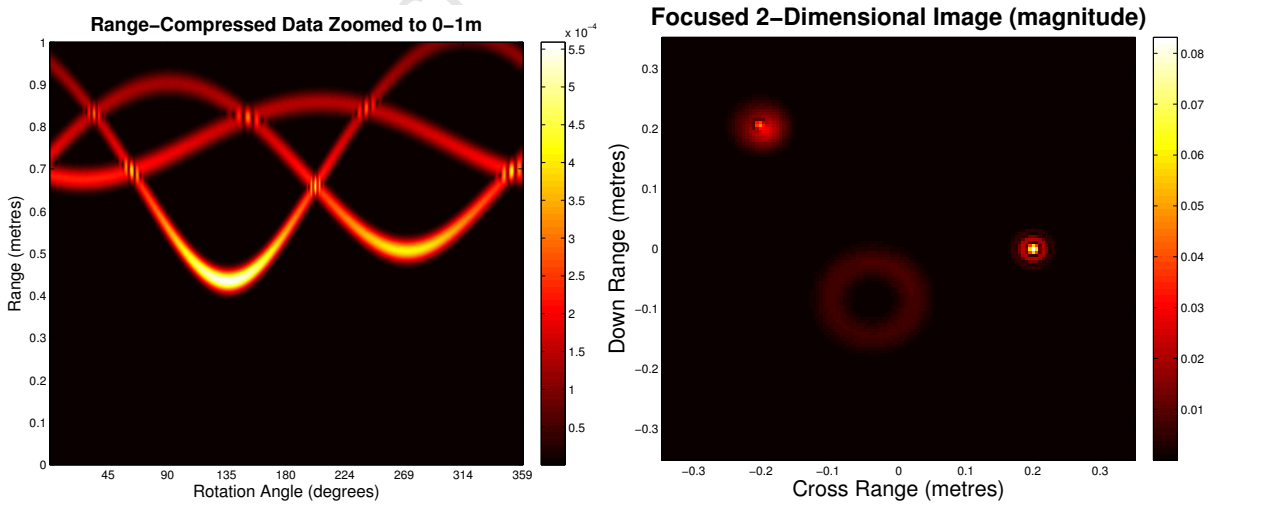

(a) Range compressed data showing locus of targets

(b) Reconstructed 2D image

Figure 4.30: Simulated processed data

4.2 3-Dimensional Simulations

A 3D simulation was run which simulates the movement of a 2-axis rotating pedestal. This is equivalent to viewing the scene from a 2D aperture. The data will be collected and then run through a 3D imaging algorithm. The viewing angle in both the azimuth and elevation direction was limited to 30 degrees with an angular increment of 1 degree, as would be expected in the experiments. The same aperture sample spacing was applied to the elevation direction as in the azimuth direction. The outputs of this simulation and the resulting 3D image can be seen in this section. The same radar parameters were used in the 3D simulations, as was used in the 2D simulations, with the addition of:

- Angular Azimuth Range: 255 - 285 degrees
- Azimuth Angular Increments: 1 degree
- Angular Elevation Range: -15 - 15 degrees
- Elevation Angular Increments: 1 degree
- Transmitter coordinates in metres (x,y,z) : (-0.0875 ,-0.7 ,0)
- Receiver coordinates in metres (x,y,z): (0.0875 ,-0.7 ,0)
- Scene Radius: 0.25 m
- Scene x-axis limits (metres): $-0.35 \leq x \leq 0.35$
- Scene y-axis limits (metres): $-0.35 \leq y \leq 0.35$
- Scene z-axis limits (metres): $-0.35 \leq z \leq 0.35$

4.2.1 Simulation of Single Target

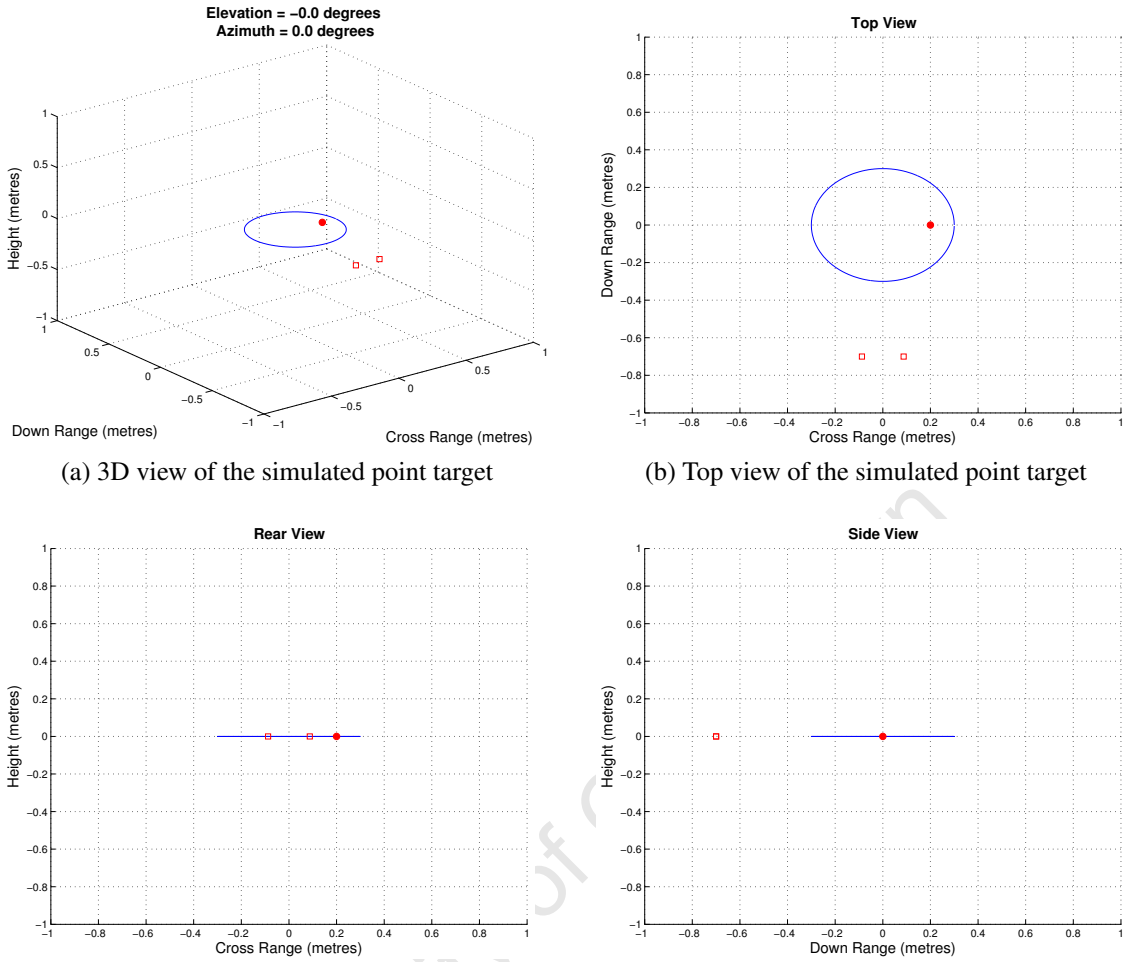

(a) 3D view of the simulated point target

(b) Top view of the simulated point target

(c) Rear view of the simulated point target

(d) Side view of the simulated point target

Figure 4.31: Figure of the simulated point target

A simulation was run for a single point target located on the platform. The location of the target can be seen in Figure 4.31. The simulation was run over a limited viewing angle of 30 degrees.

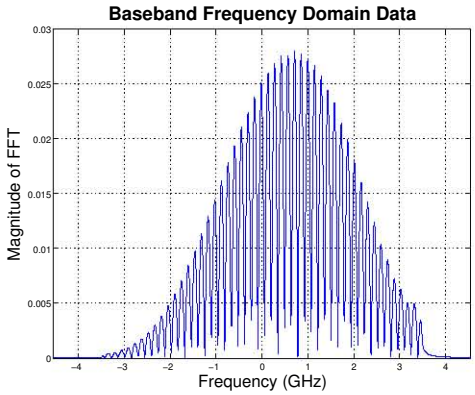

(a) Baseband frequency domain data

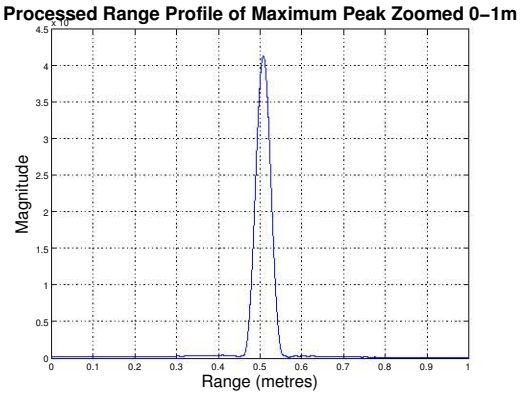

(b) Processed range profile

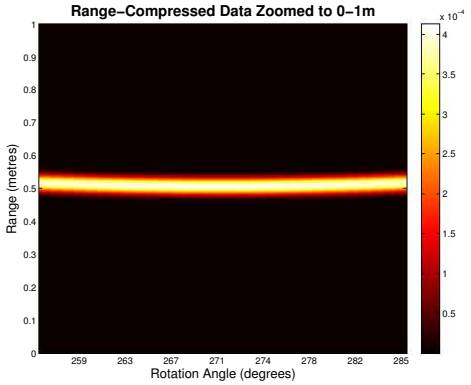

(c) Range compressed data

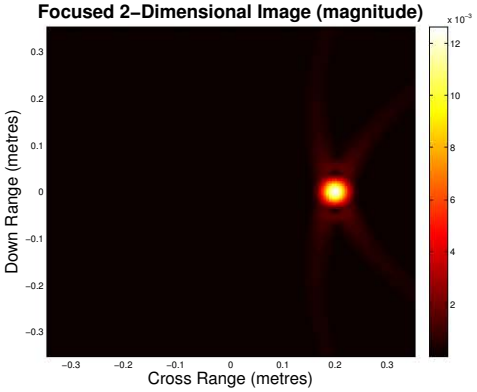

(d) Reconstructed 2D image at height of 0 m above platform

Figure 4.32: Simulated data with 10 degree viewing angle

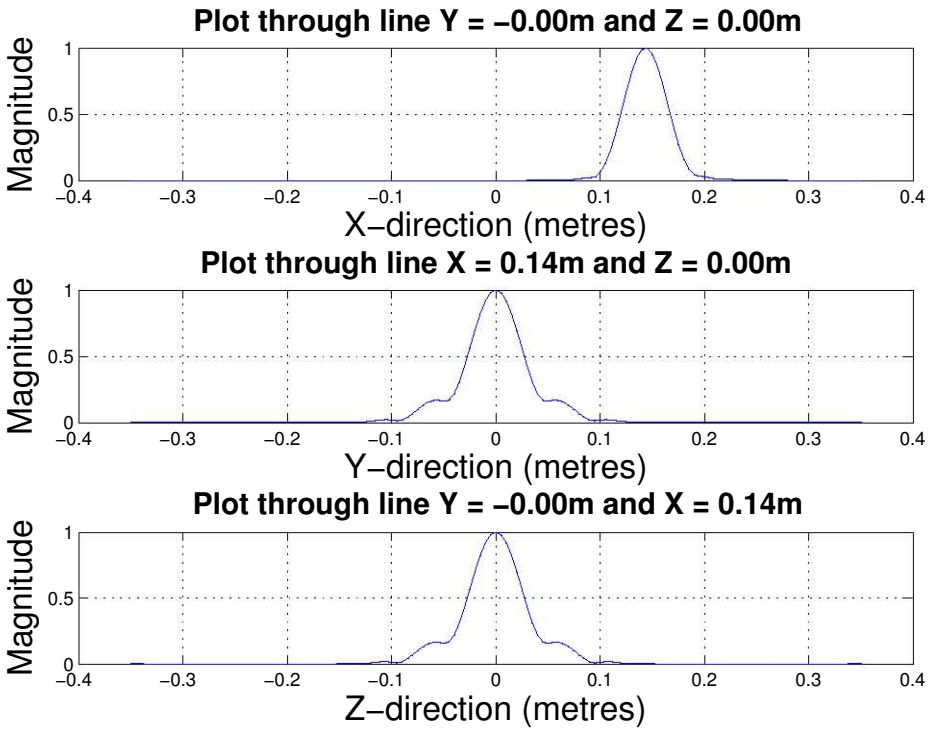

Figure 4.33: Vertical and horizontal slices

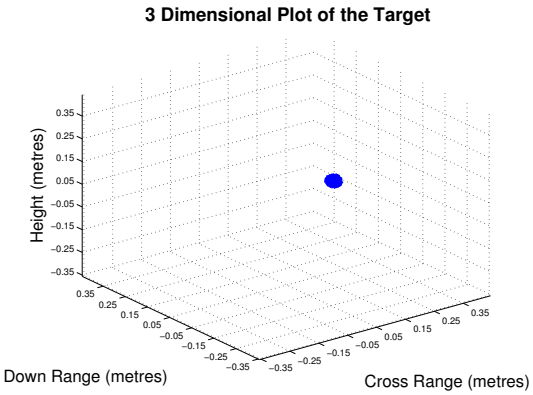

(a) 3D view of the simulated point target

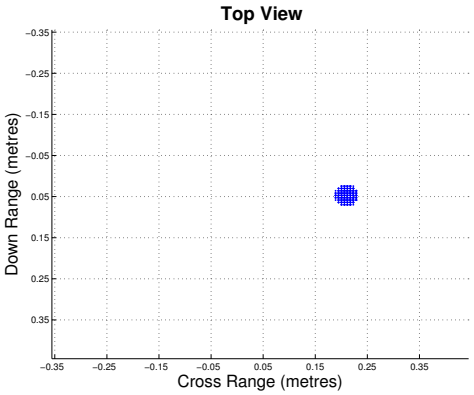

(b) Top view of the simulated point targview of the simulated point taret

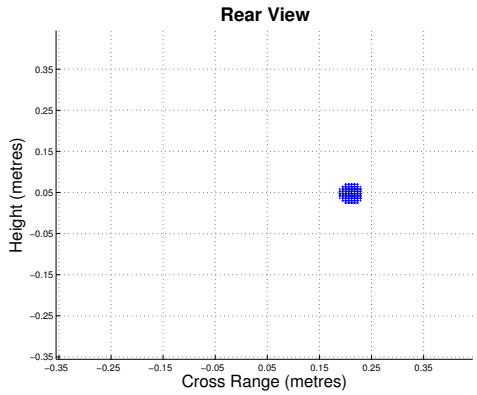

(c) Rear view of the simulated point target

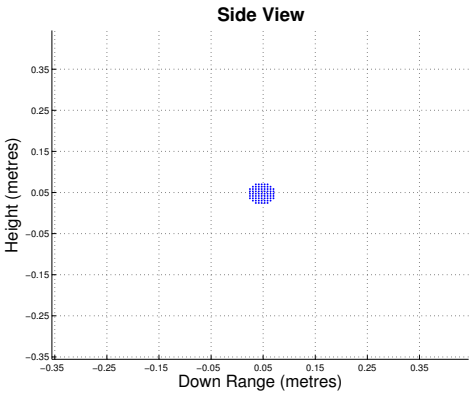

(d) Side view of the simulated point target

Figure 4.34: 3D image of the reconstructed point target

The reconstructed 3D image can be seen in Figure 4.34. This figure shows the top, rear and side view of the scene. From this image the location of the simulated point target can be seen. The frequency and time domain data as well as a 2D image of the scene at a height of 0 m above the platform can be seen in Figure 4.32. Figure 4.33 shows slices through the brightest point in 3D space where the target is located. This is done so that the resolution of the targets can be observed. The down range resolution can be read from the plot along y=0 m and z=0 m. This is shown along the line x=0.10 m and z=0 m for the azimuth direction and x=0.10 m and z=0 m for the elevation direction. From these plots along different lines in the 3D space it is evident that the cross range resolution in the azimuth and elevation directions are the same. This is because the viewing angle for each of these orientations is the same. The down range resolution is different as this is dependent on the system bandwidth.

4.2.2 Simulation of Multiple Target

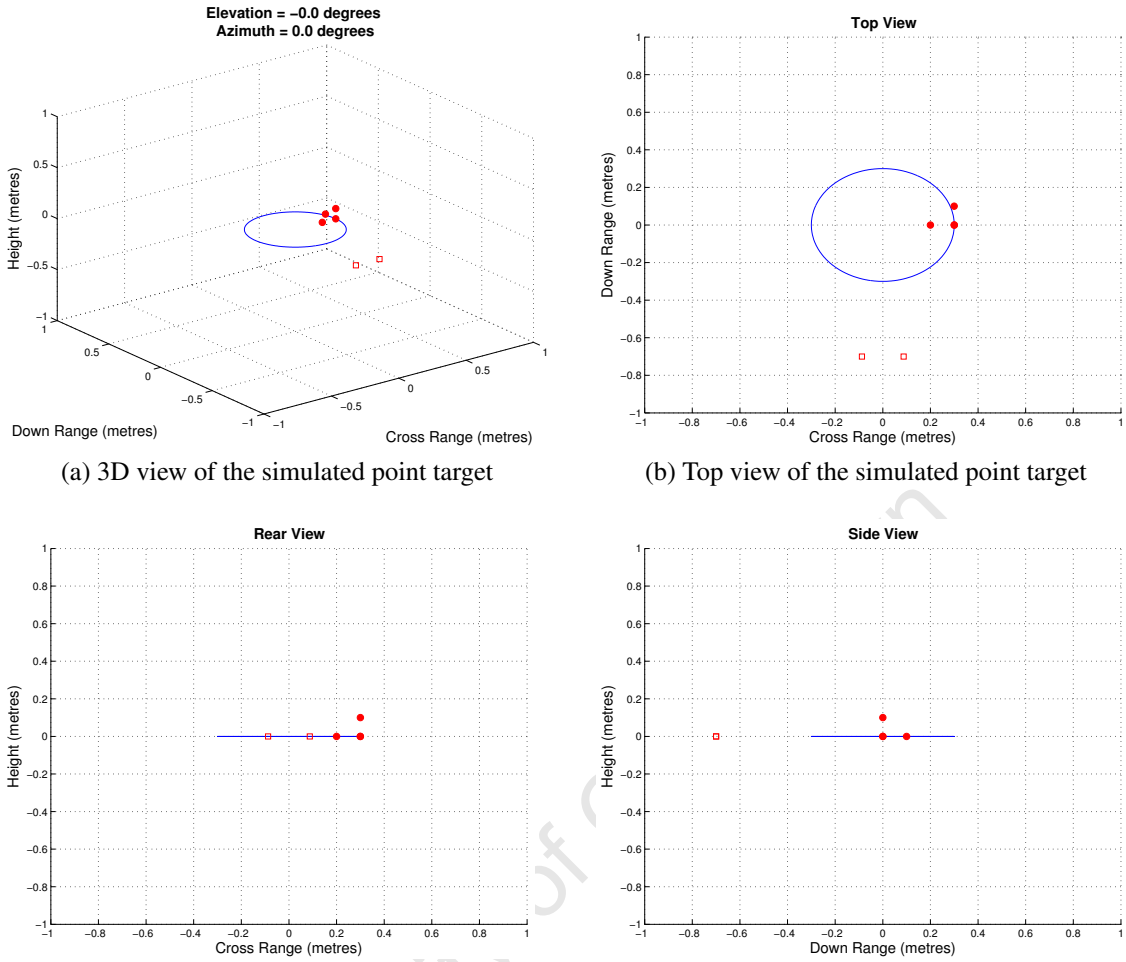

(a) 3D view of the simulated point target

(b) Top view of the simulated point target

(c) Rear view of the simulated point target

(d) Side view of the simulated point target

Figure 4.35: Figure of the simulated point target

Figure 4.35 shows the location of the point targets in the simulation. The point targets were placed in such a way that the resolution of the image can be seen in each dimension. The frequency domain data as well as the range profile of the data can be seen in Figure 4.36. As mentioned before, the experiment was simulated over a limited viewing angle. This can be seen in the range compressed data in Figure 4.36.

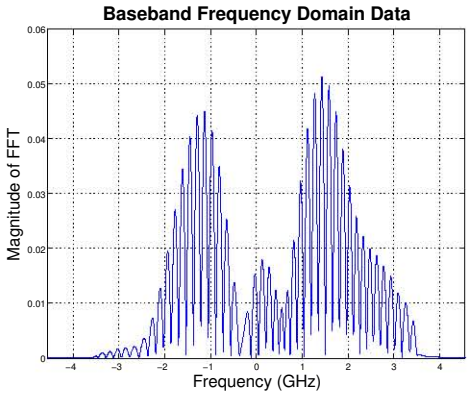

(a) Baseband frequency domain data

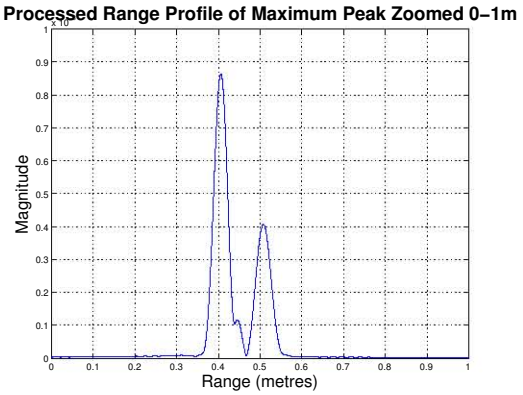

(b) Processed range profile

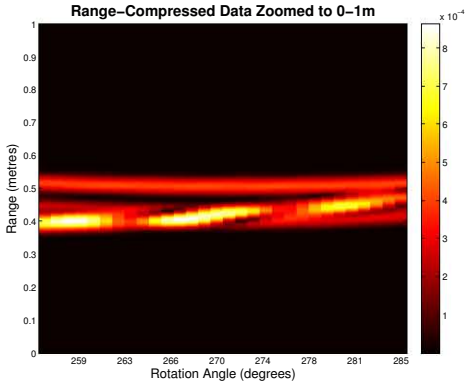

(c) Range compressed data

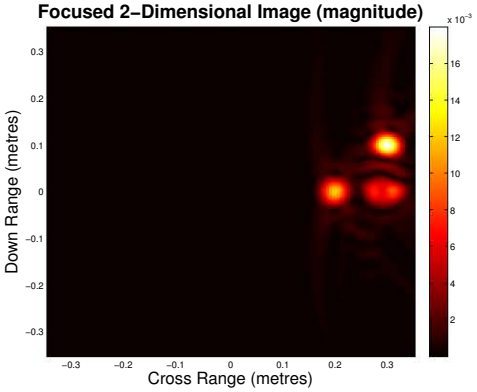

(d) Reconstructed 2D image at height of 0 m above platform

Figure 4.36: Simulated data with 10 degree viewing angle

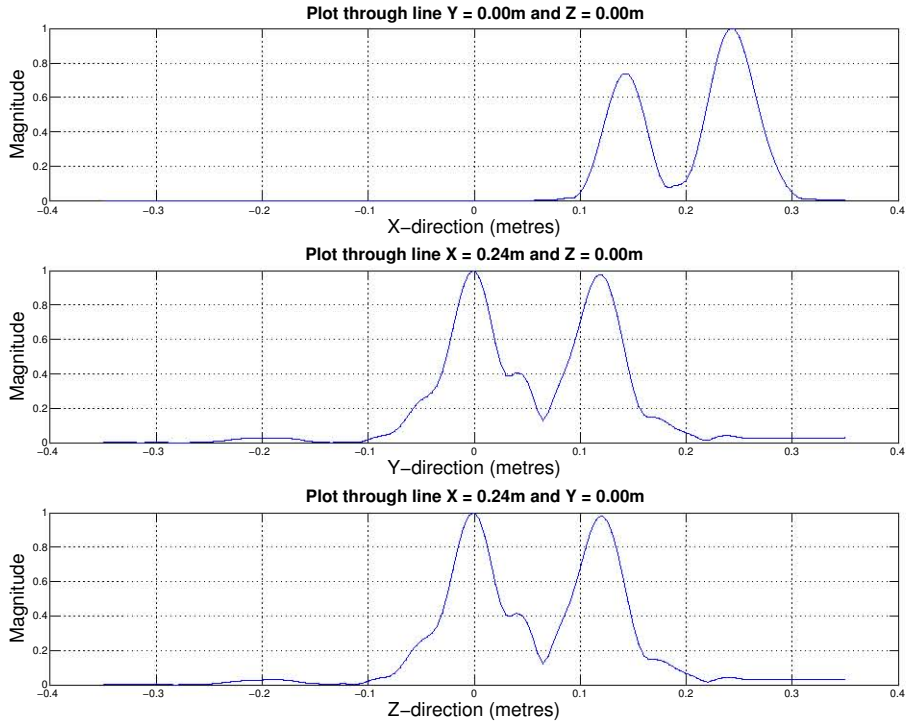

Figure 4.37: Vertical and horizontal slices

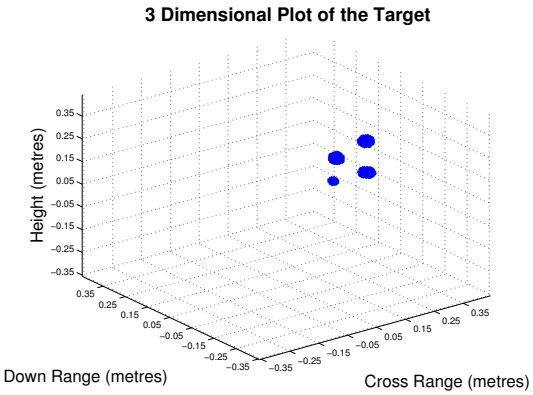

(a) 3D view of the simulated point target

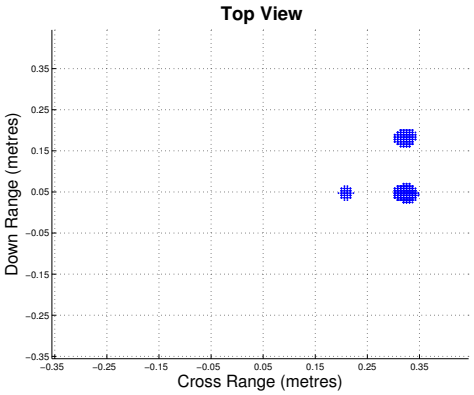

(b) Top view of the simulated point target

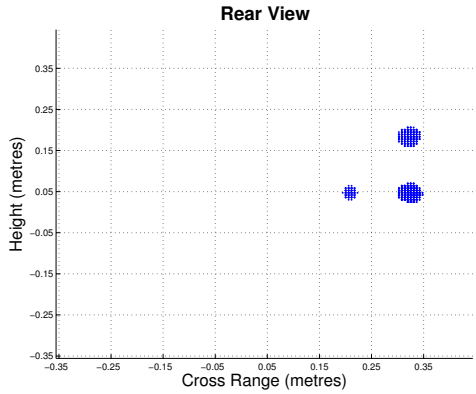

(c) Rear view of the simulated point target

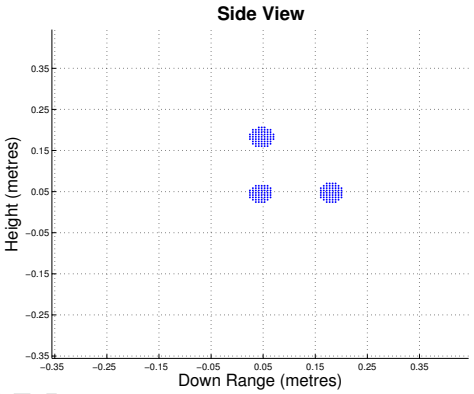

(d) Side view of the simulated point target

Figure 4.38: 3D image of the reconstructed point targets

A 2D image was reconstructed along the plane at the level of the platform. This can be seen in Figure 4.36d. Three targets were placed on this level and a fourth target vertically 10 cm above one of them. From Figure 4.36d the two targets at the same x, y position (but different heights) appear as one defocused target on the 2D image. Figure 4.37 shows slices through each position where the targets were located. This is done so that the resolution of the targets can be observed. The targets were rotated around boresight, so the down range resolution can be read from the plot along y=0 m and z=0 m. The cross range resolution is dependent on the viewing angle of the targets [30]. This is shown along the line x=0.24 m and z=0 m for the azimuth direction and x=0.24 m and z=0 m for the elevation direction.

The reconstructed 3D image of the scene can be seen in Figure 4.38. Each pixel in this image is obtained by summing up the contributions of the pixel at each location as it rotated through the azimuth and elevation positions during the experiment. See Section 3.6.5. From this image the location of the simulated point targets can be seen. This figure shows an image from the top, rear and side view so that the exact location of the targets can be read off the axes. From these plots along different lines in the 3D space it is evident that the cross range resolution in the azimuth and elevation directions are the same. This is because the viewing angle for each of these orientations is the same. The down range resolution is different as this is dependent on the system bandwidth. Figure 4.39 shows

the down range and cross range resolution through a single point target.

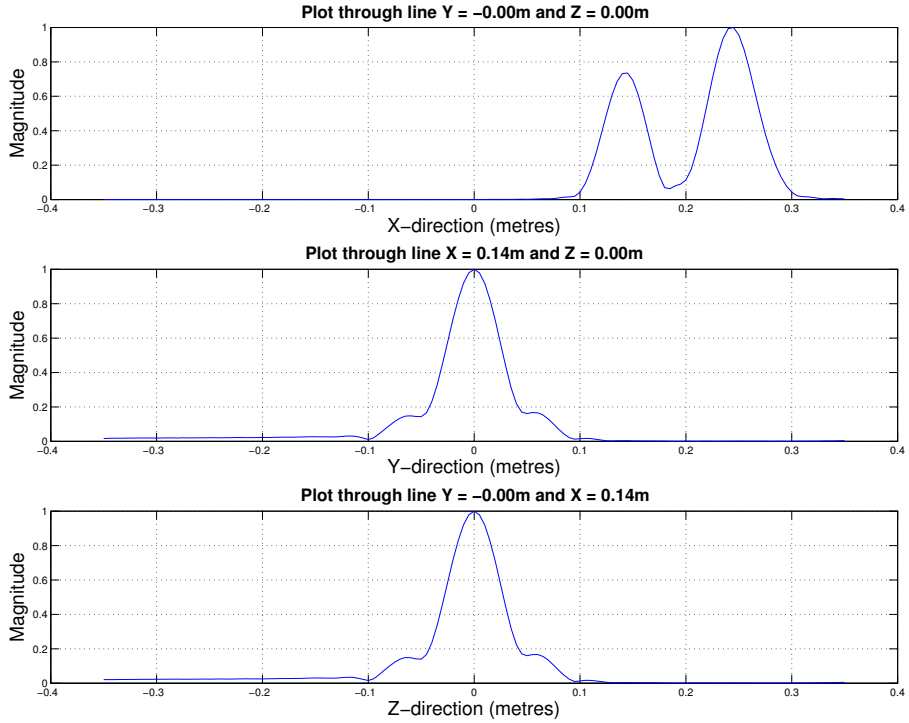

Figure 4.39: Vertical and horizontal slices through single target

Conclusion

Based on the simulations that have been carried out, it is clear that a UWB imaging system with good (cm) resolution can be achieved in both the 2D and 3D case. The data that is received from the VNA in the frequency domain can be converted to the time domain by an inverse Fourier transform and then converted to a range profile. These range profiles can then be plotted at each angular position to show the locus of the targets as the pedestal rotates. In turn this locus can then be used to reconstruct and image of the targets in both 2D and 3D space. This can achieved if the UWB system parameters are set correctly.

Chapter 5

Results

This chapter will show the experiments that were carried out in this project. It will explain how the experiments were carried out and will show the output results of the experiments. The experiments were carried out in two stages. The first stage was to set up the experiment scene using the 1-axis rotating pedestal. The targets would be placed on the pedestal in front of the antennas, rotated in the azimuth direction, and a reconstructed image created of the scene in 2D. After the success of this stage, the model was extended to 3D space. In this case the 2-axis rotating pedestal was used to rotate the objects placed in front of the antennas in 2-axes and reconstruct an image of the targets in 3D space. All the parameters of the UWB system that were set up during the experiments can be found in Chapter 4. The total experiment time for the 2D experiments, with the experiments variables as set below, was noted as approximately 15 minutes. The total experiment time for the 3D experiments was noted as 25 minutes.

5.1 2-Dimensional Experiments

For the 2D experiments that were carried out, the 1-axis rotating pedestal was used. Figure 5.1 shows a diagram of the experiment setup. The ease and speed of the 1-axis rotating pedestal allowed for a full 360 degree rotation of the pedestal so that the targets could be viewed from all angular positions by the antennas. The angular increments of the pedestal was 1.8 degrees. In Chapter 4 it was shown that an angular step of 1.8 degrees is sufficient to not introduce any ambiguity or aliasing-related artifacts in the reconstructed image.

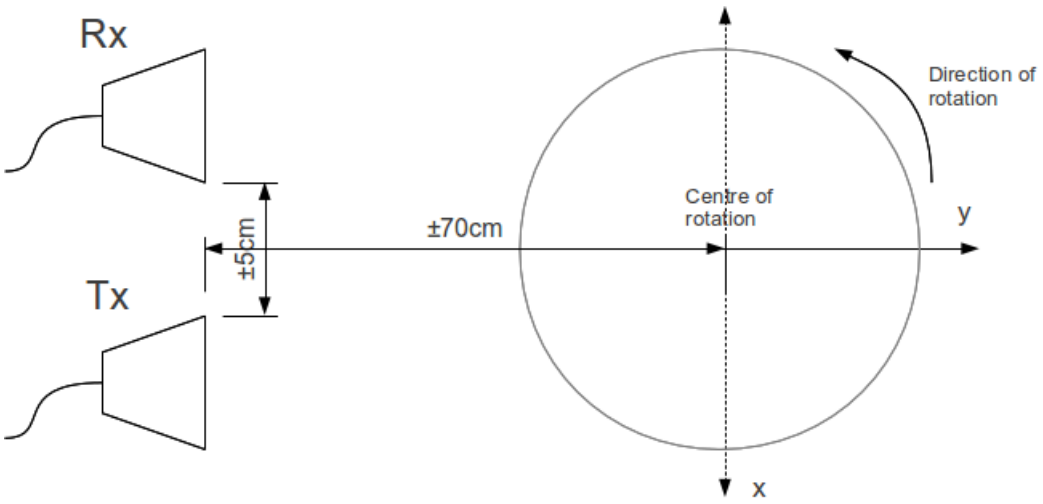

Figure 5.1: Diagram showing the experiment setup

Throughout the course of the project, many experiments were carried out using this 1-axis rotating pedestal. A selection of these experiments is described here with their corresponding pictures and reconstructed images. All targets that were used were covered with aluminum foil to increase the electromagnetic wave reflections as they interact with the surface of the object. This will give stronger echoes/reflections from the targets which are then captured by the antennas. The coordinates of the targets are given relative to the centre of rotation, with the platform in its rest position.

5.1.1 Single Thin Long Target

In this experiment one thin long target wrapped in foil, a wire with $diameter = 2\,cm$ and $height = 11\,cm$, was used and was placed on the rotating pedestal. The target was located at the following position:

- Target centre coordinates in metres (x ,y) = (-0.23 ,0)

Figure 5.2 shows a diagram of the experiment setup as well as a top view photograph of the scene showing the location of the target. Figure 5.3 shows photographs of the experiment from different positions. The antennas and VNA can be seen in Figure 5.3a. Figure 5.3b is a photograph taken from behind the antennas looking in the direction of the platform. Behind the platform was placed a piece of microwave absorbent foam to reduce the reflection from background objects.

Figure 5.4a shows the frequency domain data that was recorded directly from the VNA. This is a S_{21} measurement of the scene containing the target. Figure 5.4b shows the frequency domain data of the background scene that was recorded directly from the VNA. Figure 5.4c shows the basebanded frequency domain data that was recorded by the VNA. Figure 5.4d and 5.4e show the processed range profiles and Figure 5.4f shows the processed phase profile. Five frequency sweeps were taken by the VNA at each angular

position. The mean of these measurements was taken at each frequency sample because averaged values reduce noise. The standard deviation of these five measurements can be seen in Figure 5.5. From these plots it can be seen that the standard deviation of the measurements is $\frac{0.00055}{0.025}x100 = 2.22\%$ of the maximum value read off from the baseband frequency domain data in Figure 5.4c, which is small. This is as a result of the averaging technique, which was described in Chapter 3.4.4. The frequency domain data was passed through a Hamming window in order to reduce the sidelobes of the time domain data.

From the time domain data, the distance of the target from the antennas can be read off from the peak on the range axis. Some ringing can be observed after the peak on the graph. From an ideal point scatterer a single dominant main lobe of resolution $\frac{0.89c}{2B}x1.5 = 0.0286m\ (2.86cm)$ with sidelobe levels of -41 dB (from Hamming window - see Table 3.1). The peak is located at the distance that the target is from the antennas. This can be seen in Figure 4.4b in Chapter 4.1.2. This is however not the case as a result of the inverse filter and Hamming window that was applied and the way that the electromagnetic waves interact with the surface of the target. In order to compensate for the antennas in the system, an inverse filter was applied to the data. This filter is the inverse frequency domain data of the antennas, measured when they are facing each other. The processed range profile (0-10 m) can be seen in Figure 5.4d and the zoomed profile (0-1 m) can be seen in Figure 5.4e. The phase profile of the data is also shown in Figure 5.4f. After basebanding, for an idealized point scatterer, the phase of the time domain data is expected to be flat over the peak of the main lobe in the time domain. The phase in this plot is however not perfectly flat, but this could be related to imperfections in the inverse filter.

Figure 5.6a shows an image of the data matrix. Each column contains a range profile at a different observation angles. The bright peak forms a near-sinusoidal locus. It can be seen that the target moves closer to the antennas and then further away due to its location on the pedestal. The magnitude and phase of the peak value of the range profile was extracted along the locus. The magnitude plot can be seen in Figure 5.6c and the phase plot can be seen in Figure 5.6d. It can be seen that the magnitude of the peak varies as the target rotates closer and further away from the antennas. The plot of the phase of the peak can be used to check if the target has missed a step in the angular position or if any glitches have occurred. This can be seen at an angular distance of 200 degrees on the phase plot. This is present as a result of interference (such as a cell phone going off) experienced during the experiment. Since the VNA measures data in the frequency domain, any signal within the frequency range 300 kHz to 8.5 GHz will affect the measurements, which will in turn affect the range profiles.

Figure 5.6b shows the reconstructed image of the scene. From this figure the location of the target can be seen. A slice through the brightest point of the reconstructed image

can be seen in Figure 5.7. From this figure the location of the target along the range and cross range directions can easily be extracted. The down range resolution can be read of as approximately 2.5 cm, as was expected from the system bandwidth. The cross range resolution can be read off as approximately 3.5 cm. This is close to the expected value of 4.5 cm when rotating the target through 360 degrees read from Table 4.2. The reason for the offset could be as a result of the actual beamwidth of the antenna being a bit bigger than the theoretical $\frac{\lambda}{D}$ in the H-plane. Figure 5.8 shows a comparison between a photograph of the scene and reconstructed image of the target. From the images it is clear that the image has been successfully reconstructed.

A focusing algorithm was included in the reconstruction algorithm. This focusing algorithm estimates and adjusts the down range and cross range distance of the centre of rotation of the platform. The effects of this change can be seen in Figure 5.9. Figure 5.9a shows the effects of over estimating the down range distance of the centre of rotation by 10 cm and Figure 5.9b shows the effects of an under estimate of the down range distance by 10 cm. From the figures it can be seen that by changing the estimated down range centre of rotating distance influences the reconstructed image. The object appears to be smeared and not focused to one point. This correlates with the simulations of an over estimate and under estimate of the centre of rotation and demonstrated in Chapter 4. Figure 5.9c shows an over estimate of the cross range distance of the centre of rotation of the platform by 20 cm, while Figure 5.9d shows the effects of an under estimate of the cross range distance by 20 cm. From these figures it is clear that the image is defocused and the position of the targets appear to be shifted up or down, depending on whether the cross range distance adjustment was as over estimate or an under estimate respectively.

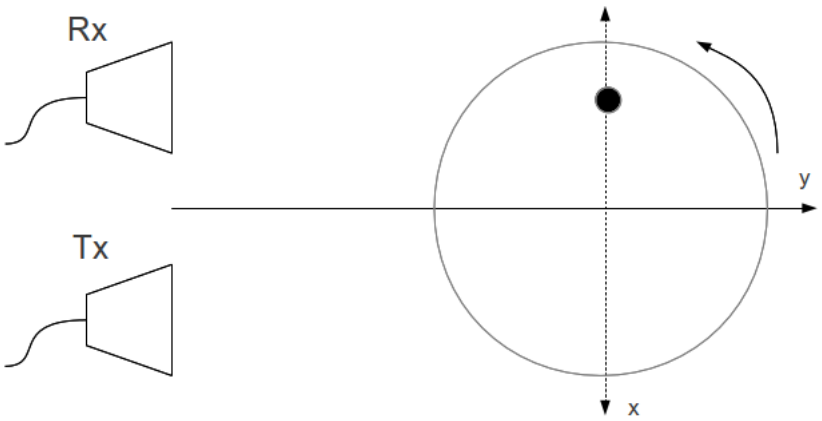

(a) Diagram of experiment scene

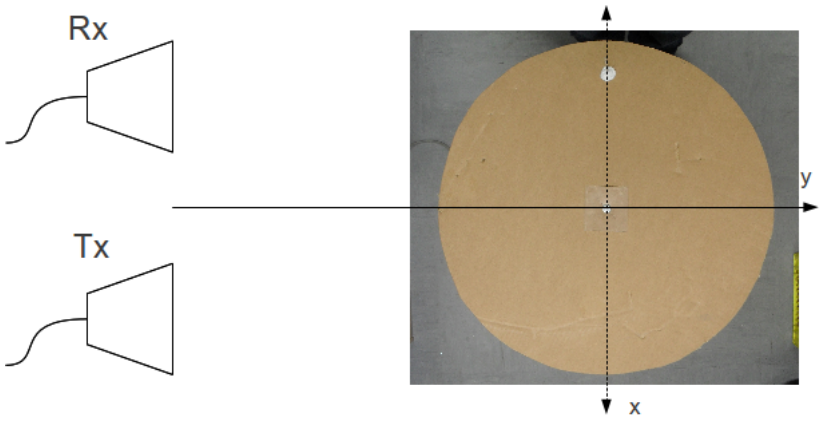

(b) Top view photograph of scene

Figure 5.2: Diagram and photograph of the experiment for a single thin long target

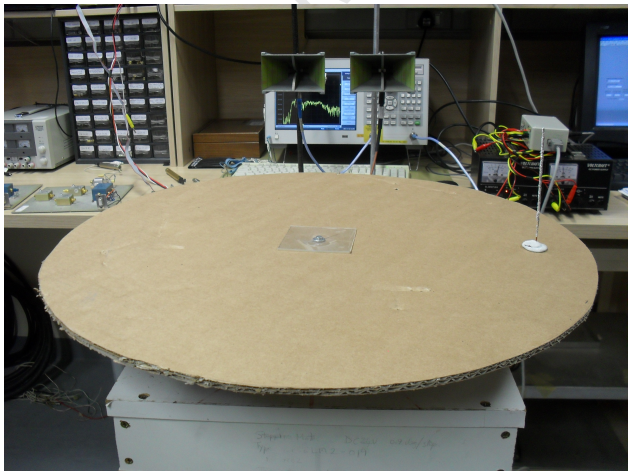

(a) Front view

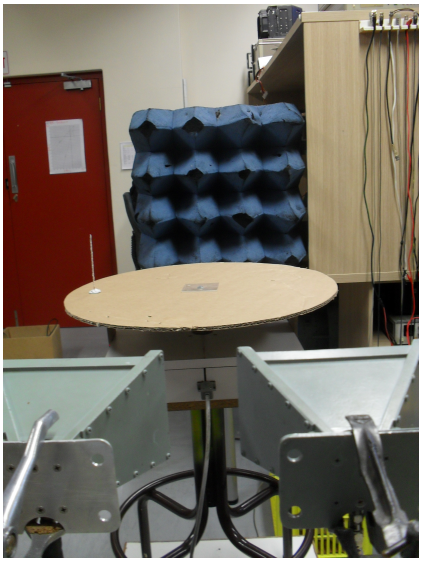

(b) Rear view

Figure 5.3: Photograph of scene for single thin long target

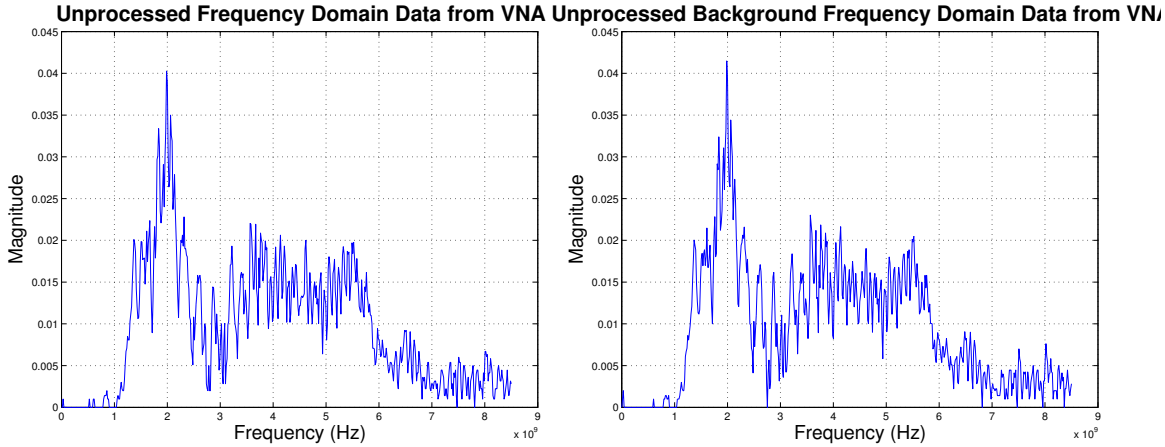

(a) Unprocessed frequency domain data from VNA at start position

(b) Unprocessed baseband frequency domain data from VNA at start position

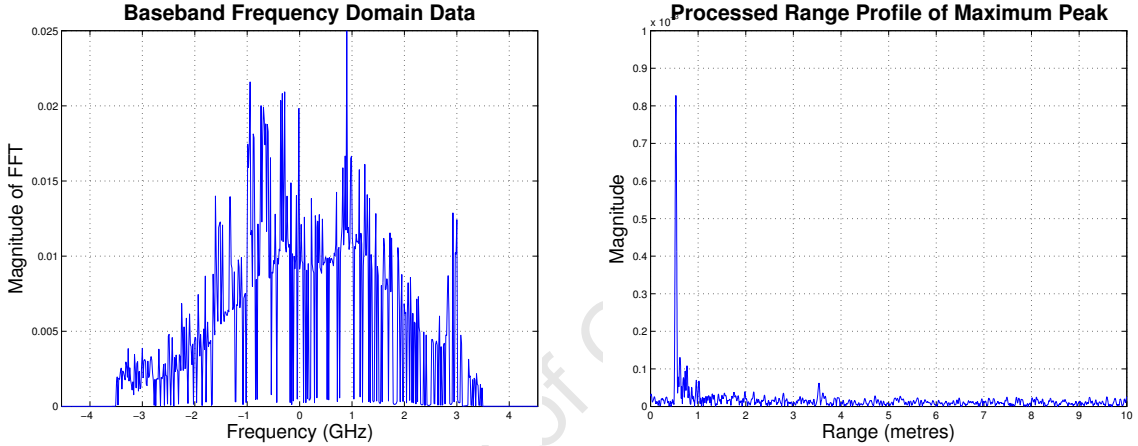

(c) Baseband frequency domain data

(d) Processed range profile up to maximum range

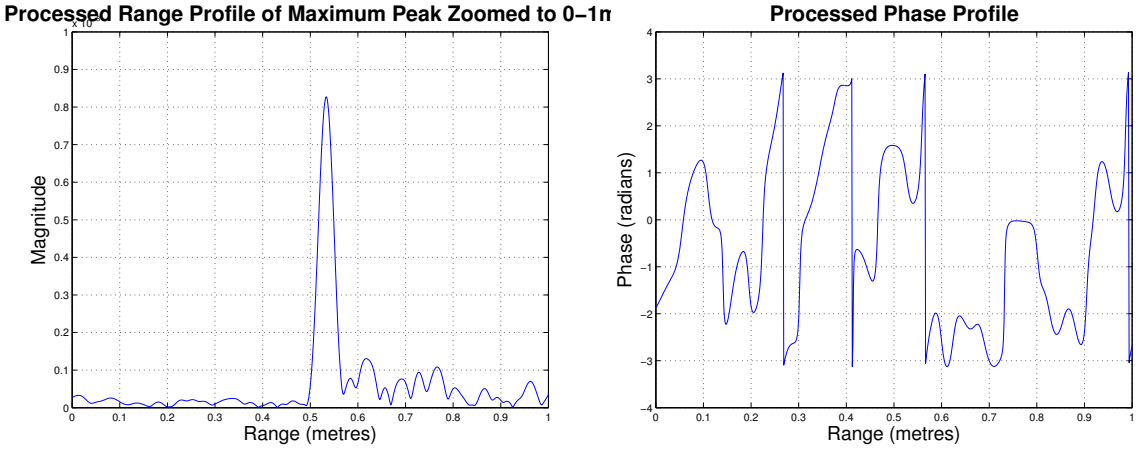

(e) Processed range profile

(f) Processed phase profile

Figure 5.4: Frequency and time domain data for single thin long target

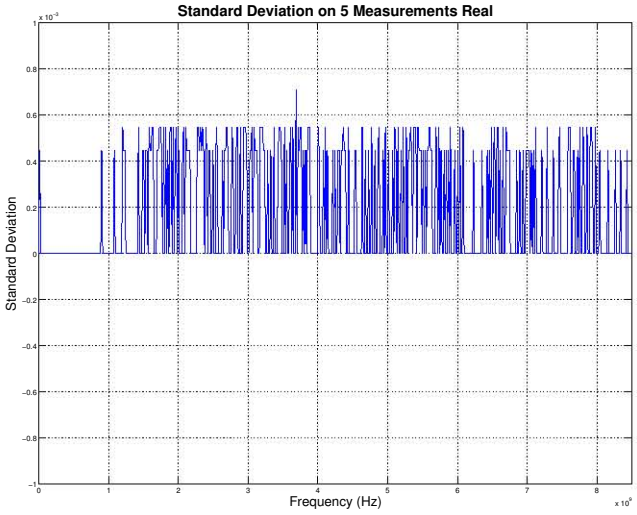

(a) Standard deviation for real measurements

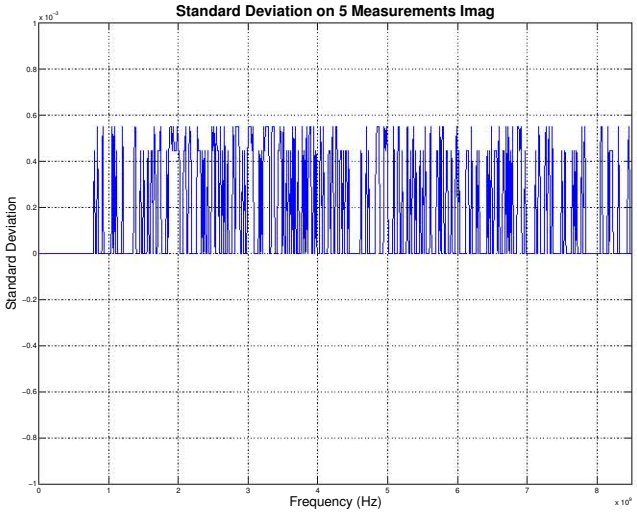

(b) Standard deviation for imaginary measurements

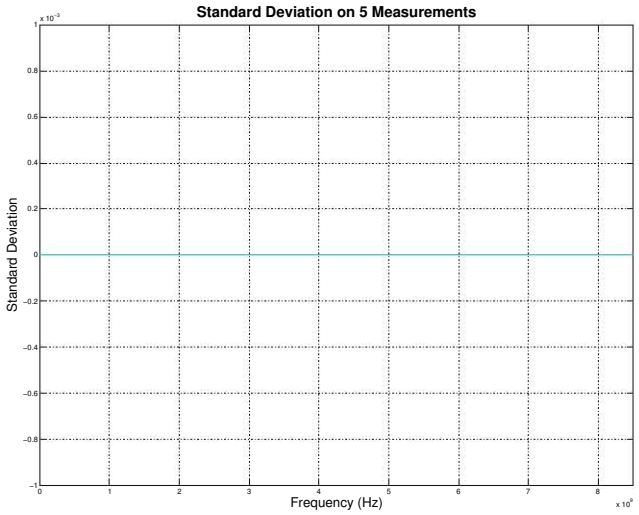

(c) Standard deviation of complex measurements

Figure 5.5: Standard deviation of 5 measurements per angular position

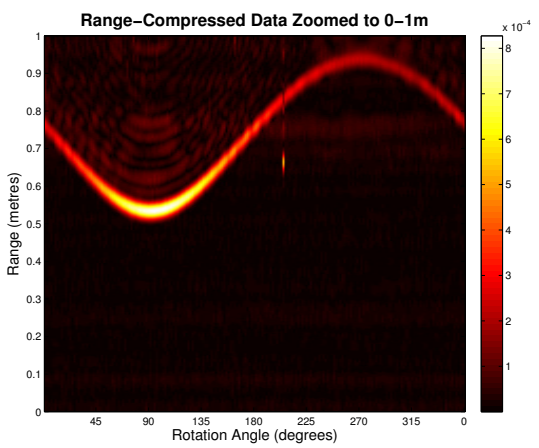

(a) Range compressed data/locus of target

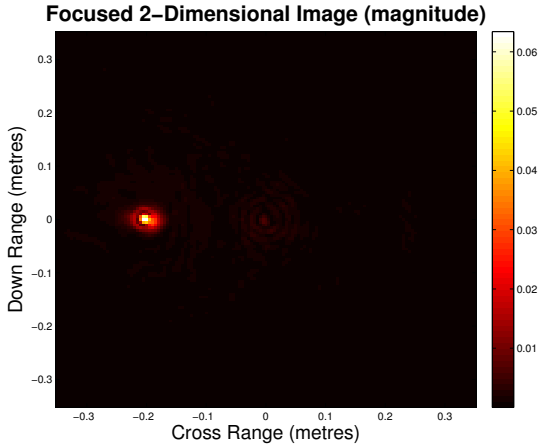

(b) 2D reconstructed image of scene

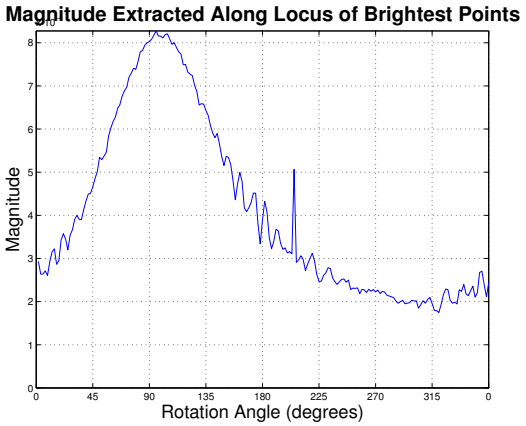

(c) Magnitude of brightest point extracted along locus

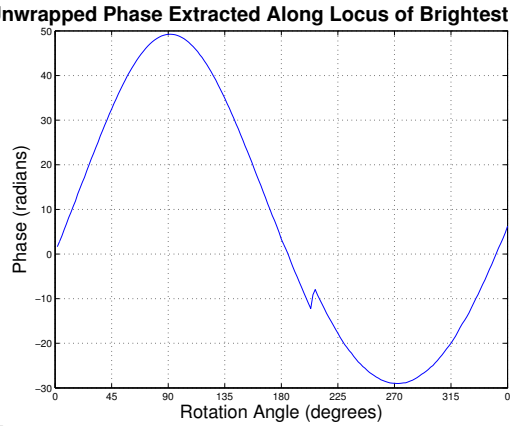

(d) Phase of brightest point extracted along locus

Figure 5.6: Locus of target and reconstructed image of scene for single thin long target

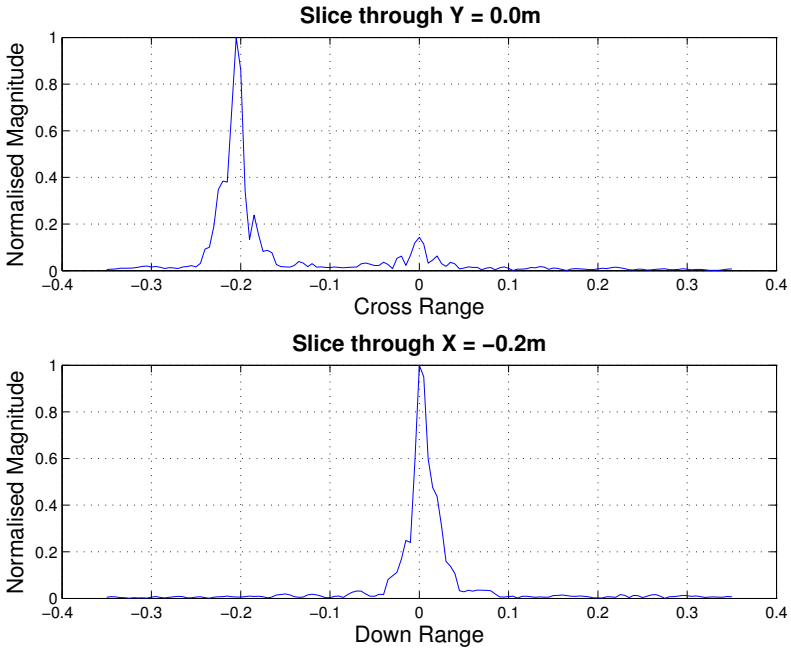

Figure 5.7: Cut through brightest point in reconstructed scene

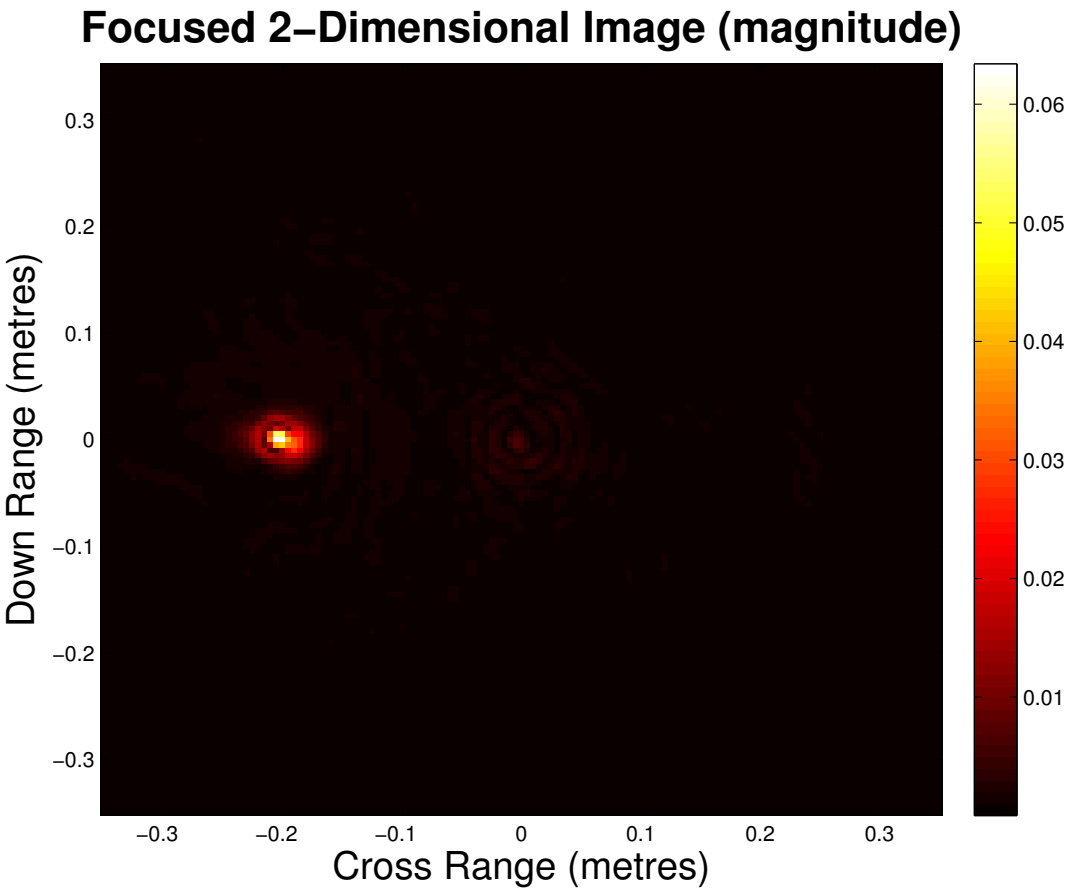

(a) 2D reconstructed image of scene

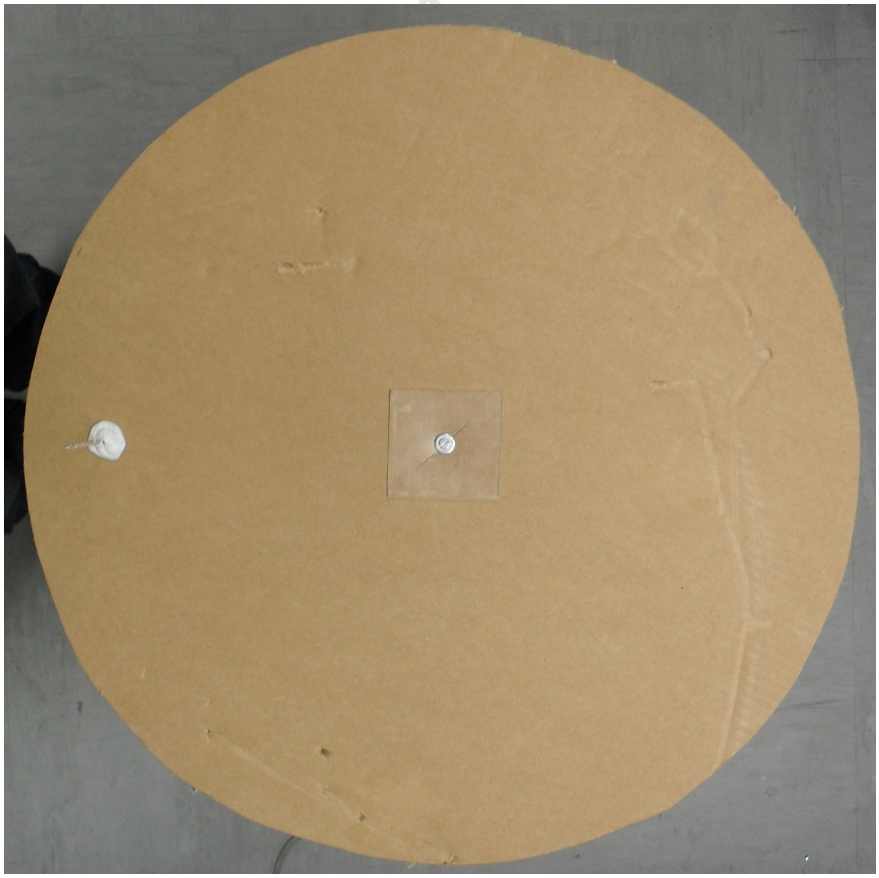

(b) Top view photograph of scene

Figure 5.8: 2D reconstructed image of scene and Top view photograph of scene

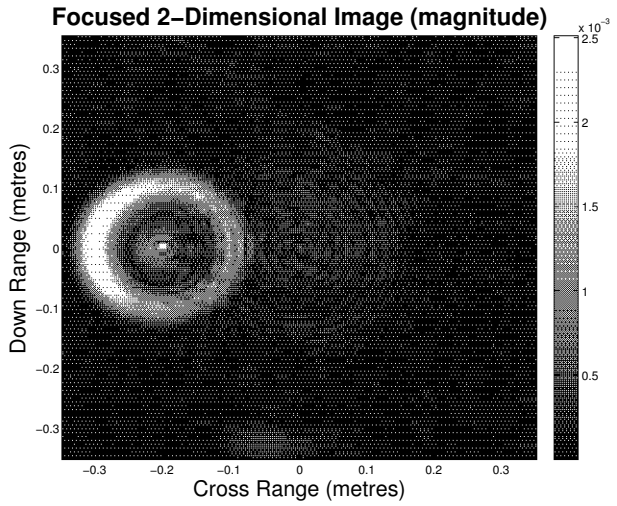

(a) 10 cm over-estimate of the down range centre of rotation location

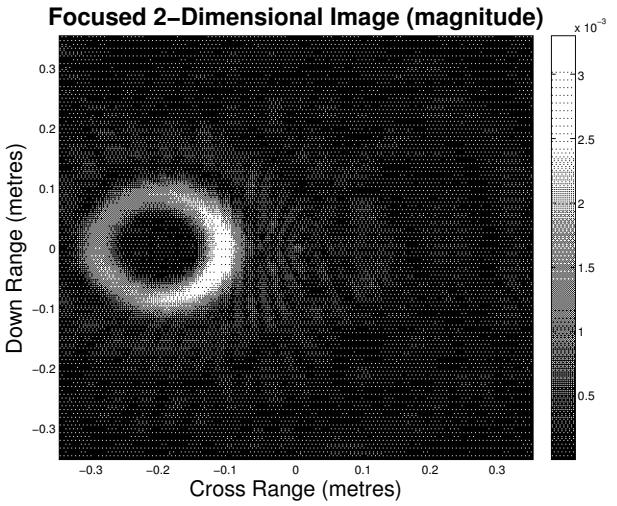

(b) 10 cm under-estimate of the down range centre of rotation location

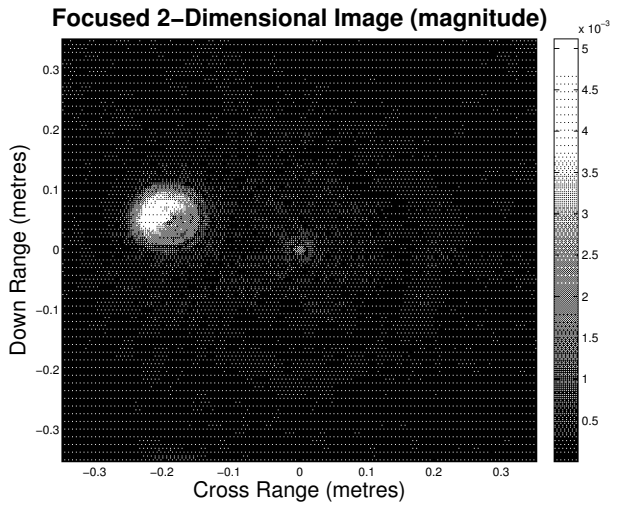

(c) 20 cm over-estimate of the cross range centre of rotation location

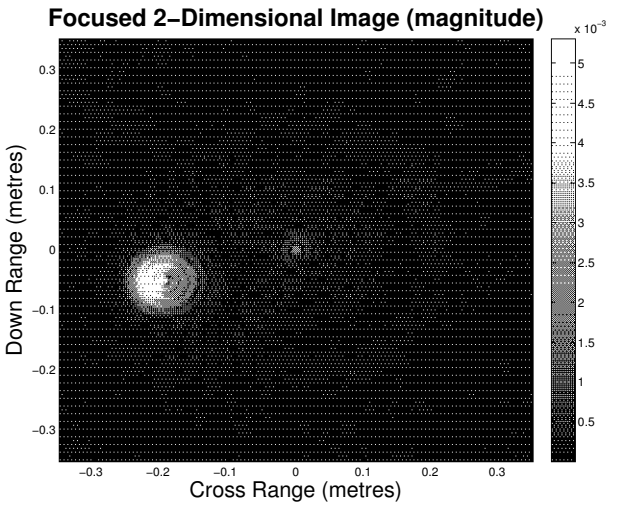

(d) 20 cm under-estimate of the cross range centre of rotation location

Figure 5.9: Focusing algorithm output by adjusting down range and cross distance of centre of rotation

5.1.2 Single Brick Shaped Target

In this experiment one brick shaped target wrapped in foil, with $length = 7.5\,cm$, $width = 6\,cm$ and $height = 10.5\,cm$, was used as a target and was placed on the rotating pedestal. The target was located at the following position:

- Target centre coordinates in metres (x ,y) = (-0.23 ,0)

Figure 5.10 shows a diagram of the experiment setup as well as a top view photograph of the scene showing the location of the target. Figure 5.11 shows photographs of the experiment from different positions.

The frequency domain data as well as the time domain data of this experiment can be seen in Figure 5.12. The range and phase profile of the experiment can also be seen in this figure. It should be noted that the phase across the main lobe of the time domain data is constant. The magnitude and phase extracted along the peak of the range profile as the target rotates (i.e. along the "sinusoidal" locus of Figure **??**) has been plotted in Figure 5.14a and 5.14b. It should be noted that there are four peaks in the magnitude plot. This is because the brick target has four flat sides and these reflect electromagnetic waves more strongly than the corners when they are perpendicular to the line of sight. The phase extracted along the peaks is also a smooth plot, which shows that no steps have been skipped.

Figure 5.13 shows a plot of the range compressed data as well as the reconstructed image scene of the target. It should be noted that the area within 0.45 m of the antennas is not completely dark. This could be as a result of the background subtraction which was not as effective. The reconstructed image shows the location of the target. Figure 5.15 shows plots of cross section slices through the centre of the target in the x and y direction. There is more than one peak in these plots due to the shape of the target. Figure5.16 shows a comparison between the imaging scene and the reconstructed scene. From this image the location of the target can be clearly seen.

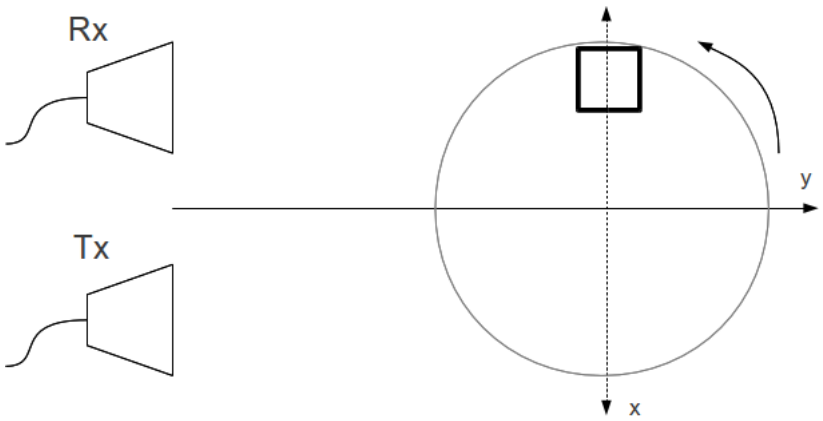

(a) Diagram of experiment scene

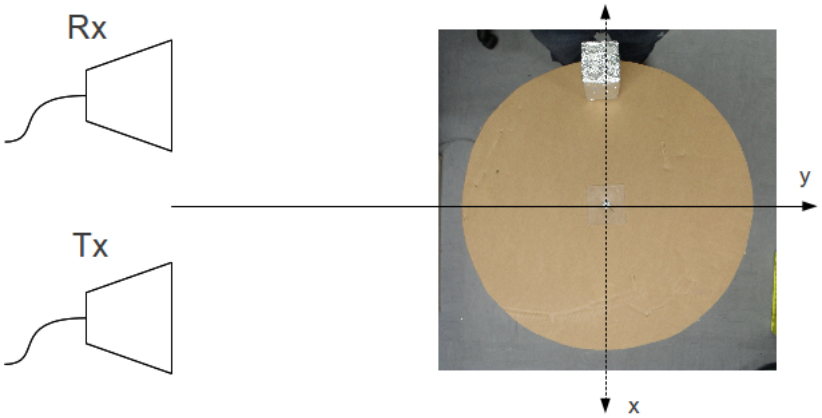

(b) Top view photograph of scene

Figure 5.10: Diagram and photograph of the experiment for a single brick shaped target

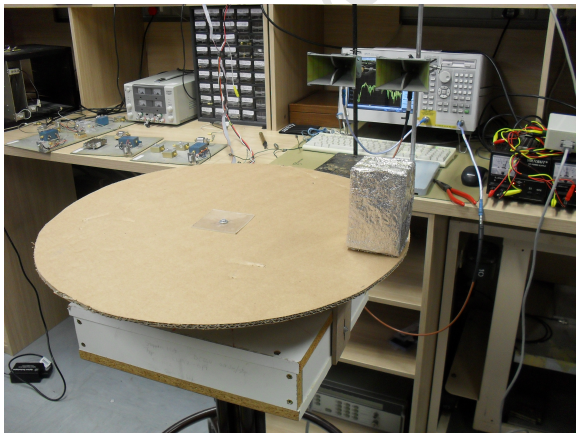

(a) Front view

(b) Rear view

Figure 5.11: Photograph of scene for single brick shaped target

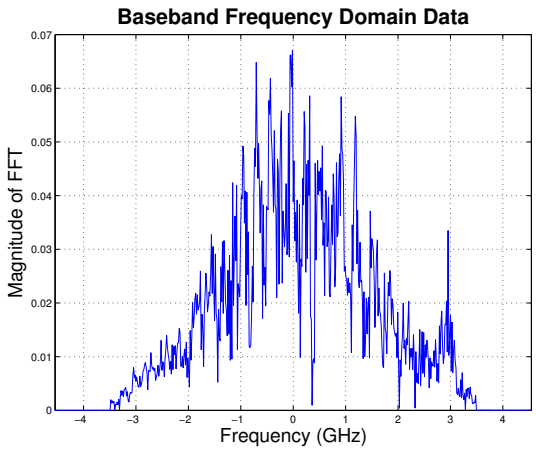

(a) Baseband frequency domain data

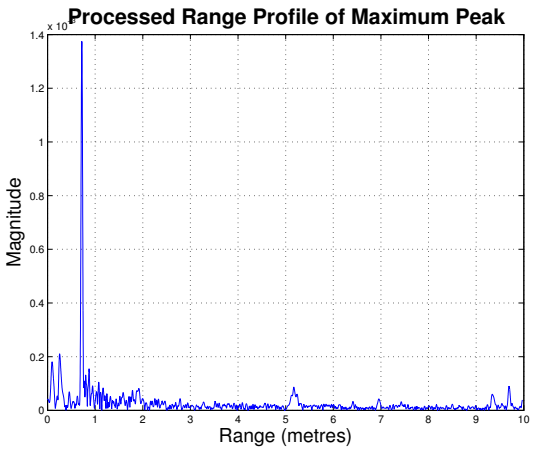

(b) Processed range profile up to maximum range

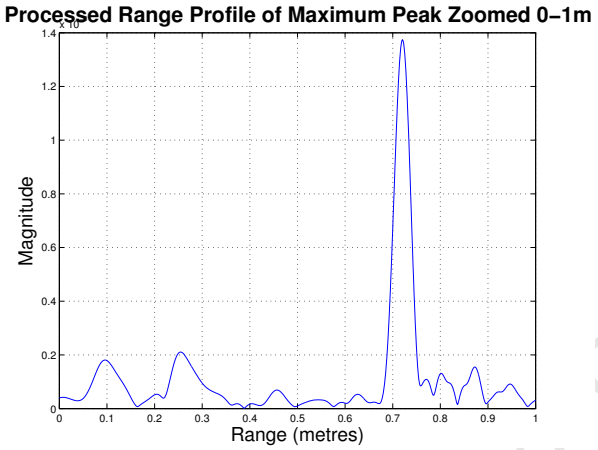

(c) Processed range profile

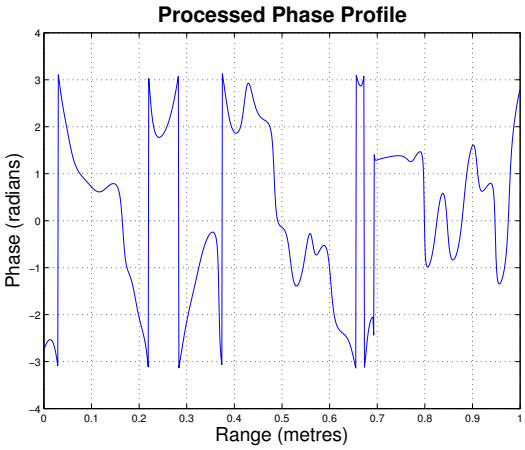

(d) Processed phase profile

Figure 5.12: Frequency and time domain data for single brick shaped target

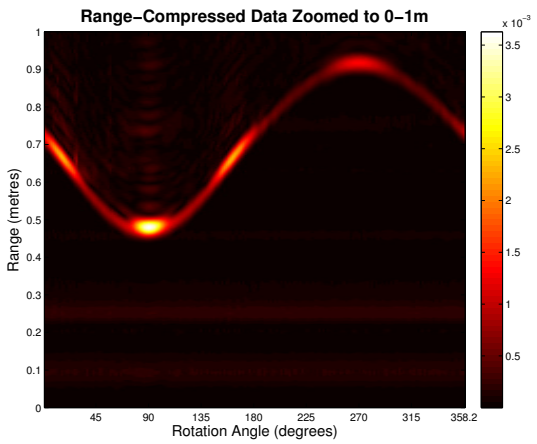

(a) Range compressed data/locus of target

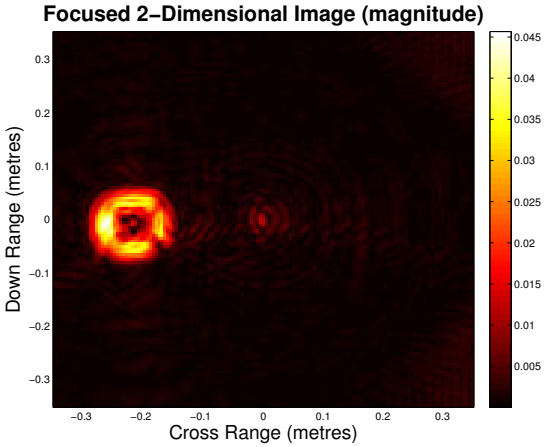

(b) 2D reconstructed image of scene

Figure 5.13: Locus of Target and Reconstructed Image of Scene for Single Brick Shaped Target

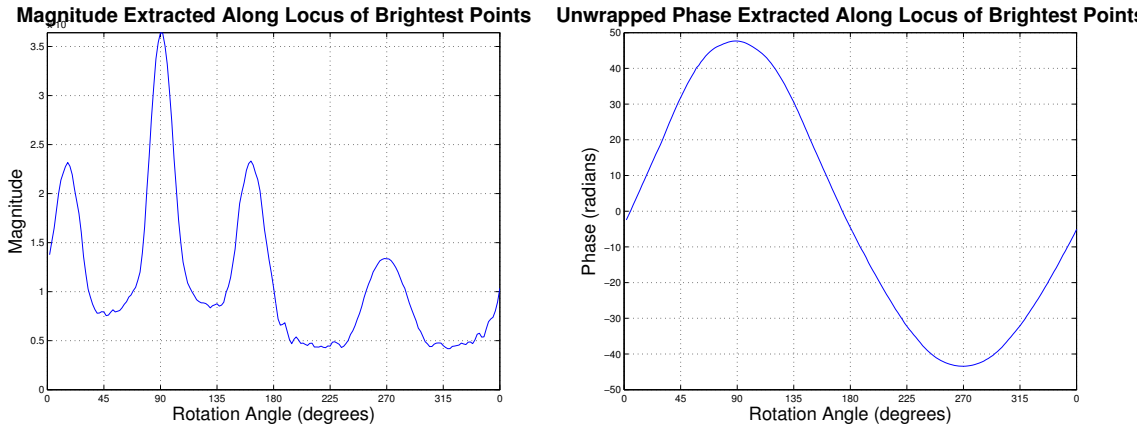

(a) Magnitude of brightest point extracted along locus

(b) Phase of brightest point extracted along locus

Figure 5.14: Magnitude and phase extracted along brightest point on locus

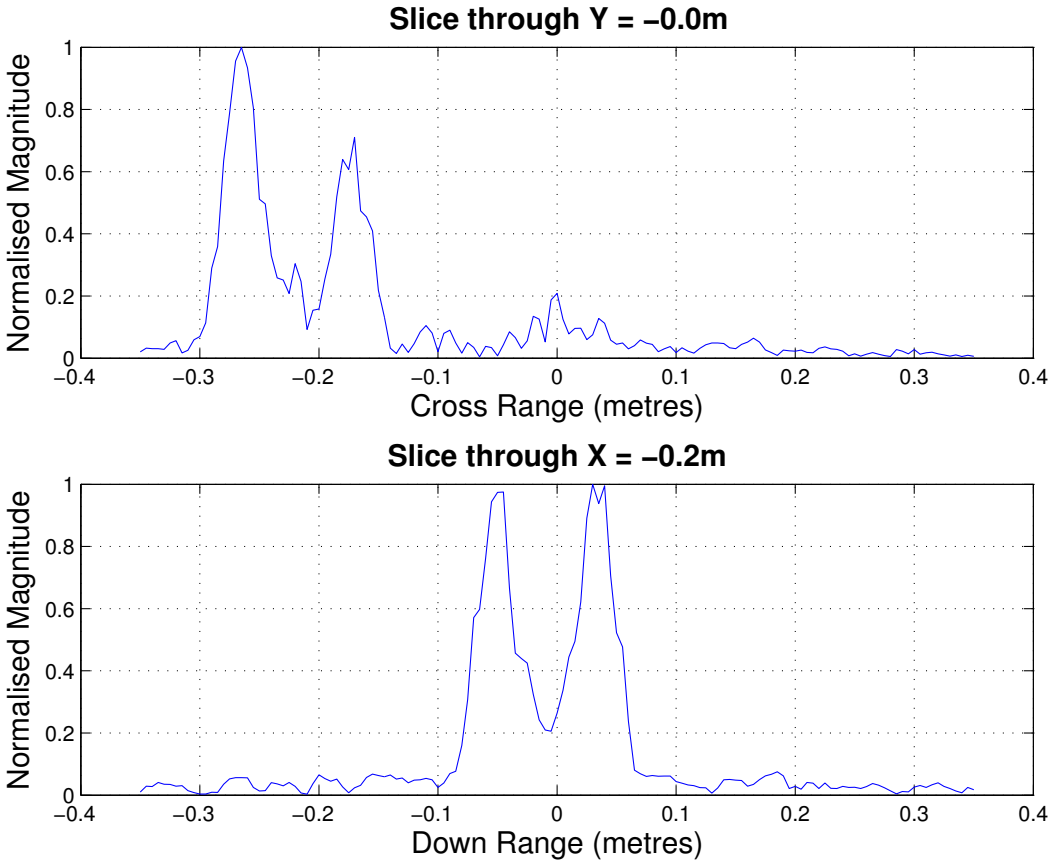

Figure 5.15: Cut through brightest point in reconstructed scene

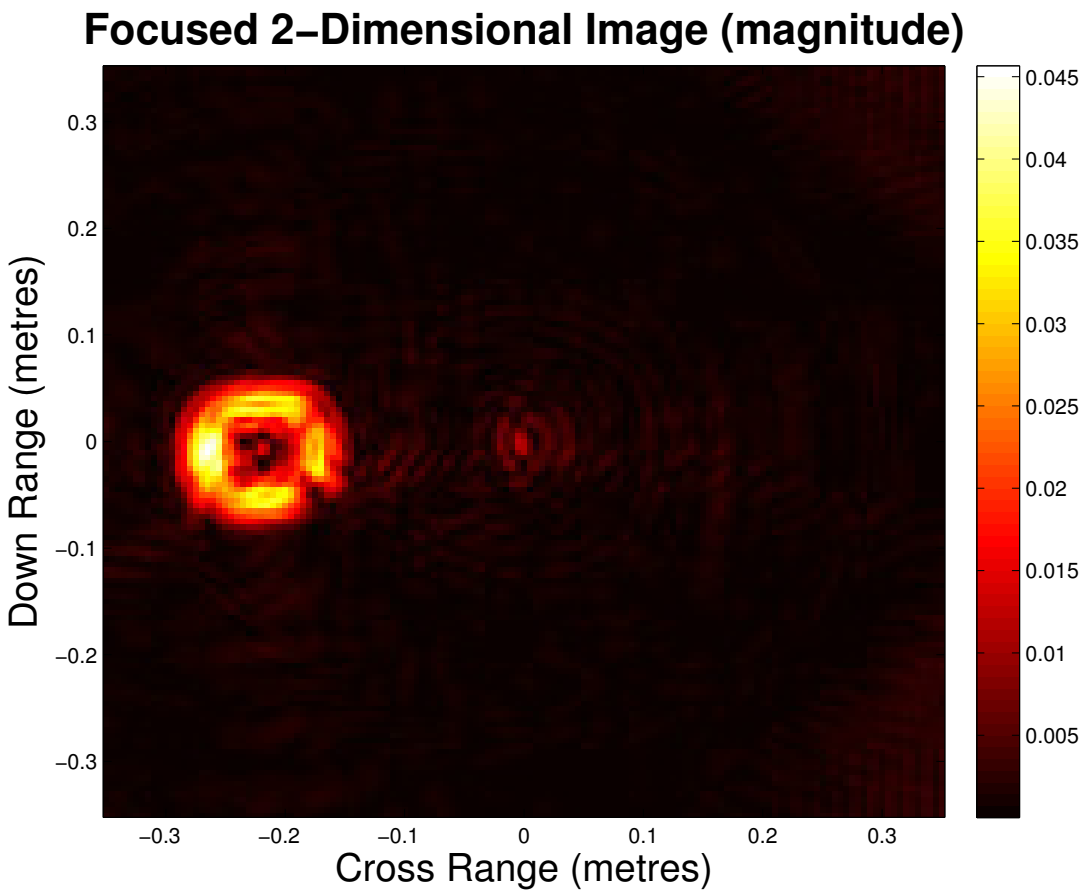

(a) 2D reconstructed image of scene

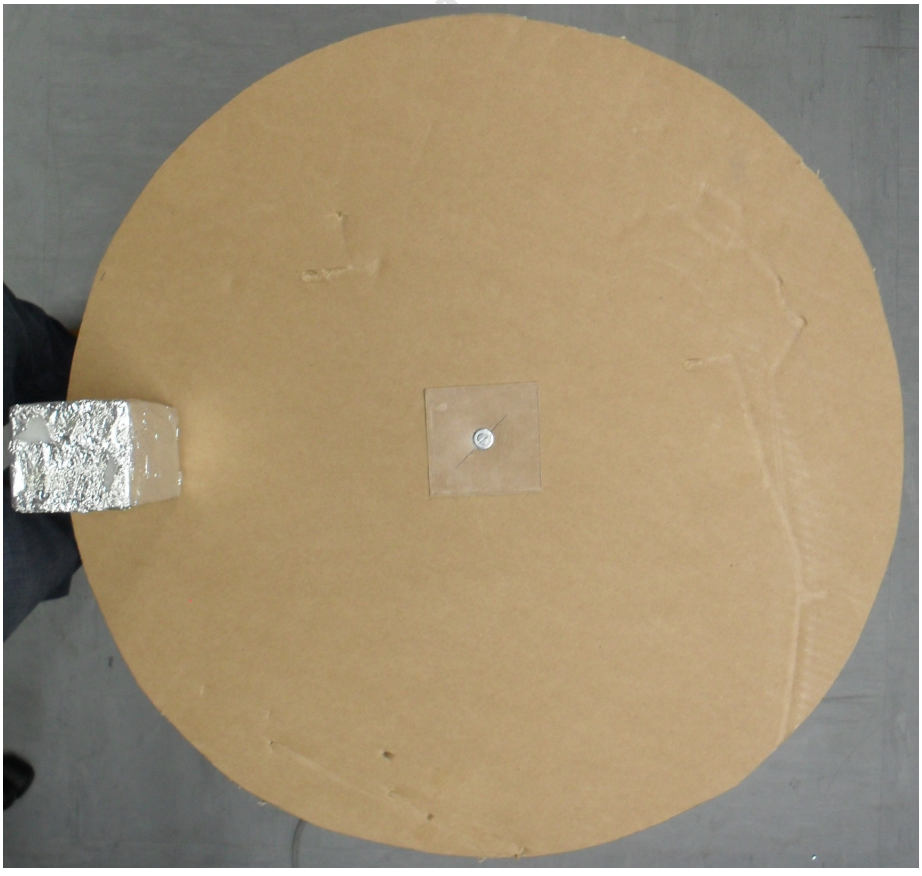

(b) Top view photograph of scene

Figure 5.16: 2D reconstructed image of scene and top view photograph of scene

5.1.3 Single Rectangular Shaped Target

In this experiment one rectangular shaped target wrapped in foil was placed on the rotating pedestal. The dimensions of this target was $length = 31.5\,cm$, $width = 4\,cm$ and $height = 22.5\,cm$. The location of the target can be seen in Figure 5.17.

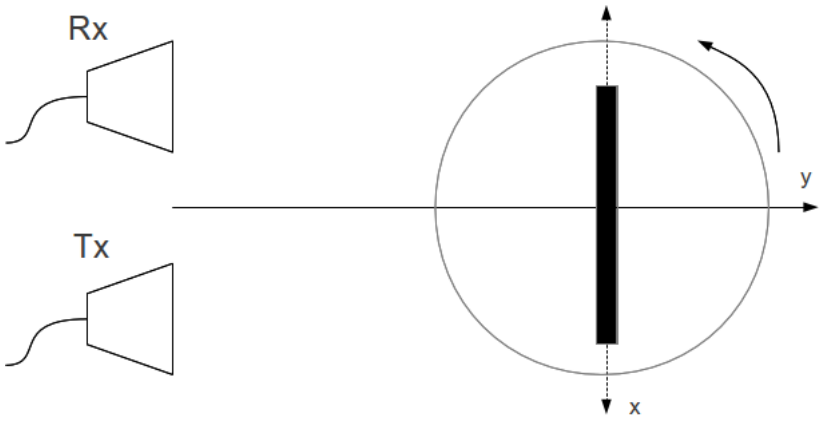

(a) Diagram of experiment scene

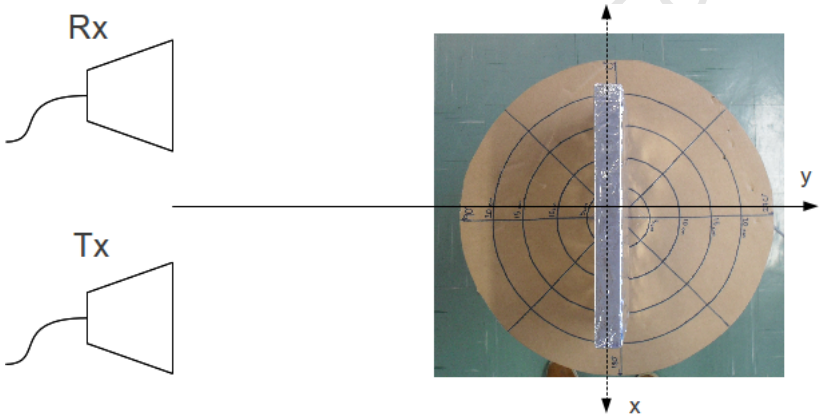

(b) Top view photograph of scene

Figure 5.17: Diagram and photograph of the experiment for a single rectangular shaped target

(a) Front view

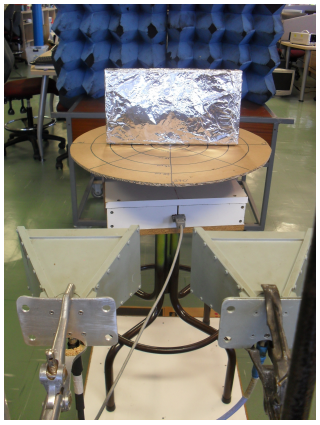

(b) Rear view

Figure 5.18: Photograph of scene for single rectangle shaped target

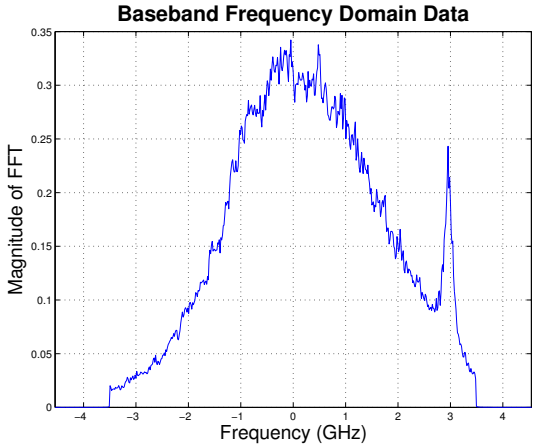

(a) Baseband frequency domain data

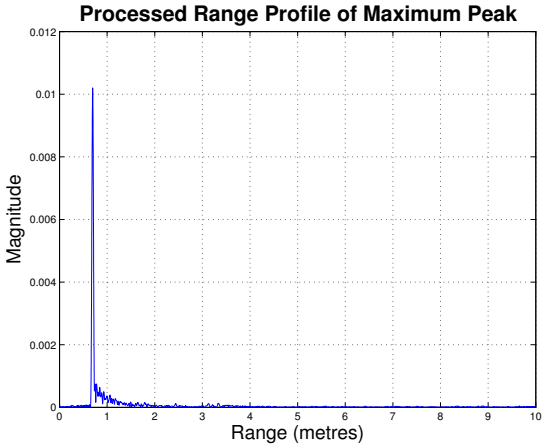

(b) Processed range profile up to maximum range

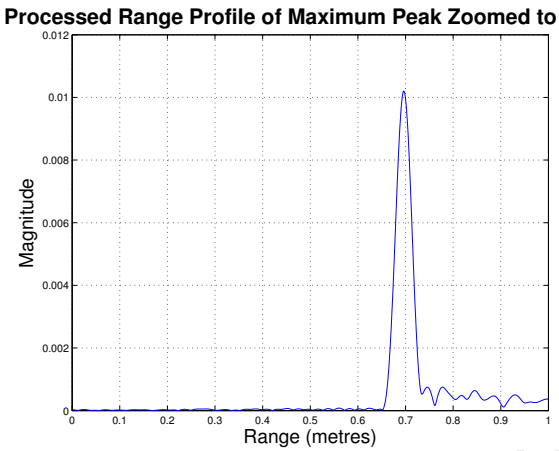

(c) Processed range profile zoomed to 0-1 m

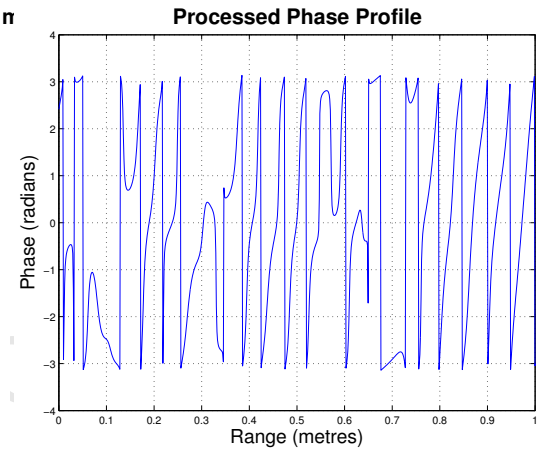

(d) Processed phase profile zoomed to 0-1 m

Figure 5.19: Frequency and time domain data for single rectangular shaped target

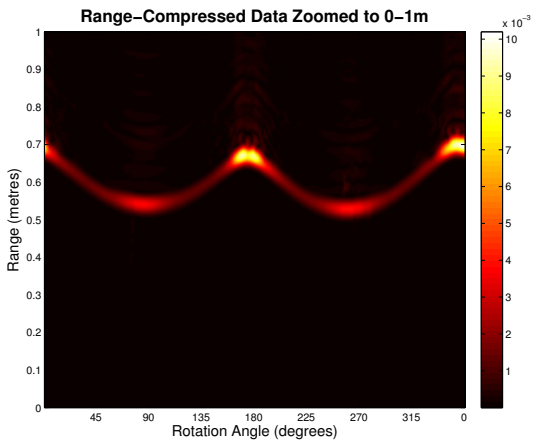

(a) Range compressed data/locus of target

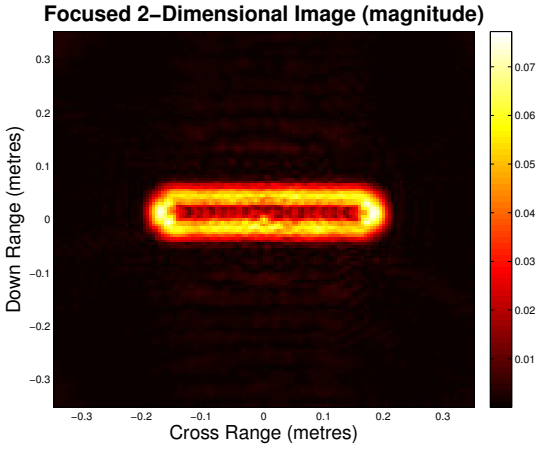

(b) 2D reconstructed image of scene

Figure 5.20: Locus of target and reconstructed image of scene for single rectangular shaped target

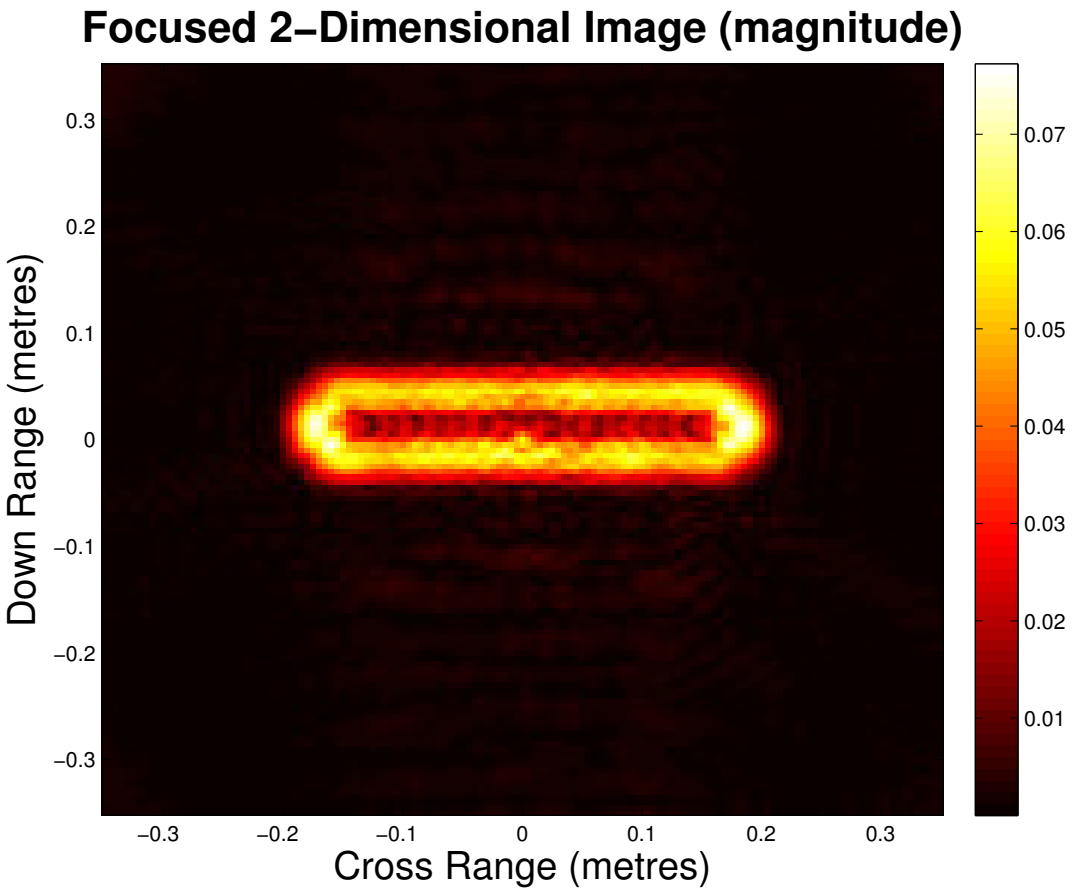

(a) 2D reconstructed image of scene

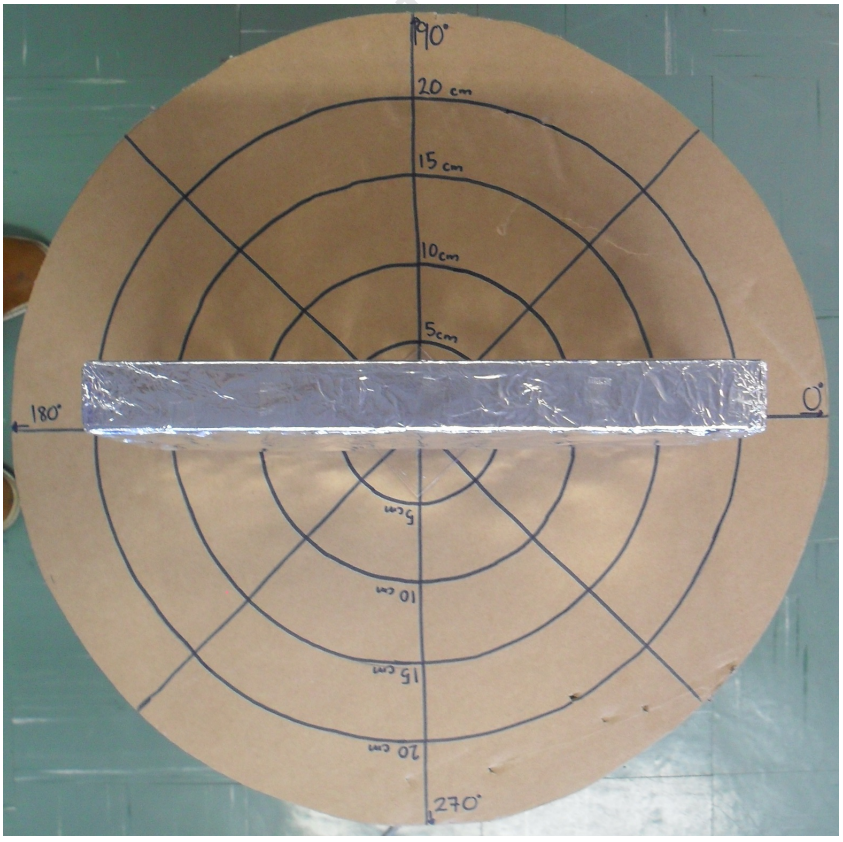

(b) Top view photograph of scene

Figure 5.21: 2D reconstructed image of scene and top view photograph of scene

5.1.4 Multiple Cylindrically Shaped Targets

In this experiment three cylindrically shaped targets wrapped in foil were used. These have dimensions of $diameter = 4\,cm$ and $height = 10\,cm$. The location of the target can be seen in Figure 5.22.

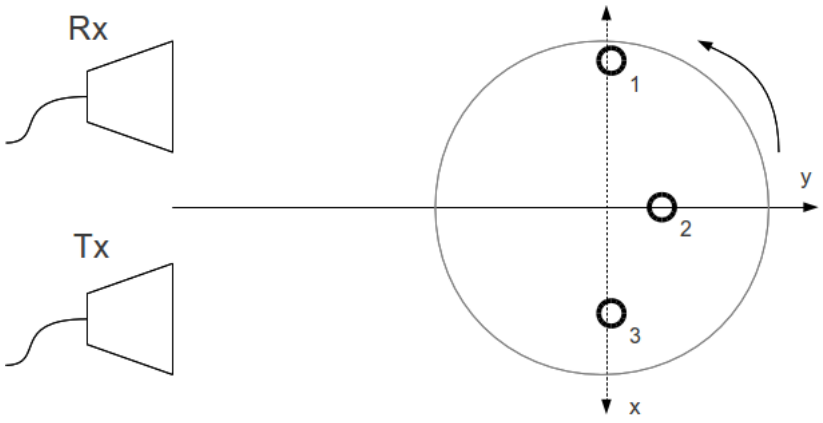

(a) Diagram of experiment scene

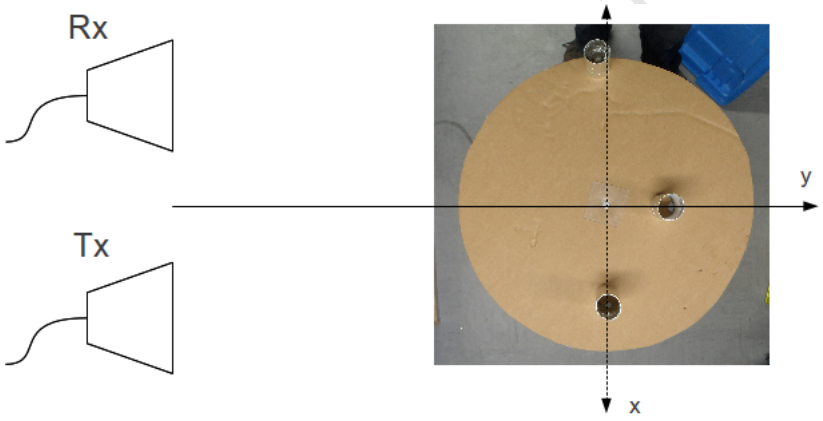

(b) Top view photograph of scene

Figure 5.22: Diagram and photograph of the experiment for multiple cylindrically shaped targets

(a) Front view

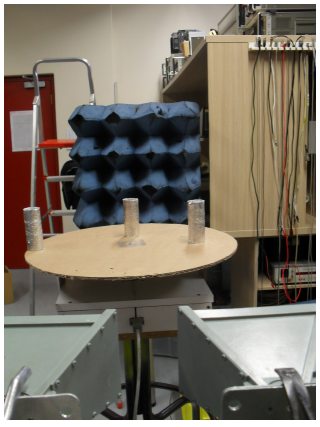

(b) Rear view

Figure 5.23: Photograph of experiment for multiple cylindrically shaped targets

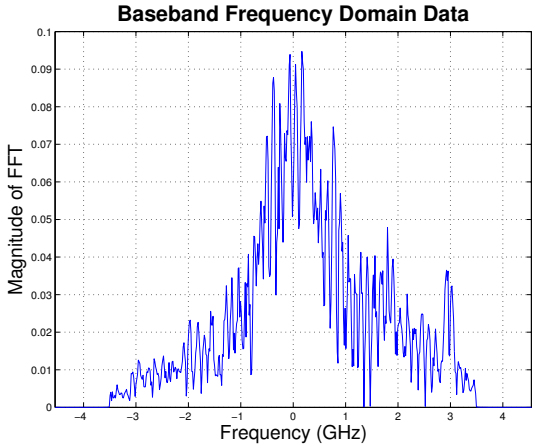

(a) Baseband frequency domain data

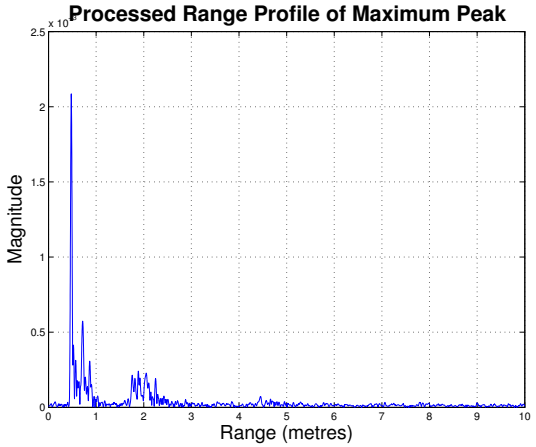

(b) Processed range profile up to maximum range

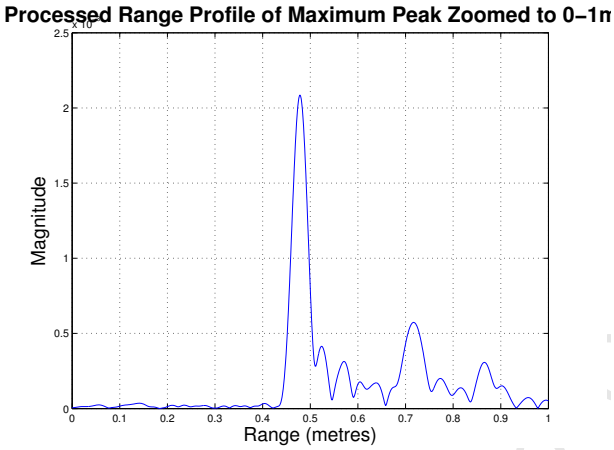

(c) Processed range profile

(d) Processed phase profile

Figure 5.24: Frequency and time domain data for multiple cylindrically shaped targets

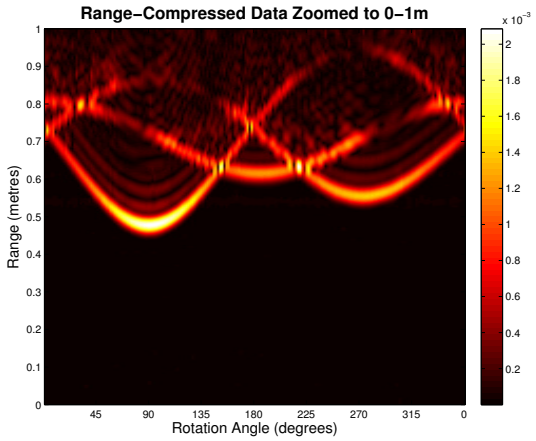

(a) Range compressed data/locus of target

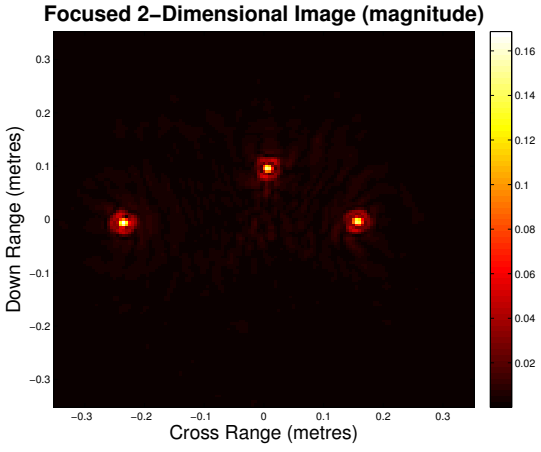

(b) 2D reconstructed image of scene

Figure 5.25: Locus of target and reconstructed image of scene for multiple cylindrically shaped targets

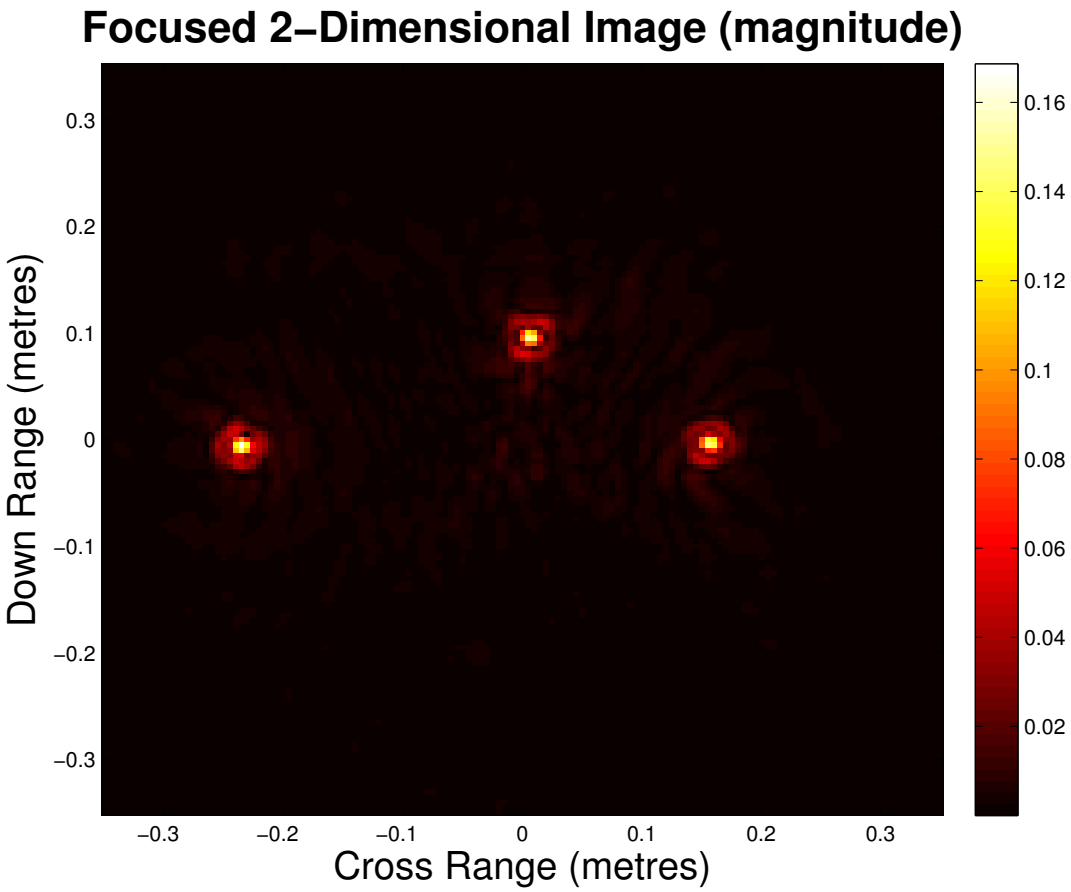

(a) 2D reconstructed image of scene

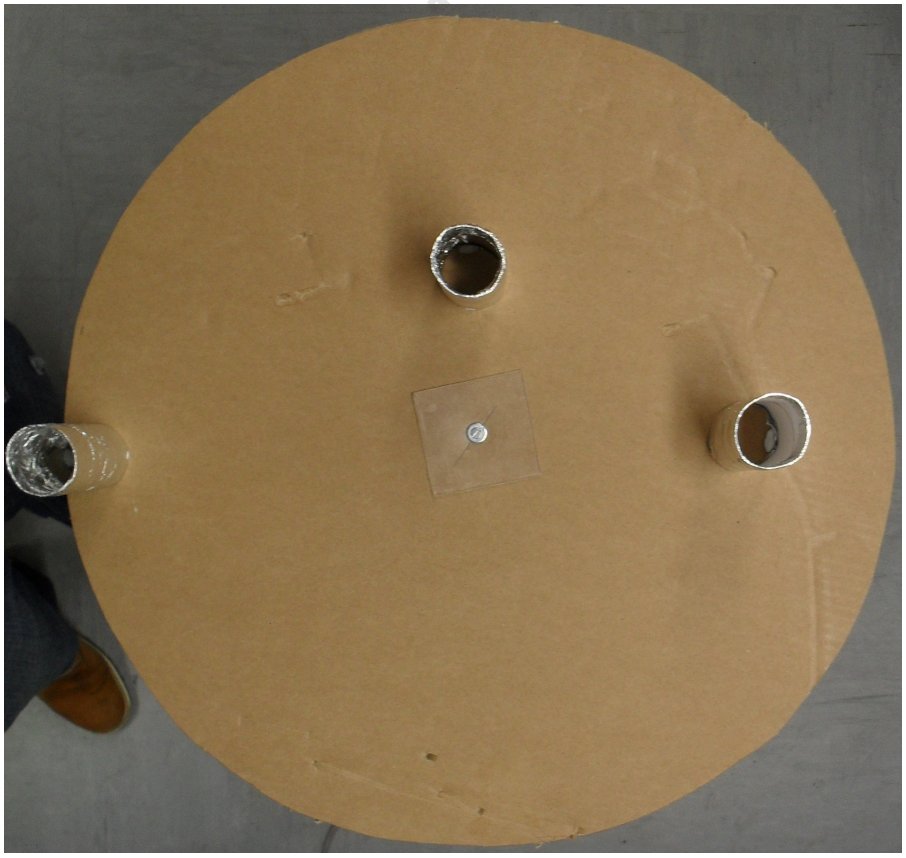

(b) Top view photograph of scene

Figure 5.26: 2D reconstructed image of scene and top view photograph of scene

5.1.5 Multiple Targets with Various Shapes

In this experiment three targets with different shapes were used. The dimensions of these targets are the same as those used in the previous experiments. The shapes and location of the targets can be seen in Figure 5.27.

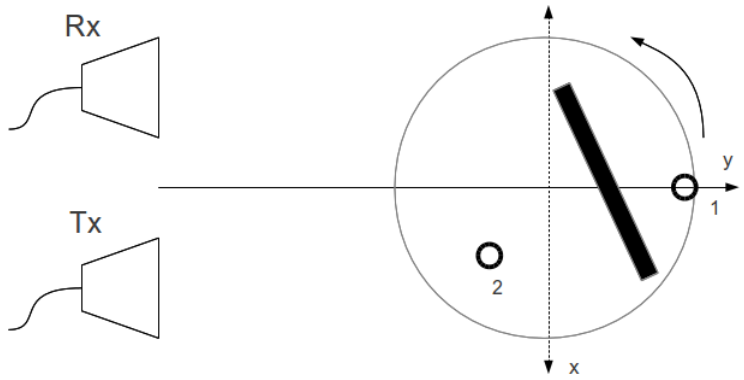

(a) Diagram of experiment scene

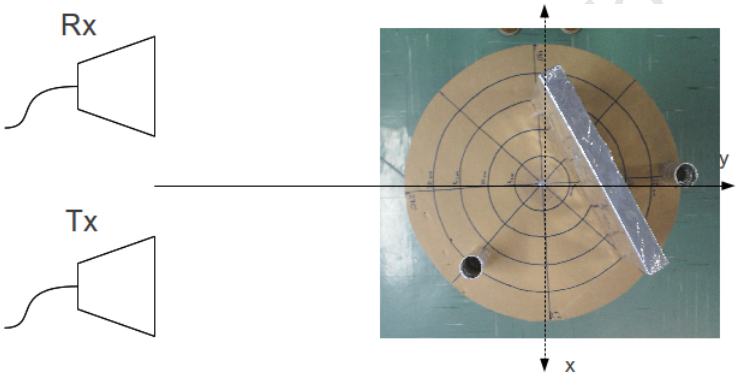

(b) Top view photograph of scene

Figure 5.27: Diagram and photograph of the experiment for multiple various shaped targets

(a) Front view

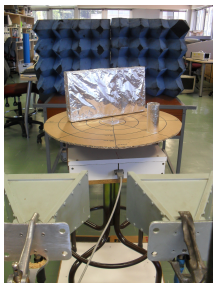

(b) Rear view

Figure 5.28: Photograph of experiment for multiple various shaped targets

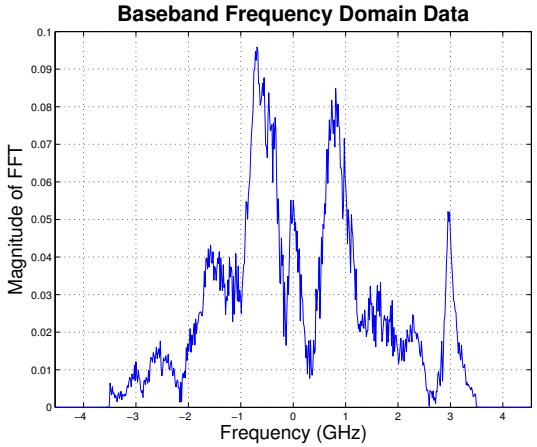

(a) Baseband frequency domain data

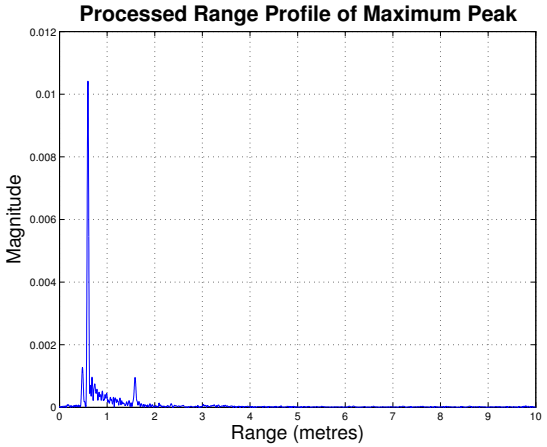

(b) Processed range profile up to maximum range

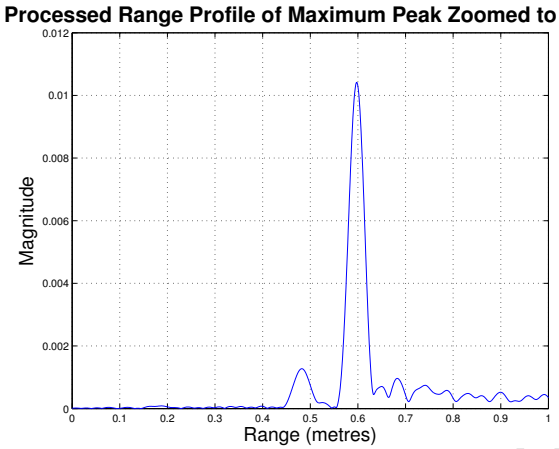

(c) Processed range profile Zoomed to 0-1 m

(d) Processed phase profile Zoomed to 0-1 m

Figure 5.29: Frequency and time domain data for multiple various shaped targets

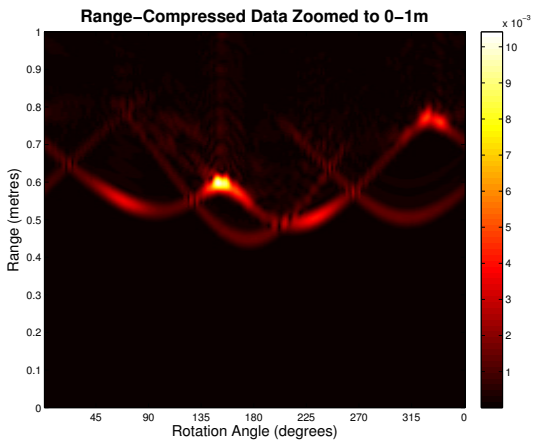

(a) Range compressed data/locus of target

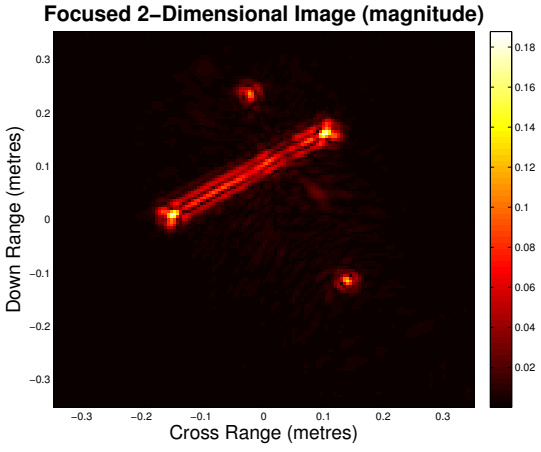

(b) 2D reconstructed image of scene

Figure 5.30: Locus of target and reconstructed image of scene for multiple various shaped targets

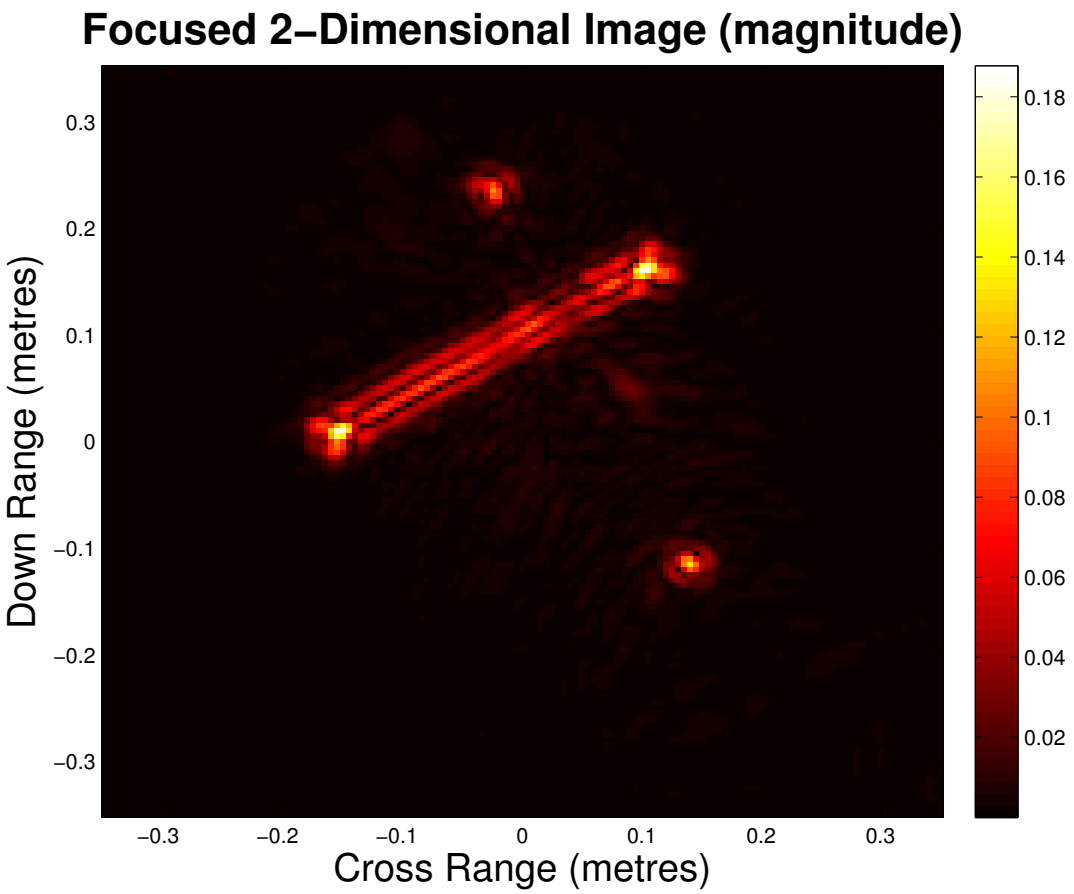

(a) 2D reconstructed image of scene

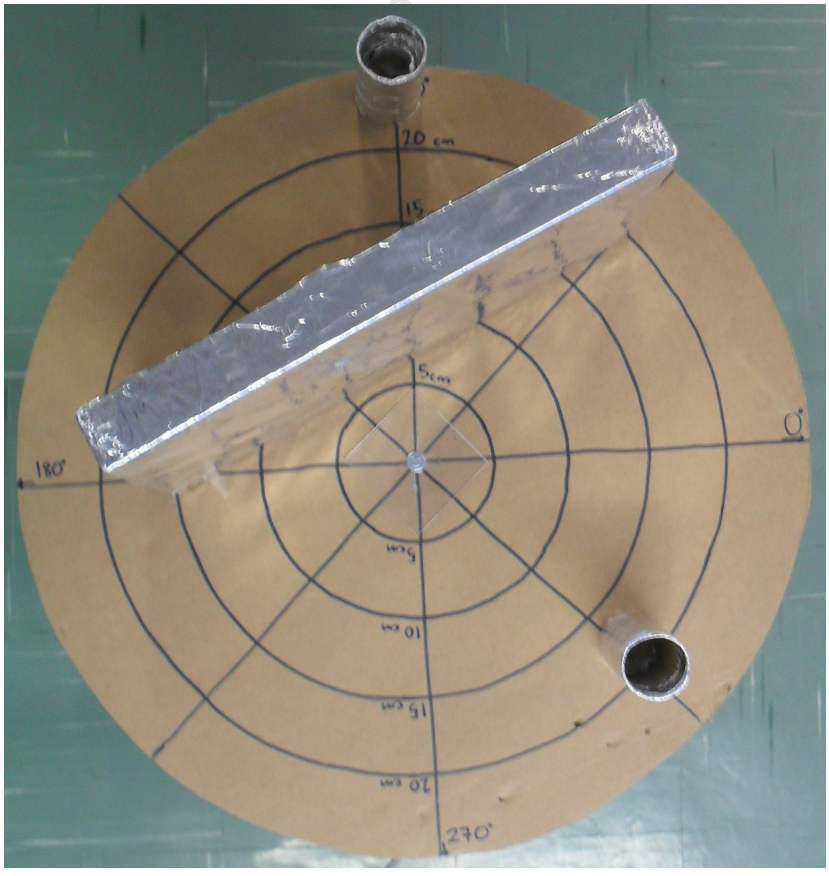

(b) Top view photograph of scene

Figure 5.31: 2D reconstructed image of scene and top view photograph of scene

In this experiment multiple targets with different shapes were used. The shapes and location of the targets can be seen in Figure 5.32a.

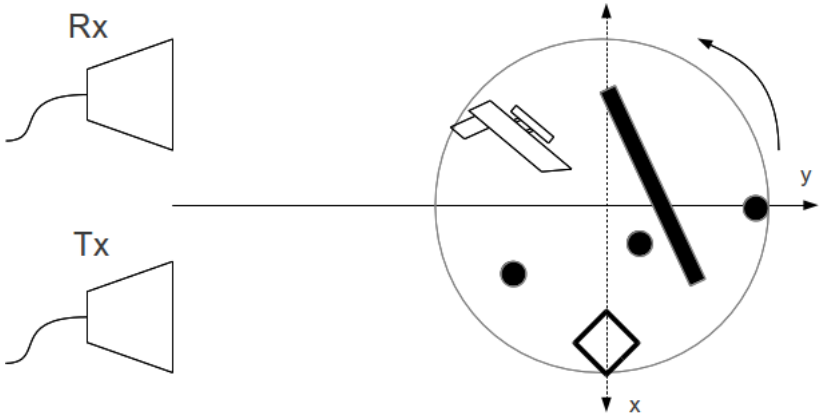

(a) Diagram of experiment scene

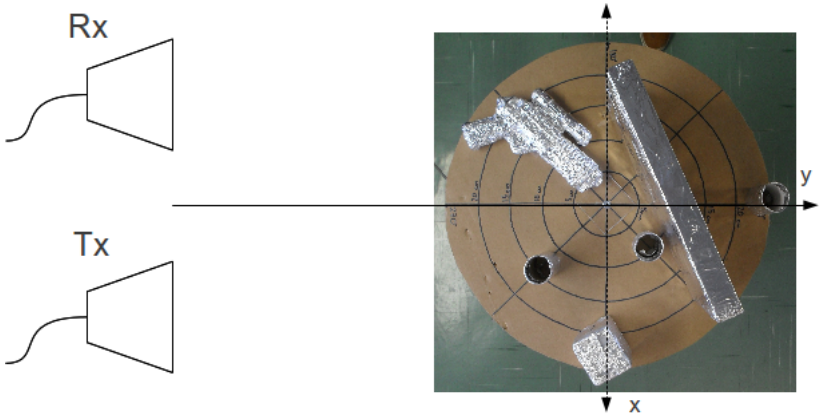

(b) Top view photograph of scene

Figure 5.32: Diagram and photograph of the experiment for multiple various shaped targets

(a) Photograph of the scene from the front of the antennas

(b) Photograph of the scene from behind the antennas

Figure 5.33: Diagam showing the setup of the experiment and position of multiple various shaped targets

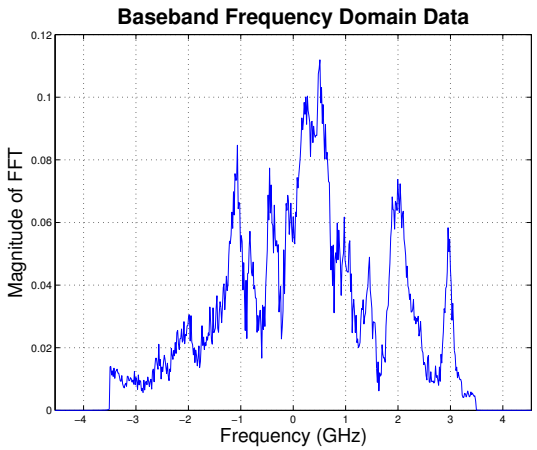

(a) Baseband frequency domain data

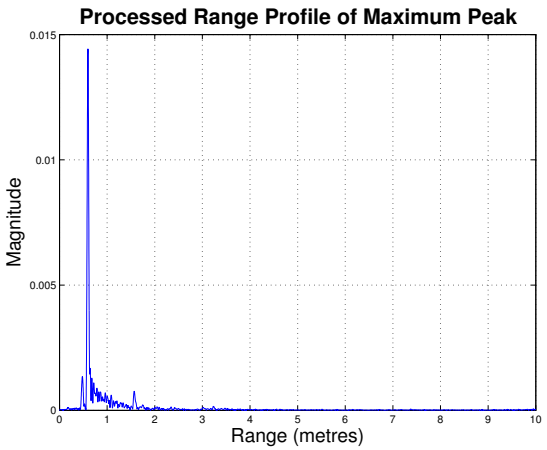

(b) Processed range profile up to maximum range

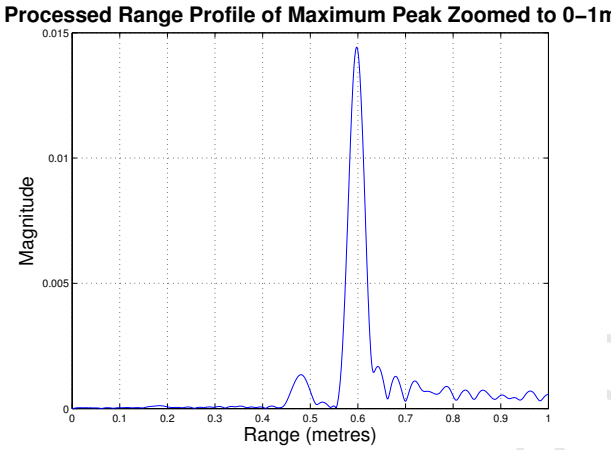

(c) Processed range profile zoomed to 0-1 m

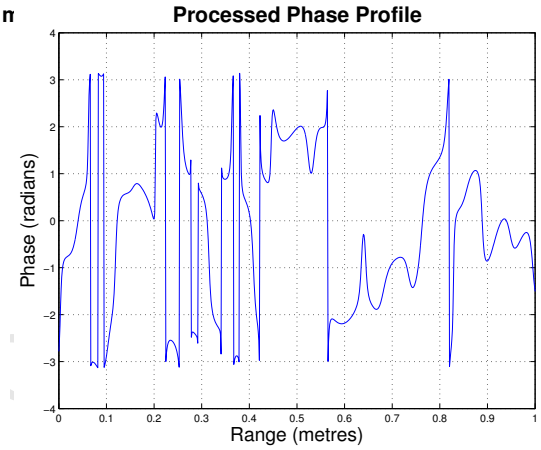

(d) Processed phase profile zoomed to 0-1 m

Figure 5.34: Frequency and time domain data for for multiple various shaped targets

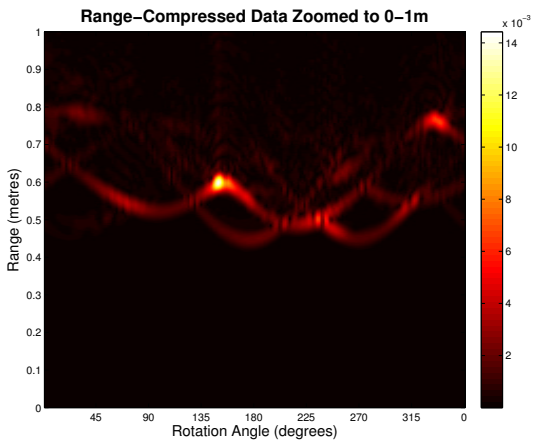

(a) Range compressed data/locus of target

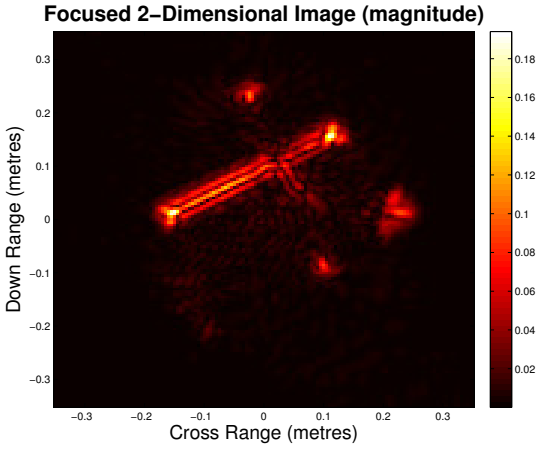

(b) 2D reconstructed image of scene

Figure 5.35: Locus of target and reconstructed image of scene for for multiple various shaped targets

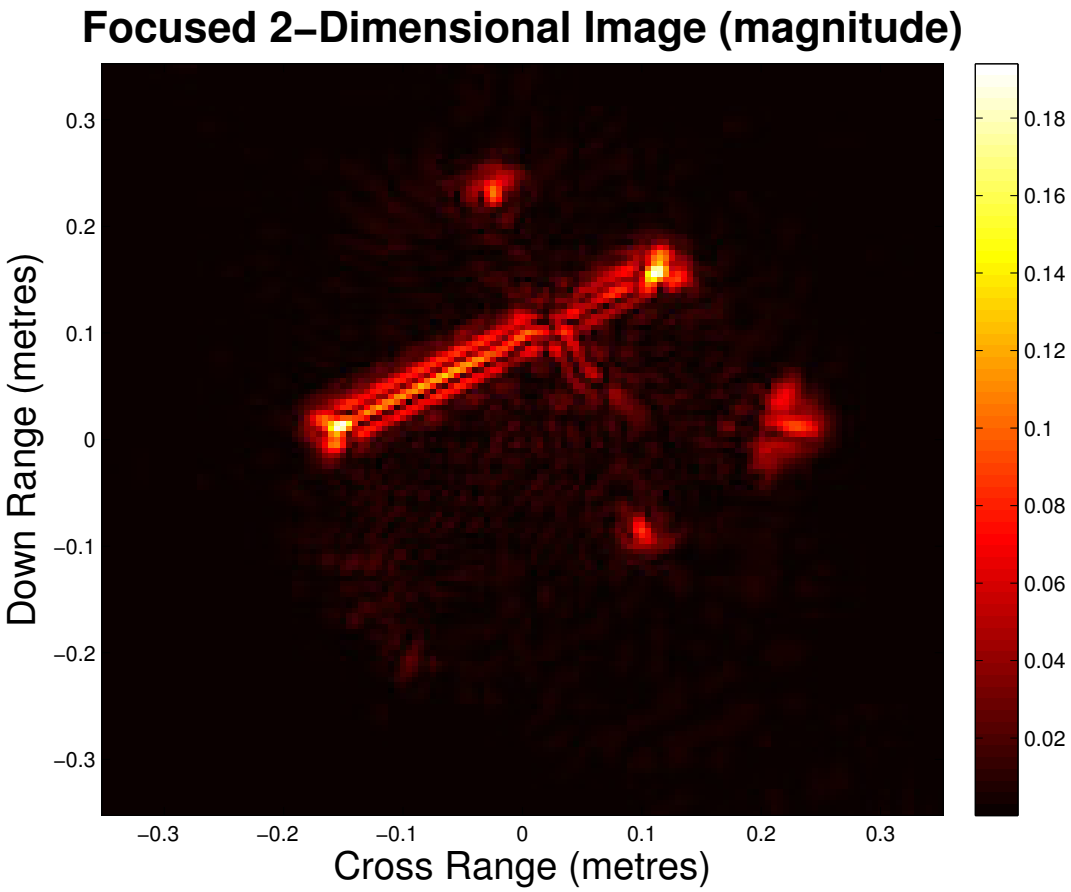

(a) 2D reconstructed image of scene

(b) Top view photograph of scene

Figure 5.36: 2D reconstructed image of scene and top view photograph of scene

5.1.6 Complex Target

In this experiment three complex targets, 3-pin plugs, were used as targets. The dimensions of the pins were $diameter = 0.9\,cm$ and $height = 3\,cm$ for the longer pin and $diameter = 0.7\,cm$ and $height = 2\,cm$ for the two smaller pins. The shapes and location of the targets can be seen in Figure 5.37.

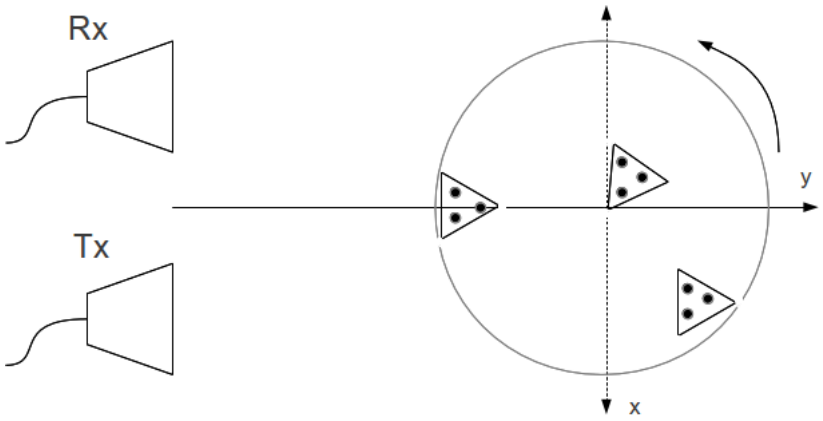

(a) Diagram of experiment scene

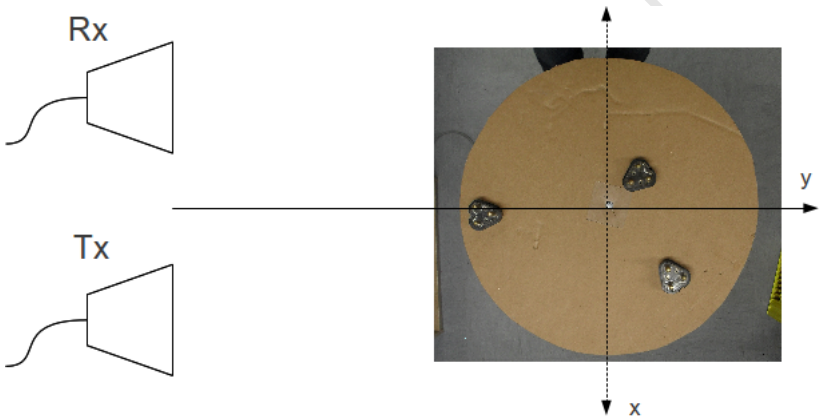

(b) Top view photograph of scene

Figure 5.37: Diagram and photograph of the experiment for multiple complex targets

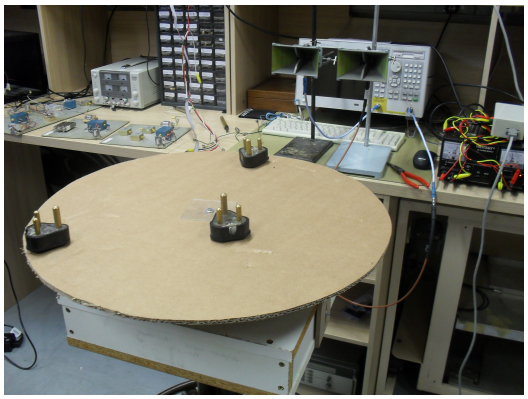

(a) Photograph of the scene from the front of the antennas

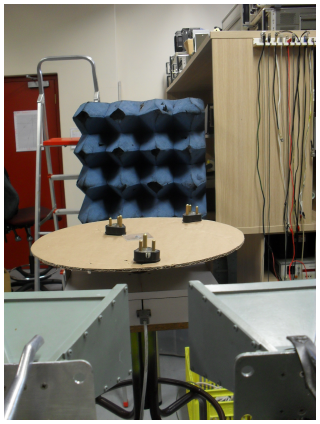

(b) Photograph of the scene from behind the antennas

Figure 5.38: Photograph of experiment for multiple complex targets

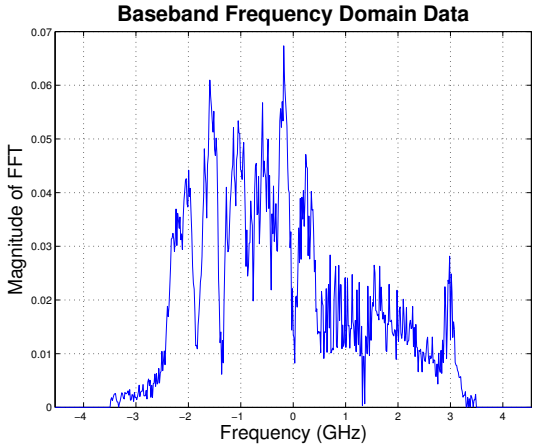

(a) Baseband frequency domain data

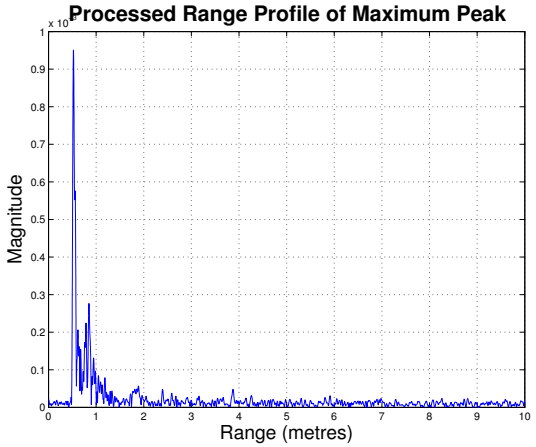

(b) Processed range profile up to maximum range

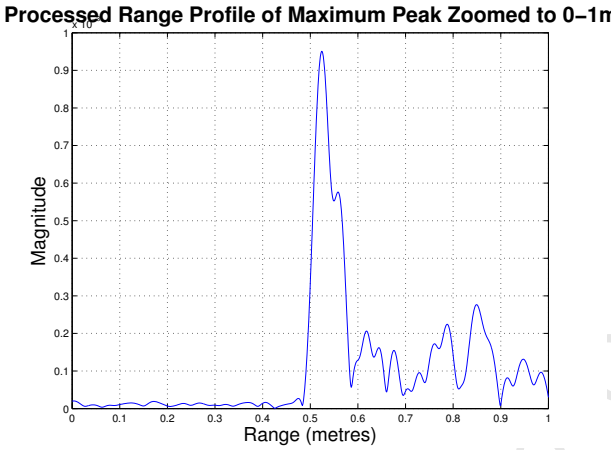

(c) Processed range profile zoomed to 0-1 m

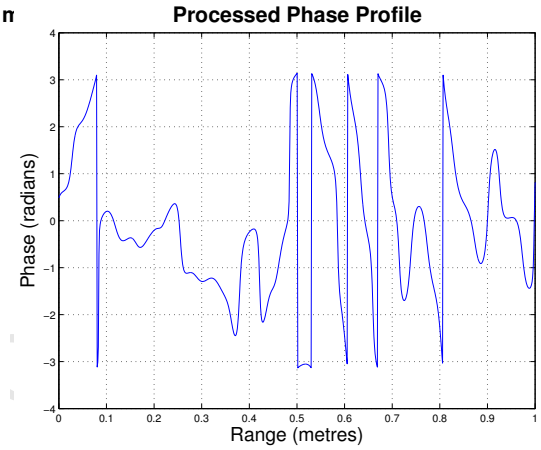

(d) Processed phase profile zoomed to 0-1 m

Figure 5.39: Frequency and time domain data for multiple complex targets

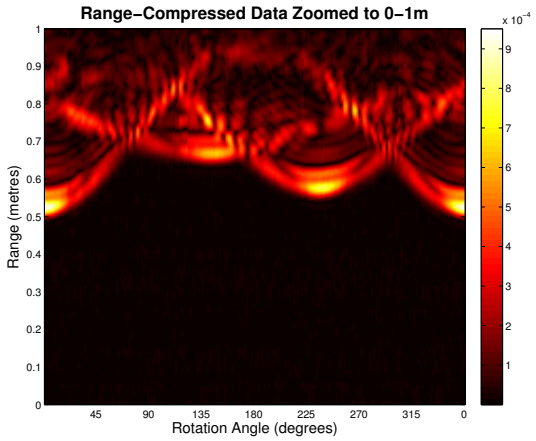

(a) Range compressed data/locus of target

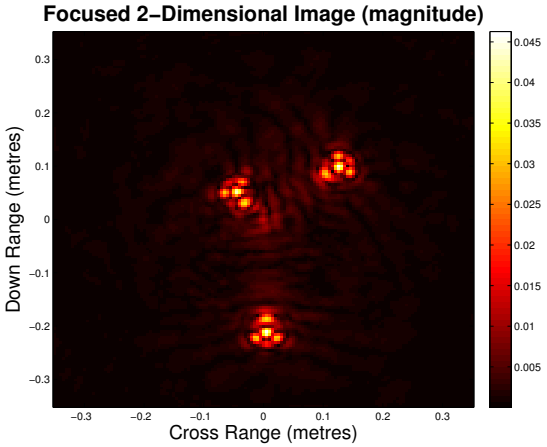

(b) 2D reconstructed image of scene

Figure 5.40: Locus of target and reconstructed image of scene for multiple complex targets

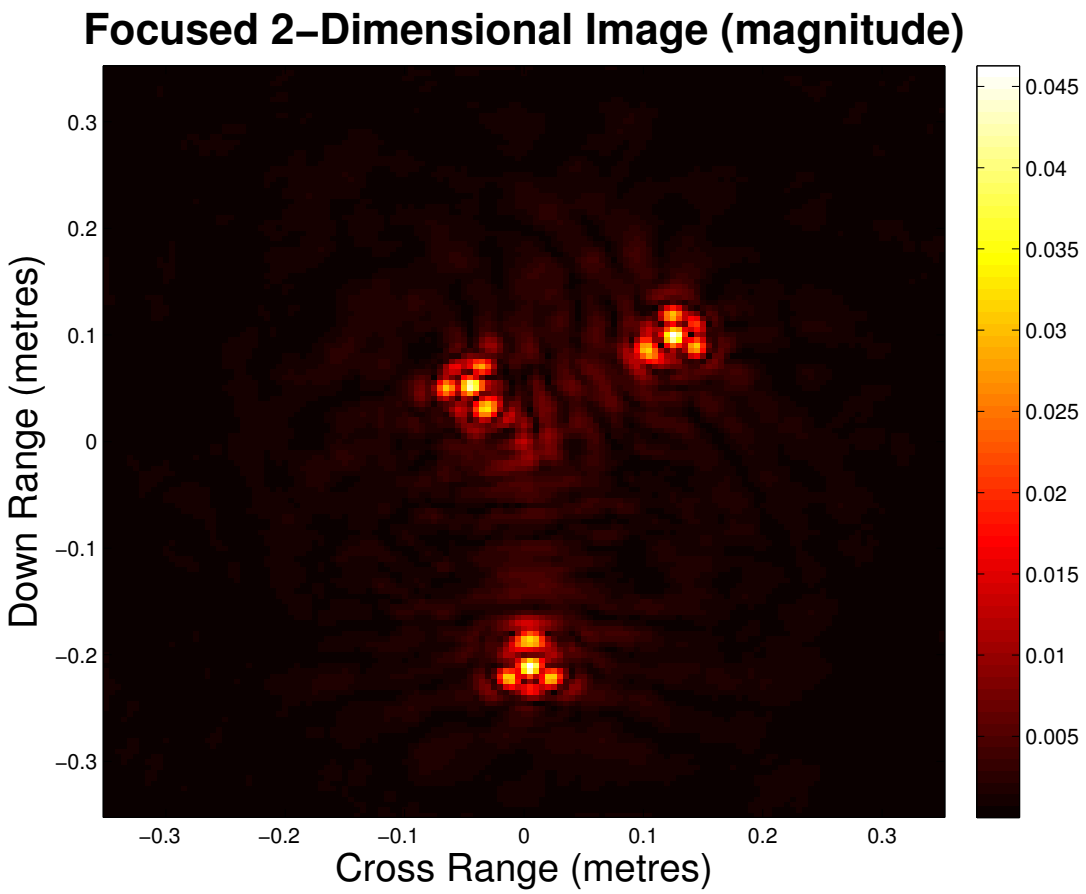

(a) 2D reconstructed image of scene

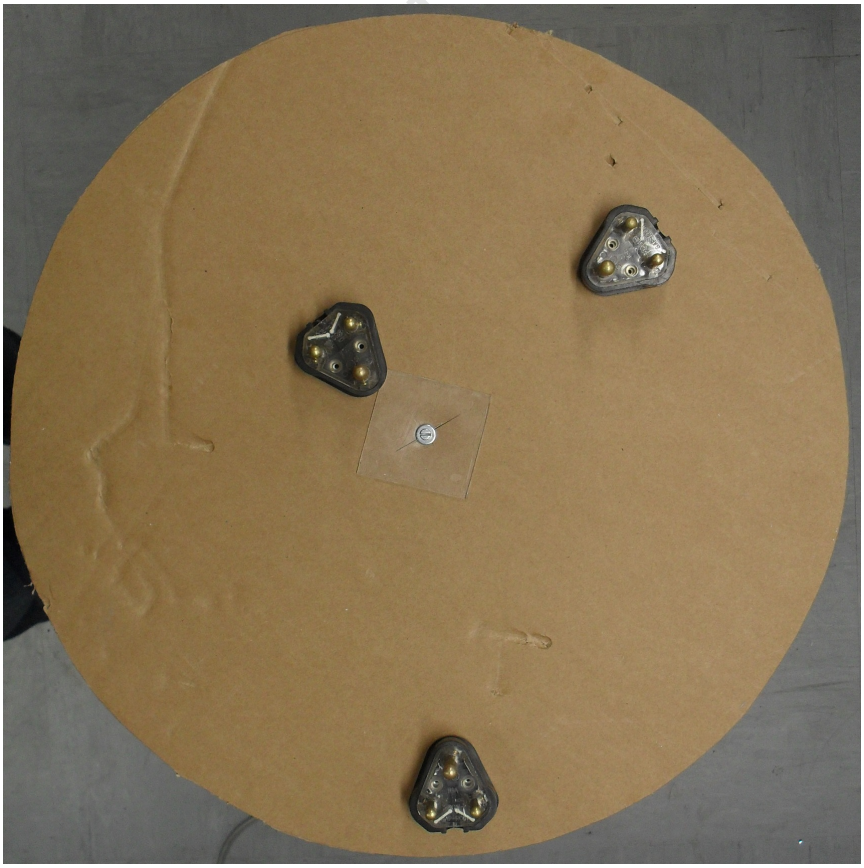

(b) Top view photograph of scene

Figure 5.41: 2D reconstructed image of scene and top view photograph of scene

In this experiment a complex target, plastic toy gun along with a thin wire wrapped in foil, was used as targets. The dimensions of the wire is the same as mentioned previously and the dimensions of the gun were $barrel = 20.5\,cm$, $hand - grip = 11.5\,cm$, $scope\ length = 11.5\,cm$ and $width = 3\,cm$.

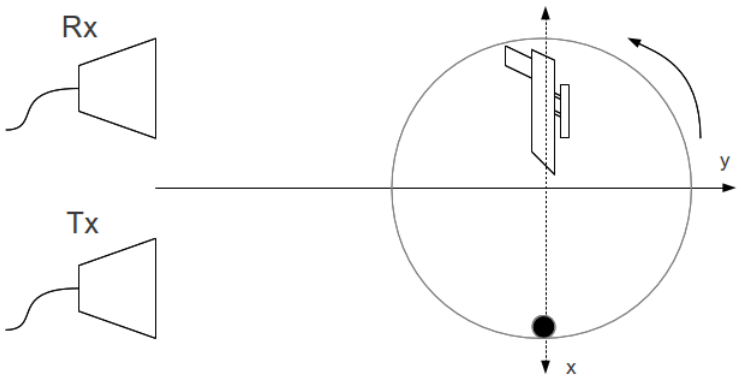

(a) Diagram of experiment scene

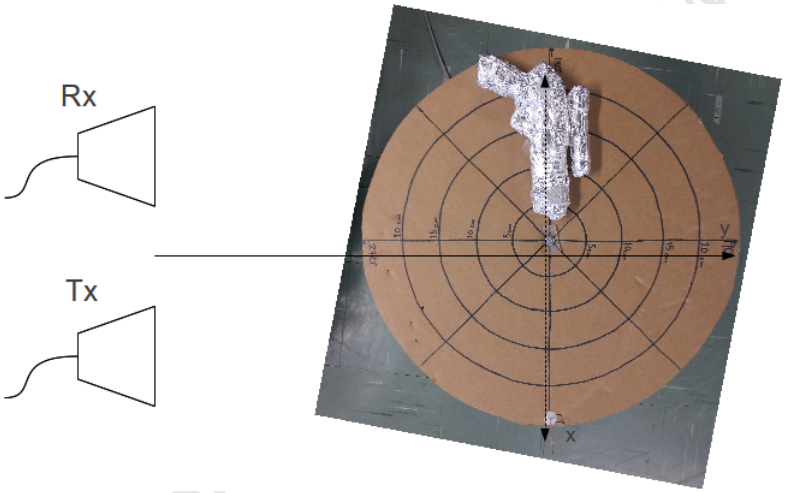

(b) Top view photograph of scene

Figure 5.42: Diagram and photograph of the experiment for multiple complex targets

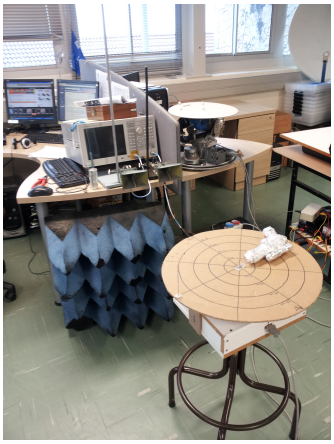

Figure 5.43: Photograph of the scene from the front of the antennas

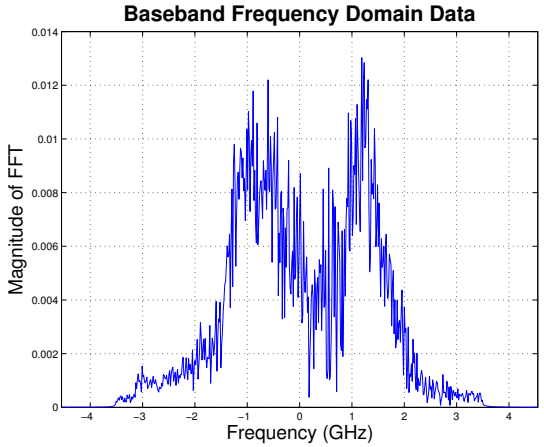

(a) Baseband frequency domain data

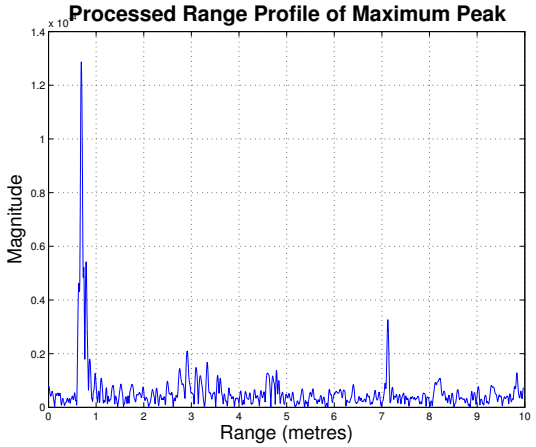

(b) Processed range profile up to maximum range

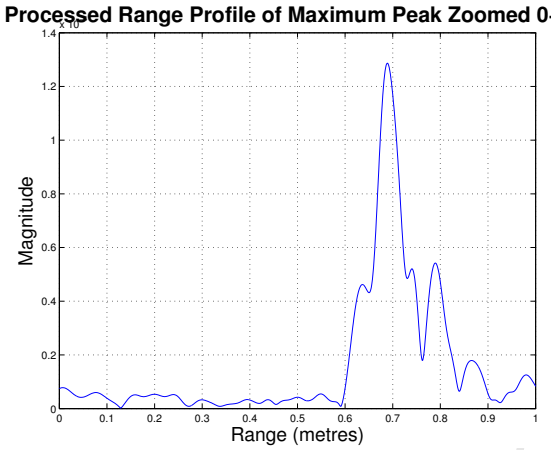

(c) Processed range profile zoomed to 0-1 m

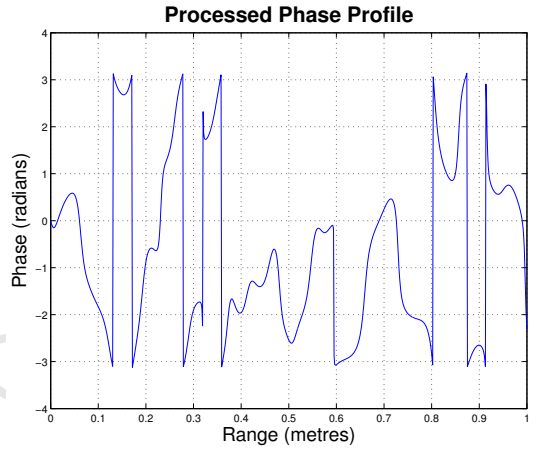

(d) Processed phase profile zoomed to 0-1 m

Figure 5.44: Frequency and time domain data for multiple complex targets

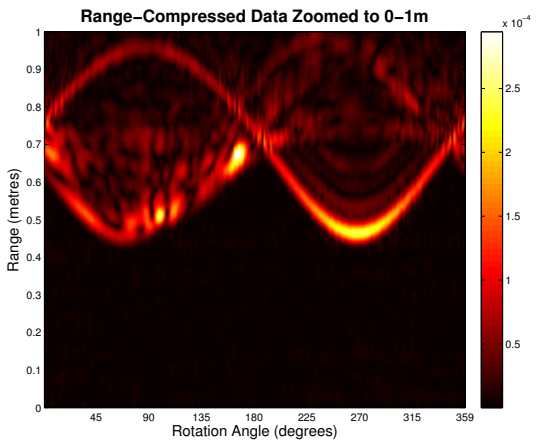

(a) Range compressed data/locus of target

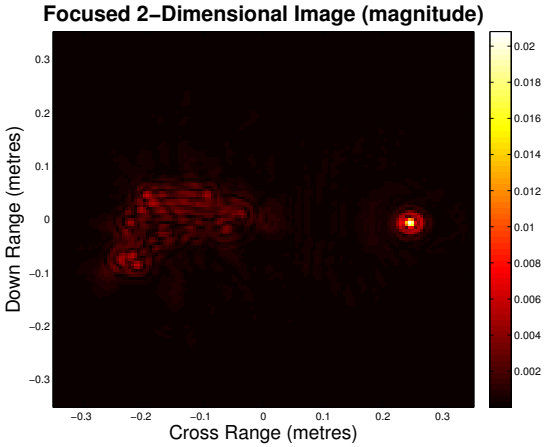

(b) 2D reconstructed image of scene

Figure 5.45: Locus of target and reconstructed image of scene for multiple complex targets

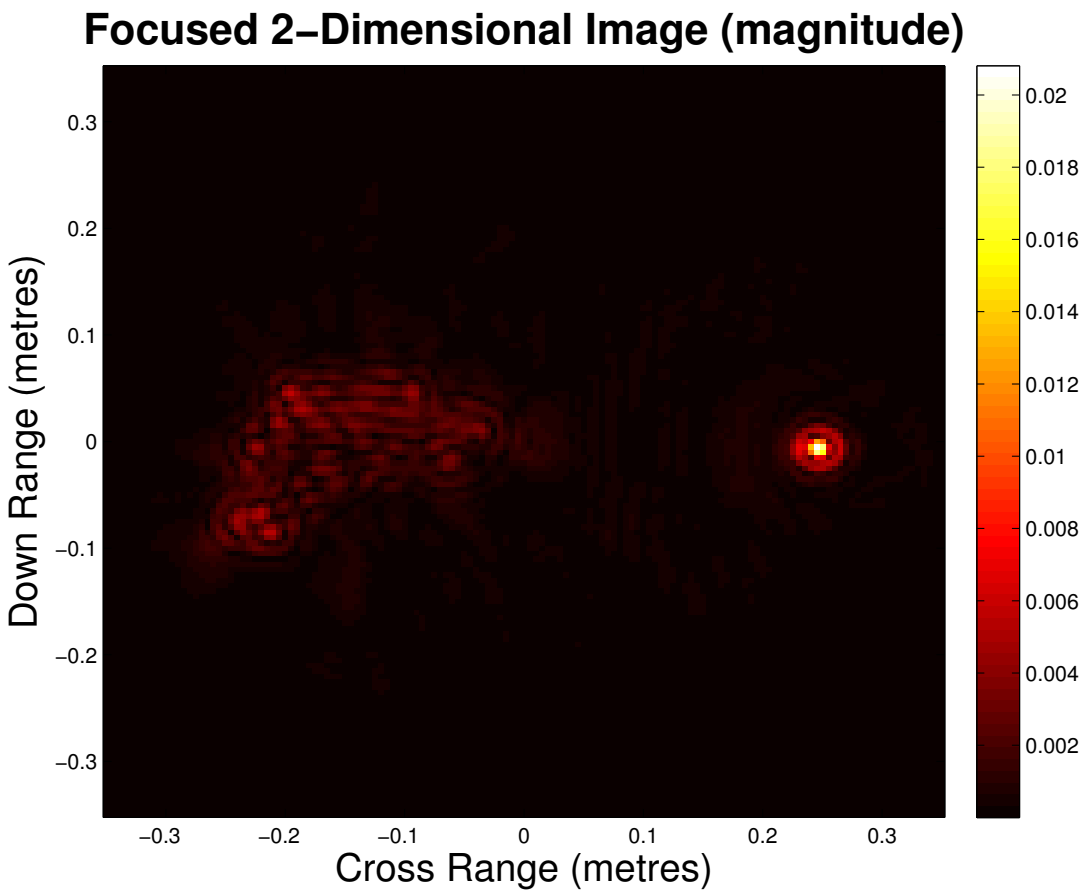

(a) 2D reconstructed image of scene

(b) Top view photograph of scene

Figure 5.46: 2D reconstructed image of scene and top view photograph of scene

The reflected echoes from the gun are much weaker than those of the surrounding targets, which makes the gun less visible in Figure 5.36a and Figure 5.46a.

5.2 3-Dimensional Experiment

After the 2D experiments were carried out successfully, it was decided that the experiments and reconstruction algorithm would be extended to 3D space. These experiments would make use of the 2-axis rotating pedestal. This pedestal is capable of rotating in both the azimuth and elevation direction. The information about this pedestal can be found in Chapter 3.3 and [26]. The experiments that would be carried out by the 2-axis rotating pedestal were similar to that of the 1-axis rotating pedestal. The user would specify the start and stop elevation angle, as well as the incremental elevation angle steps that would be taken to get from the start to the stop elevation angle. The user would also specify the start and stop azimuth angle and the incremental azimuth angle steps that would be taken to get from the start to the stop azimuth angle. The experimental setup with regards to the antenna location relative to the centre of rotation and the other parameters were set up in the same way as for the 2D experiments.

From the simulations in Chapter 4 it was concluded that in order to reconstruct a clear image of the scene the viewing angle of the antennas should be a minimum of 30 degrees. From the calculations of the synthesized aperture sampling it was determined that an angular increment of 4 degrees or less would not introduce any ambiguity with regards to the position of the pedestal. The time it would take for the experiment to be complete would depend on the start and stop angle in both the elevation and azimuth direction as well as the angular increment. For this reason it was decided to allow for a 30 degree viewing angle of the targets in both the azimuth and elevation direction, with an angular increment of 2 degrees. The angular positions are as follows:

- Start azimuth angle = 255 degrees
- Stop azimuth angle = 285 degrees
- Angular increment = 2 degrees
- Start elevation angle = -15 degrees
- Stop elevation angle = 15 degrees
- Angular increment = 2 degrees

The coordinates of the targets are indicated relative to the centre of rotation.

5.2.1 Single Point Target

In this experiment a piece of aluminum foil was rolled up into a small ball, with $diameter = 1.5\,cm$ (smaller than down range resolution, $2.86\,cm$, of the system as well as the wavelength, $\lambda = 3.5\,cm$, of the highest frequency of $8.5\,GHz$), so that it would represent a point target. This was then placed on the rotating pedestal. The target was located at the following position:

- Target coordinates in metres (x,y,z) = (0.2,0,0)

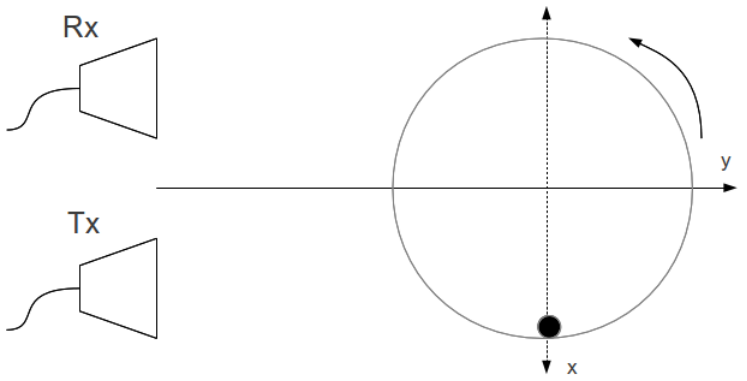

(a) Diagram of experiment scene

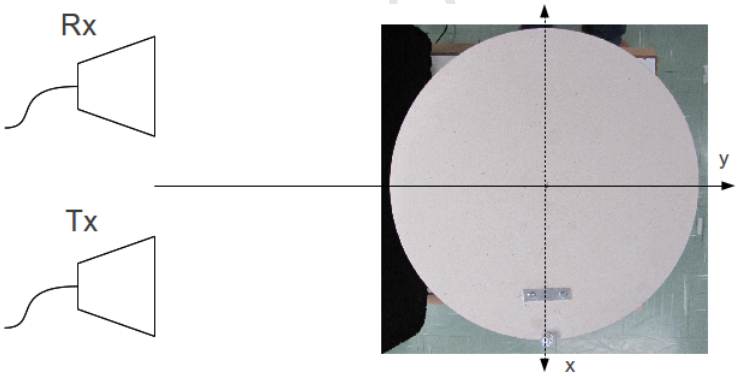

(b) Top view photograph of scene

Figure 5.47: Diagram and photograph of the experiment for a single point target

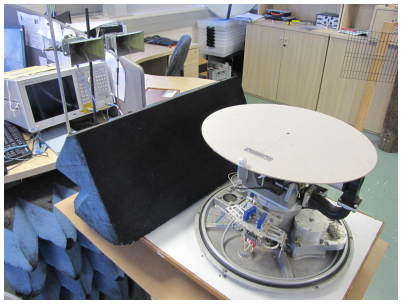

(a) Front view

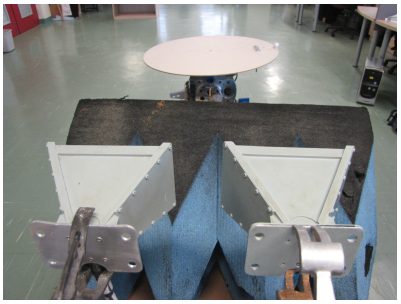

(b) Rear view

Figure 5.48: Photograph of scene for single point target

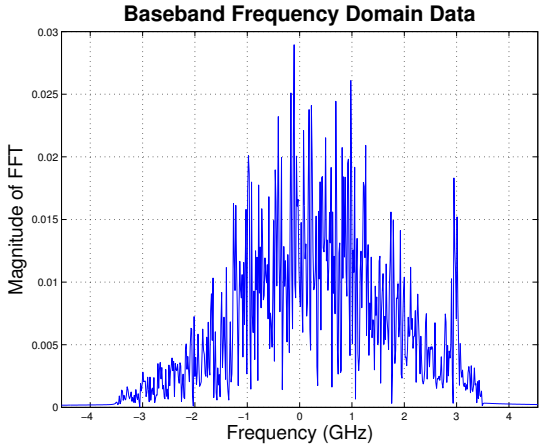

(a) Baseband frequency domain data

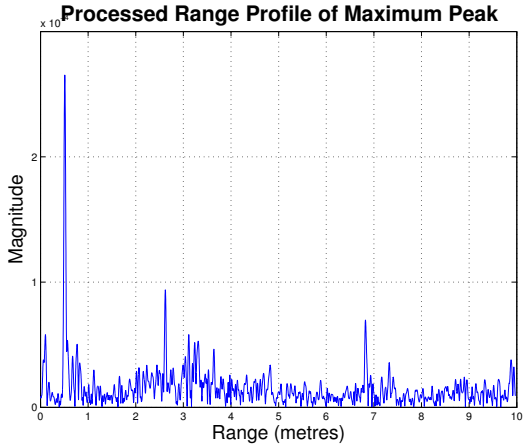

(b) Processed range profile Over Full Imaging Range

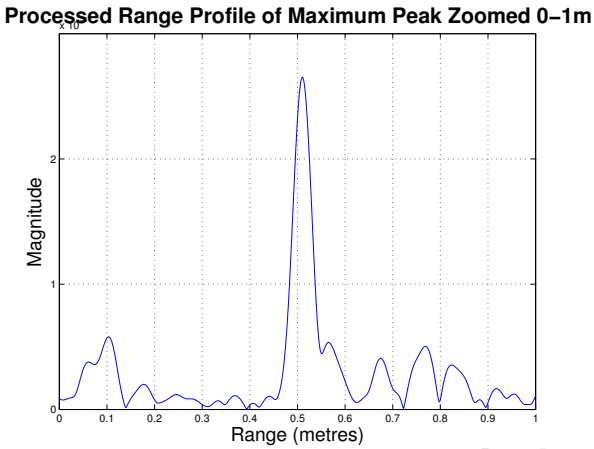

(c) Processed range profile

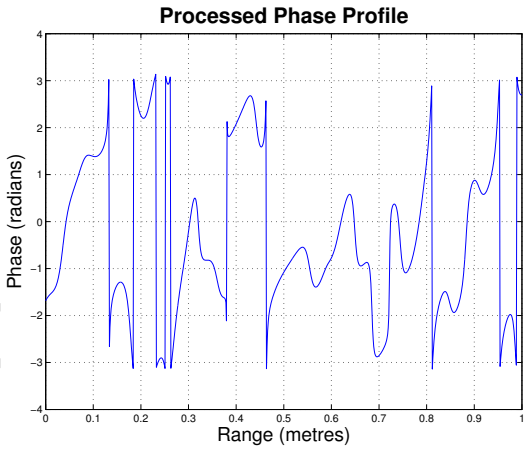

(d) Processed phase profile

Figure 5.49: Frequency and time domain data for single point target at height of platform

Figure 5.47 shows a diagram of the experiment setup as well as a top view photograph of the scene showing the location of the target. Figure 5.48 shows photographs of the experiment from different positions. The pedestal that was used has many metallic parts, which would influence the readings that are recorded by the VNA. For this reason, electromagnetic foam was placed in front of the base of the pedestal to prevent as much reflections from the metal parts of the pedestal as possible. This foam is a good absorber of electromagnetic waves. A background scene measurement was also taken at each azimuth and elevation angle to get rid of this interference on the measurements via background subtraction.

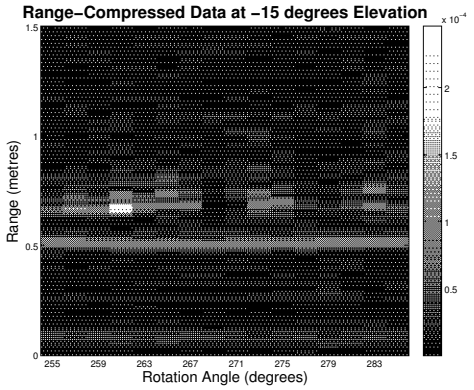

(a) -15 degrees elevation

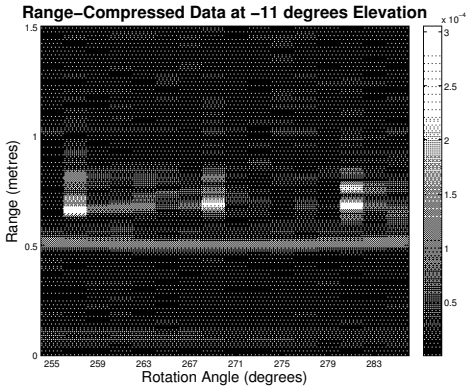

(b) -11 degrees elevation

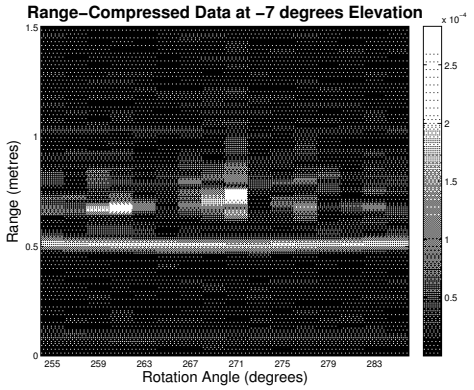

(c) -7 degrees elevation

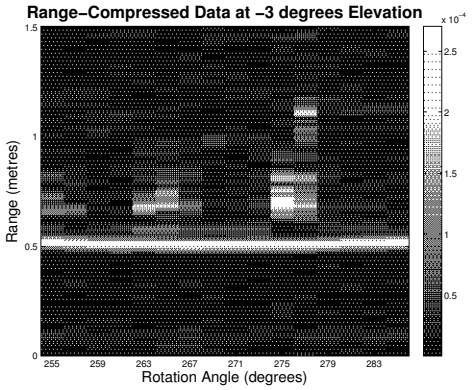

(d) -3 degrees elevation

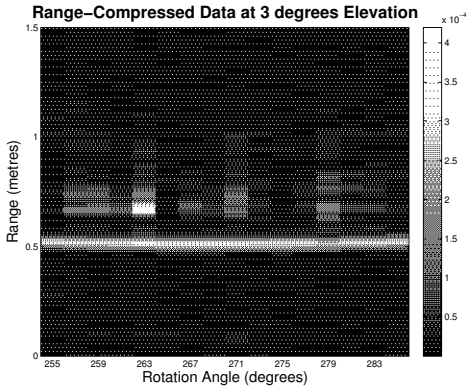

(e) 3 degrees elevation

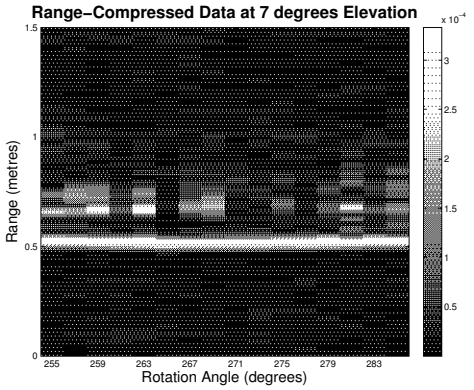

(f) 7 degrees elevation

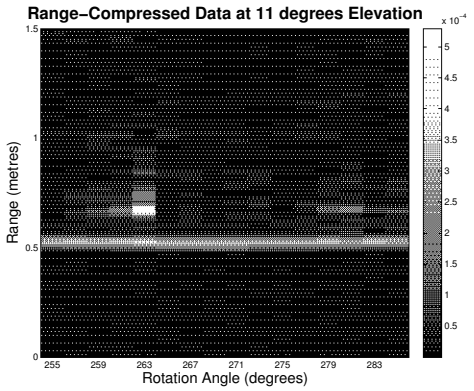

(g) 11 degrees elevation

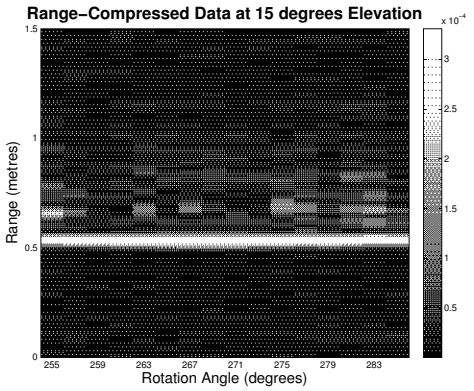

(h) 15 degrees elevation

Figure 5.50: Locus of target at different elevation angles

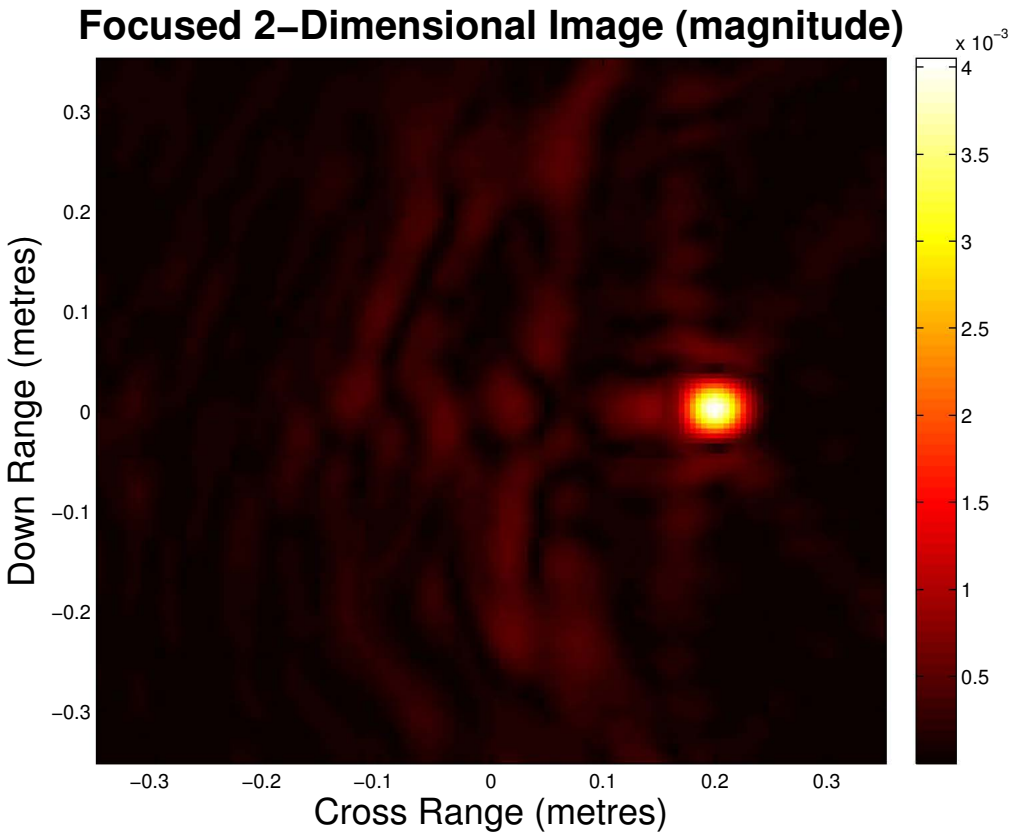

(a) 2D reconstructed image of scene at height of platform

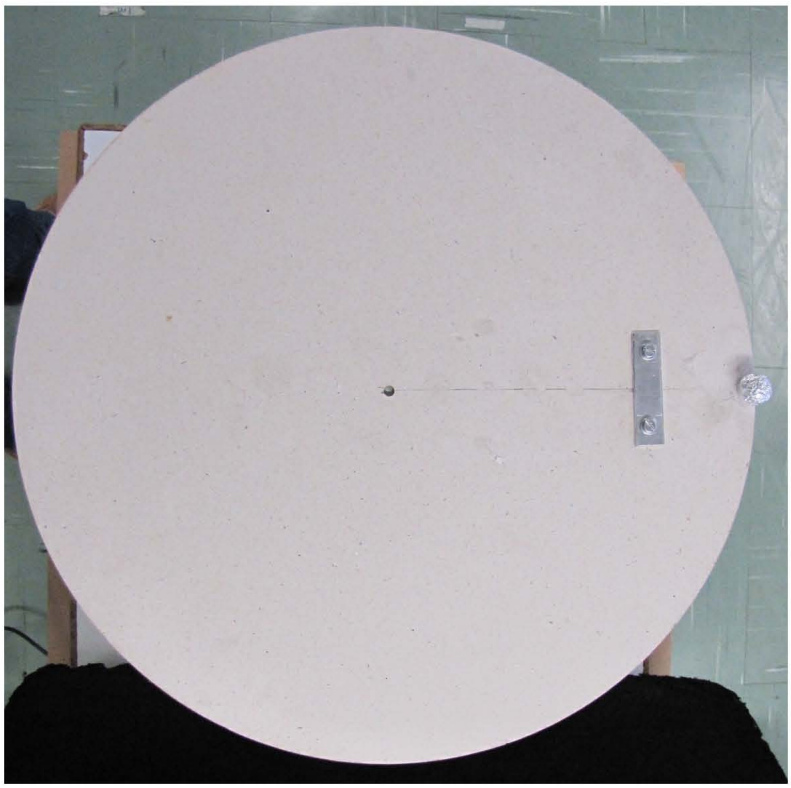

(b) Top view photograph of scene

Figure 5.51: 2D reconstructed image of scene at height of platform and top view photograph of scene

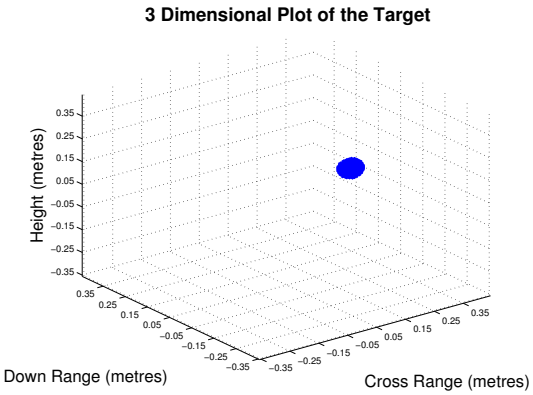

(a) 3D view of the reconstructed scene

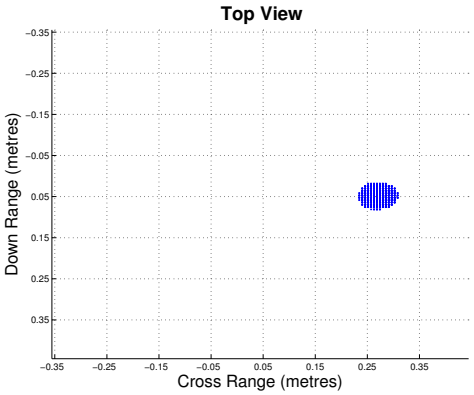

(b) Top view of reconstructed scene

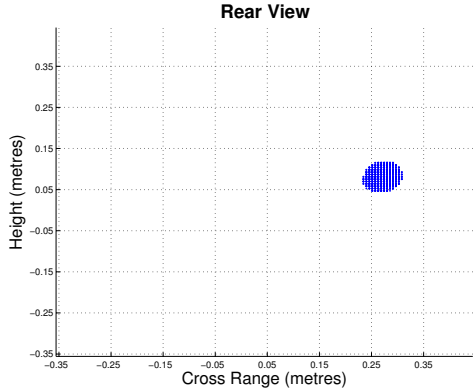

(c) Rear view of reconstructed scene

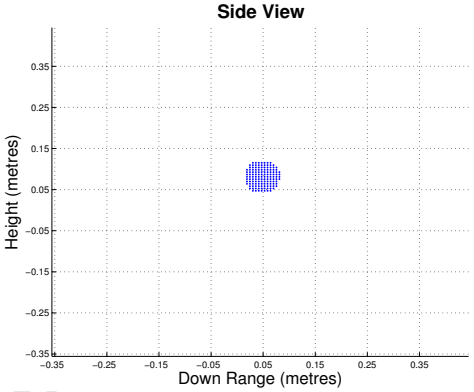

(d) Side view of reconstructed scene

Figure 5.52: 3D image of reconstructed scene

As the pedestal rotates through each elevation and azimuth angle, the locus of the target is recorded. This can be seen in Figure 5.50a - 5.50h. These figures show the locus of the target at different elevation positions. The bright line in the figures show the locus of the target as it rotates on the pedestal at different elevation angles. The other bright spots in the images are reflections from the pedestal (which is made from reflective materials) which were not successfully removed by the background subtraction process. Only a limited number of elevation angles has been displayed, but the locus was recorded for each elevation as specified by the user. It should be noted that the distance of the target from the antennas does change with each elevation angle, even though it is small (centimetre changes). From the figures of the range compressed data it is evident that there are many reflective surfaces on the pedestal which is picked up by the antennas. This has not totally been removed by background subtraction. This would introduce artifacts in the final image, but this is then removed by limiting in the reconstruction algorithm.

Figure 5.51 shows a 2D reconstructed image of the scene at the level of the pedestal as well as a top view photograph of the scene. From this figure the single point target (ball) can be seen at the location where it is on the pedestal. Figure 5.53 shows slices through the location of the target. From these slices, the down range and cross range resolution in both the azimuth and elevation direction can be seen. It can be seen that the cross range resolution along the azimuth and elevation directions are similar. This was

because the viewing angle in both the azimuth and elevation directions were the same. The down range resolution is different as it is dependent on the system bandwidth. The results from this experiment fit in well with the expected results that were obtained from the simulations in Chapter 4.

Figure 5.52 shows and 3D image of the reconstructed image of the scene. This figure also shows the top, side and rear view of the scene. From the figure the location of the single point target in 3D space can be seen. From the 3D reconstructed image of the target, the position of the target is offset by 5 cm in the down range, cross range and height direction. This error could be as a result of the position of the equipment within the experiment. The placement of the equipment needs to be done accurately. There is human error involved when placing the antennas, rotating pedestal as well as the targets on the pedestal.

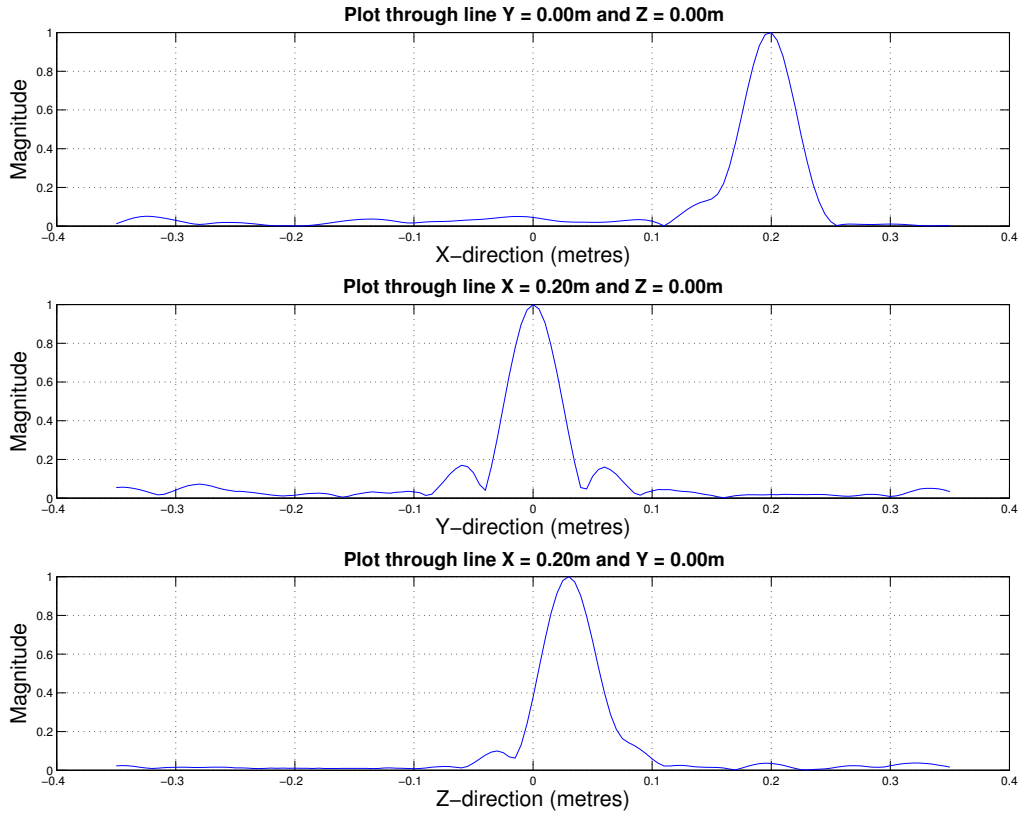

Figure 5.53: Cut through brightest point in reconstructed scene

5.2.2 Multiple Point Targets

In this experiment multiple point targets were placed on the pedestal and at different heights above the pedestal. The same foil balls were used as in the single point target experiment. The targets were located at the following positions:

- Targets coordinates in metres (x ,y ,z) = (0.2 ,0 ,0) ; (0.3 ,0 ,0) ; (0.2 ,0.1 ,0) ; (0.1 ,0 ,0.1)

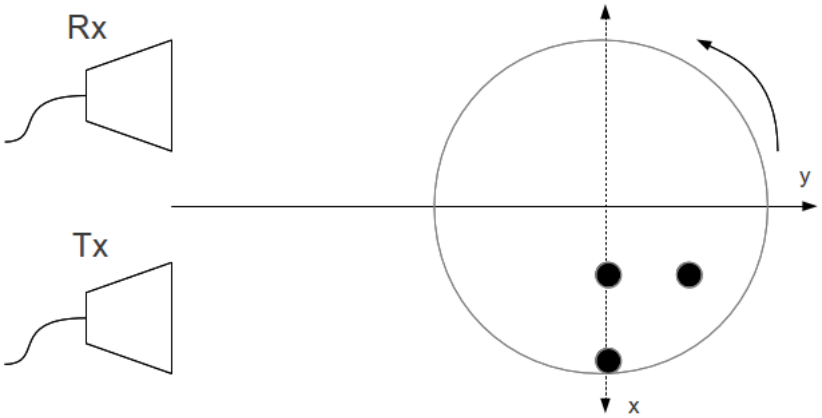

(a) Diagram of experiment scene

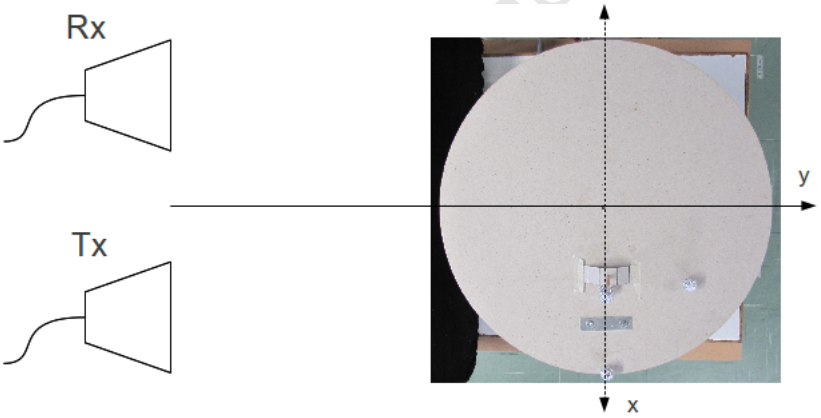

(b) Top view photograph of scene

Figure 5.54: Diagram and photograph of the experiment for a multiple point targets

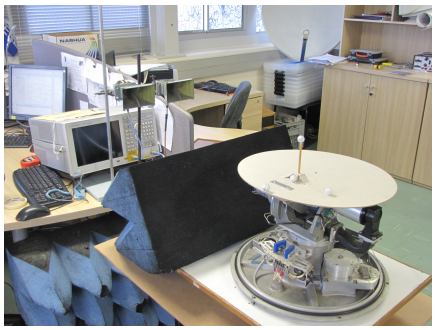

(a) Front view

(b) Rear view

Figure 5.55: Photograph of scene for multiple point targets

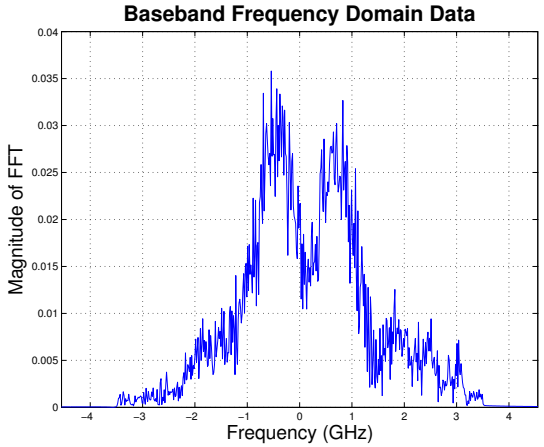

(a) Baseband frequency domain data

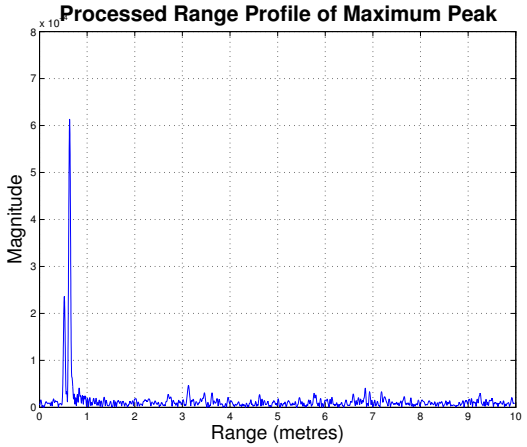

(b) Processed range profile Over Full Imaging Range

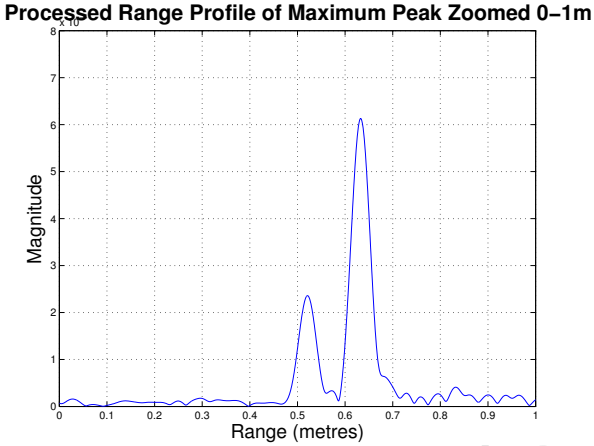

(c) Processed range profile

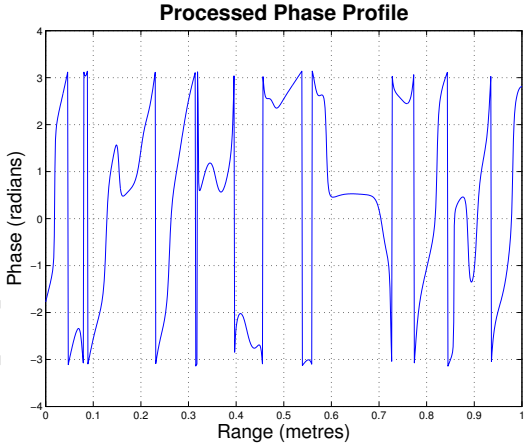

(d) Processed phase profile

Figure 5.56: Frequency and time domain data for multiple point targets at different heights above platform

Figure 5.54 shows a diagram of the experiment setup as well as a top view photograph of the scene showing the location of the target. Figure 5.55 shows photographs of the experiment from different positions. The locus of the targets as they rotate on the pedestal can be seen in in Figure 5.57. This figure shows the locus of the target at difference elevation positions. Figure 5.58 shows a 2D reconstructed image of the scene at the level of the pedestal as well as a top view photograph of the scene. From this figure, four single point targes can be seen at the location where it is on the pedestal. Slices through the location of the targets can be seen in Figure 5.60. Figure 5.59 shows and image of the reconstructed image of the scene. This reconstructed image shows the location of the four targets that were present in the scene.

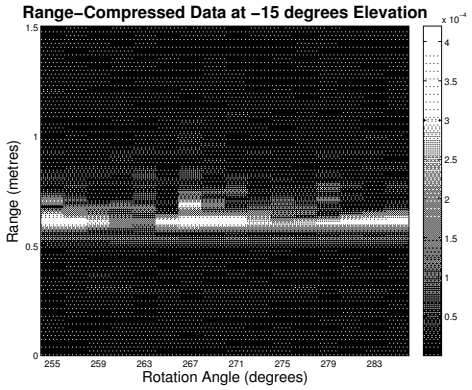

(a) -15 degrees elevation

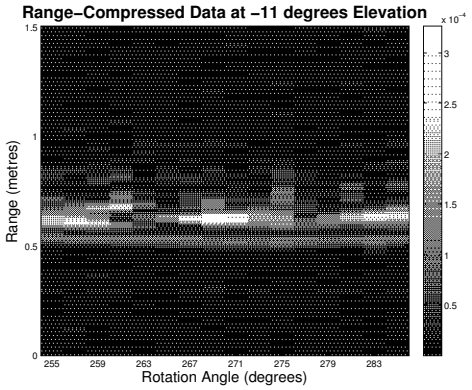

(b) -11 degrees elevation

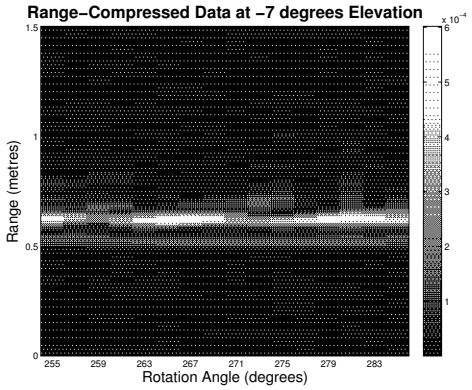

(c) -7 degrees elevation

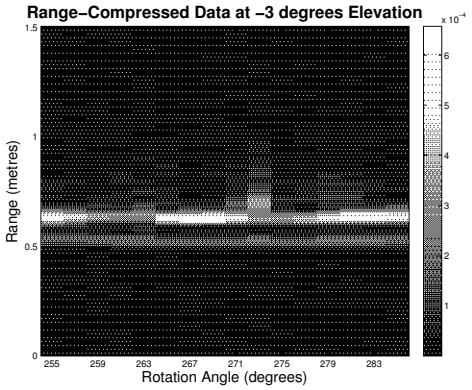

(d) -3 degrees elevation

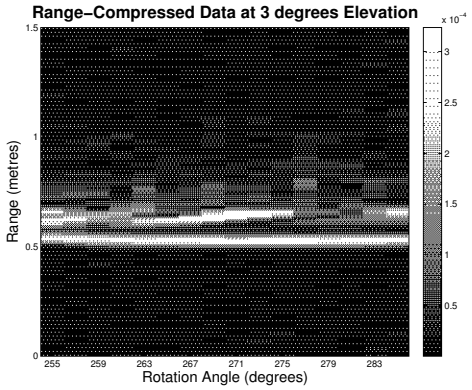

(e) 3 degrees elevation

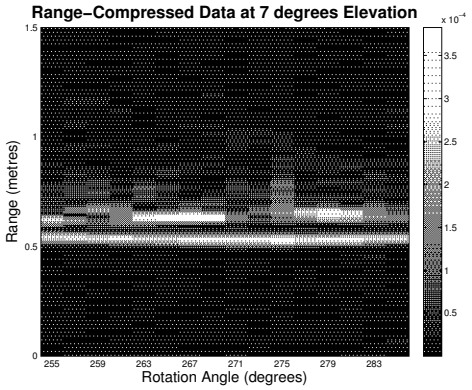

(f) 7 degrees elevation

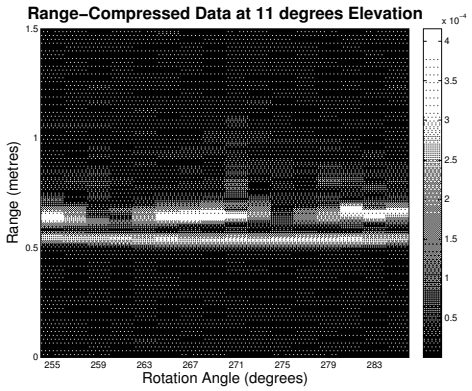

(g) 11 degrees elevation

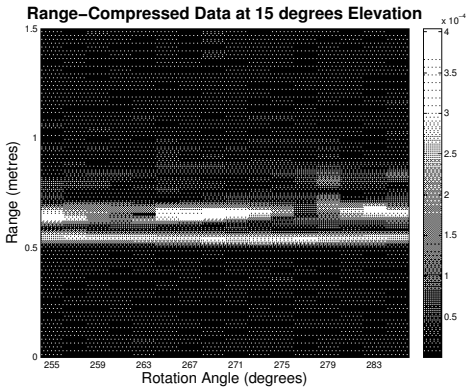

(h) 15 degrees elevation

Figure 5.57: Locus of target at different elevation angles

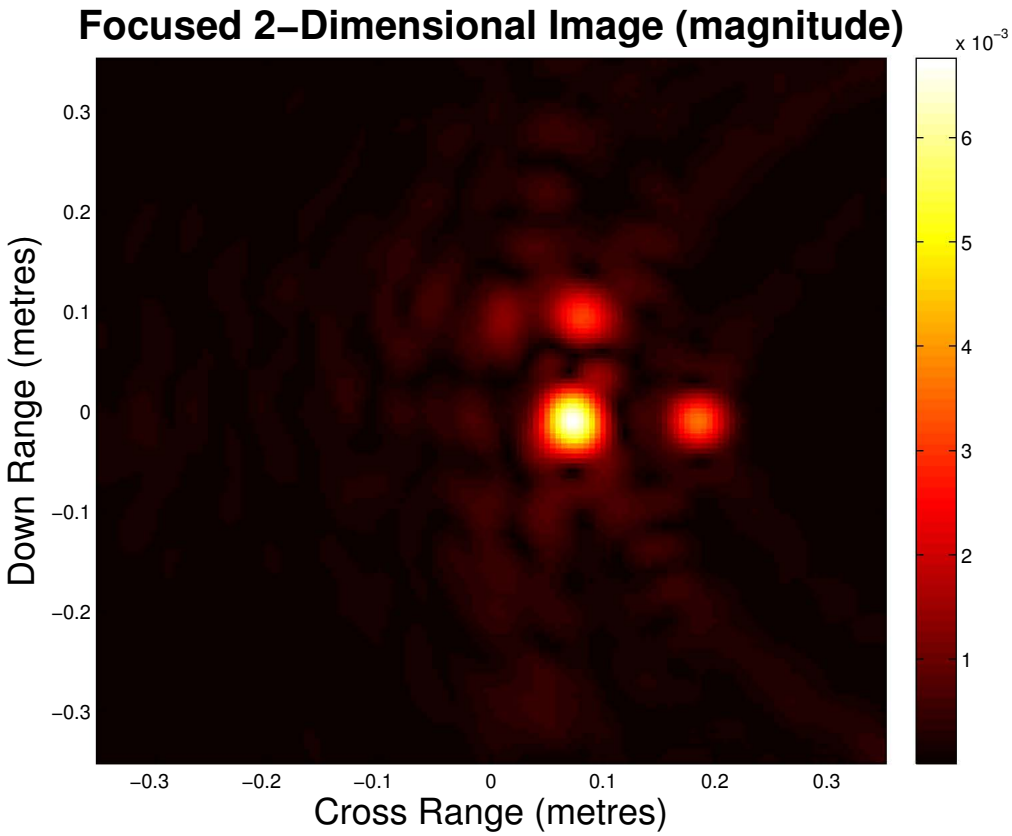

(a) 2D reconstructed image of scene at height of platform

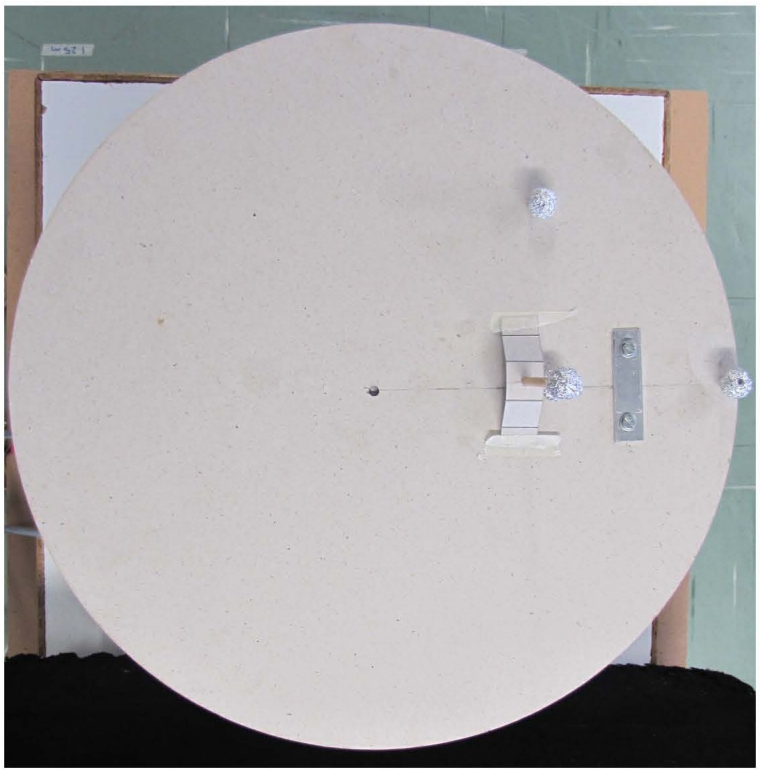

(b) Top view photograph of scene

Figure 5.58: 2D reconstructed image of scene at height of platform and top view photograph of scene

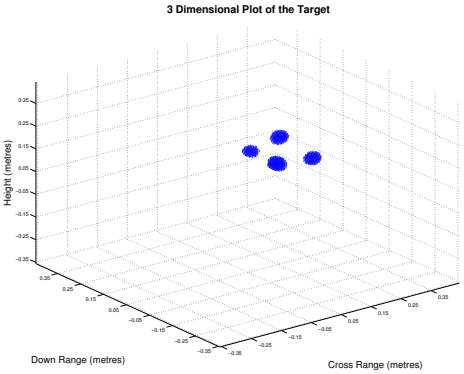

(a) 3D view of the reconstructed scene

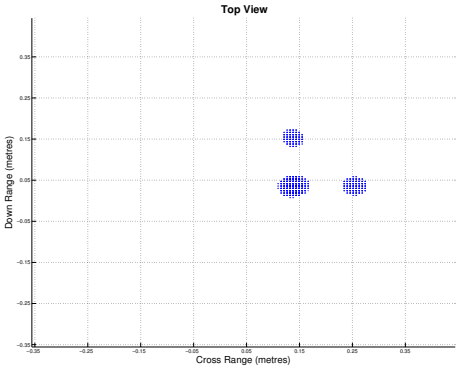

(b) Top view of reconstructed scene

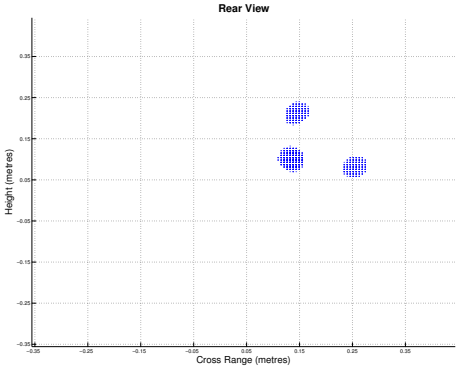

(c) Rear view of reconstructed scene

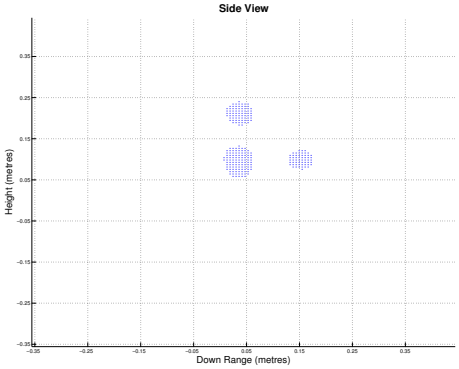

(d) Side view of reconstructed scene

Figure 5.59: 3D image of reconstructed scene

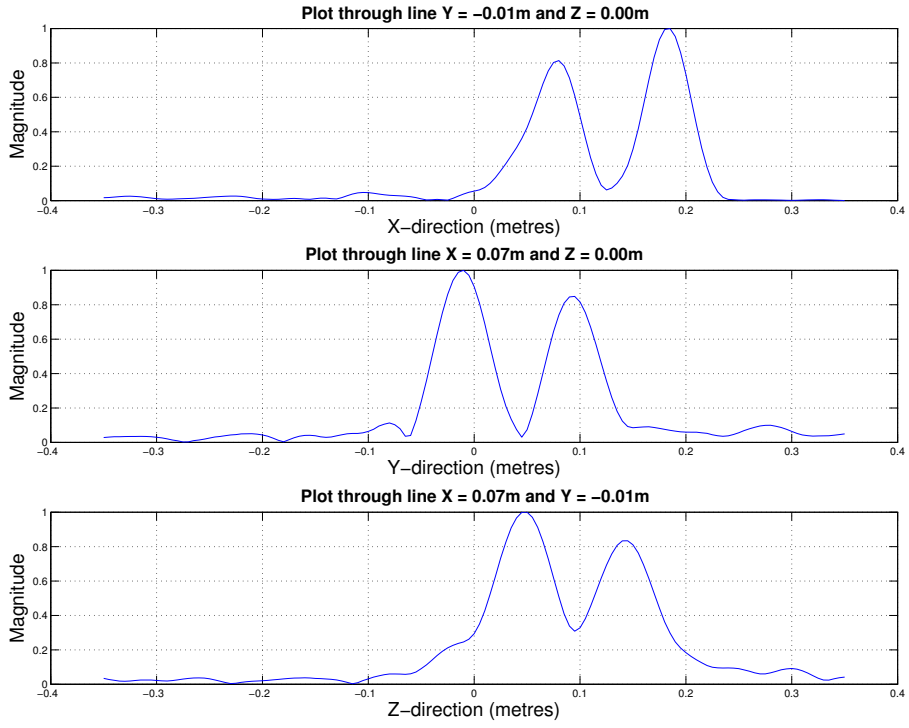

Figure 5.60: Cut along location of targets in reconstructed scene

5.2.3 Single cylindrically Target

In this experiment one cylindrically shaped target wrapped in foil, toilet roll with the same dimensions as the toilet roll used in the 2D experiments, was used and was placed on the rotating pedestal. The target was located at the following position:

- Target coordinates in metres (x ,y ,z) = (0.2 ,0 ,0)

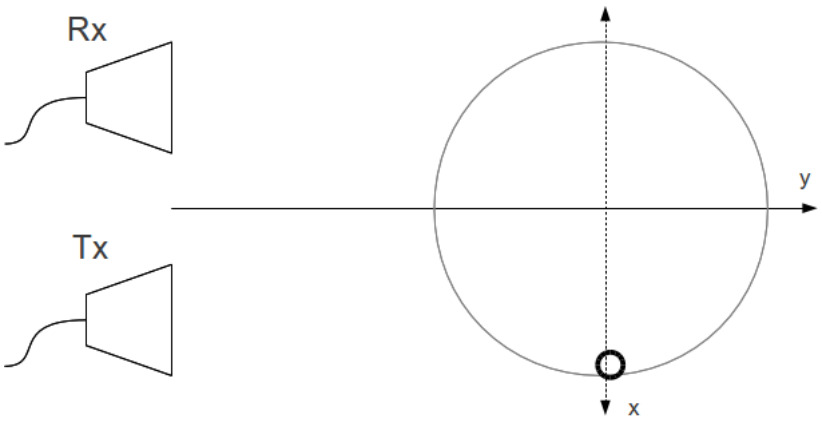

(a) Diagram of experiment scene

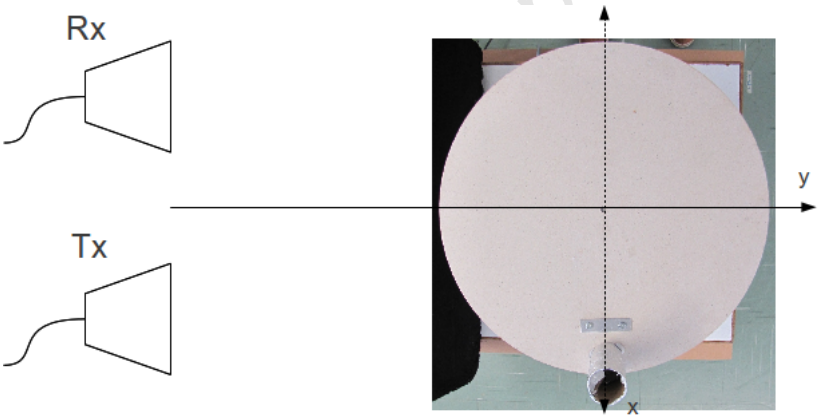

(b) Top view photograph of scene

Figure 5.61: Diagram and photograph of the experiment for a single cylindrically shaped target

(a) Front view

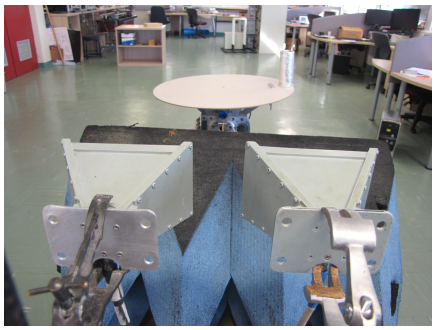

(b) Rear view

Figure 5.62: Photograph of scene for single cylindrically shaped target

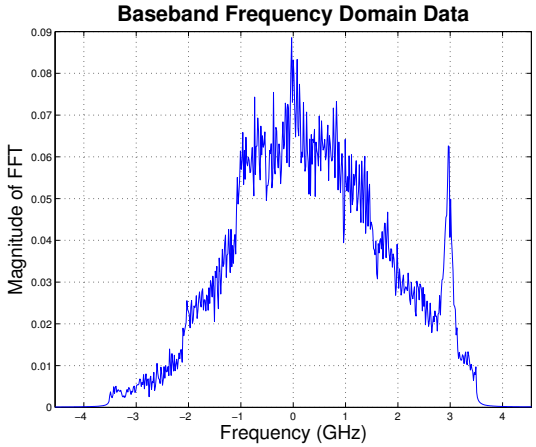

(a) Baseband frequency domain data

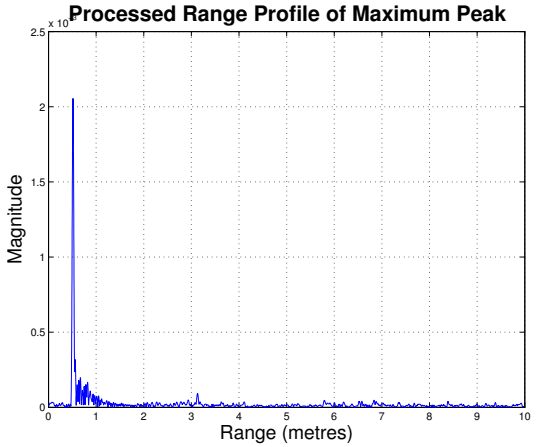

(b) Processed range profile Over Full Imaging Range

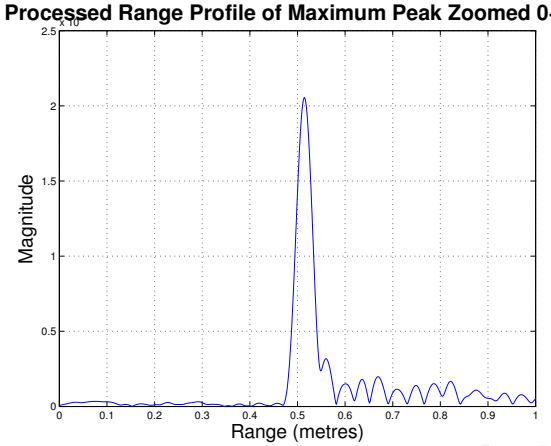

(c) Processed range profile

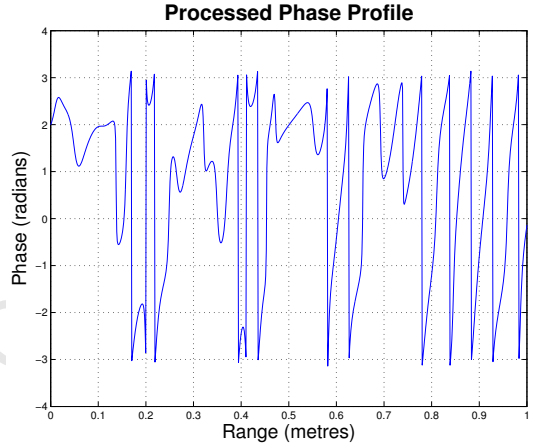

(d) Processed phase profile

Figure 5.63: Frequency and time domain data for single cylindrically target at height of platform

The reconstructed 3D image of the scene can be seen in Figure 5.66 shows the reconstructed image of the scene. The location and shape of the target can be seen from this target. The shape of this reconstructed image is elongated along the z-axis. From Figure 5.67 shows slices through the target. From these figures the resolution of the target can be seen. The slice through the z-axis shows the length of the target. This shows the elongation of the target.

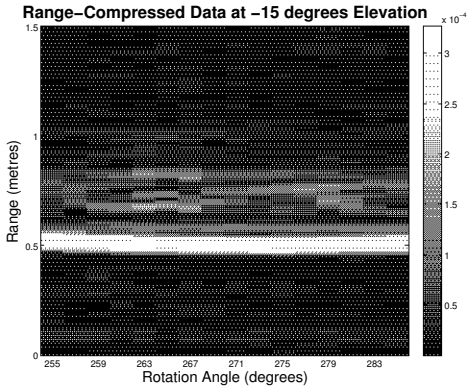

(a) -15 degrees elevation

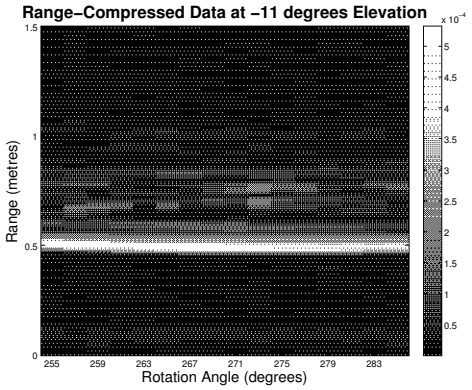

(b) -11 degrees elevation

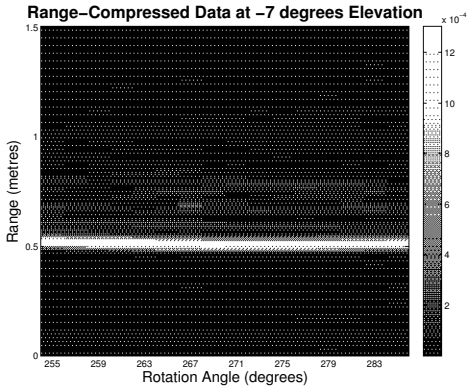

(c) -7 degrees elevation

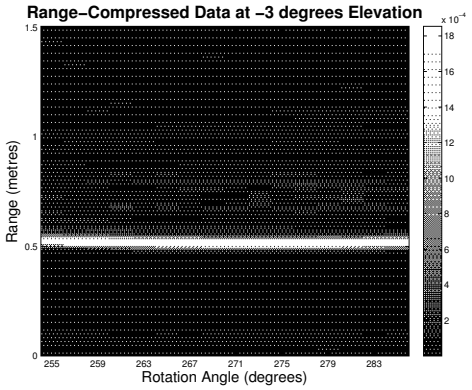

(d) -3 degrees elevation

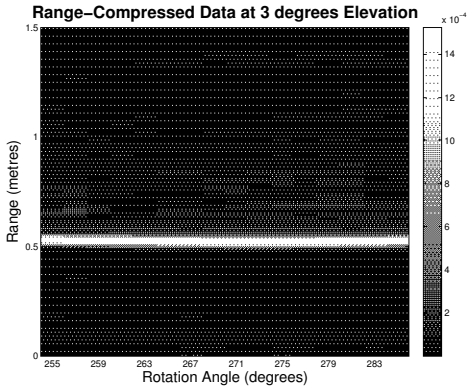

(e) 3 degrees elevation

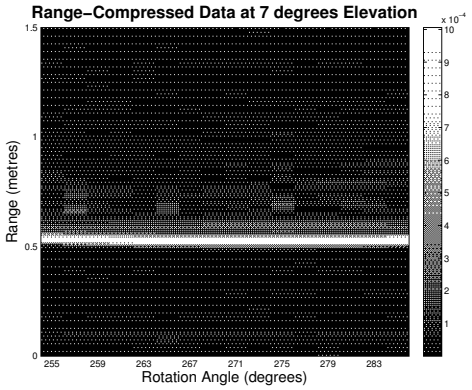

(f) 7 degrees elevation

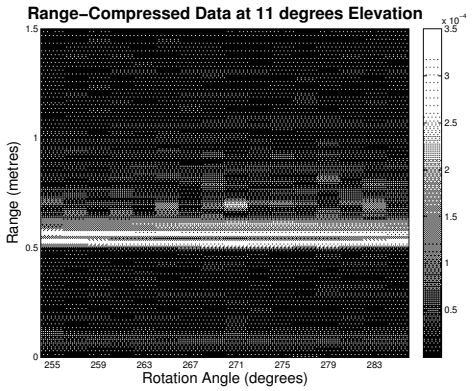

(g) 11 degrees elevation

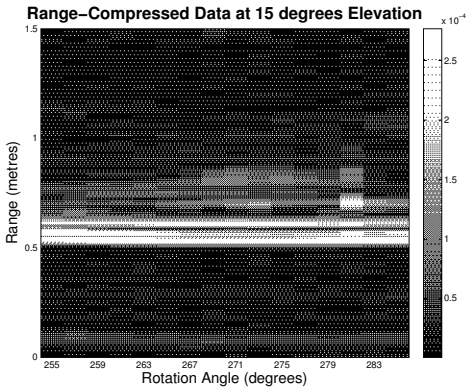

(h) 15 degrees elevation

Figure 5.64: Locus of Target at Different Elevation Angles

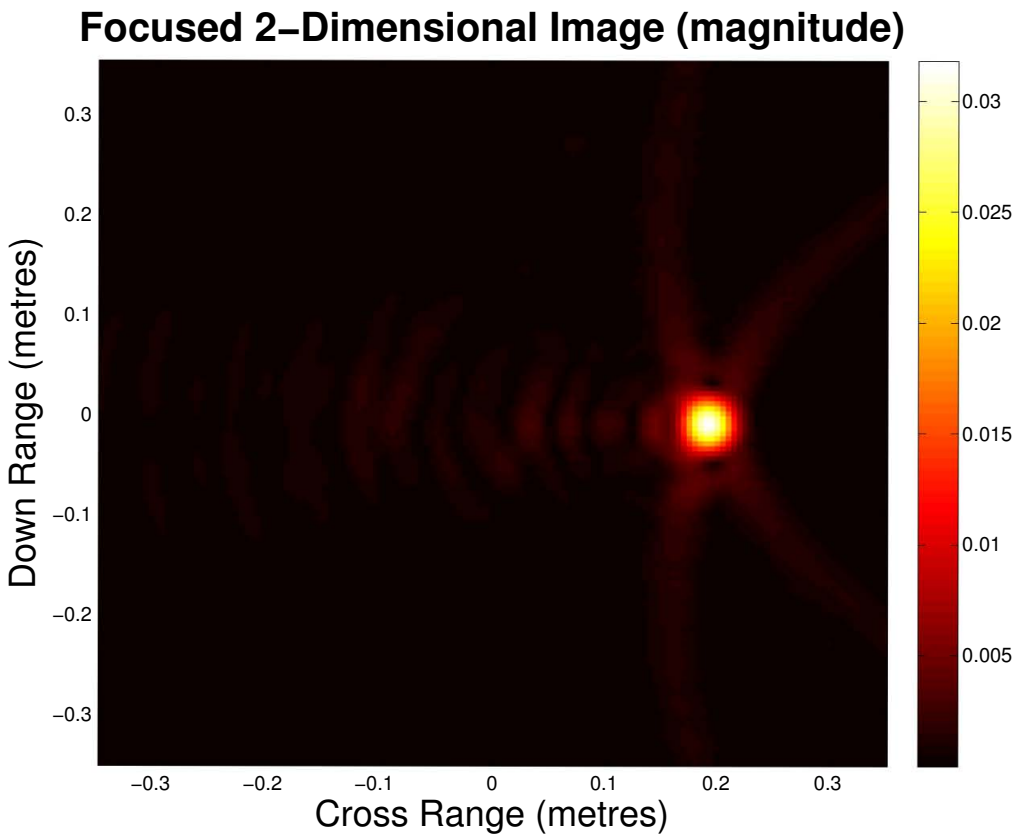

(a) 2D reconstructed image of scene at height of platform

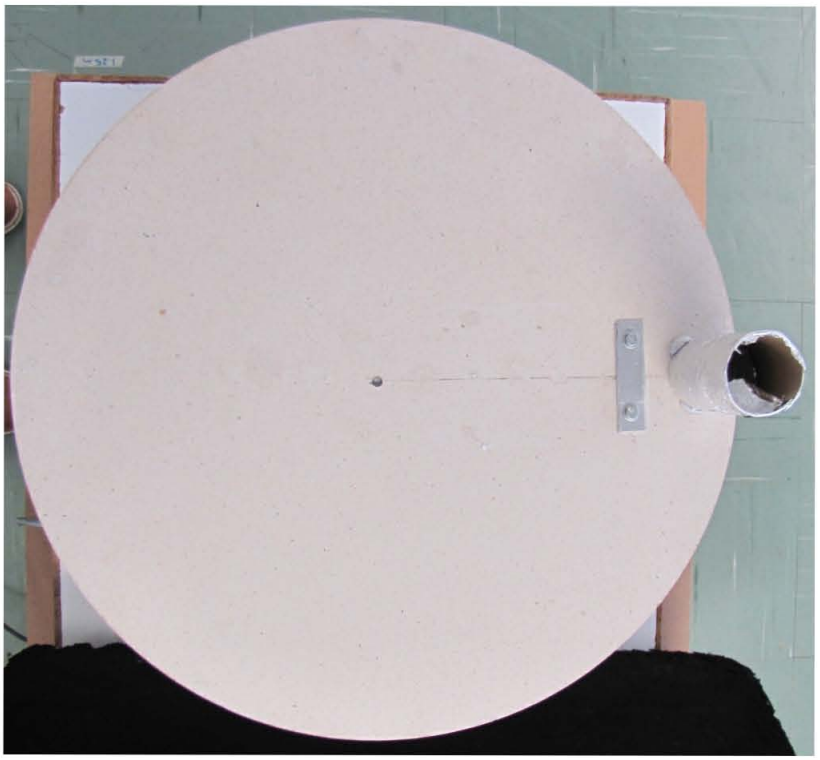

(b) Top view photograph of scene

Figure 5.65: 2D reconstructed image of scene at height of platform and top view photograph of scene

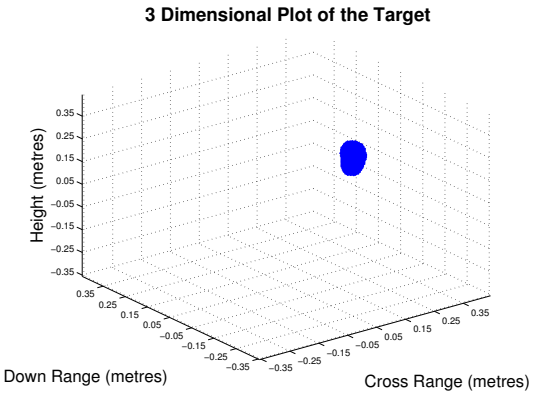

(a) 3D view of the reconstructed scene

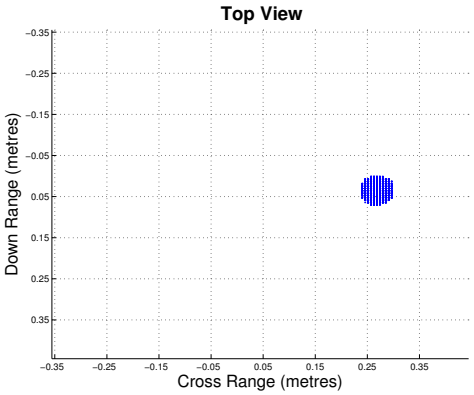

(b) Top view of reconstructed scene

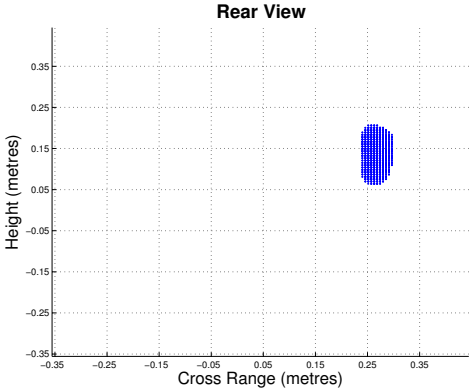

(c) Rear view of reconstructed scene

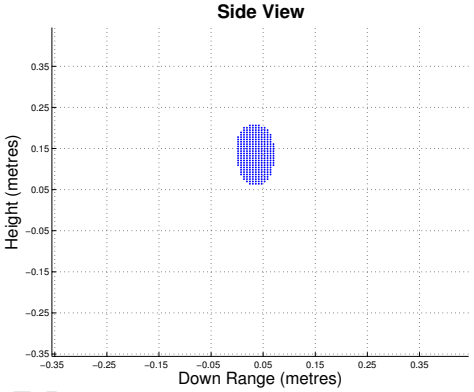

(d) Side view of reconstructed scene

Figure 5.66: 3D image of reconstructed scene

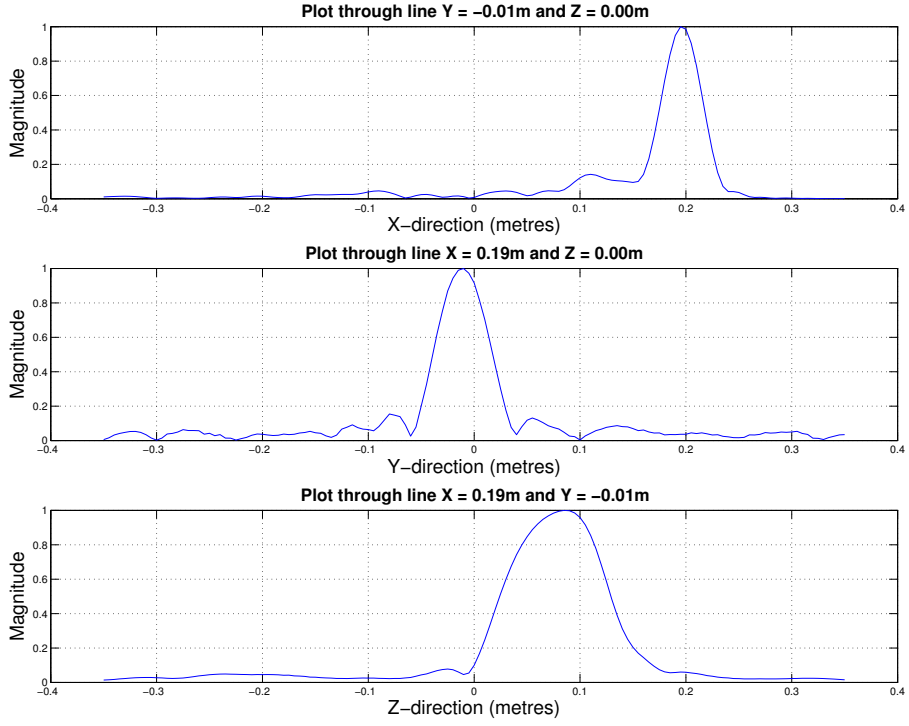

Figure 5.67: Cut along location of targets in reconstructed scene

Conclusion

The results that were obtained from the experiments show that this system works. The experimental data for both the 2D and 3D cases correlates well with the simulated data. In the 2D case, the frequency domain data that is received from the VNA is converted to the time domain by an inverse Fourier transform. This time domain plot is then converted to a range profile. The range profiles created from the experiments are similar to those of the simulations. A peak can be seen at the distance that the target is located from the antennas. The range profiles from each angular position were then stacked together to form an image of the locus of the targets as they rotated on the platform. The results showed that the shape of this locus is near sinusoidal, which corresponds to the expected locus shape from the simulations. The locus data matrix was then put through a reconstruction algorithm which recreated an image of the scene. The reconstruction algorithm was successful and a 2D image of the scene, along the plane of the platform, was successfully created. The results from the 3D experiments also correlated well with the simulations. The same range profiles (as for the 2D case) were successfully created for each elevation and azimuth angle. For each elevation angle the range profiles were stacked together for each azimuth position to create a locus of the targets at each elevation position. These loci corresponded to the expected loci as was seen in the simulations. These loci were put through a 3D reconstruction algorithm, which successfully recreated a 3D image of the scene. The scene was successfully reconstructed.

Chapter 6

Conclusions and Recommendations

An UWB radar imaging system using a vector network analyzer was developed in this thesis. This system is capable of reconstructing images of targets in 2D space as well as 3D space, using a 1-axis or 2-axis rotating pedestal respectively. Based on the objectives of the project as set out in Chapter 1, the following objectives have been achieved:

- Successful design of an UWB Radar Tomography system, using an Agilent E5071B vector network analyzer, capable of creating 2D and 3D images of targets placed in front of a transmitter/receiver pair.
- Simulations of the UWB system in Matlab. This simulation was carried out in both 2D and 3D space and the outcome of these simulations showed the successful reconstruction of the scene.
- Design and implementation of a GUI in LabVIEW for controlling the operation of the UWB tomographic system.
- Control of the VNA using LabVIEW. The parameters of the VNA can be set by using the LabVIEW GUI that was created.
- Control of the 1-axis and 2-axis rotating pedestal using LabVIEW.
- Implementation of time domain back-projection algorithm for both 2D and 3D reconstruction of scene.

This project was the first of its kind at UCT which involved the use of a VNA as a tomographic radar imaging system. Using this device allows for very high bandwidths which in turn allows for very fine spatial resolution. For this reason, the system can be used for imaging targets which are small and closely spaced.

There are many recommendations that could be made to improve the system. These are listed below:

- The UWB system that was used made use of a VNA which relies on AC mains power to operate. By using a VNA such as the Agilent N9923A FieldFox Handheld

RF vector network analyzer will allow the system to be portable. The system could then be taken into an outdoor environment and measurements taken.

- The VNA that was used is operational between 300 kHz to 8.5 GHz. This allowed for a range resolution 2.5 cm. By using a VNA which has a higher operational frequency (and hence a wider available bandwidth) will allow for even finer range resolution.

- An investigation could be done into different types of signals being radiated from the VNA and the effects thereof. The VNA has many functions which could be explored such as sweep time, averaging, sweep mode, sweep type, etc.

- In this project, two UWB horn antennas were available for use in the system. Experiments could be carried out with other types of antennas and the effects of the antennas can be shown.

- The 2-axis rotating pedestal was controlled via feedback through two potentiometers which were mounted to the motors on each rotating axis. The potentiometers can be replaced with digital shaft encoders which will give more accurate measurements as the the angular position of the motors.

- The 2-axis rotating pedestal has several speed movements that can be adjusted by a binary number. For this project only one speed was used. The full speed range of the motors can be taken advantage of, so as to allow for better control of the motors and more accurate positioning of the motors. This would also decrease the time which it takes for the experiment to be complete.

- The 2-axis pedestal that was used had many metal parts which influence the measurements that were taken from the VNA. An investigation into other types of 2-axis rotating pedestals can be done, so as to use one which would reduce the amount of backscatter produced from the pedestal itself.

- This UWB system was used to image objects which were placed on a rotating pedestal. An investigation could be done into using this system for different applications, such as ground penetrating radar and through-wall imaging.

- The time domain back-projection algorithm was implemented in this project. An investigation can be done into different reconstruction algorithms.

- There are many ways in which the data can be recorded. In this project the reflection waves from the target were recorded and used to reconstruct an image. The forward scattered waves can also be used and measured.

- Measurement of different polarizations for illumination and reflection.

As previously mentioned, applications for UWB systems as well as ISAR systems have been developed for use in the real world. This includes systems for breast cancer detection, systems for extraction of helicopter blade parameters as well as systems which have been designed for the detection of concealed weapons. The system designed in this project can also be used in the future for industrial tomographic imaging of objects. It can also be applied to tomographic SAR for height mapping of a landmass. It could also be applied in applications for non-cooperative target recognition systems where the motion of the target is unknown as well as bi-static radar imaging of moving targets. The UWB system that was designed in this project can be applied to a variety of radar and tomographic applications. The results of these experiments indicates a successful future for UWB radar imaging using this system.

Appendix A

Cobham H-1498 Series Broadband Horn Antenna

H-1498 Series

Broadband Horn Antennas

2009 Data Sheet

The most important thing we build is trust

Cobham Sensor Systems' H-1498 series broadband linear horn antennas provide superior performance for use in a wide variety of laboratory, commercial and military applications. With excellent input VSWR, these antennas provide high gain across the frequency range and consistent pattern performance. They have become a laboratory standard as a reference horn in anechoic chambers and outdoor ranges.

The H-1498 is available with SMA female connector (standard) and TNC female connector (H-1498T). A further option is a radome/aperture cover (H-1498R) for outdoor use.

Applications include:

- Laboratory Standards and References
- Low Power Transmit Applications
- Flight Line Test Set Signal Sources
- Applications Requiring Small Size, High Gain

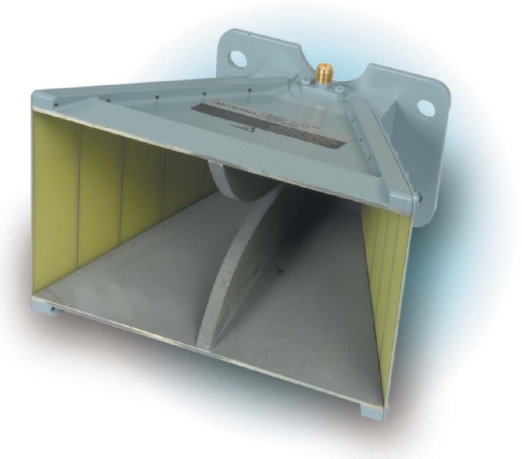

Key Fearures

- Ultra Broadband Frequency Performance (2.0-18.0 GHz)
- High Gain
- Small Size and Light Weight
- Industry Standard Mounting Flange
- Rugged, Simple Design for Excellent Durability

H-1498 Typical Antenna Characteristics						
Frequency Band	2 to 18 GHz	L x W x H: (in)	4.9 x 3.2 x 3.9		Weight:	10 oz.
VSWR	Maximum	3:1	Typical:	<2.5:1	Power (CW):	50 W
Gain:	2 GHz=	6 dBLi	9 GHz=	11 dBLi	18 GHz=	11 dBLi
3dB Beamwidth:	80□E-Plane	50□H-Plane	Note: At the lowest frequency the beamwidth increases to 100 deg.			

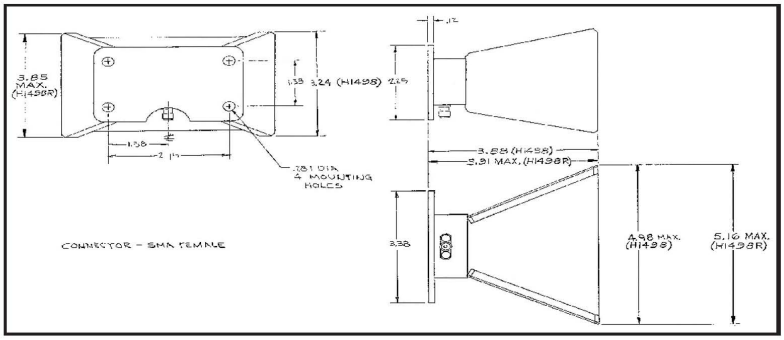

For more information, please contact:

Cobham Sensor Systems
305 Richardson Road
Lansdale, PA 19446-1485
T: 215-996-2416 or 215-996-2000
F: 215-996-2076

Appendix B

Bourns 6539/6639 Precision 10 $k\Omega$ Potentiometer

Features

- Essentially infinite resolution
- Excellent rotational life
- High quality, rugged construction
- General purpose applications
- Non-standard features available
- Cost and space saving

6539/6639 - Precision Potentiometer

	6539 Servo Mount	6639 Bushing Mount
Electrical Characteristics[1]		
Standard Resistance Range	1K to 100K ohms	1K to 100K ohms
Resistance Tolerance		
Standard	±15%	±15%
Independent Linearity		
Standard	±2.0%	±2.0%
Resolution	Essentially infinite	Essentially infinite
Effective Electrical Angle	340° +3°	340° +3°
End Voltage	0.5% maximum	0.5% maximum
Output Smoothness	0.1%	0.1%
Power Rating (Voltage Limited By Power Dissipation or 300 VAC, Whichever is Less)		
+70°C	1.0 watt	1.0 watt
+125°C	0 watt	0 watt
Dielectric Withstanding Voltage	MIL-STD-202, Method 301	MIL-STD-202, Method 301
Sea Level	750 VAC minimum	750 VAC minimum
Insulation Resistance (500 VDC)	500 megohms minimum	500 megohms minimum
Environmental Characteristics[1]		
Operating Temperature		
Static Operation Temp Range	-65°C to +125°C	-65°C to +125°C
Dynamic Temp Range	+1°C to +125°C	+1°C to +125°C
Vibration	15G	15G
Wiper Bounce	0.1 millisecond maximum	0.1 millisecond maximum
Shock	50G	50G
Wiper Bounce	0.1 millisecond maximum	0.1 millisecond maximum
Rotational Life (No Load)	10,000,000 shaft revolutions	10,000,000 shaft revolutions
Total Resistance Shift	±10% maximum	±10% maximum
Mechanical Characteristics[1]		
Mechanical Angle	Continuous, Stops (340° +8°, -0°) available	Continuous, Stops (340° +8° -0°) available
Backlash	0.1° maximum	0.1° maximum
Shaft Runout	0.005 in. (0.13mm) T.I.R.	0.005 in. (0.13mm) T.I.R.
Shaft End Play	0.005 in. (0.13mm) T.I.R.	0.005 in. (0.13mm) T.I.R.
Shaft Radial Play	0.005 in. (0.13mm) T.I.R.	0.005 in. (0.13mm) T.I.R.
Pilot Diameter		
Runout	0.0025 in. (0.06mm) T.I.R.	
Lateral Runout	0.003 in. (0.08mm) T.I.R.	
Torque (Starting & Running)	0.5 oz.-in. (0.40 Ncm) max.	0.5 oz.-in. (0.40 Ncm) max.
Terminals	Rear Turret Type	Rear Turret Type
Bearing Type	Brass Sleeve	Nickel Plated Brass
Markings	Manufacturer's name, part number, resistance value and tolerance, linearity tolerance, wiring diagram and date code.	Manufacturer's name, part number, resistance value and tolerance, linearity tolerance, wiring diagram and date code.

[1]At room ambient: +25°C nominal and 50% relative humidity nominal, except as noted.

Recommended Part Numbers

Part Number	Resistance (Ω)
6539S-1-102	**1,000**
6539S-1-502	**5,000**
6539S-1-103	**10,000**

BOLD-FACE LISTINGS ARE IN STOCK AND READILY AVAILABLE THROUGH DISTRIBUTION.

FOR OTHER OPTIONS CONSULT FACTORY.

Part Numbers		Resistance (Ω)
Bushing Mount	Mechanical Stops	
6639S-1-102	**6639S-301-102**	**1,000**
6639S-1-202		**2,000**
6639S-1-502	**6639S-301-502**	**5,000**
6639S-1-103	**6639S-301-103**	**10,000**
6639S-1-203		**20,000**

6539

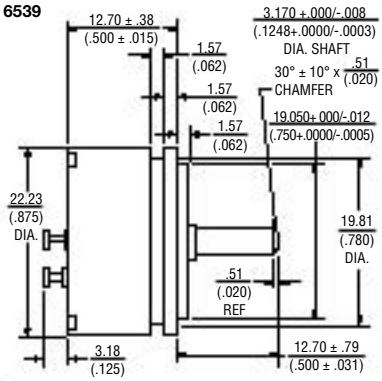

6639

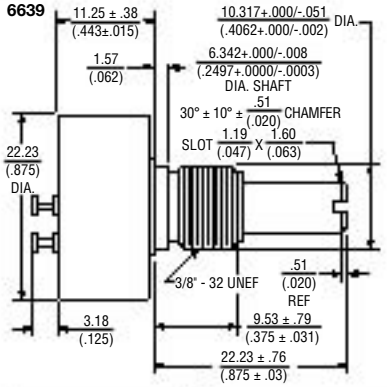

65/6639

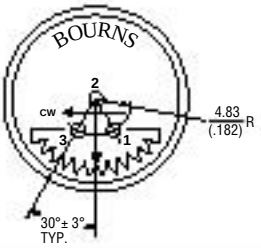

TOLERANCES: EXCEPT WHERE NOTED

DECIMALS: .XX ± .38 (.015) .XXX ± .13 (.005)

FRACTIONS: ±1/64

DIMENSIONS: MM (IN.)

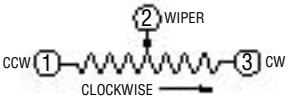

Specifications are subject to change without notice.

Appendix C

LabVIEW GUI

C.1 Control Pedestal Function

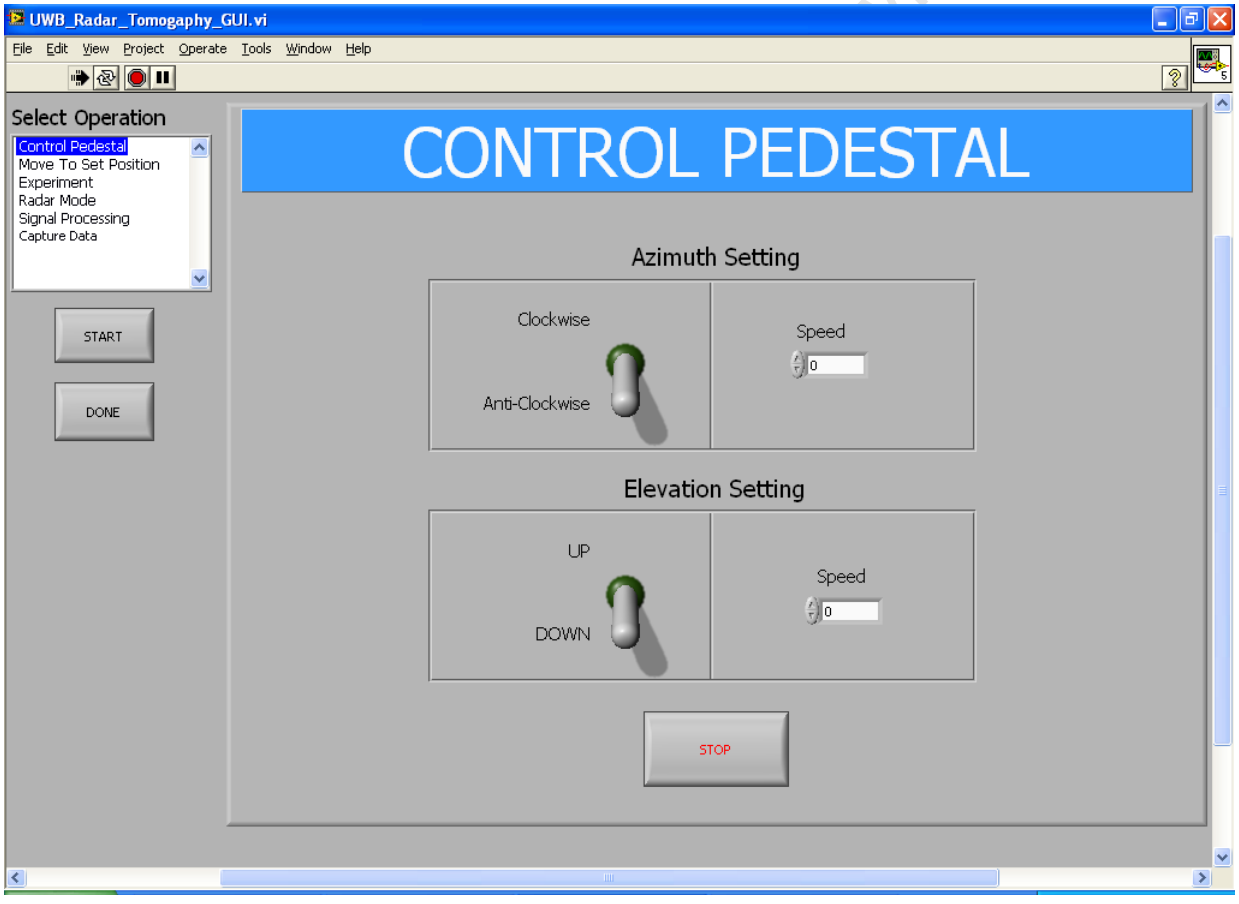

C.2 Move to Set Position Function

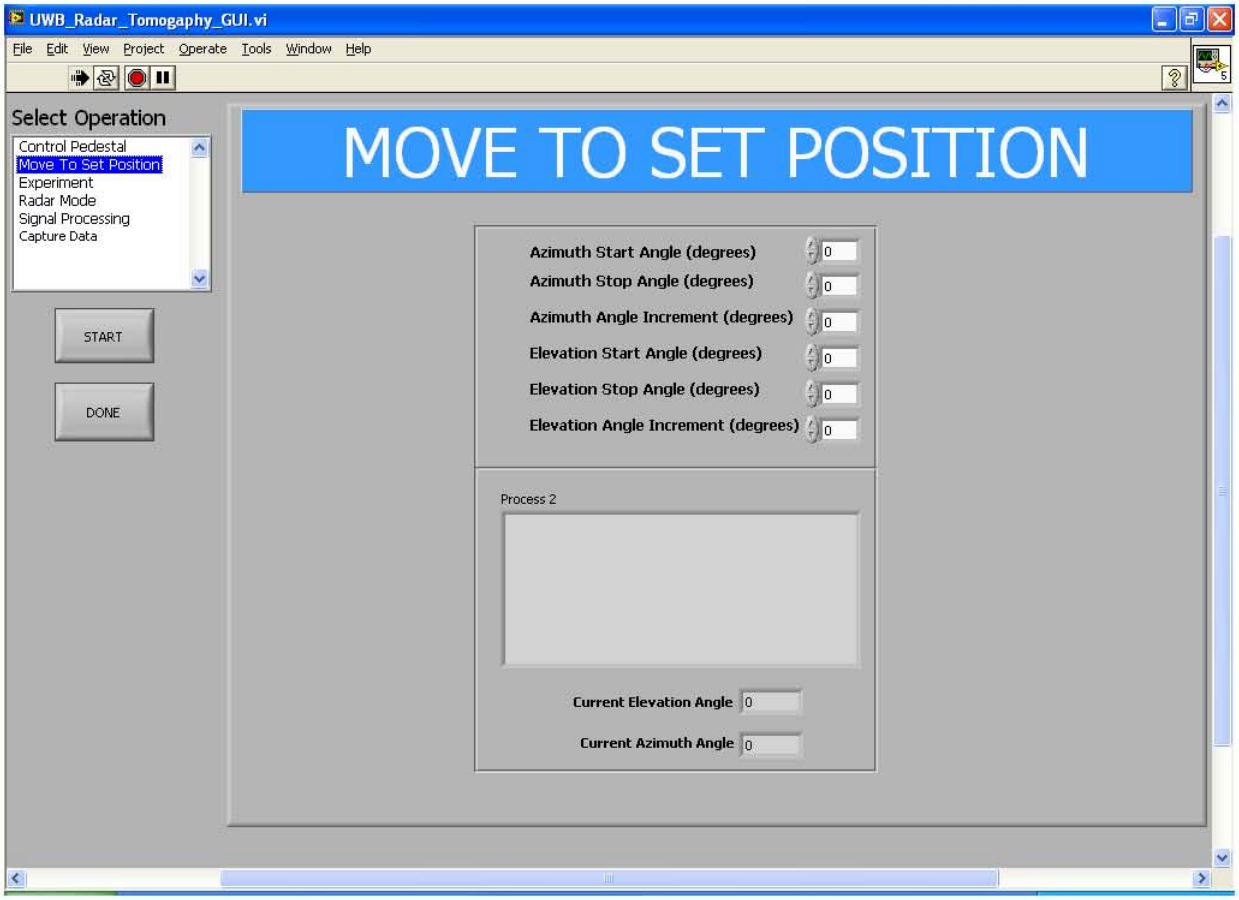

C.3 Experiment Function

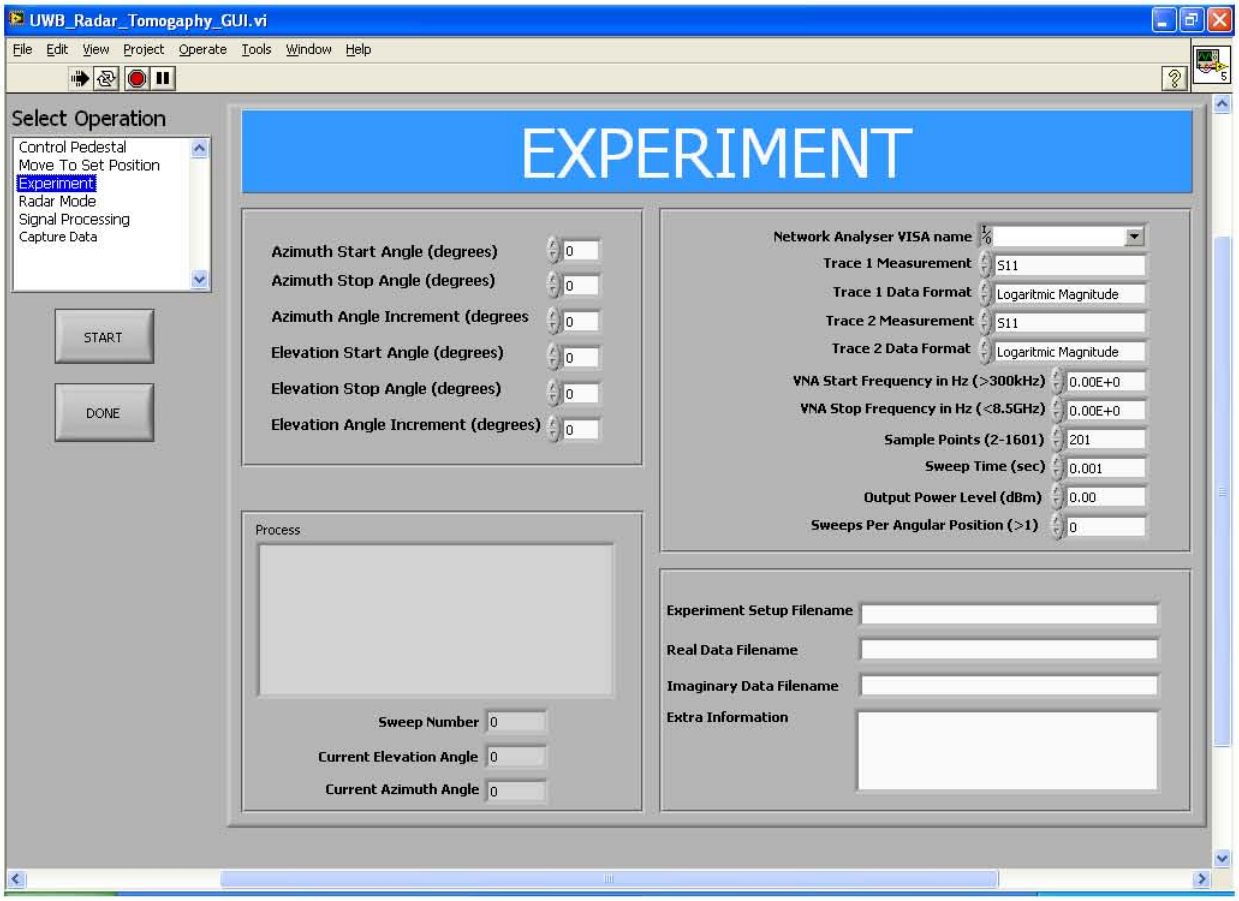

C.4 Radar Mode Function

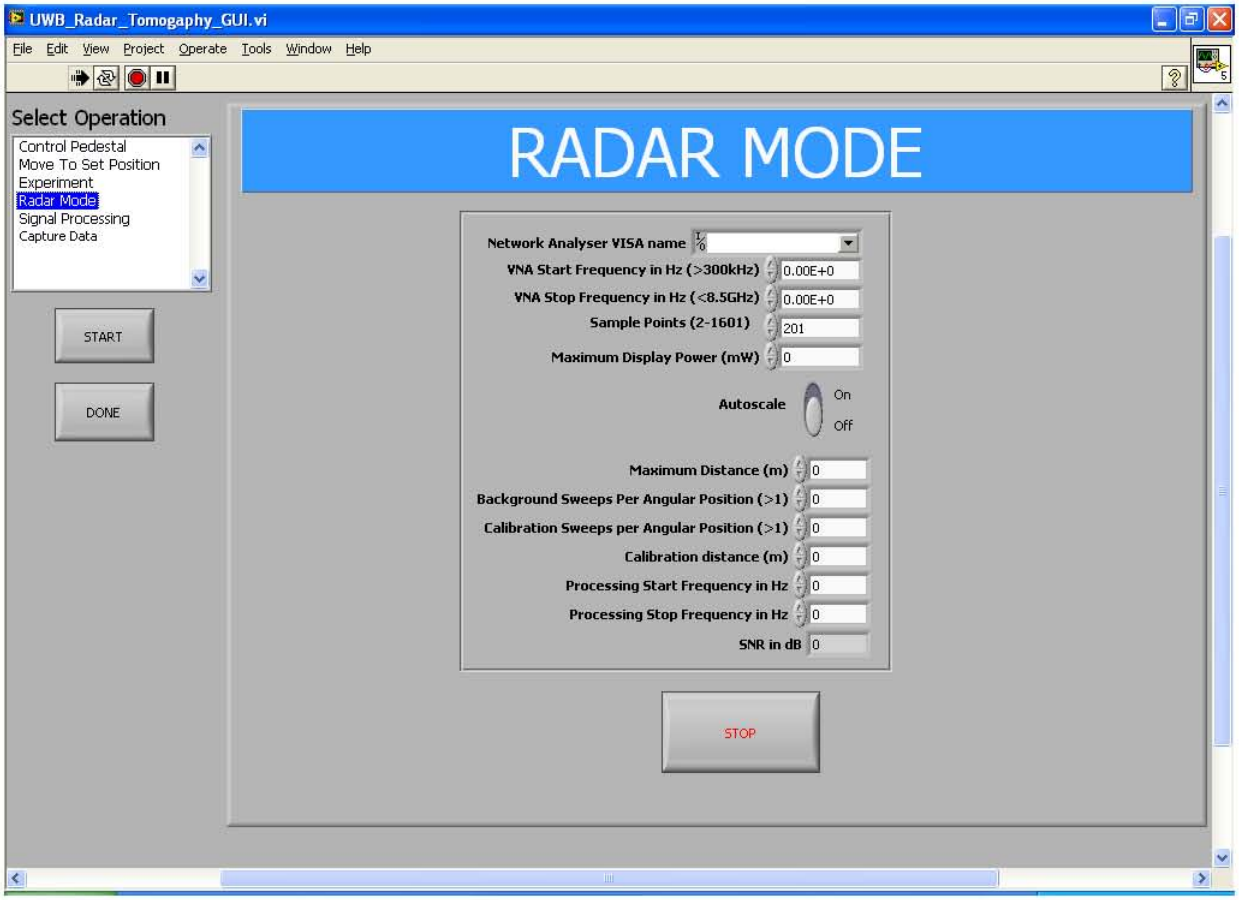

C.5 Signal Processing Function

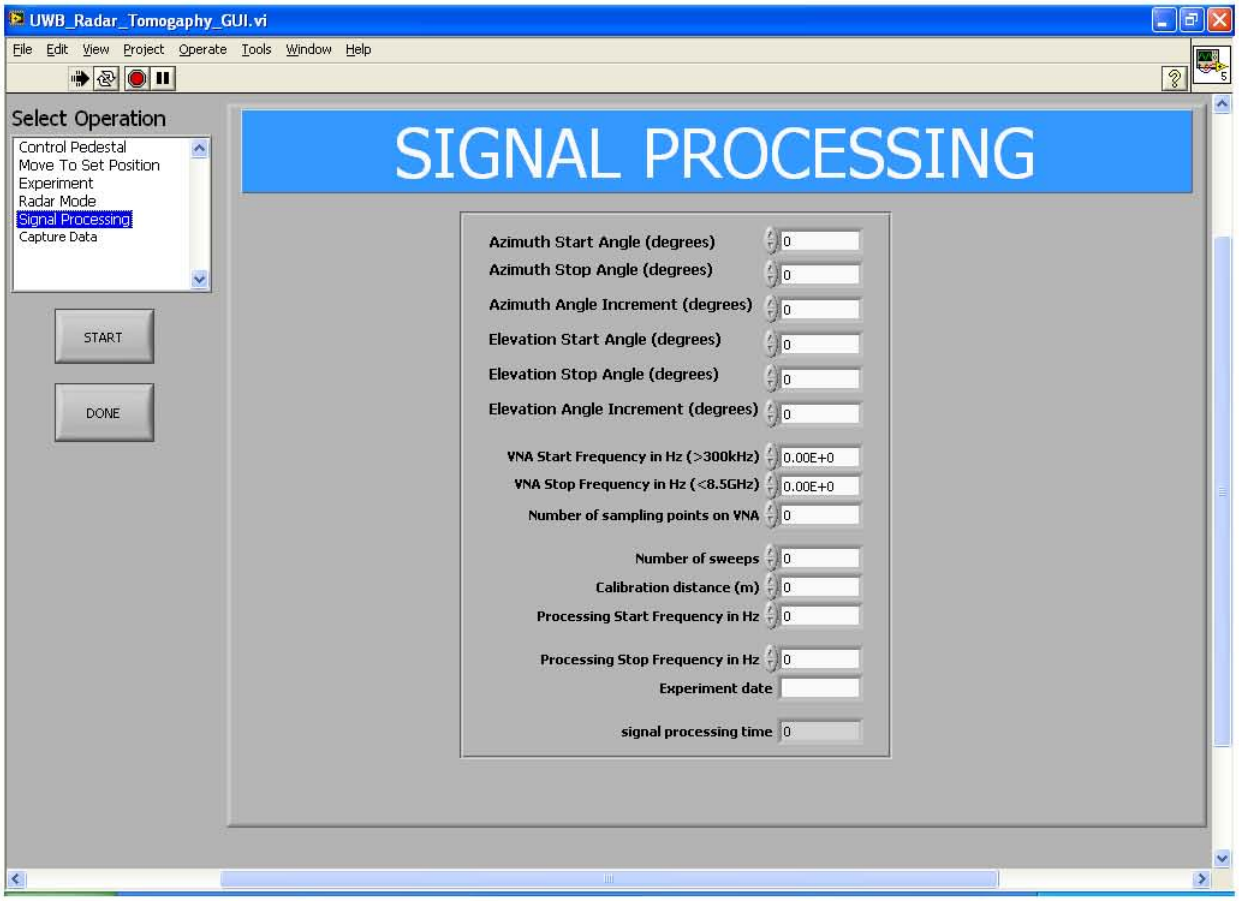

C.6 Capture Data Function

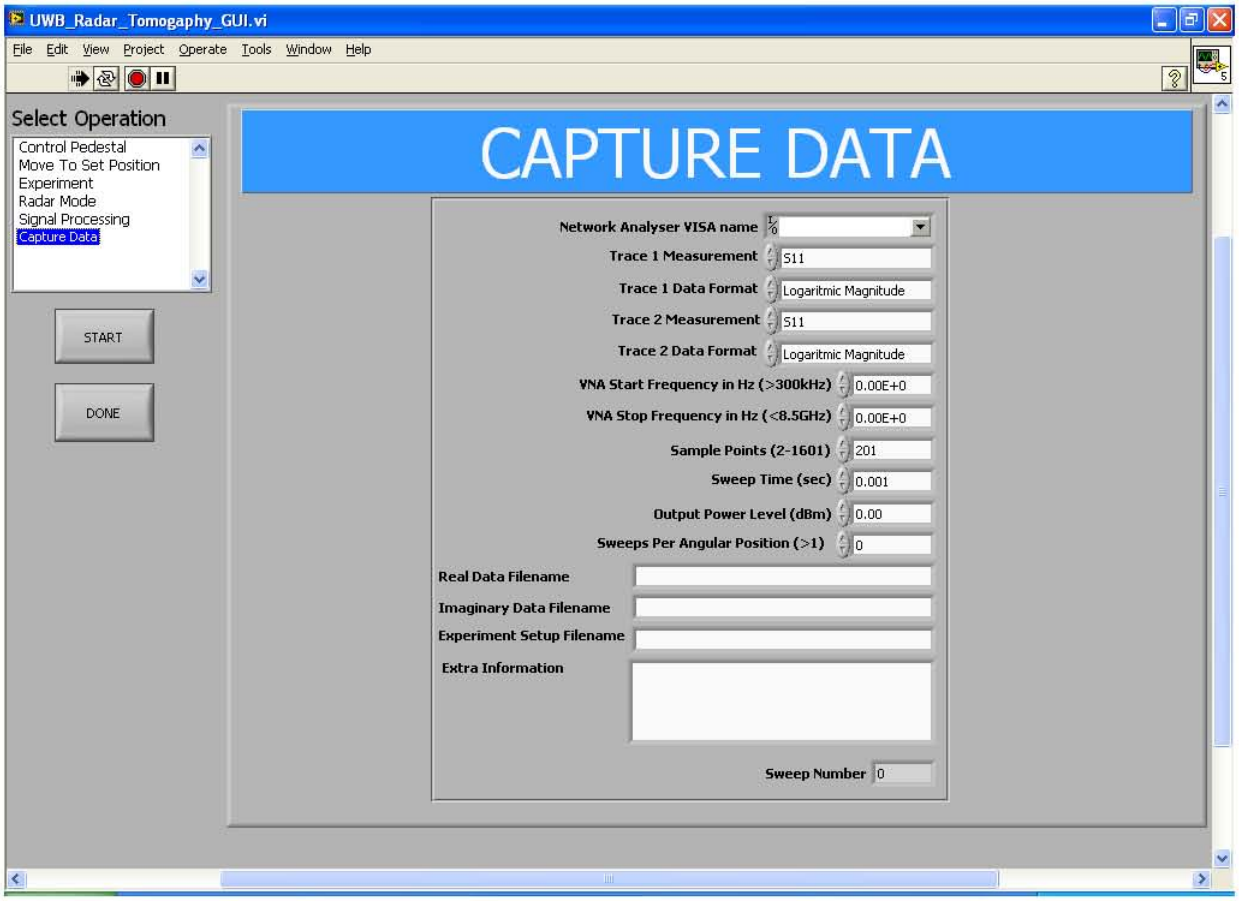

Appendix D

Software Source Code

The software source code for this project can be obtained by contacting the author or Assoc. Prof. A.J.Wilkinson.

Bibliography

[1] Federal communication commission (fcc) - rules & regulations.

[2] *Radar Range Profiles*, chapter 2, pages 7–21. Joris Portegies Zwart, 2003.

[3] *UWB Tomographic Radar Imaging of Penetrable and Impenetrable Objects*, 2009.

[4] W. N. A. Cilliers. Helicopter parameter extraction using joint time-frequency and tomographic techniques. Technical report, Council for Scientific and Industrial Research (CSIR), 2008.

[5] A. P. A.J.Wilkinson. Radar/sonar signal processing. EEE4001F, 2010.

[6] C. A. Balanis. *Antenna Theory Third Edition Analysis and Design*. A John Wiley & Sons, Inc., Publication, 2005.

[7] M. E. Bwakea. Ultra-wideband radar tomography imaging, 2010.

[8] N. C.F.Hu, J.D.Xu and L.X.Zhang. A low-frequency rcs measurement system in an anechoic chamber. Technical report, Northwestern Polytechnic University, China, 2010.

[9] P.-Y. Choa. Ultra-wideband phased array radar for short-range imaging applications. Master's thesis, University of Cape Town, 2009.

[10] N. Dahlback. Implementation of a fast method for reconstruction of isar images. Master's thesis, Linkopings University, 2003.

[11] J. Dr.B.Levitas. Uwb radar high resolution isar imaging. Technical report, 2009.

[12] C. for Scientific and I. Research. Radar theory. CSIR Ledger Vacation Work Program, 2009.

[13] B. Forssell. High-resolution radar (hrr) waveforms. In Lecture Notes in Navigation Systems, Norwegian University of Science and Technology, 2005.

[14] N. K. Hui. Radar imaging using isar, 1998.

[15] M. G. Hussain. Ultra-wideband impulse radar - an overview of the principles. Technical report, Kuwait University, 1998.

[16] N. Instruments. Reducing the effects of noise in a data aquisition system by averaging, September 2006.

[17] J.D.Taylor, editor. *Ultra-Wideband Radar Technology*. CRC Press LLC, 2001.

[18] A. Kak and M. Slaney. *Principles of Computerized Tomographic Imaging*. IEEE Service Center,Piscataway, NJ, 1988.

[19] A. P. R. B. I. C. M. Klemm, J. Leendertz. Clinical and phantom trials of a uwb imaging radar. Technical report, Centre for Communications Research, University of Bristol, UK.

[20] W. H. M.A. Richards, J.A. Scheer. *Principles of Modern Radar, Basic Principles*. Scitech Publishing Inc., 2010.

[21] M. Martorella. Bistatic isar imaging formation in presence of bistatic angle changes and phase synchronisation errors. Technical report, University of Pisa, Italy.

[22] S. S. J. M.Guardiola, L.Jofre. Toward 3d uwb tomographic imaging system for breast tumor detection. Technical report, Universitat Politecnica de Catalunya, 2009.

[23] Microwave101.com. S-parameters, December 2009.

[24] A. R. I. M.Klemm, J.Leendertz. Clinical and phantom trials of uwb imaging radar. Technical report, Centre for Communications Research, University of Bristol, UK, 2010.

[25] D. F. Nicolls. Discrete-time signals and systems. EEE4001F, 2010.

[26] J. C. Russel. A control system and application program invterface (api) for an elevation over azimuth tracking pedestal. October 2008.

[27] A. Schutz. Inverse synthetic aperture sonar imaging using a rotating platform. October 2010.

[28] M. E. C. S.Demirci, H.Cetinkaya and A.Vertiy. Back-projection algorithm for isar imaging of near-field concealed objects. Technical report, Department of Electrical-Electronics Engineering, Mersin University International Laboratory for High Tech (ILHT), Material Institute, 2011.

[29] R. Sharma. Analysis of circular aperture sar image formation. Technical report, Norhrop Grumman Electronic Systems, 7323 Aviation Boulevard, Valtimore, MD 21240, 2009.

[30] M. Skolnik. *Radar Handbook*. McGraw-Hill Professional, 2008.

[31] J. S.Primak and B.Zhang. Microwave image reconstruction methods. Technical report, The University of Western Ontario, London, 1998.

[32] J. Taylor, editor. *Introduction to Ultra-Wideband Radar Systems*. CRC Press, 1995.

[33] A. Technologies. *Agilent Network Analyzer Basics*. http://cp.literature.agilent.com/litweb/pdf/5965-7917E.pdf.

[34] A. d. R. Victor C.Chen and R. Lipps. Bi-static isar range-doppler imaging and resolution analysis. Technical report, Radar Division Naval Research Laboratory Washington DC, 2009.

[35] M. Zhenbo Zhu. Bistatic inverse synthetic aperture radar imaging. Technical report, Naval University of Engineering, China, 2005.